# Design, Optimisation and Experimental Validation of a Soft X-Ray Compton Backscattering Experiment at the AWAKE Run 2 Test Injector



Vlad Mușat

Jesus College

University of Oxford

A thesis submitted for the degree of

*Doctor of Philosophy*

Hilary 2026

*"Imagine how much harder physics would be if electrons had feelings."*

— Richard P. Feynman

*"For every subtle and complicated question, there is a perfectly simple and straightforward answer, which is wrong."*

— David Graeber, *Debt: The First 5000 Years*

# Abstract

This thesis presents a soft X-ray Compton backscattering (CBS) experiment carried out at the AWAKE Run 2 Test Injector (ARTI) facility. The ARTI electron beamline was optimised to maximise the photon flux produced in the CBS interaction. A detailed numerical model of the beamline was developed using the RF-Track particle tracking code and employed to predict the properties of the generated CBS radiation.

The RF-Track model was benchmarked against experimental electron beam measurements to ensure an accurate representation of the machine. The validated model was then used to define a target parameter space capable of delivering a low-emittance, high-density electron bunch at the interaction point with a laser pulse. Experimentally, the optimisation involved precise alignment of key lattice elements, namely the solenoid and laser position on the cathode, followed by parametric scans made to identify the inputs that maximise the scattered photon flux. During beamline characterisation, a previously unidentified source of beam halo in the photoinjector was observed. Combined experimental studies and simulations revealed that the halo originated from multiple reflections within the laser's optical transport system.

For the CBS experiment, a dedicated infrared laser transport line and an interaction chamber equipped with a movable microchannel plate X-ray detector were installed. A measurement campaign was conducted to achieve precise temporal and spatial overlap of the electron and laser beams. Successful alignment resulted in the detection of a CBS signal, enabling parametric studies of the interaction region. The measured photon yield and trends were found to be in good agreement with simulations performed using the RF-Track CBS module.

# Contents


**1 Introduction** **1**

1.1 Particle Accelerators . . . 3

1.2 Particle colliders . . . 3

1.2.1 Future Colliders . . . 4

1.2.1.1 The Compact Linear Collider (CLIC) . . . 5

1.3 The AWAKE Experiment . . . 9

1.4 Beam Dynamics . . . 11

1.4.1 Coordinate system . . . 11

1.4.2 Bending magnets . . . 12

1.4.3 Focusing magnets . . . 13

1.4.4 Hill's equation . . . 14

1.4.5 Twiss parameters . . . 15

1.5 Compton backscattering . . . 17

1.5.1 Applications of CBS sources . . . 19

1.5.2 Theory of Compton backscattering . . . 21

**2 The AWAKE Run2c Test Injector (ARTI)** **26**

2.1 Accelerator baseline . . . 26

2.1.1 Electron gun . . . 26

2.1.2 Solenoid . . . 28

2.1.3 Imaging viewport . . . 29

2.1.3.1 YAG screen . . . 30

2.1.3.2 OTR screens . . . 31

2.1.4 Dipole spectrometer . . . 35

2.1.5 Faraday cup . . . 37

2.1.6 Vacuum pumping port . . . 37
2.1.7 Electron beam characterisation . . . 37
2.2 Photoinjector laser . . . 39
2.2.0.1 UV laser beamline . . . 41
2.2.0.2 IR laser beamline . . . 44
2.2.0.3 Characterisation of the IR laser beam at the IP . . 45

**3 Optimisation of the ARTI Beamline 51**
3.1 RF-Track . . . 51
3.1.1 RF-Track CBS module . . . 52
3.1.1.1 Implementation . . . 53
3.1.2 Algorithm . . . 54
3.2 RF-Track benchmark against other codes . . . 54
3.3 RF-Track Model of ARTI . . . 61
3.4 ARTI optimisation in RF-Track . . . 64
3.4.1 Optimised beam parameters . . . 65
3.4.2 $q$-Gaussian beam shaping at the interaction point . . . 68
3.5 Quantum efficiency study of the photoinjector cathode . . . 71
3.6 Beam-based alignment of the ARTI beamline . . . 73
3.6.1 A novel offset inference method . . . 75
3.6.2 Experimental correction of the ARTI beamline offsets . . . 81
3.6.2.1 Alignment of the laser position on the cathode . . . 82
3.6.2.2 Alignment of the solenoid . . . 85
3.6.3 Results from the lattice element alignment . . . 90
3.7 Parametric scans of the beam parameters . . . 93
3.8 Novel beam halo source studies at ARTI . . . 101
3.8.1 Measurement of the beam halo . . . 102
3.8.1.1 Benchmark of the YAG screen imaging set-up against the OTR screen set-up . . . 102
3.8.1.2 Halo-Core Percentage . . . 104
3.8.2 Mechanism for the halo generation at ARTI . . . 106
3.8.2.1 Observation of a different energy bunch at ARTI . . 107

3.8.2.2 Photoinjector halo generation via ps-delayed laser pulses generating additional bunches in the same RF pulse . . . 110
3.8.3 Characterisation of the novel halo source observed at ARTI . 112
3.8.3.1 Experimental derivation of the time delay between the two laser pulses . . . 113
3.8.4 RF-Track reconstruction of the measured beam profile . . . . 115
3.8.5 Halo mitigation strategies . . . 116
3.9 Conclusions from the optimisation of the ARTI beamline . . . 117

**4 A Soft X-ray CBS Experiment at CTF2 119**
4.1 The Electromagnetic Water Window . . . 119
4.2 X-ray detector set-up . . . 121
4.2.1 The microchannel plate . . . 123
4.2.2 The vacuum detection chamber . . . 128
4.2.3 Measurement of the MCP's electrical continuity . . . 128
4.2.4 Detector calibration . . . 130
4.2.4.1 Measurement of the MCP's detection efficiency . . . 132
4.2.4.2 Measurement of the gain response . . . 135
4.3 Background mitigation for the MCP . . . 140
4.4 Alignment of the CBS X-ray to the MCP detector . . . 147
4.5 Temporal alignment of the laser and electron beams . . . 149
4.6 Spatial alignment of the laser and electron beam . . . 152
4.7 Measurement of the CBS signal . . . 158
4.7.1 Parametric scans of the CBS signal . . . 159
4.7.1.1 Realistic simulations of the output photon flux from the CBS interaction . . . 162
4.7.1.2 Main results of the CBS experiment at ARTI . . . 163
4.8 Conclusions and achievements of the CBS experiment . . . 171

**5 Conclusions and Further Work 177**

**A RF-Track Example Code 180**

**Bibliography** **183**

# List of Figures


1.1 The elementary particles of the Standard Model of Particle Physics. (image credit: Wikipedia) . . . . . 2
1.2 Schematic layout of the CLIC complex at 380 GeV, with a double beam-delivery system (BDS) operating with two detectors. (image credit: Erik Adli) . . . . . 6
1.3 The CLIC main linac footprint near CERN, showing the inital 380 GeV and a 1.5 TeV high-energy stage. (image credit: CLIC) . . 7
1.4 The CLIC X-band accelerating structure. Waveguides are shown in the foreground, which transmit power from the source (e.g., klystron or drive beam) to the accelerating structure. (image credit: CLIC) . 8
1.5 Schematic of the AWAKE set-up (credit: AWAKE). . . . . 10
1.6 The co-moving coordinate system used to describe particle motion. (credit: [34]) . . . . . 12
1.7 Single particle trajectory in a dipole bend. (credit: [34]) . . . . . 13
1.8 Field and force components in a quadrupole. (credit: [34]) . . . . . 14
1.9 The phase space ellipse of particle motion in the x-x'-plane. (credit: [34]) . . . . . 16
1.10 Photo of the Compact X-ray Light Source (CXLS) at Arizona State University (ASU), spanning 9 metres in length. (credit: ASU) . . . . 18
1.11 Partial landscape of CBS sources. Main figure of merit parameters are used for positioning the CBS sources on the landscape, the photon beam energy and the total scattered photon flux, respectively. The sources are classed based on whether they are based on a storage ring, linac, or ERL, and also on whether they are in the design phase, commissioned, or existing. Adapted from [52]. . . . . 19

1.12 Schematic of the Compton backscattering process. The input laser of photon energy $E_L$ is up-scaled to an X-ray of energy $E_X$. . . . . 22
1.13 Energy spectrum of the Compton backscattered photons for three different collimation half-angles, $\theta$ = 1.0 mrad (red), 0.8 mrad (green), and 0.5 mrad (blue). The horizontal axis shows the scattered photon energy $E'$ in keV, while the vertical axis represents the differential photon yield normalised per $10^4$ electrons and per keV bin. The vertical grey band indicates the 0.1% energy window around the spectral peak. . . . . 24

2.1 CAD design of the ARTI electron gun set-up. The distance from the cathode to the viewport is 0.57 m. Not shown: the dipole spectrometer, pumping port, X-ray detection chamber, and Faraday cup. . . . . 27
2.2 Schematic diagram of the AWAKE Run2 Test Injector set-up used for the CBS experiment. . . . . 28
2.3 CAD design of the double-coil solenoid used for ARTI. . . . . 30
2.4 One-dimensional longitudinal field profiles of the electron gun and the solenoid as a function of the longitudinal coordinate $s$. The accelerating electric field of the gun and the magnetic field of the solenoid are shown in normalised units, with each field scaled to its respective peak amplitude, to allow direct comparison of their spatial distributions. The gun field is localized near the cathode region, whereas the solenoid field extends over a broader region to provide transverse focusing and emittance compensation. . . . . 31
2.5 Technical drawing of the screen slots available from the actuator installed at ARTI. . . . . 32
2.6 Photos of the two versions of the OTR screens used at ARTI. The first design (a) was robust and provided a good light yield, but it was too thick for the laser to pass through. The second design (b) consisted in a 99.5% pure Aluminium foil of 25 µm thickness. . . . . 33

2.7 Photo under a microscope of one of the holes laser-cut into the OTR screen. The laser's excellent resolution allowed for a consistently round shape, and a diameter of 619 µm. . . . . 34
2.8 Dependence of the beam energy (left) and relative energy spread (right) on the RF phase, as measured for the ARTI beamline. The beam energy exhibits a maximum near on-crest acceleration, while the energy spread increases monotonically with RF phase over the scanned range. Error bars represent the statistical uncertainties of the measurements. . . . . 35
2.9 Beam profile obtained from the dipole spectrometer, through a fluorescent Chromox screen. Note the characteristic tail of the profile, proportional with the energy spread. . . . . 36
2.10 Sensitivity measurements of the electron beam. (a) Shot-to-shot stability measurements of the horizontal and vertical electron beam position, as seen on the OTR screen. (b) Shot-to-shot stability measurements of the horizontal and vertical RMS spot size of the electron beam, from the OTR screen. (c) Shot-to-shot stability measurement of the bunch charge, performed with the Faraday cup. 38
2.11 Schematic of the laser transport and timing systems installed at the ARTI beamline for the Compton backscattering experiment. The infrared (red) and ultraviolet (blue) laser beamlines originate from the Pharos laser system and are transported from the laser laboratory to the accelerator area. The UV beam is directed onto the photocathode for electron bunch generation, while the IR beam is delivered to the interaction point (IP) for Compton backscattering. The optical system incorporates attenuation, beam steering, focusing, and timing diagnostics to control the laser spot size, pulse energy, and temporal overlap between the laser and electron beams. (credit: Eduardo Granados) . . . . . 40

2.12 Autocorrelation measurements of the longitudinal pulse profiles for the UV (a) and IR (b) laser systems at their respective working points. The normalised laser intensity is plotted as a function of the autocorrelator's temporal delay for different operating settings. High-frequency noise was reduced using a moving-average filter. The pulse duration was determined from the deconvoluted full width at half maximum obtained via a Gaussian fit to the autocorrelation traces. (credit data: Eduardo Granados) . . . . . 41
2.13 Representative attenuation scans of the UV (a) and IR (b) laser systems. For the UV laser, the attenuator setting is varied to control the emitted electron bunch charge, while for the IR laser the pulse energy is monitored as a function of attenuator position. In both cases, the measured data are fitted with a sinusoidal function, as indicated in the legend, reflecting the periodic transmission of the rotating attenuator. . . . . 42
2.14 Typical image on the virtual cathode of the UV laser at the cathode location. The left plot corresponds to the UV laser profile, while the plots on the right correspond to horizontal (top) and vertical (bottom) projections of the 2D image data. . . . . 43
2.15 Photograph of the last section of the IR beamline, including the focus and motorised mirror. . . . . 45
2.16 The measured IR laser profile at the interaction point, using the same digital camera used to observe the electron beam transverse distribution. Gaussian fits of the horizontal and vertical distributions are included. Note that the beam size measurement is limited by the camera pixel size. . . . . 46

2.17 Experimental characterisation of the IR laser beam at the CBS interaction point. (a) Samples of the IR centroid in space. (b) Shot-by-shot stability measurement of the horizontal and vertical beam centroid. (c) Shot-by-shot stability measurement of the peak signal registered by the beam profiler, proportional to the beam intensity. (d) Shot-by-shot stability of the effective $1/e^2$ beam diameter. (e) Shot-by-shot variation of the IR $1/e^2$ diametral spread around the centroid. The black circle corresponds to the measurement average. (f) Sample of the transverse beam profile as measured by the beam profiler. (data credit: Eduardo Granados) . . . . . 48
2.18 Measurements of IR beam parameters at the IP for different positions of the delay stage. (a) Pointing stability for four different delay stage positions. (b) Shot-by-shot measurements of the beam intensity for the same four position settings, showing beam clipping at 40 mm. (data credit: Eduardo Granados) . . . . . 49

3.1 Comparison of total flux and average brilliance results from RF-Track with their corresponding referenced values. The errors obtained in RF-Track for both average brilliance and total flux are too small to be noticeable. . . . . 57
3.2 Comparison of plots from ThomX simulation using RF-Track (top) and CAIN (bottom). (a) The photon energy spectrum in a 1 mrad and 5 mrad collection angle, along with the full angle spectrum. (b) The transverse source size. (c) The angular emission distribution. (d) The number of photons/mrad$^2$/s against energy and collection angle. . . . . 58
3.3 Comparison of plots from BriXSinO simulations using RF-Track (top) and CAIN (bottom), similarly to Fig. 3.2. An added contribution, showcased in RF-Track, is the CBS interaction with a linearly polarised laser. . . . . 59

3.4 Comparison of cERL photon spectra computed in CAIN and RF-Track for different values of emittance. CAIN photon spectra at (a) $\epsilon^N = 1\,\text{mm mrad}$ and (c) $\epsilon^N = 5\,\text{mm mrad}$. RF-Track photon spectra at (b) $\epsilon^N = 1\,\text{mm mrad}$ and (d) $\epsilon^N = 5\,\text{mm mrad}$. Figures for three distinct collection angles are shown, along with the full energy spectrum. The data used for the plots corresponding to the CAIN simulation were taken from [50]. . . . . 62
3.5 Tracking of the electron beam RMS spot size, bunch length, transverse emittance, and 4D normalised emittance along the ARTI beamline for beam configurations optimised for the Compton backscattering experiment. The optimisation was performed independently for four distinct bunch charges. The blue and red shaded regions indicate the longitudinal locations of the electron gun and solenoid magnet, respectively. . . . . 66
3.6 Sampler of $q$-Gaussian distributions (a), and a Gaussian and $q$-Gaussian fit of the optimised electron beam distribution at the IP (b). Note that for $q \to 1$, the distribution is equivalent to a Gaussian. $q > 1$ define heavy-tailed distributions, while $q < 1$ generate tail cut-offs. The $q$-Gaussian fit parameters from Eq. 3.1 in (b) are $q = 2.6$ and $\beta = 6117$. . . . . 69
3.7 Characterisation of the quantum efficiency of the copper photocathode installed at ARTI for three UV laser spot sizes. (a) Measured bunch charge as a function of incident UV pulse energy, showing the onset of charge saturation at higher laser energies. (b) Corresponding quantum efficiency as a function of UV pulse energy for each laser spot size. . . . . 72
3.8 Quantum efficiency of the copper photocathode as a function of the incident laser fluence for three different RMS laser spot sizes. The data demonstrate an approximately linear dependence of the quantum efficiency on fluence within the investigated range, with variations arising from the different transverse spot size configurations. 73

3.9 Evolution of the transverse normalised emittance as a function of transverse displacement for the gun and solenoid sections. The horizontal and vertical emittances are shown separately. The secondary axis indicates the corresponding relative increase in emittance with respect to the nominal aligned configuration. The results illustrate the sensitivity of beam quality to transverse misalignment in both elements. . . . . 75
3.10 Comparison of measured and simulated beam response in a solenoid scan. The beam centroid position in the horizontal and vertical planes (left) and the RMS transverse spot size (right) are shown as functions of the solenoid magnetic field. Experimental data are compared with RF-Track simulations performed using the offset parameters obtained from the simplex-based inference procedure. . . . 78
3.11 Comparison between the measured transverse beam profile and RF-Track simulation. The measured distribution is shown together with the corresponding simulated profile and a Gaussian fit. . . . . 79
3.12 Normalised measured phase scan compared with RF-Track simulations performed for different accelerating gradients. The experimental data are overlaid with simulated phase scans corresponding to gradients between 100 and 120 MV/m. The best agreement is obtained for an accelerating gradient of 112 MV/m, indicating this value as the effective operating gradient. . . . . 80
3.13 RF-Track simulations of the beam trajectory from cathode to the interaction point, provided the derived offsets are implemented. The red lines define the beam envelope at $1\sigma$. . . . . 82
3.14 Transverse electron beam profile under RF focusing at ARTI. This configuration was employed to align the laser on the photocathode with respect to the gun axis. The two-dimensional intensity distribution is shown together with the corresponding horizontal and vertical projections. The beam was recorded on a YAG screen positioned 0.57 m downstream of the photocathode. . . . . 84

3.15 Beam-based alignment of the ARTI photocathode laser to the gun axis. The electron beam position under an RF phase scan is shown for three different iterations of the alignment: before the alignment process, after the initial laser shift (required in order to deduce the optimal position), and after the alignment. The lack of beam drift under a change in beam energy, as seen in the post-alignment data, indicates that the laser has been centred on the gun axis. . . . . 86
3.16 Simulated dependence of the transverse beam position on solenoid strength for a range of imposed horizontal (a) and vertical (b) offset values. The evolution of the beam trajectory with magnetic field is shown for different initial misalignments. These simulations were used to identify the dominant transverse offset component during the solenoid alignment procedure by comparison with the measured beam response. . . . . 87
3.17 Measured transverse electron beam position for different values of the solenoid magnetic field strength. Each data point represents the beam centroid position recorded at a fixed solenoid setting, illustrating the field-dependent trajectory of the beam during the solenoid scan. . . . . 88
3.18 Measured electron beam trajectory obtained from a solenoid strength scan, overlaid with RF-Track simulations for a range of assumed transverse solenoid offset values. The simulated trajectories correspond to increasing horizontal and vertical offsets, allowing direct comparison with the experimental data to determine the effective solenoid misalignment. . . . . 89
3.19 RMS vertical electron spot size at the interaction point as a function of solenoid magnetic field strength, measured before and after beamline alignment. The post-alignment scan exhibits a more symmetric dependence and a reduced minimum spot size. The beam profile was recorded on a YAG screen. . . . . 91

3.20 Comparison of solenoid scans measured with a YAG screen and an OTR screen, illustrating saturation effects at high charge densities near the beam focus. The RMS horizontal (left) and vertical (right) beam sizes are shown as a function of the solenoid magnetic field strength. Around the focal point, the YAG measurement exhibits a plateau due to scintillator saturation, leading to an overestimation of the minimum beam size. Linear fits to the low- and high-field regions are included to indicate the apparent waist position and to highlight the discrepancy between the saturated YAG profile and the unsaturated OTR measurement. . . . . 92
3.21 Experimental measurement of the bunch charge as a function of RF phase, performed at ARTI. . . . . 95
3.22 Experimental scan of the laser focus motor coordinate against the bunch charge (left), along with the measured RMS laser spot size on the cathode against the focus motor coordinate (right). The later plot was used to calibrate the first. Outside the saturation effect of the cathode (occurring for small enough spot sizes), the dependence of the extracted bunch charge against the laser spot size appears strictly linear. Bunch charge measurements were taken using a Faraday cup, while the laser spot size measurements were taken using the virtual cathode set-up. . . . . 96
3.23 The dependence of the cathode laser spot size (left) and position (right) on the motorised focus setting. Note the noticeable drift in the laser beam position under a change in focus, indicating a misalignment of the lenses in the focusing telescope. The measurement was taken using the virtual cathode set-up at ARTI. . . . . 97
3.24 Comparisons between simulations (left) and measured data (right) of electron beam size as a function of the solenoid strength with respect to the RF phase (top) and laser spot size (bottom). . . . . 98
3.25 RF-Track-simulated dependence of the beam energy on the laser offset. . . . . 100

3.26 Comparisons between simulated and measured data corresponding to the minimum electron spot size sigma in the horizontal and vertical, against the RF phase (top) and laser spot size on the cathode (bottom) for the horizontal (left) and vertical (right) axes. . . . . 101
3.27 Measured transverse electron beam distribution on the YAG screen at the solenoid focal point (a). Comparison of the corresponding horizontal beam profile obtained from the two primary analysis methods used at ARTI, namely the sliced profile and the projected profile (b). . . . . 103
3.28 Comparison of YAG and OTR screen measurements of a solenoid scan at ARTI, against RF-Track simulations. The scans tracked both the horizontal (a) and vertical (b) spot sizes. The measured RMS electron spot size is plotted against its corresponding solenoid magnetic field value. Note that the YAG measurement predicts consistently higher values for the RMS beam size measurement than the OTR. The OTR and RF-Track beam size measurements match within less than one sigma. . . . . 105
3.29 The measured profile of the electron beam, optimised for the smallest spot size. Gaussian fits of the beam core and halo are shown for the horizontal and vertical distributions. . . . . 106
3.30 Two-dimensional beam profile taken from the ARTI dipole spectrometer, showcasing the separation of the core and halo bunches. . 107
3.31 Measurement of the bunch charge versus the spectrometer dipole current. The dipole current is quoted in Ampere units. Besides the Gaussian distribution observed for the main electron bunch, there is an additional "bump" in charge observed for a dipole current in the range 0-0.1 A. The additional distribution would correspond to an additional bunch different in energy and charge to the main one. 108
3.32 Spectrometer beam profile obtained for an RF-phase corresponding to an equal bunch charge for both the halo and core profiles. . . . . 109
3.33 Gaussian fits of the beam core and halo from the horizontal distribution, measured using the dipole spectrometer. . . . . 110

3.34 Schematic showing the generation of secondary time-delayed laser pulses through multiple reflection. . . . . 112
3.35 Normalised experimental RF phase scan showing the beam energy as a function of RF phase. The circled regions highlight the energy difference between the core and halo components of the bunch, illustrating their distinct phase-dependent energy response. . . . . 114
3.36 Beam profiles generated with RF-Track, showing the halo (a), core (b), and reconstructed beam profile (c). For each plot, the 2D beam profile is shown on the left, while the right contains the horizontal (top) and vertical (bottom) projections, respectively. . . . . 117

4.1 Samples of 2D cryo imaging performed with a laboratory water window X-ray source. Taken from [72]. . . . . 120
4.2 Calculated X-ray transmission in air as a function of propagation distance for photon energies between 1 and 10 keV. The horizontal axis shows the distance travelled in air, while the vertical axis represents the transmitted fraction of the initial intensity. For photon energies below 1 keV, such as the 200 eV X-rays generated in the CBS experiment, the attenuation length in air is on the order of millimetres, resulting in nearly complete absorption over very short distances. . . . . 122
4.3 Structure and operating principle of an MCP (a) and a schematic of the MCP used for the CBS experiment, model F9890-13 (b). (credit: Hamamatsu) . . . . . 123
4.4 Measured voltage waveform from the microchannel plate detector corresponding to a single X-ray event. The horizontal axis shows the time relative to the trigger in nanoseconds, while the vertical axis represents the measured voltage in millivolts. The pulse has a full width at half maximum of approximately 900 ps. . . . . 124
4.5 Measured absolute (a) and relative (b) X-ray detection efficiency for a microchannel plate, versus the incident photon energy. The MCP configuration used for the CBS experiment corresponded to the one used for the Parkes et al. study from 1970. (credit: Hamamatsu) . . 125

4.6 Wiring example of the MCP, that was used during its operation at ARTI. (credit: Hamamatsu) . . . . . 127
4.7 The integrated vacuum chamber housing the microchannel plate detector (left), and a CAD sketch of the detection chamber (right). 129
4.8 Measurement of the linearity response of the MCP used for the CBS experiment. The input MCP voltage is plotted as a function of the induced strip current. The linear fit of the data was used to derive the MCP internal resistance of $52.08 \pm 0.27\,\mathrm{M\Omega}$. . . . . 130
4.9 Schematic of the Fe-55 radioactive source used in the MCP calibration experiment. The source was electrochemically deposited on a copper plate and sealed in a welded monel metal capsule with a brazed beryllium window. The outer diameter $D$ is $7.925 \pm 0.025\,\mathrm{mm}$, the window diameter $d$ is $4.0 \pm 0.1\,\mathrm{mm}$, and the capsule height $H$ is $5.0 \pm 0.2\,\mathrm{mm}$. . . . . 131
4.10 Photo of the 3D-printed holder for the Fe-55 radioactive source used to calibrate the MCP detector. The Fe-55 source is shown placed in the holder, with a mask screwed in to hold it in place. . . . . 133
4.11 Example of a typical oscilloscope trace made during the measurement of the MCP's detection efficiency. The measured waveform voltage is plotted as a function of the time relative to the oscilloscope trigger. . . . . 134
4.12 The gain of the microchannel plate used for the CBS experiment, plotted as a function of the input supply voltage. . . . . 137
4.13 Gain calibration curves obtained with an Fe-55 source from the MCP. The peak-to-peak (a) and area (b) of the signal waveform is shown as a function of the input supply voltage. . . . . 138

4.14 Pulse height distributions (PHDs) of the microchannel plate (MCP) detector for supply voltages between 1600 V and 2400 V. The horizontal axis shows the waveform area (or the integrated pulse charge multiplied by 50 Ω) in units of pVs, while the vertical axis represents the number of recorded events. As the supply voltage increases, the distribution shifts towards larger pulse areas and exhibits a broader spread, indicating increased gain and a corresponding rise in measurement fluctuations. . . . . 139
4.15 Pulse height resolution versus the applied supply voltage, as measured for the MCP. . . . . 140
4.16 Detection efficiency of the MCP versus the UV wavelength. (Taken from: [134]) . . . . . 142
4.17 Comparison of the MCP voltage waveforms recorded under two operating conditions: with the ultraviolet (UV) laser incident on the cathode and the RF system inactive ("UV ON"), and with both the UV laser and RF field active ("UV ON, RF ON"). The horizontal axis shows time after trigger in seconds, and the vertical axis represents the measured signal voltage in volts. . . . . 143
4.18 The MCP waveform area (left) and peak-to-peak (right) shown as a function of the motor coordinates of the UV laser intensity attenuator. The setting corresponding to the absence of RF signal and presence of the UV laser on the cathode is shown is included, along with the setting where the RF signal is active and the UV laser reaches the cathode. The plots indicate that there is a significant background detected by the MCP from the reflection of the UV laser from the cathode. . . . . 144
4.19 Scan of the MCP signal area versus the magnetic strength of ARTI's solenoid, in the background-only case. . . . . 145
4.20 Scan of the MCP signal area versus the magnetic strength of ARTI's dipole, in the background-only case. . . . . 146

4.21 Two dimensional scan of the signal area against the position of the electron beam impinging on the MCP. The shape of the MCP's active area is clearly distinguishable as the maximum signal area plateau. UVCATHOR and UVCATVER represent the controls for the horizontal and vertical position of the UV laser on the cathode, respectively. . . . . 148
4.22 Schematic of the set-up used to align the UV and IR laser beams. . 150
4.23 Calibration plot for the motorised delay stage installed at ARTI. The temporal offset between the IR and UV laser beams (measured in picoseconds) is shown versus the position coordinate of the delay stage. The motor's step position was correlated to the time offset of the laser beam measured by an ultrafast photodiode using a 10 GHz oscilloscope. . . . . 152
4.24 Waveform traces recorded with the 10 GHz oscilloscope during the temporal alignment of the UV and IR laser pulses for the CBS experiment. The measured voltage amplitude (V) is shown as a function of time relative to the trigger (ns). The signals prior (a) and after (b) the temporal alignment are displayed. . . . . 153
4.25 The first design of the OTR screen, as seen installed under vacuum. The holes placed diagonally across the screen's surface were made using a laser cutter, and subsequently used for the spatial alignment of the laser and electron beams. . . . . 154
4.26 Spatial alignment scan used to centre the IR laser beam on one of the apertures of the OTR screen. The measurement was performed using the first design iteration of the OTR screen. The horizontal and vertical axes represent the transverse displacement of the mirror directing the IR beam towards the IP, while the colour scale shows the integrated pixel intensity (a.u.) corresponding to the laser signal transmitted through the aperture. . . . . 155

4.27 Two-dimensional spatial scan used to align the electron beam with the centre of an aperture in the first-generation OTR screen. The horizontal and vertical axes show the transverse displacement of the UV beam on the cathode in millimetres, while the colour scale represents the integrated pixel intensity in arbitrary units. The minimum in the pixel sum corresponds to the beam passing through the aperture, thereby identifying the optimal alignment position. . . 156
4.28 Two-dimensional spatial scan used to align the electron beam with the laser-bored aperture in the second-generation OTR screen. The horizontal and vertical axes indicate the transverse displacement of the UV beam on the cathode in millimetres, while the colour scale represents the integrated pixel intensity in arbitrary units. Compared to the initial OTR design, the central minimum corresponding to the beam passing through the aperture is confined to a significantly smaller region, demonstrating the improved localisation and alignment sensitivity of the modified OTR screen. . . . . 157
4.29 Two-dimensional image of the electron beam profile at the interaction point (IP), recorded using the OTR screen. The horizontal and vertical axes represent the transverse beam coordinates in millimetres, while the colour scale indicates the integrated pixel intensity in arbitrary units. The image reveals a tightly focused beam core with a slight tilt in the transverse plane. . . . . 160
4.30 Averaged CBS signal and background response from the MCP. The measured voltage (Volts) is plotted as a function of time relative to the trigger (µs). . . . . 161
4.31 Histogram of the number of detected photons by the MCP, as predicted by RF-Track. The histogram was obtained from 1000 samples, and the laser and electron beam jitter parameters at the interaction point were included. The distribution peaks at 13 photons per bunch. . . . . 164

4.32 Scan of the number of CBS photons detected by the MCP against the arrival time of the IR laser at the IP. Experimental measurements (red) are compared with simulations performed in RF-Track (blue). The error bars in the experimental data correspond to the standard error on the mean. . . . . 165
4.33 Scan of the number of CBS photons detected by the MCP against the horizontal position of the IR laser at the IP. Experimental measurements (red) are compared with simulations performed in RF-Track (blue). The error bars in the experimental data correspond to the standard error on the mean. . . . . 166
4.34 Scan of the number of CBS photons detected by the MCP against the vertical position of the IR laser at the IP. Experimental measurements (red) are compared with simulations performed in RF-Track (blue). The error bars in the experimental data correspond to the standard error on the mean. . . . . 167
4.35 Scan of the number of CBS photons detected by the MCP against the electron bunch charge at the IP. Experimental measurements (red) are compared with simulations performed in RF-Track (blue). The error bars in the experimental data correspond to the standard error on the mean. Note that from the experimental dataset, the 25% contribution from the halo was removed. . . . . 168
4.36 Scan of the number of CBS photons detected by the MCP against the laser pulse energy at the IP. Background-subtracted experimental measurements (red) are compared with simulations performed in RF-Track (blue). The error bars in the experimental data correspond to the standard error on the mean. . . . . 169
4.37 Two-dimensional scan of the horizontal and vertical position of the IR laser around the IP, against the number of CBS photons detected by the MCP in the RF-Track simulation (a) and experimental measurement (b). . . . . 173

4.38 Two-dimensional scan of the vertical position and arrival time of the IR laser around the IP, against the number of CBS photons detected by the MCP in the RF-Track simulation (a) and experimental measurement (b). . . . . 174
4.39 Two-dimensional scan of the horizontal position and arrival time of the IR laser around the IP, against the number of CBS photons detected by the MCP in the RF-Track simulation (a) and experimental measurement (b). . . . . 175
4.40 Three-dimensional scan of the horizontal and vertical position of the IR laser around the IP, along with the laser's arrival time, against the number of CBS photons detected by the MCP in the RF-Track simulation (a) and in the experimental measurement (b). The 3D plots represent isosurfaces, with an amplitude threshold set as 40% of the maximum flux value. . . . . 176

# Chapter 1

# Introduction

Particle physics represents the study of the fundamental constituents of matter and the forces of nature. Historically, it was developed from a series of breakthroughs in quantum mechanics in the first half of the 20th century. The theoretical basis of particle physics is the Standard Model (SM), one of the most successful theories in the history of science [1].

Figure 1.1 presents the particle content of the Standard Model. Within this framework, all constituents of matter are described as fermions, elementary particles with spin 1/2 that obey the Pauli exclusion principle. Each fermion is associated with a corresponding antiparticle carrying opposite conserved quantum numbers. Fermions are divided into two categories, quarks and leptons. Quarks carry colour charge and are therefore subject to the strong interaction, forming colour-neutral bound states known as hadrons, such as protons and neutrons. Owing to colour confinement, quarks are not observed as free particles; their properties are instead inferred from hadronic spectra and decay processes.

Leptons do not carry colour charge and consequently do not experience the strong interaction. Both quarks and leptons couple to the weak interaction, which mediates flavour-changing processes and governs phenomena such as beta decay. In addition, the charged leptons, namely the electron, muon, and tau, interact electromagnetically, whereas neutrinos, being electrically neutral, do not couple to the electromagnetic field.

Apart from fermions, the SM also includes bosons, subatomic particles of integer spins. Vector bosons have a spin of 1, while scalar ones have a spin of 0. As

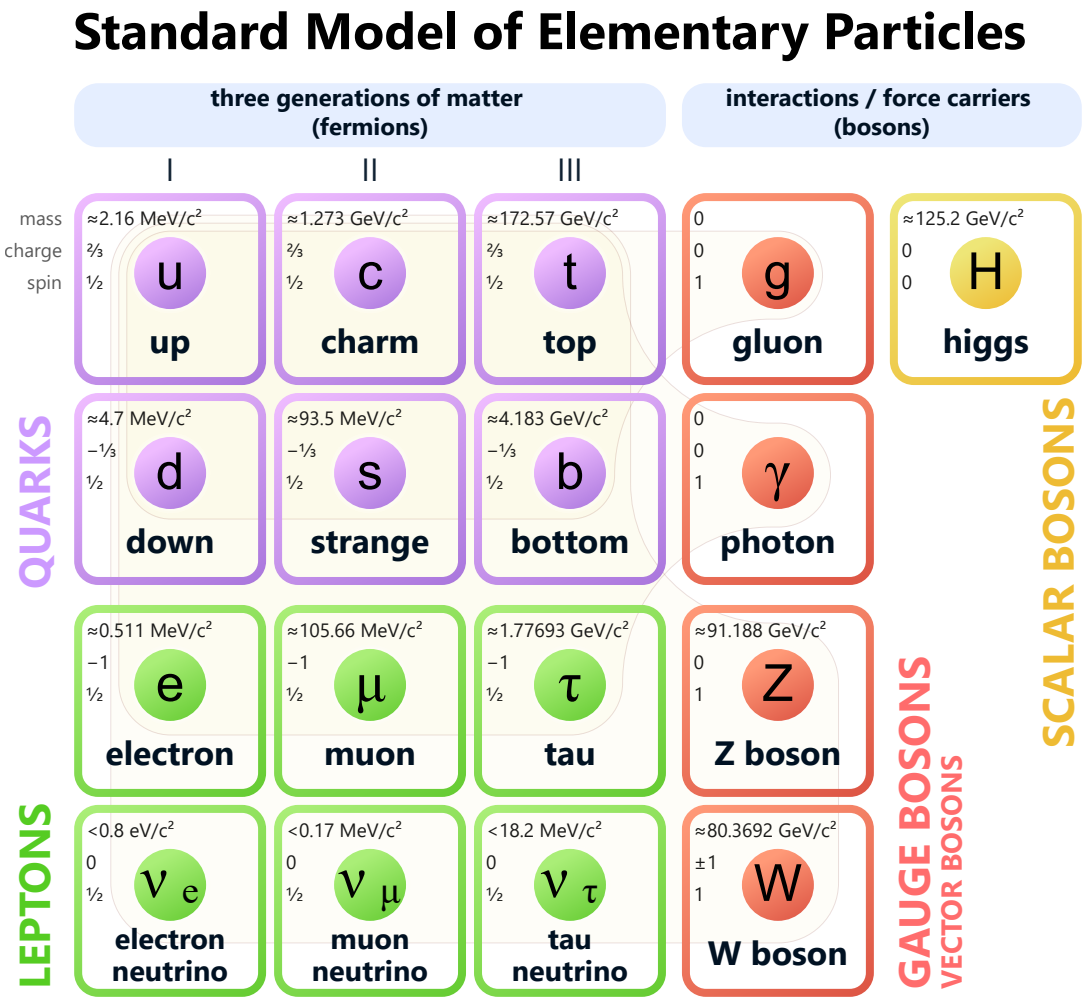



Figure 1.1: The elementary particles of the Standard Model of Particle Physics. (image credit: Wikipedia)

part of vector (or gauge) bosons, the gluon accounts for the strong force, the photon for the electromagnetic force, and the Z and W bosons for the weak force. The only scalar boson, Higgs, allows the fundamental particles to gain mass through their interaction with the Higgs field [1].

Following the initial discovery of electrons by J.J. Thomson in 1897 [2], a total of 17 fundamental particles have been detected in accordance with the SM. The muon was discovered through cloud chamber experiments of cosmic rays in

1937 [3], the existence of quarks was first experimentally validated in 1968 at SLAC [4], the charm quark was first detected at SLAC and BNL in 1974 [5], the tau lepton at SLAC in 1975 [6], the bottom quark at Fermilab in 1977 [7], gluons at DESY in 1979 [8], the W and Z bosons at CERN in 1983 [9], the top quark at Fermilab in 1983 [10], concluding with the discovery of the Higgs boson at CERN in 2012 [11]. Many current particle physics experiments are aimed at searches beyond the standard model, in order to test the limits of the SM, and trace a path towards a new physics capable of explaining current anomalies, i.e., the inclusion of gravitational force, dark matter, dark energy, and the vacuum catastrophe. These searches typically target explorations of TeV energy collisions of particles [12].

## 1.1 Particle Accelerators

Most fundamental particles have been discovered using particle accelerators, machines employing electromagnetic fields to propel charged particles to ultra-relativistic speeds and contain them within well-defined beams [13]. Through fixed-target or collider experiments enabled by accelerators, particle showers are created, tracked, and analysed to test the validity of the SM. There are two frontiers recognised in particle searches: the energy frontier and the intensity one. The intensity frontier is focused on precision searches of rare events associated with existing particles. This requires high-luminosity machines and collisions of fundamental particles (typically fermions) providing clean signals. The energy frontier aims to explore high collision energies, in the hopes of finding new physics processes predicted by more exotic theories [14].

## 1.2 Particle colliders

There are two main types of particle colliders: circular and linear. The main figures of merit for accelerator performance are the beam energy and luminosity. The latter is defined as the quantity that measures the ability of a collider to produce the required number of particle events. For Gaussian beams colliding

head-on with equal beam sizes, the luminosity $L$ is calculated from

$$L = \frac{N_1 N_2 f N_b}{4\pi\sigma_x\sigma_y}, \tag{1.1}$$

where $N_{1/2}$ is the number of particles per bunch, $f$ is the repetition rate, $N_b$ is the number of bunches, and $\sigma_{x/y}$ is the root mean squared beam size at the interaction point.

Circular colliders recirculate beams at high repetition rates. The maximum energy in a circular hadron accelerator is limited by the magnetic bending field. Straight sections are also required for the inclusion of RF cavities for energy ramp-up in the ring. Electron-Positron ($e^+e^-$) circular colliders are severely limited by constant energy loss due to the emission of synchrotron radiation with the bending of particle trajectories. Compared with hadron colliders, $e^+e^-$ colliders offer much cleaner signals, with the opportunity for precision measurements of known SM parameters. The current largest collider is a circular one, the Large Hadron Collider (LHC), which led to the discovery of the Higgs boson in 2012 [15].

Linear colliders offer a potentially limitless increase in beam energy via the extension of their length. They also have a more compact footprint compared to circular colliders. Additionally, polarised beams can be generated and collided at high luminosities in linear colliders [16]. The Stanford Linear Collider (SLC) remains the largest such machine ever built [17]. Note that for $e^+e^-$ linear colliders, an enhancement factor is added to the luminosity equation, typically in the order of 1.5-2 [18].

### 1.2.1 Future Colliders

Past and present efforts to build a Higgs factory have led to the conceptualisation of several future colliders at CERN. As part of the 2020 European Strategy for Particle Physics an $e^+e^-$ Higgs factory was decided as the highest future priority of particle physics [19]. In its 2025 update, the European Strategy Group recommended the electron-positron Future Circular Collider (FCCee) as the preferred option for the next collider. If the FCC is to be deemed unfeasible, the main alternative will be the Linear Collider Facility (LCF) [20] or the Compact Linear Collider (CLIC) [21].

Other future collider studies not based at CERN include the International Linear Collider (ILC) and the Circular Electron Positron Collider (CEPC). The ILC is a linear accelerator concept based on superconducting radio-frequency technology, designed to provide centre-of-mass energies of up to 500 GeV, with a possible upgrade path to 1 TeV. Its linear geometry avoids synchrotron radiation losses, making it well suited for precision studies of the Higgs boson, top quark, and potential physics beyond the Standard Model. In contrast, the CEPC is a circular collider proposed in China with a circumference of approximately 100 km. It is primarily intended to operate as a Higgs factory at a centre-of-mass energy of around 240 GeV, while also enabling precision measurements at the Z pole and the W-pair production threshold. The CEPC infrastructure has additionally been proposed as a precursor to a future high-energy proton collider, extending its long-term scientific potential.

#### 1.2.1.1 The Compact Linear Collider (CLIC)

CLIC represents a mature proposal for a multi-TeV high-luminosity linear $e^+e^-$ collider based at CERN. A schematic of the accelerator complex is shown in Fig. 1.2. Exploiting the flexibility of linear colliders, CLIC has been designed to be deployed in three possible collision energy stages, 380 GeV at 11.4 km, 1.5 TeV at 29 km, and 3 TeV at 50 km, as seen in Fig. 1.3. The CLIC study brought significant technological advances in compact beam acceleration, namely X-band accelerating structures, high-efficiency klystrons, and drive beam-based acceleration. The two-beam acceleration technique is enabled by normal-conducting accelerating structures operating at gradients of 72-100 MV/m.

The initial design of CLIC began in 1985 and led to the construction of three CLIC Test Facilities (CTFs), in 1991, 1996, and 2004. The latest facility, CTF3, investigated the drive beam concept and, in 2016, part of the beamline was repurposed for the CERN Linear Electron Accelerator for Research (CLEAR). In 2012, the CLIC collaboration published its conceptual design report (CDR) [22], followed by an updated energy staging scenario in 2018 [23].

As of the input to the 2025 Update on the European Strategy for Particle Physics, the design luminosity at 380 GeV is $4.5 \times 10^{34}\,\mathrm{cm}^{-2}\,\mathrm{s}^{-1}$ [24]. To increase the luminosity of CLIC, a double beam delivery system was designed, allowing

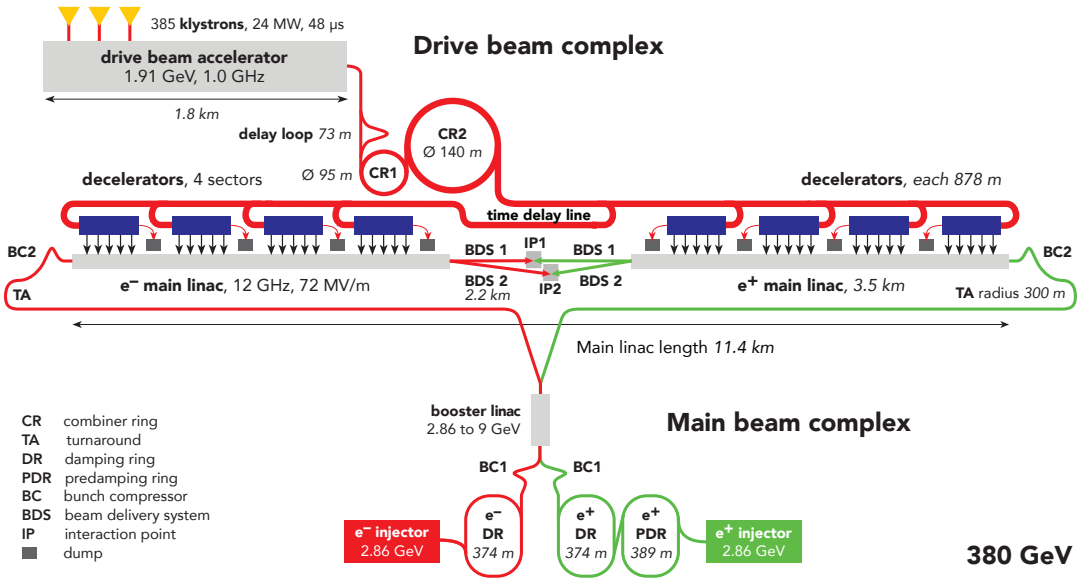



Figure 1.2: Schematic layout of the CLIC complex at 380 GeV, with a double beam-delivery system (BDS) operating with two detectors. (image credit: Erik Adli)

for two interaction regions and two subsequent detectors. The 380 GeV option is supposed to operate at 100 Hz, and the 1.5 TeV option at 50 Hz. The location of the machine has been optimised according to the regional geology and the local environment to be fully contained in a molasse rock region and thus avoiding the complex geological structures.

The electron bunches are generated using a conventional radio frequency (RF) injector, allowing for polarised beams. Damping rings are installed to reduce the beam emittance. The positron beam is created through a fixed target collision of a 2.86 GeV electron beam with a tungsten block, generating photons and subsequent electron-positron pairs. The positrons are selected and accelerated to 2.86 GeV, and sent to a pre-damping and damping ring for emittance reduction. Both the electron and positron beams are further accelerated up to the main linac system, while also compressing the bunch length. The main linacs then accelerate the beams to the desired collision energy of 190 GeV for the 380 GeV centre of mass configuration. To maximise the luminosity, nanobeams are required at the IP, which is achieved by the BDS, which also removes transverse tails and off-energy

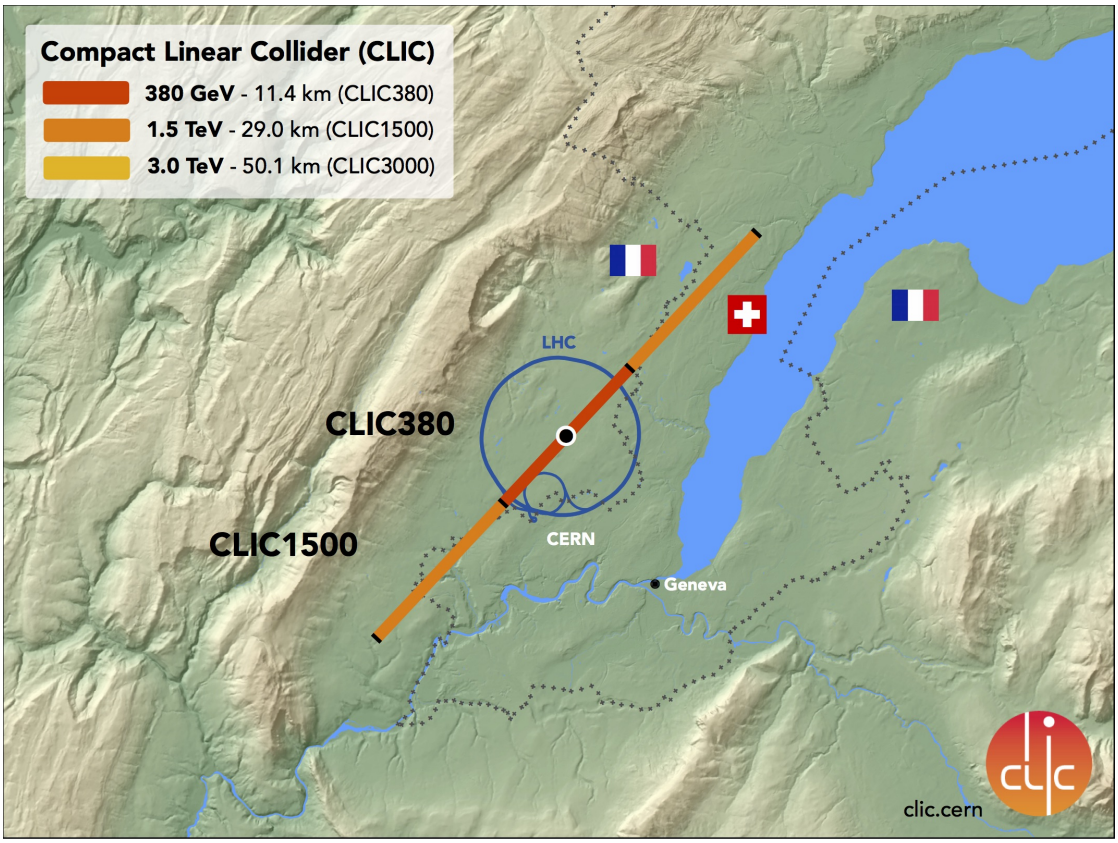



Figure 1.3: The CLIC main linac footprint near CERN, showing the inital 380 GeV and a 1.5 TeV high-energy stage. (image credit: CLIC)

particles with collimators. Following the collision, the bunches are transported to beam dumps.

To achieve high accelerating gradients, X-band accelerating structures require short, high-peak-power RF pulses, which are challenging to generate efficiently with conventional klystrons. To overcome this limitation, the CLIC two-beam acceleration scheme employs low-frequency klystrons to efficiently produce long RF pulses and store their energy in a high-current drive-beam pulse. This beam is subsequently manipulated to generate a large number of short, high-power RF pulses that are distributed along the main linac. The RF energy is obtained from the drive beam's deceleration in power extraction and transfer structures (PETS), and transported via waveguides to the accelerating structures. Compared with a conventional klystron-based RF system, the drive-beam concept significantly

reduces both the operational cost and the overall power consumption of CLIC. The feasibility of this scheme has been successfully demonstrated at CTF3.

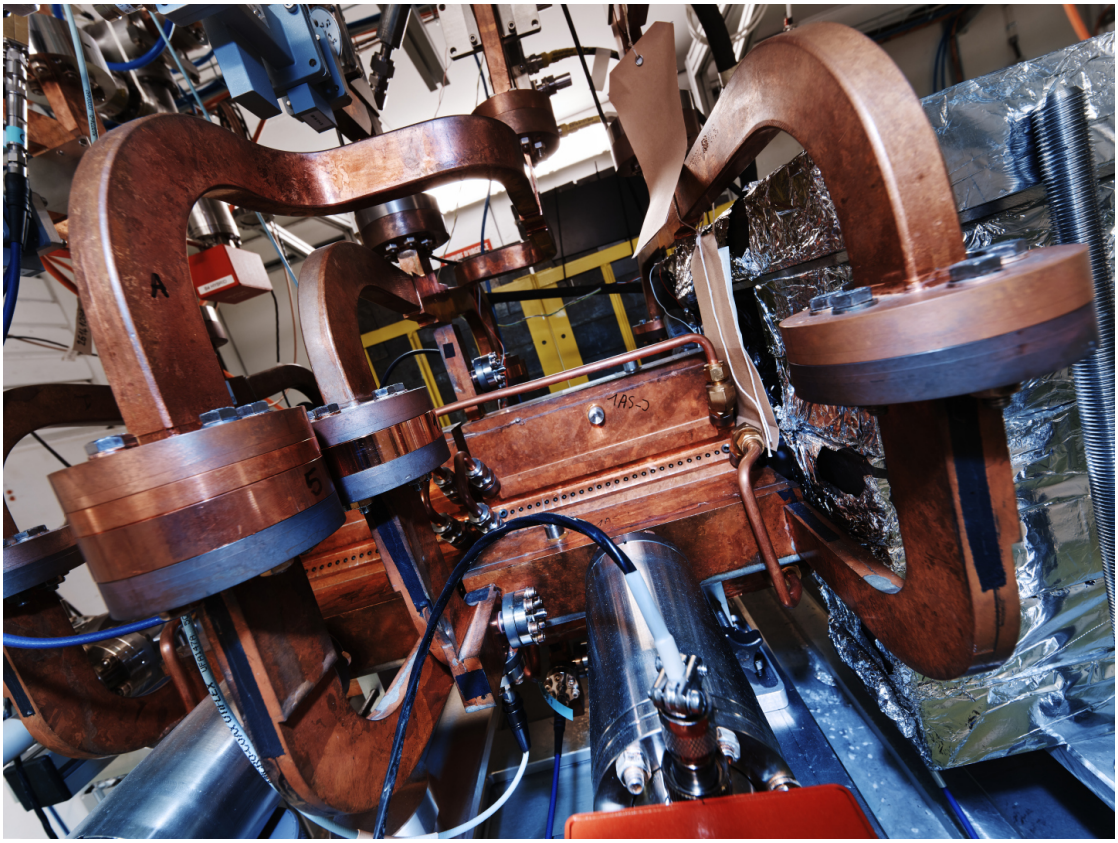


Figure 1.4: The CLIC X-band accelerating structure. Waveguides are shown in the foreground, which transmit power from the source (e.g., klystron or drive beam) to the accelerating structure. (image credit: CLIC)

The CLIC study has therefore led to many innovations in technology, namely techniques for compact high-energy acceleration. The X-band accelerating structures developed for CLIC (see Fig. 1.4) have been integrated in design studies for neutron beam generation for material analysis and very high energy electron (VHEE) therapy [25–27]. The transfer of knowledge of CLIC technology to industry has been enabled by the cost efficiency and reduced footprint characteristic of X-band accelerating structures.

This thesis examines the use of compact X-band accelerating technology for driving a high energy and high intensity Compton backscattering gamma source.

In addition to X-band technology, plasma wakefield acceleration has also been investigated at CERN as an alternative high-gradient acceleration scheme.

## 1.3 The AWAKE Experiment

The Advanced Proton Driven Plasma Wakefield Experiment (AWAKE) at CERN is a proof-of-principle experiment focusing on electron acceleration via plasma wakefields generated by a proton drive bunch. In proton-driven plasma wakefield acceleration, a high-energy proton bunch is sent through a plasma, where its electric fields displace plasma electrons from the beam path. As the displaced electrons are attracted back towards the positively charged ions, oscillations are established within the plasma, generating regions of strong longitudinal electric field known as wakefields behind the proton bunch. Electrons injected at an appropriate phase of the wakefield can gain energy from these fields in a manner analogous to a surfer riding an ocean wave. Since plasma wakefields can sustain accelerating gradients several orders of magnitude larger than those achievable in conventional radio-frequency accelerators, proton-driven plasma wakefield acceleration offers a promising route towards more compact high-energy accelerators [28].

The experimental layout of AWAKE, shown in Fig. 1.5, consists of a proton beamline, a plasma source, an ionising laser, and an externally injected electron beam. Proton bunches, shown in red, are extracted from the CERN-based Super Proton Synchrotron (SPS) every 15 to 30 s with an energy of 400 GeV, an RMS bunch length of 6 cm to 8 cm, and a population of $2.5 \times 10^{11}$ to $3.1 \times 10^{11}$ protons per bunch. Prior to entering the plasma source, the beam is focused to an RMS transverse size of approximately 200 µm. The bunch then traverses a 10 m rubidium vapour cell operated at densities between $10^{14}\,\mathrm{cm}^{-3}$ and $10^{15}\,\mathrm{cm}^{-3}$. [29]

A short laser pulse with a wavelength of 780 nm and pulse energy of approximately 450 mJ co-propagates with the proton bunch and ionises the rubidium vapour, thereby creating the plasma channel. Efficient excitation of large-amplitude wakefields requires the drive bunch length to be comparable to the plasma wavelength, which for the chosen plasma densities is of the order of 1 mm. As the SPS proton bunch is 5 cm to 8 cm long, the self-modulation instability is exploited to transform the bunch into a train of micro-bunches resonantly spaced

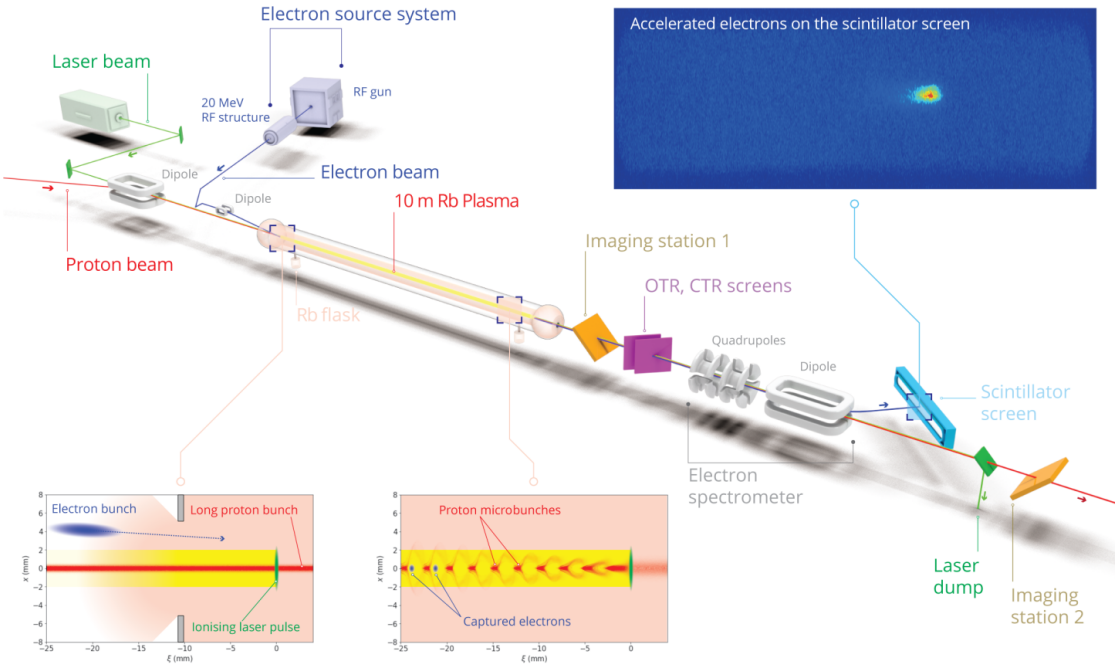



Figure 1.5: Schematic of the AWAKE set-up (credit: AWAKE).

at the plasma wavelength, enabling the generation of wakefields with accelerating gradients approaching 1 GV/m. [30]

The witness electron beam is produced by a photocathode injector operating at 10 Hz. The electrons are generated with an energy of approximately 5 MeV and subsequently accelerated to 10 MeV to 20 MeV in a booster linac. Typical bunch parameters include a charge corresponding to $0.6\times10^9$ to $6.2\times10^9$ electrons, an RMS bunch length of 4 ps, and a normalised emittance of approximately 2 mm mrad. [31]

Run 1 of the AWAKE experiment at CERN, which ended in 2018, achieved all milestones [28]. It demonstrated phase-stable and reproducible self-modulation of the proton bunch in the plasma, consequently achieving high gradients, and accelerated externally injected electrons to GeV beam energies using proton-driven plasma wakefields for the first time [29]. Run 2, which began in 2021, aims to demonstrate the acceleration of electrons with high gradients (1 GV/m) while controlling the beam quality and showing the scalability of this process. Once this is demonstrated, the AWAKE technology will be ready for use for various particle physics experiments.

Run 2 is staged in four phases (2a-d) and lasts for several years. While Run 2a (2021-2022) demonstrated that the electron bunch seeds the proton bunch self-modulation in the plasma, the goal of Run 2b (2023-2024) is to demonstrate that high-amplitude wakefields can be maintained over long distances. Run 2c, foreseen to start in 2028, aims for the acceleration of a witness electron bunch while maintaining a sustained beam quality. In Run 2d, the accelerating plasma source will be replaced with a longer one to achieve even higher electron energies.

For Run 2c and 2d, which will start after CERN's Long Shutdown 3, a new electron injector will be required, able to provide high quality electron bunches to the plasma cell with low emittance and energy spread.

## 1.4 Beam Dynamics

Any accelerator is designed with a fixed nominal trajectory, which represents the ideal (or reference) path. This trajectory can be a straight line, as in linacs, or circular, as in storage rings. The basic function of particle accelerators is to guide and steer particle beams around the nominal trajectory. This is achieved by applying electromagnetic fields to the beamline, interacting with the beam under the effect of the Lorentz force,

$$\mathbf{F} = q(\mathbf{E} + \mathbf{v} \times \mathbf{B}), \tag{1.2}$$

where $q$ is the particle charge, $\mathbf{E}$ the electric field, $\mathbf{B}$ the magnetic field, and $\mathbf{v}$ the particle velocity [32]. At relativistic speed, $v \approx c$, the effect of the magnetic field is amplified by the large numeric value of the speed of light. Therefore, in order to match a feasible magnetic field of 1 T, an E-field of $3 \times 10^8\,\mathrm{V\,m^{-1}}$ would be needed, which is much more challenging to produce. Due to this, magnets are typically used to steer and focus beams, while electric fields are used for beam acceleration. The fundamentals of beam steering and focusing, named in an allusion to the transport of light as beam optics, were set by Courant and Snyder in 1958 [33].

### 1.4.1 Coordinate system

The coordinate system of particle motion in an accelerator is defined with respect to its nominal trajectory. The geometric formalism is shown in Fig. 1.6. A hori-

zontal displacement is equivalent to a movement in the $x$ direction, while a vertical kick corresponds to the $y$ coordinate. The path tangential to the design orbit is traced by $s$, and $\rho$ denotes the bending radius.

Given these coordinates, the divergence angles (horizontal and vertical) are defined as: $x' = dx/ds$ and $z' = dz/ds$. These coordinates are crucial in determining corrections for beam steering.

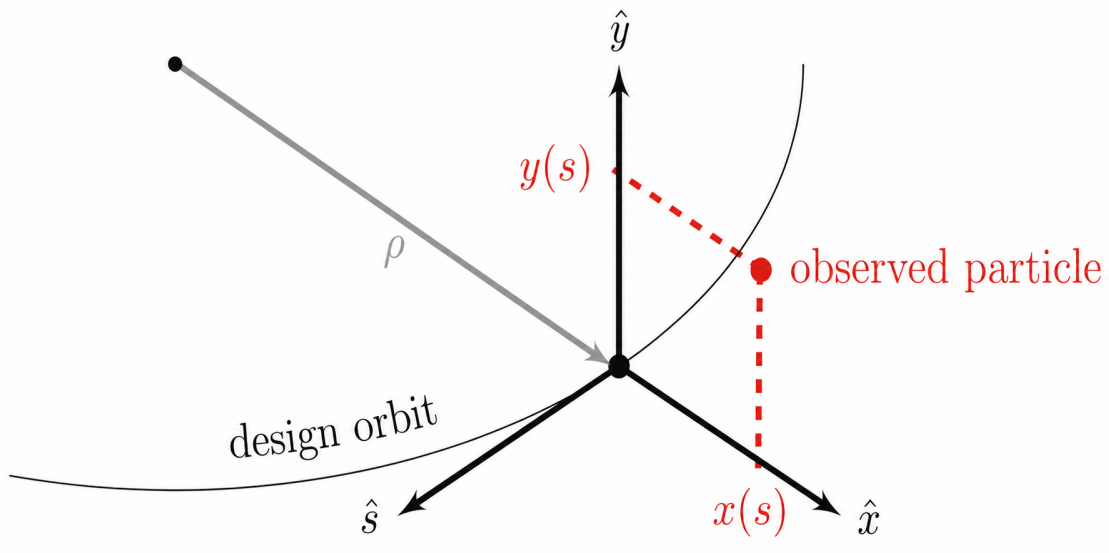



Figure 1.6: The co-moving coordinate system used to describe particle motion. (credit: [34])

### 1.4.2 Bending magnets

Using the previously defined beam geometry and assuming that the beam is only under a B-field, and the field and plane of motion are orthogonal, one can define the beam rigidity,

$$B\rho = \frac{p}{q}, \tag{1.3}$$

where $p$ is the beam momentum. For a fixed ring, the maximum energy traversing the design orbit is limited by the bending field.

The trajectory of a particle in a dipole bending magnet of length $l$, as seen in Fig. 1.7 is determined by

$$\sin\frac{\theta}{2} = \frac{l}{2\rho} = \frac{lB}{2(B\rho)}. \tag{1.4}$$

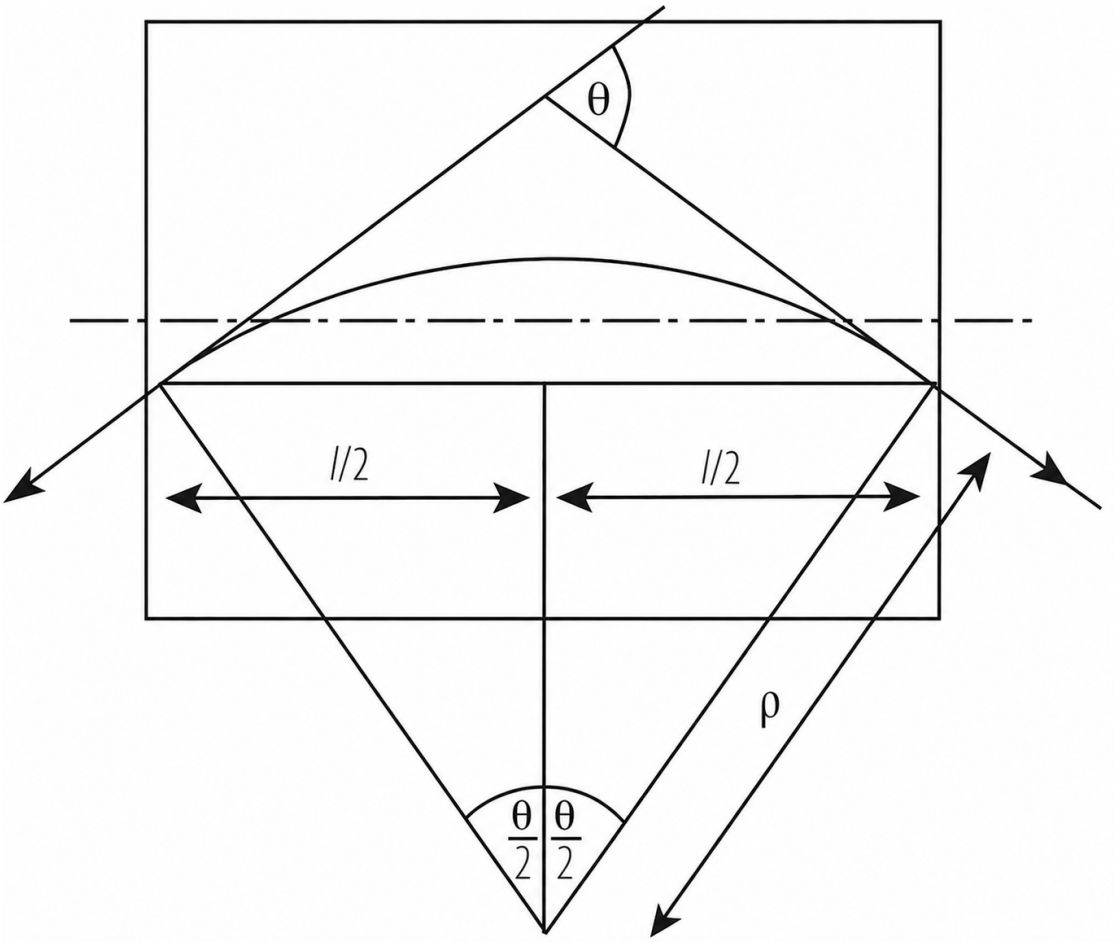



Figure 1.7: Single particle trajectory in a dipole bend. (credit: [34])

For a typical angle $\theta \ll \pi/2$,

$$\theta \approx \frac{lB}{B\rho}. \tag{1.5}$$

### 1.4.3 Focusing magnets

The most popular focusing element for relativistic particles is the quadrupole magnet. Its field, shown in Fig. 1.8, is zero in the centre. The magnetic field increases linearly with distance from the axis. The field polarity allows for focusing in one direction and defocusing in the orthogonal.

The quadrupole strength $k$ is determined by its gradient $dB_z/dx$,

$$k = \frac{1}{B\rho}\frac{dB_z}{dx}. \tag{1.6}$$

One can determine then the angular deflection under a quadrupole kick of length $l$ for a displacement of $x$,

$$\Delta x' = \frac{lB}{B\rho} = lkx. \tag{1.7}$$

By analogy with a converging lens in optics, where

$$\Delta x' = -\frac{x}{f}, \tag{1.8}$$

the focal length of a horizontally focusing quadrupole can be defined as

$$f = -\frac{1}{kl}. \tag{1.9}$$

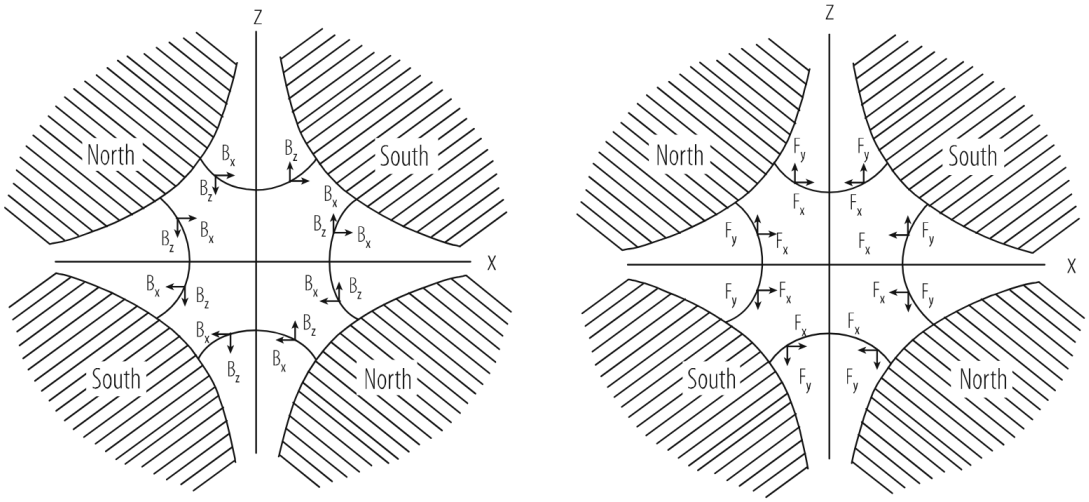



Figure 1.8: Field and force components in a quadrupole. (credit: [34])

### 1.4.4 Hill's equation

From Eq. 1.6, the $z$ angular deflection through a quadrupole can be obtained, $dz' = -kzds$, from which a differential equation of motion can be deduced,

$$z'' + k(s)z = 0. \tag{1.10}$$

The resulting formula is called Hill's equation. In the horizontal plane, subject to dipole fields, the equation becomes

$$x'' + \left[\frac{1}{\rho^2(s)} - k(s)\right]x = 0. \tag{1.11}$$

Exploiting the similarity of this equation with the one for simple harmonic motion with the restoring constant $k(s)$, the solution to Hill's equation can be derived.

$$x = \sqrt{\beta(s)\epsilon}\cos\left[\phi(s) + \phi_0\right], \tag{1.12}$$

and its differential,

$$x' = -\sqrt{\frac{\epsilon}{\beta(s)}}\sin\left[\phi(s) + \phi_0\right] + \left[\frac{\beta'(s)}{2}\right]\sqrt{\frac{\epsilon}{\beta(s)}}\cos\left[\phi(s) + \phi_0\right]. \tag{1.13}$$

A typical phase space plot is shown in Fig. 1.9, with semi-axis $\sqrt{\beta\epsilon}$ in $x$ and $\sqrt{\epsilon/\beta(s)}$ in $x'$. The area of this ellipse is $\pi\epsilon$, which makes $\epsilon$, the geometrical emittance, an invariant of motion essential for beam optics. Additionally, the beta function $\beta(s)$ is used to describe betatron envelopes that bound the evolution of the beam spot size along the nominal trajectory.

### 1.4.5 Twiss parameters

The solution to Hill's equation along with its differential can be used to define transport matrices that track their value at a given $s$. Turning linear differential equations, such as Hill's equation, into matrices, which in turn allows for lattice element discretisation, is especially useful for turning the algebraic problem of beam tracking in an accelerator to a computational one.

The matrix formalism can be used to define the beam transfer matrix $M_{21}$ from $s_1$ to $s_2$ as

$$\begin{pmatrix} y(s_2) \\ y'(s_2) \end{pmatrix} = \begin{pmatrix} a & b \\ c & d \end{pmatrix}\begin{pmatrix} y(s_1) \\ y'(s_1) \end{pmatrix} = M_{21}\begin{pmatrix} y(s_1) \\ y'(s_1) \end{pmatrix}. \tag{1.14}$$

By substituting the solutions for $y$ and $y'$ and solving four simultaneous equations for $a$, $b$, $c$, $d$, one obtains

$$M_{12} = \begin{pmatrix} \sqrt{\frac{\beta_1}{\beta_2}}\cos\phi - \sqrt{\beta_2\beta_1'}\sin\phi & \sqrt{\beta_1\beta_2}\sin\phi \\ -\frac{1+\sqrt{\beta_1\beta_1'\beta_2\beta_2'}}{\sqrt{\beta_1\beta_2}}\sin\phi - \left(\sqrt{\frac{\beta_1'}{\beta_2}} - \sqrt{\frac{\beta_2'}{\beta_1}}\right) & \sqrt{\frac{\beta_1}{\beta_2}}\cos\phi + \sqrt{\beta_1\beta_2'}\sin\phi \end{pmatrix}. \tag{1.15}$$

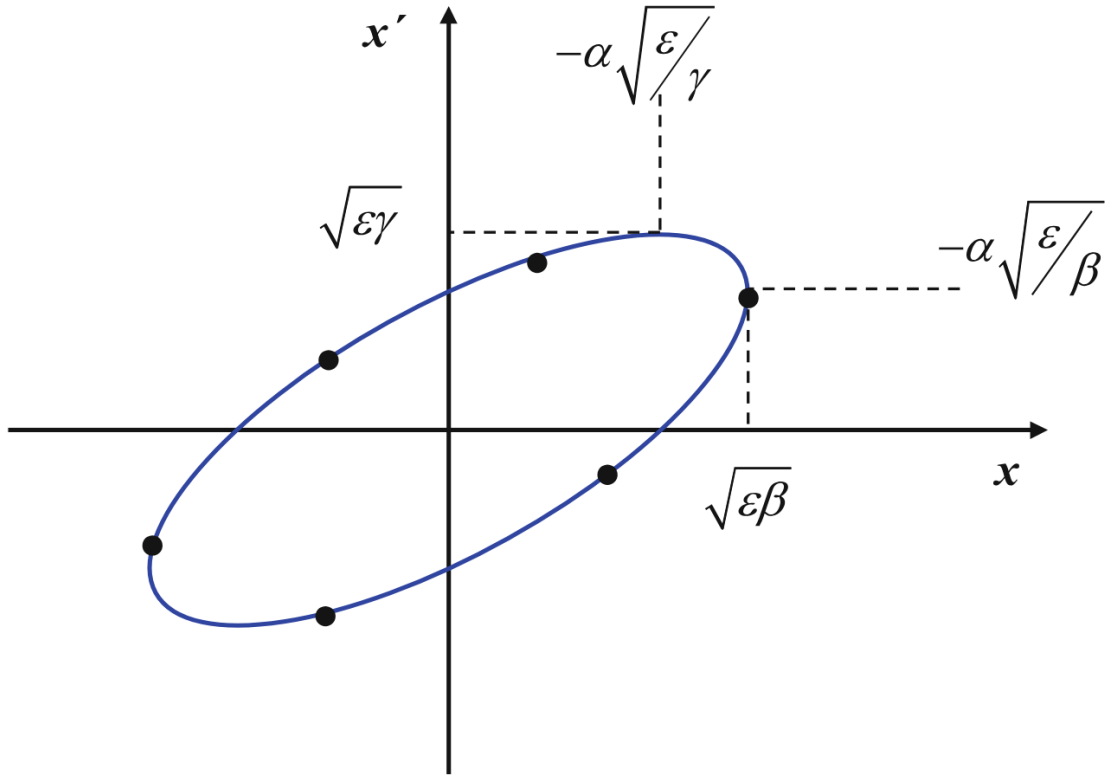



Figure 1.9: The phase space ellipse of particle motion in the x-x'-plane. (credit: [34])

In periodic lattices, this formula can be simplified by adding the periodicity condition of $M$ between the two points, which equates $\beta_1 = \beta_2$, $\beta_1' = \beta_2'$ and $\phi$ becomes the phase advance per cell, $\mu$,

$$M = \begin{pmatrix} \cos\mu - \sqrt{\beta\beta'}\sin\mu & \beta\sin\mu \\ -\frac{1+\beta\beta'}{\beta}\sin\mu & \cos\mu + \sqrt{\beta\beta'}\sin\mu \end{pmatrix}. \tag{1.16}$$

We can define the following Twiss parameters, $\beta$,

$$\alpha = -\frac{\beta'}{2}, \tag{1.17}$$

$$\gamma = \frac{1+\alpha^2}{\beta}. \tag{1.18}$$

These parameters can be used to rewrite the prior equation as

$$M = \begin{pmatrix} \cos\mu + \alpha\sin\mu & \beta\sin\mu \\ -\gamma\sin\mu & \cos\mu - \alpha\sin\mu \end{pmatrix}. \tag{1.19}$$

$M$ represents the Twiss matrix and represents the basic matrix for periodic lattices.

Lastly, using the newly defined Twiss parameters, the initial ellipse equation can be modified to obtain the Courant-Snyder invariant,

$$\gamma(s)y^2 + 2\alpha(s)yy' + \beta(s)y'^2 = \epsilon. \tag{1.20}$$

Liouville's theorem states that the area of the phase space contour (or $\epsilon$) remains constant under magnetic focusing or bending. As stated in [35]: "In the vicinity of a particle, the particle density in phase space is constant if the particles move in an external magnetic field or in a general field in which the forces do not depend upon velocity."

## 1.5 Compton backscattering

The scattering of a low energy photon from a relativistic electron resulting in a high energy X-ray is defined as inverse Compton scattering (ICS), or Compton backscattering (CBS) [36]. Due to their compactness and ability to generate quasi-monochromatic X-ray/gamma beams, CBS has been used as a driver of small scale light sources, a cheaper alternative to current generation light sources i.e., synchrotrons and free electron lasers (FELs). Their commercial availability allows for potential applications in the medical field (tomography, cancer therapy), material science (crystallography), security (X-ray scanners), and material analysis (wafer inspection, non-destructive nuclear assay), among others. CBS was first described in 1948 by Feenberg and Primakoff in the context of astrophysical measurements [37], and the first CBS source was proposed in the 1960s [38, 39]. However, contemporary technology only allowed for operation within research institutes. Recent developments in high power compact lasers led to a regained interest in ICS for compact light sources [40]. Since the 2000s, the number of existing CBS sources has gradually increased. The first commercially produced source, the Munich Compact Light Source (MuCLS), is currently used for medical imaging research, such as K-edge subtraction [41] and phase contrast imaging [42]. The Tsinghua Thomson Scattering X-ray source (TTX) in China [43], HI$\gamma$GS in Durham [44], ThomX in France [45] are among the current CBS sources. More recently, the Compact X-ray Light Source (CXLS) at Arizona State University

(ASU), shown in Fig. 1.10, has been developed as a compact alternative to conventional synchrotron light sources, with a total length of approximately 9 m [46].

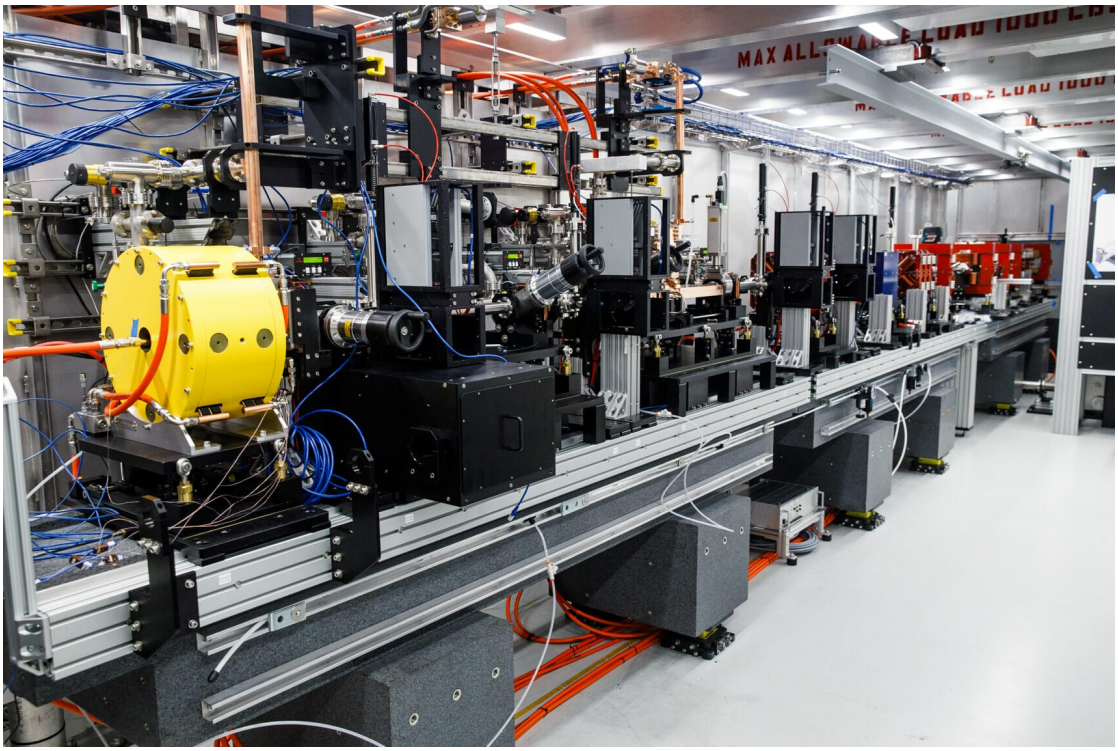


Figure 1.10: Photo of the Compact X-ray Light Source (CXLS) at Arizona State University (ASU), spanning 9 metres in length. (credit: ASU)

Given the available accelerator technology, three classes of ICS sources have been proposed: storage-ring-based (SR), linac-based, and energy-recovery-linac-based (ERL). The first is the most common; notable examples include MuCLS and ThomX. Due to beam recirculation, storage rings can reach high values for flux; however, quantum excitation in the bending magnets limits the minimum emittance, hampering the ICS performance. Linacs have also been considered for compact ICS designs; for example, TTX in China, BoCXS in Bologna [47], and STAR in Consenza, Italy [48, 49]. Compared to storage rings, linacs feature limited repetition frequency; this is compensated for by the lower electron beam emittance and shorter bunches, which are both critical parameters in X-ray production. More recently, ERLs have also garnered interest, and CBS experiments have been conducted at ERL facilities [50]. Designs for ERL-based sources, such

as BriXSinO, have also been proposed [51]. However, ERLs require superconducting technology, which is costly and not easily available to hospitals or small laboratories. A summary of the flux and brilliance values for various ICS sources is included in Figure 1.11.

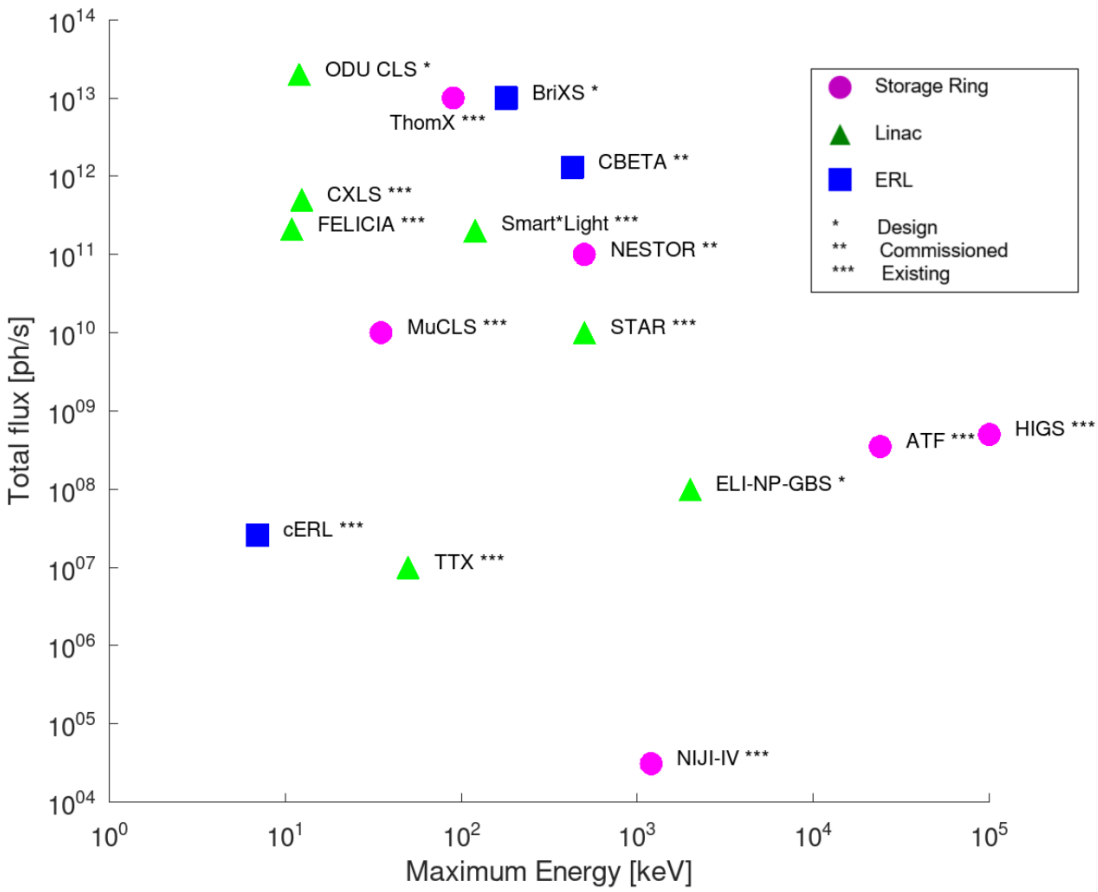



Figure 1.11: Partial landscape of CBS sources. Main figure of merit parameters are used for positioning the CBS sources on the landscape, the photon beam energy and the total scattered photon flux, respectively. The sources are classed based on whether they are based on a storage ring, linac, or ERL, and also on whether they are in the design phase, commissioned, or existing. Adapted from [52].

### 1.5.1 Applications of CBS sources

CBS sources have potential use in various applications, most originating from studies at synchrotron sources. Due to limited availability in current generation

light sources and need for long-range transportation, CBS sources are becoming a popular alternative. Clinical applications, for example, benefit from treatments in hospitals rather than requiring travel to large scale sources. The main challenge for CBS sources currently is to achieve high intensity and high energy X-rays with a high reproducibility and stability.

Several clinical studies have been conducted at MuCLS for K-edge subtraction (KES) and phase contrast imaging (PCI). KES, first proposed in 1953, involves taking X-ray images at energies slightly below and above the 53 keV K-edge of a contrast medium. KES has been used to visualise kidney stones [53] and for coronary angiography [41]. This method exploits the tunability and high-energy properties of ICS sources.

In phase contrast imaging, a quasi-spatial coherent radiation illuminates an object, which gives rise to a spatially varying phase shift. As the radiation propagates through the sample, parts of the wavefront interfere, resulting in a characteristic phase contrast pattern. The resulting signal can be visualised if the transverse coherence of the source is sufficiently large and the point source size is small [42]. Studies in dynamic respiratory imaging were conducted in 2018 [54].

ICS sources have also been considered for cancer therapy. CBS sources such as ThomX have been shown to be able to reproduce beam parameters for Stereotactic Synchrotron Radiation therapy (SSRT) [55]. In particular, proof of concept studies of microbeam radiation therapy (MRT) have been conducted at MuCLS, indicating the ability of MRT to slow the tumour growth rate, despite a much lower dose than that used in SSRT studies [56]. To optimise MRT, the photon flux and peak-to-valley-dose ratio should be maximised, and a typical X-ray energy of 100 keV to 300 keV should be used [57].

FLASH radiotherapy (FLASH-RT) is a novel cancer therapy method that could be adapted for ICS sources. It applies high intensity doses in a much smaller timeframe than conventional radiotherapy (CONV-RT), typically $100\,\mathrm{Gy\,s^{-1}}$ compared to $1\,\mathrm{Gy\,s^{-1}}$ in CONV-RT [58]. Successful experiments have been performed at the ESRF with 102 keV photons, where the authors recommended that future studies be conducted at high intensity CBS sources [59].

Protein crystallography has also been considered as a potential application of ICS sources. Studies at Lyncean Technologies' CLS have shown that ICS X-ray

diffraction (XRD) can be used to determine the structure of protein crystals [60]. XRD is also used in the pharmaceutical industry to determine the crystal structure of drug substances [61].

CBS sources can also be used for cultural heritage studies. ThomX would be able to generate X-rays for such imaging [62]. X-ray fluorescence (XRF), a potential analysis method, was used to discover a hidden Van Gogh painting [63].

High-intensity megavoltage X-rays could be used in nuclear resonance fluorescence. There have been proposals of non-destructive assay systems for radioactive nuclides, which would require a CBS source [64]. This process would be non-destructive and applicable to difficult-to-measure or stable nuclides. This application is particularly attractive, as the energy required for it far exceeds the one achievable by synchrotrons and FELs, and the required photon bandwidth is far narrower than the one provided by bremsstrahlung radiation, making CBS the preferred choice against other light source types.

### 1.5.2 Theory of Compton backscattering

The geometry of the interaction is shown in Figure 1.12. The energy of CBS-generated photons, $E_{\mathrm{X}}$, depends on the primary electrons' relativistic factor, $\gamma$, the photon energy of the laser, $E_{\mathrm{laser}}$, the angle between the electron and the laser beam $\phi$, and the scattering angle between the generated photon beam and the electron beam, $\theta$. Assuming ultra-relativistic electrons and a laser photon energy much smaller than the electron rest mass [65],

$$E_{\mathrm{X}} = 2\gamma^2 E_{\mathrm{laser}} \frac{1 + \cos\phi}{1 + \gamma^2\theta^2}. \tag{1.21}$$

The maximum X-ray energy of $4\gamma^2 E_{\mathrm{laser}}$ is obtained in head-on collisions, where $\phi \approx 0$.

Assuming a linear Compton regime, round Gaussian transverse intensity distributions for both the electron and laser beams, and neglecting the hourglass effects, the total number of photons generated by CBS, $N_\gamma$, depends on the crossing angle, $\phi$, the number of electrons in the bunch, $N_{\mathrm{e}}$, and the number of laser photons in

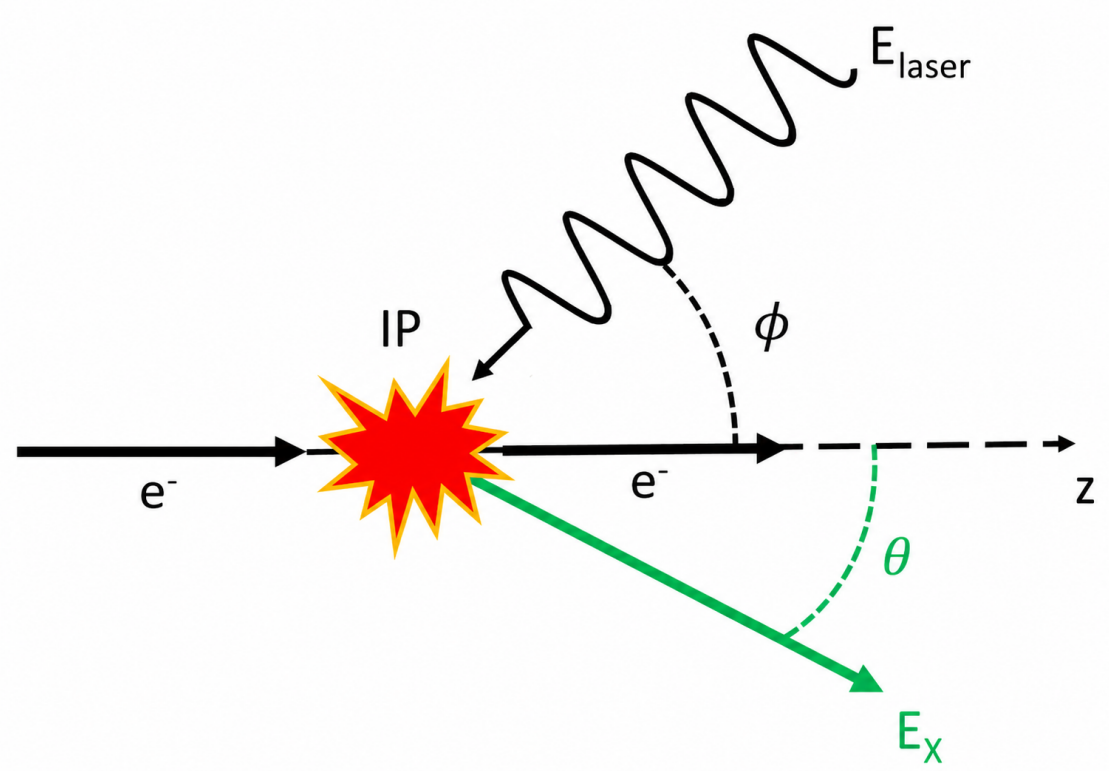



Figure 1.12: Schematic of the Compton backscattering process. The input laser of photon energy $E_{\mathrm{L}}$ is up-scaled to an X-ray of energy $E_{\mathrm{X}}$.

the pulse, $N_{\mathrm{laser}}$,

$$N_{\gamma} = \sigma_{\mathrm{c}} \frac{N_{\mathrm{e}} N_{\mathrm{laser}} \cos(\phi/2)}{2\pi\sigma_{\gamma,y}\sqrt{\sigma_{\gamma,x}^2 \cos^2(\phi/2) + \sigma_{\gamma,z}^2 \sin^2(\phi/2)}}, \tag{1.22}$$

where $\sigma_{\mathrm{c}}$ is the Klein-Nishina cross-section, $\sigma_{\gamma,i}$, with $i = x, y, z$, the source spot size, a convolution of the electron $\sigma_i$ and laser $\sigma_{\mathrm{laser}}$ beam size in each direction at the interaction point (IP) [66]. In order to maximise the number of scattered photons from Eq. (1.22), a strongly focused collision of high-density particle bunches is required.

At sufficiently high laser intensities, the interaction between the electron and the electromagnetic field becomes non-linear, and Compton backscattering proceeds via multiphoton absorption processes involving a single electron. The onset of the non-linear regime is determined by the laser field strength parameter $a_0$,

$$a_0 = \frac{eE\lambda_{\mathrm{laser}}}{2\pi mc^2}, \tag{1.23}$$

where $\lambda_{\text{laser}}$ is the input laser's wavelength and $E$ the laser's transverse electric field, dependent on the laser intensity [36]. For $a_0 \ll 1$, the CBS interaction is under a strictly linear regime. As the laser pulse energy increases to several tens of Joules, $E$ increases, shifting $a_0$ towards 1 and triggering the onset of the non-linear regime.

The Klein–Nishina cross-section describes the probability of photon scattering in the inverse Compton scattering process [67]. At the low energy limit, where the input laser photon energy is much smaller than the rest mass energy of the charged particle beam, the approximation $\sigma_c \simeq \sigma_T$ can be used, where $\sigma_T \simeq 0.665$ barns is the Thomson cross section [2].

The number of photons per second, or flux $\mathcal{F}$, can be derived by taking the time derivative of $N_\gamma$. In sources with a high repetition rate, $f$,

$$\mathcal{F} = \dot{N}_\gamma = N_\gamma f. \tag{1.24}$$

Assuming head-on collisions through a small collection angle and negligible recoil, the bandwidth of a scattered photon beam can be expressed as the sum in quadrature of different contributions:

$$\frac{\sigma_{E_\gamma}}{E_\gamma} = \sqrt{\left(\frac{\sigma_{E_\theta}}{E_\theta}\right)^2 + \left(2\frac{\sigma_{E_e}}{E_e}\right)^2 + \left(\frac{\sigma_{E_{\text{laser}}}}{E_{\text{laser}}}\right)^2 + \left(\frac{\sigma_{E_\epsilon}}{E_\epsilon}\right)^2}, \tag{1.25}$$

where $\sigma_{E_\theta}/E_\theta$ is the contribution from the collection angle $\theta$, $\sigma_{E_e}/E_e$ and $\sigma_{E_{\text{laser}}}/E_{\text{laser}}$ are the relative energy spreads of the electron and laser, and $\sigma E_\epsilon/E_\epsilon$ is the contribution due to the electron beam emittance [68]. Typically, the greatest contribution to the relative bandwidth is given by the collection angle $\theta$ and the electron beam energy $E_e$.

An important derivation from Eq. 1.22 is the flux in a 0.1% bandwidth at the Compton edge [36],

$$\mathcal{F}_{0.1\%} \simeq 1.5 \times 10^{-3} \dot{N}_\gamma. \tag{1.26}$$

The section of the photon spectra from which $\mathcal{F}_{0.1\%}$ can be derived is evidenced in Fig 1.13. The term $1.5 \times 10^{-3}$ is obtained from the spectral energy density of scattered photons in the linear Thomson backscatter limit [36].

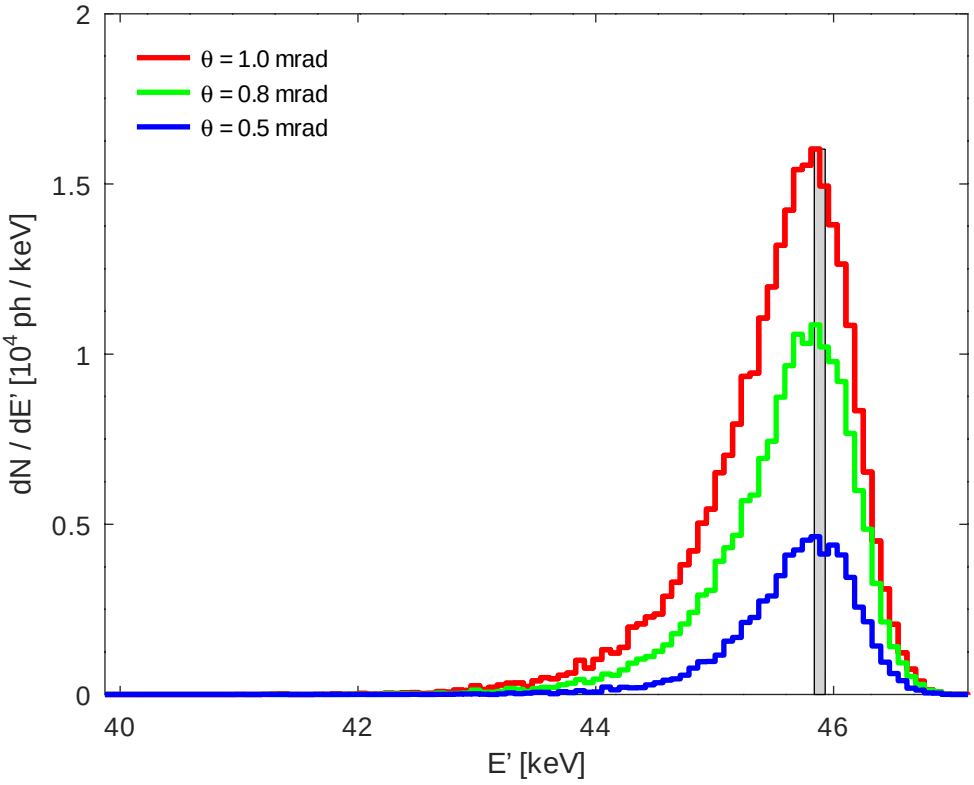



Figure 1.13: Energy spectrum of the Compton backscattered photons for three different collimation half-angles, $\theta$ = 1.0 mrad (red), 0.8 mrad (green), and 0.5 mrad (blue). The horizontal axis shows the scattered photon energy $E'$ in keV, while the vertical axis represents the differential photon yield normalised per $10^4$ electrons and per keV bin. The vertical grey band indicates the 0.1% energy window around the spectral peak.

The spectral brilliance ($\mathcal{B}$) is the density of photons in the six-dimensional space containing the beam [36],

$$\mathcal{B} = \frac{\mathcal{F}_{0.1\%}}{4\pi^2 \sigma_{\gamma,x}\sigma_{\gamma,x'}\sigma_{\gamma,y}\sigma_{\gamma,y'}}, \tag{1.27}$$

where $\sigma_{\gamma,i'}$ is the beam divergence. $\mathcal{B}$ is measured in ph/(s mm$^2$ mrad$^2$ 0.1%BW). In a non-diffraction limited beam, where $\sigma_{\gamma,x'} \approx \sqrt{\epsilon_x/\beta_x}$,

$$\mathcal{B} = \frac{\mathcal{F}_{0.1\%}}{4\pi^2 \sigma_{\gamma,x}\sqrt{\epsilon_x/\beta_x}\sigma_{\gamma,y}\sqrt{\epsilon_y/\beta_y}}. \tag{1.28}$$

Compact sources further benefit from the approximation $\sigma_{\gamma,x} \approx \sigma_x = \sqrt{\beta_x \epsilon_x}$. $\mathcal{B}$ can then be expressed only in terms of photon flux, electron beam energy, and normalised emittance $\epsilon_i^N = \beta\gamma\epsilon_i$,

$$\mathcal{B} \approx \frac{\gamma^2 \mathcal{F}_{0.1\%}}{4\pi^2 \epsilon_x^N \epsilon_y^N}. \tag{1.29}$$

The peak brilliance ($\hat{\mathcal{B}}$) is defined as the normalisation of $\mathcal{B}$ with respect to the rms duration of generated X-rays $\sigma_t$ [69],

$$\hat{\mathcal{B}} = \frac{1}{\sqrt{2\pi}} \frac{\mathcal{B}}{f\sigma_t}. \tag{1.30}$$

# Chapter 2

# The AWAKE Run2c Test Injector (ARTI)

The requirements of AWAKE Run 2c and 2d led to the proposal of a new injection scheme, consisting of an S-band photoelectron gun, followed by two X-band accelerating structures. This design would allow for bunch lengths smaller than 200 fs, and a beam energy of around 150 MeV [70]. A prototype of the new injector for AWAKE, denoted AWAKE Run2c Test Injector, has been commissioned at the CLIC Test Facility 2 (CTF2).

## 2.1 Accelerator baseline

The main components of the ARTI gun, references throughout the thesis, are introduced in this section. The current beamline, as seen in Fig. 2.1 consists of an S-band electron gun, double-coil solenoid, imaging viewport, dipole spectrometer, and, not shown, an X-ray detection chamber, and a Faraday cup. A schematic of the operating gun, as it was used for the CBS experiment, is shown in Fig. 2.2. A summary of the main laser and electron parameters is included in Table 2.1.

### 2.1.1 Electron gun

The S-band electron gun was manufactured with brazing-free technology and its prototype was commissioned at INFN Frascati [71]. The electron gun is very compact, with a length of 0.12 m. It is equipped with a copper cathode that is

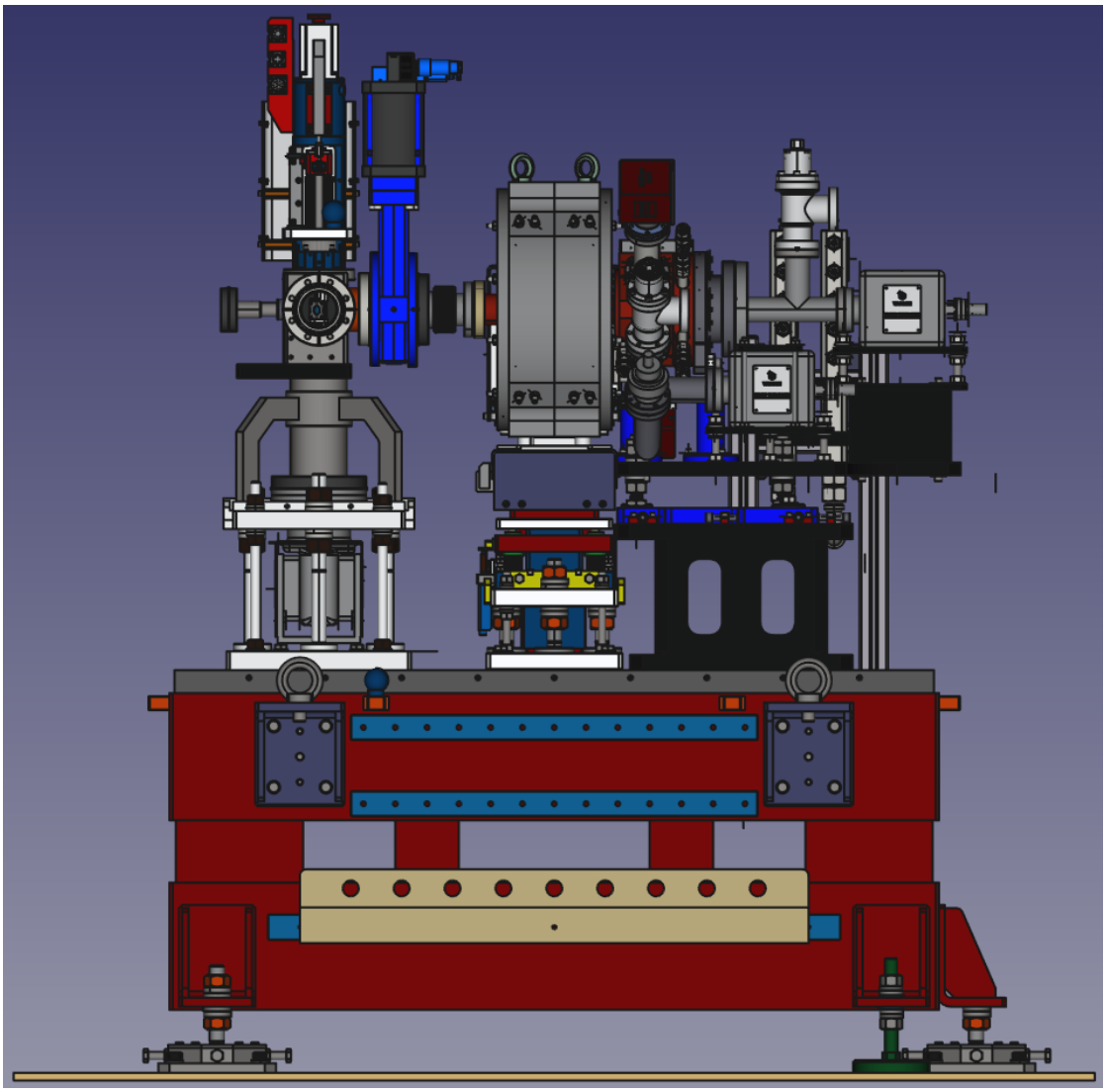


Figure 2.1: CAD design of the ARTI electron gun set-up. The distance from the cathode to the viewport is 0.57 m. Not shown: the dipole spectrometer, pumping port, X-ray detection chamber, and Faraday cup.

capable of generating small emittance electron bunches under a moderate vacuum level. Copper, and metallic cathodes in general, offer ultra-fast rise and decay times, which ensures an almost one-to-one copy of the laser profile to the generated electron bunch. The major disadvantage of copper cathodes, compared to other cathode materials used at CERN, i.e., Caesium Telluride, is the very low quantum efficiency of $10^{-4}$.

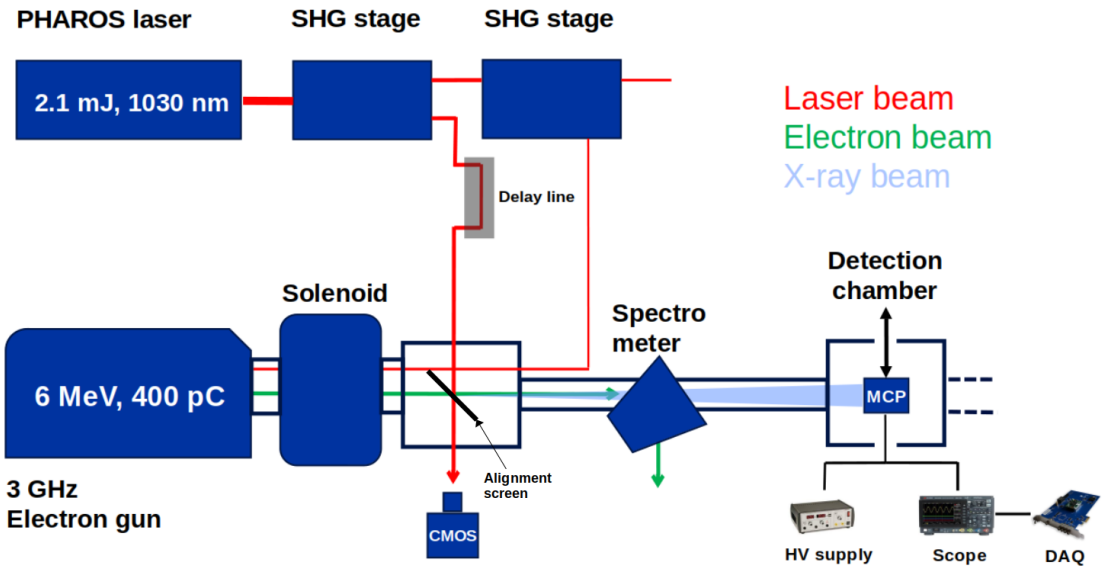



Figure 2.2: Schematic diagram of the AWAKE Run2 Test Injector set-up used for the CBS experiment.

Using Eq. 1.21 and the parameter Table 2.1, it can be deduced that the expected CBS X-ray energy is around 267 eV, which is close to the water window regime [72]. It should be noted that this value is also close to the K X-ray emission line of Carbon [73].

### 2.1.2 Solenoid

Once accelerated by the S-band gun, the electron bunch is focused to a small spot by a double-coil solenoid with a plus-plus polarity, shown in Fig. 2.3. The magnet polarity can be manipulated to variations of plus-minus combinations; however, for nominal operation, the plus-plus configuration was used, as it provided the strongest focusing for the CBS experiment. The solenoid polarity was verified using a Hall probe. The 1D fields of both the electron gun and the solenoid are shown in Fig. 2.4. The combined fields span 0.5 m, starting from the position of the cathode. The solenoid is equipped with a set of movers, allowing for the transverse displacement of the solenoid magnet and, subsequently, its field position. This is an essential feature, as it allows for the correction of field misalignments, which reduces the beam emittance at the interaction point. In practice, the solenoid

Table 2.1: Nominal Electron and Laser Beam Parameters

| Parameter | Unit | Value |
|---|---|---|
| RF gradient | MV/m | 112 |
| Electron beam energy | 5.4 | MeV |
| Solenoid strength | 0.33 | T |
| Energy spread | ‰ | 2 |
| Minimum $e^-$ RMS spot size @ IP | µm | 50 |
| Bunch charge | pC | 200 |
| Laser wavelength | nm | 1030 |
| Pulse duration (RMS) | ps | 0.19 – 10 |
| Max pulse energy | mJ | 2 |
| Repetition rate | Hz | 10 |
| Minimum laser RMS spot size @ IP | µm | 20 |

was extensively used for magnetic strength scans at the interaction point (which corresponded to the imaging screen location). These allowed for obtaining the optimal solenoid strength providing the smallest electron spot at the IP.

A few centimetres after the solenoid's location, a magnet corrector is placed. However, since it had a too small magnetic strength and was placed too close to the imaging viewport to generate an electron beam drift larger than 1 mm, this corrector was not used throughout the study.

### 2.1.3 Imaging viewport

The solenoid is followed by a gate valve meant to contain the gun-solenoid in its own vacuum sector. This eases the venting and vacuum pumping process, as most installations are done in the vacuum sector housing the beam diagnostics. At a distance of 0.57 m from the cathode, an imaging viewport is installed, used to visualise the transverse beam profile. The imaging system provides the means for measuring the beam size and position against tuning parameters: the RF phase, the laser spot size and position on the cathode, along with the solenoid magnetic strength and transverse position. The vacuum chamber housing the viewport also contains a motorised actuator equipped with a set of three screen ports of various sizes. A technical drawing of the screen ports connected to the actuator is shown

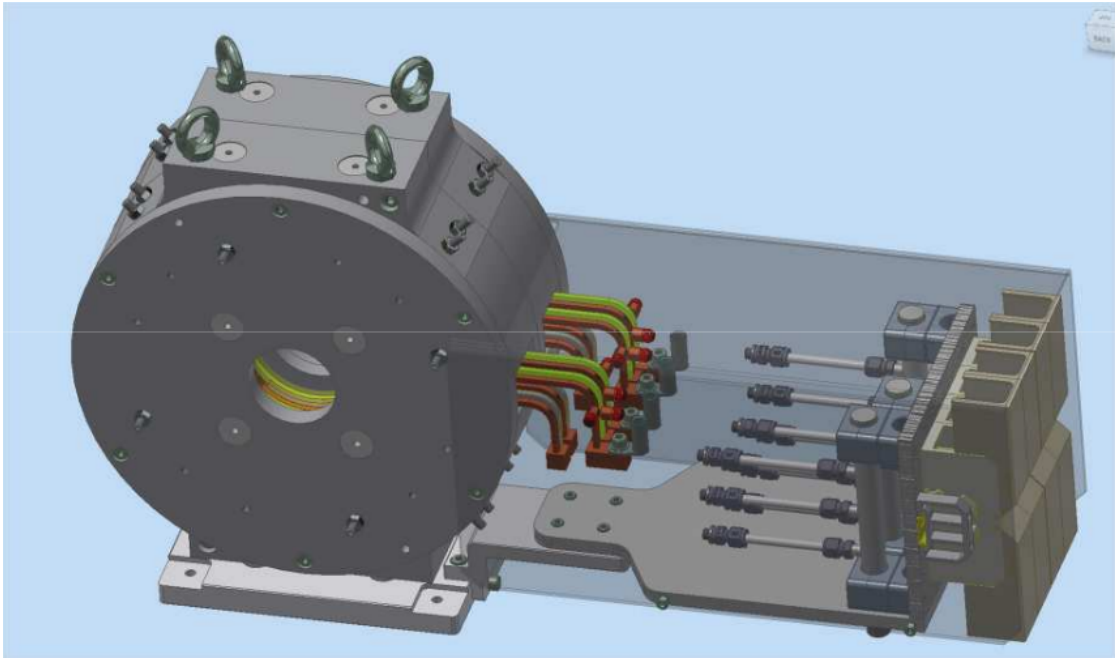


Figure 2.3: CAD design of the double-coil solenoid used for ARTI.

in Fig. 2.5.

#### 2.1.3.1 YAG screen

At the tip of the actuator, a thin Yttrium Aluminium Garnate (Cerium) (YAG:Ce) screen is installed, orthogonal to the beam direction. The YAG screen has a metallic coating which blocks reflections of the UV laser from the cathode from reaching a digital CMOS camera. For the light fluoresced from the YAG to reach the camera (placed orthogonally to the beamline, as shown in Fig. 2.2), a 45°angled mirror is placed a few centimetres after the screen. This rectilinear observation geometry ensures minimal beam profile distortion and excellent resolution at low beam energies, and is also used in the SwissFEL photoinjector [74]. YAG screens are fluorescent, capable of high light yields, and robust. However, they have a decay time of a few nanoseconds, making them unable to measure standard ps-long bunch lengths. Additionally, they are susceptible to saturation at high beam intensities and to multiple scattering, which limits their resolution [75]. The YAG screen was therefore used in the initial optimisation of the electron beam, and

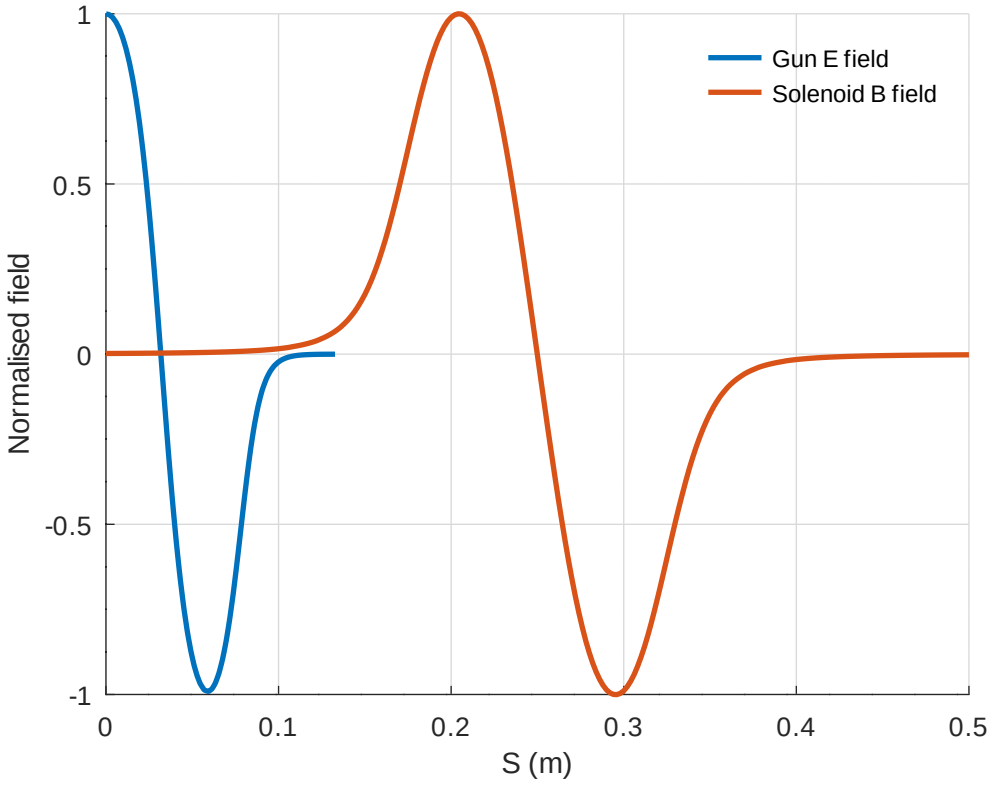



Figure 2.4: One-dimensional longitudinal field profiles of the electron gun and the solenoid as a function of the longitudinal coordinate $s$. The accelerating electric field of the gun and the magnetic field of the solenoid are shown in normalised units, with each field scaled to its respective peak amplitude, to allow direct comparison of their spatial distributions. The gun field is localized near the cathode region, whereas the solenoid field extends over a broader region to provide transverse focusing and emittance compensation.

later replaced with optical transition radiation (OTR) screens during the CBS experiment.

#### 2.1.3.2 OTR screens

Optical transition radiation is generated when a relativistic charged particle beam crosses the interface of two materials with different permittivity $\epsilon_r$. The radiation emitted is in the optical range, and scattered in a cone of angular width $\pm 1/\gamma$.

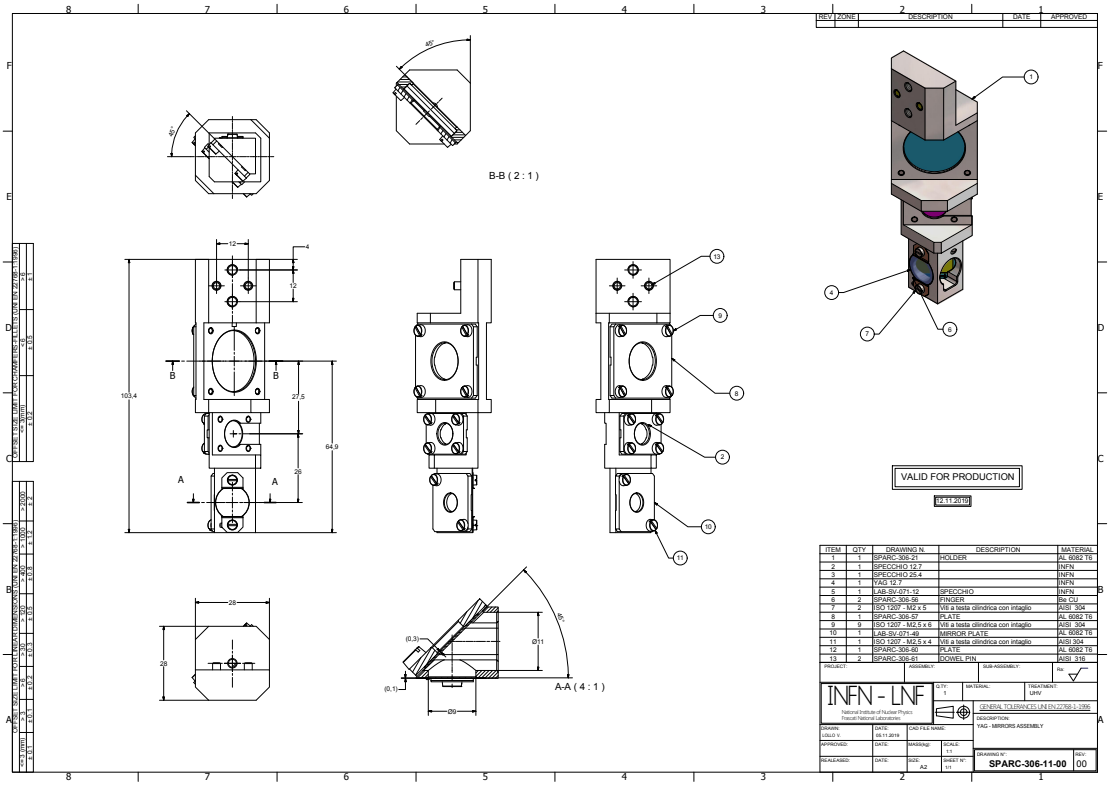



Figure 2.5: Technical drawing of the screen slots available from the actuator installed at ARTI.

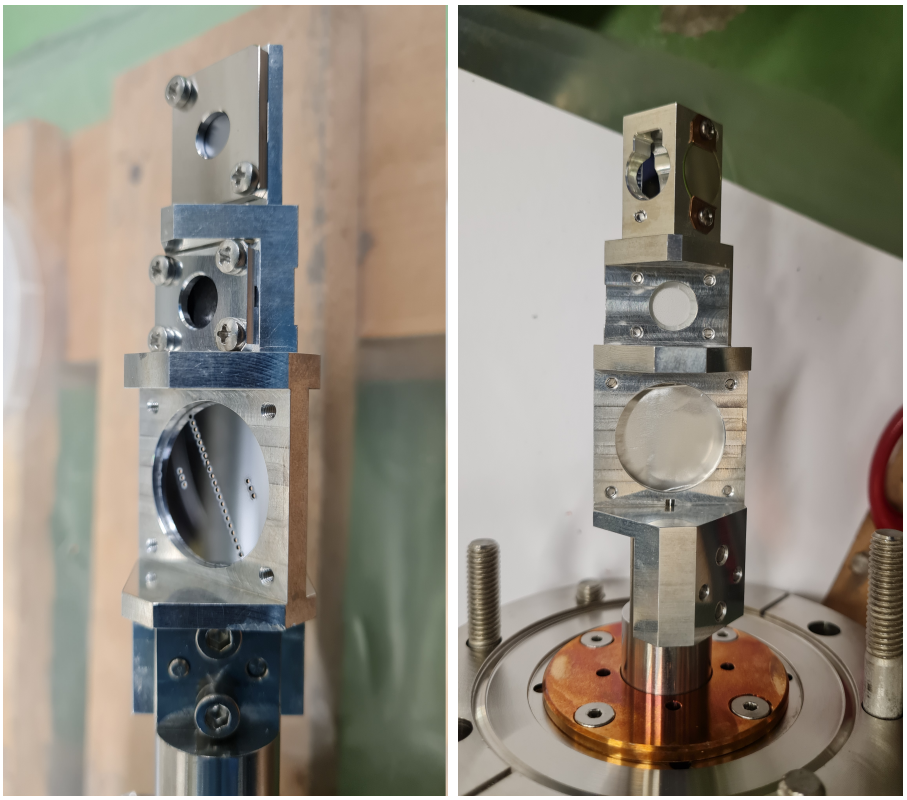
The number of OTR photons thus generated, $N_{ph}$, is

$$N_{ph} = \frac{\alpha}{\pi}(2\ln\gamma - 1)\ln\frac{\nu_2}{\nu_1}, \tag{2.1}$$

where $\alpha$ is the fine structure constant, $\gamma$ the relativistic factor of the electron beam, and $\nu_{1/2}$ the photon frequency region [75]. OTR screens are deemed as "references" since they provide excellent temporal and spatial resolution, along with a very high saturation level. Their main disadvantage is the significantly lower light yield compared to fluorescent screens. Additionally, given the inverse dependence of the cone spread with respect to the beam energy, at low beam energies (such as the one used at CTF2), a large camera aperture is required to capture most of the emitted light.

The actuator configuration permitted the installation of two OTR screens, each oriented at 45° with respect to both the camera axis and the electron beam.

Following an initial discrepancy between the smallest beam spot size measured with the YAG screen and that predicted by simulations (see Chapter 3), the first version of the OTR screen was installed, as shown in Fig. 2.6a. The initial OTR



(a) (b)

Figure 2.6: Photos of the two versions of the OTR screens used at ARTI. The first design (a) was robust and provided a good light yield, but it was too thick for the laser to pass through. The second design (b) consisted in a 99.5% pure Aluminium foil of 25 µm thickness.

screen consisted of a 400 µm thick silicon wafer coated with an 100 nm Aluminium substrate. This configuration ensured an excellent screen flatness and therefore maximised the light yield and its uniformity. To suit the spatial alignment of the CBS experiment, several round holes were drilled with an industrial laser in the wafer. The dimensions of the screen holes are shown in Fig. 2.7. These 0.6 mm-diameter holes established the spatial alignment between the laser and electron beam, since they allowed the IR laser to pass through the IP and reach the digital

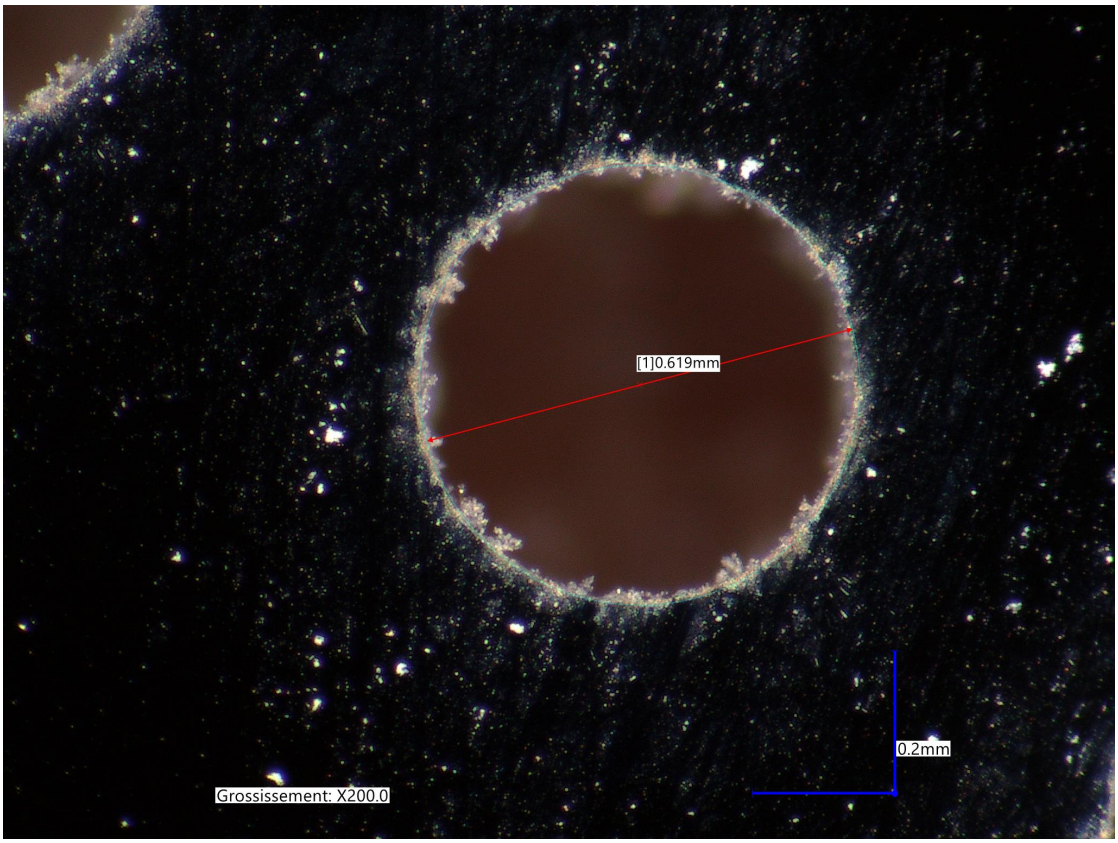



Figure 2.7: Photo under a microscope of one of the holes laser-cut into the OTR screen. The laser's excellent resolution allowed for a consistently round shape, and a diameter of 619 µm.

camera. Namely, if the laser passes through the centre of a targeted hole, its intensity as seen on the camera is maximised, while for the electron beam, it would be minimised. However, it was found that the millimetre hole led to a poor spatial resolution of the IP, and a new type of OTR screen was installed in place of it.

Ideally, the smallest hole that could be made and serve as a reference was one made by the actual laser used for the interaction. To achieve this, a thin metallic screen was needed, for which a 25 µm thick high purity (99.5%) Aluminium foil was used, shown in Fig. 2.6b. This was the set-up from which soft X-rays were observed. One disadvantage was that there was a notable decrease in light yield due to a reduction in screen flatness. This could have been prevented by using

a thicker Aluminium sheet of 100 µm. However, experimental tests showed that photoinjector laser was unable to punch a hole through the thicker screen.

### 2.1.4 Dipole spectrometer

A dipole spectrometer placed after the viewport is used for beam energy and energy spread measurements. Based on field measurements, the following relation was used to determine the beam energy $E_{\text{peak}}$ given the position of the electron beam $x$ on the imaging screen and the dipole current $I_c$ [76],

$$E_{\text{peak}}[\text{MeV}] = 0.496 I_c (1 + x/D), \tag{2.2}$$

where $D$ is the beam dispersion, 620 mm. A typical phase scan measuring the drift in beam energy and in spread against the RF phase is shown in Fig. 2.8. The on-crest phase, corresponding to the maximum beam energy given a specific gun gradient, varied according to the temperature inside the klystron hall, so this measurement was repeated daily.

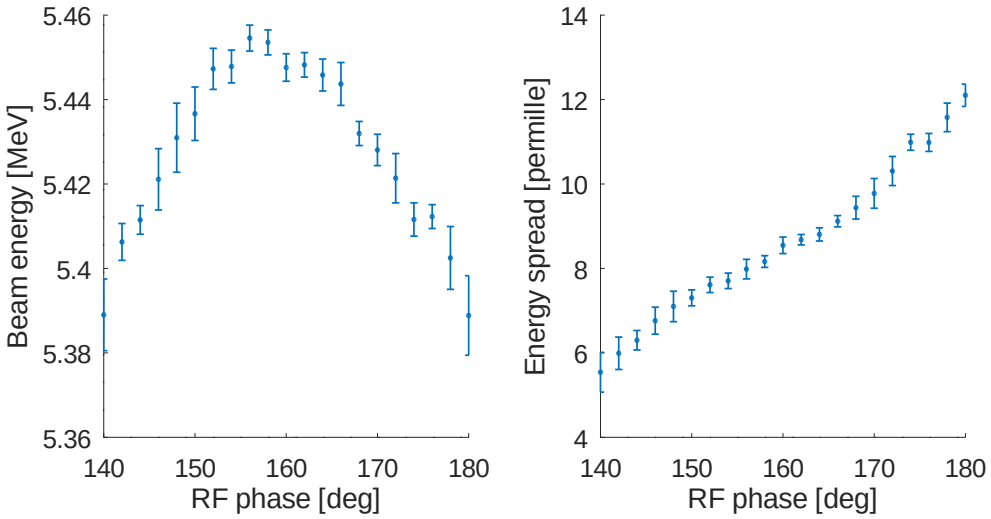



Figure 2.8: Dependence of the beam energy (left) and relative energy spread (right) on the RF phase, as measured for the ARTI beamline. The beam energy exhibits a maximum near on-crest acceleration, while the energy spread increases monotonically with RF phase over the scanned range. Error bars represent the statistical uncertainties of the measurements.

The screen used to obtain a light output from the bended electron beam is a Chromox. This fluorescent screen can be more easily manufactured in large sizes, in correspondence with the dispersive tail of the bended electron beam, and it presents a good light yield, similar to a YAG, making it preferable for use in a spectrometer. However, the decay time also spans for several seconds, requiring appropriate adjustments in data taking intervals to avoid parasitic interference from previous beam settings. A sample image profile from the dipole spectrometer is shown in Fig. 2.9.

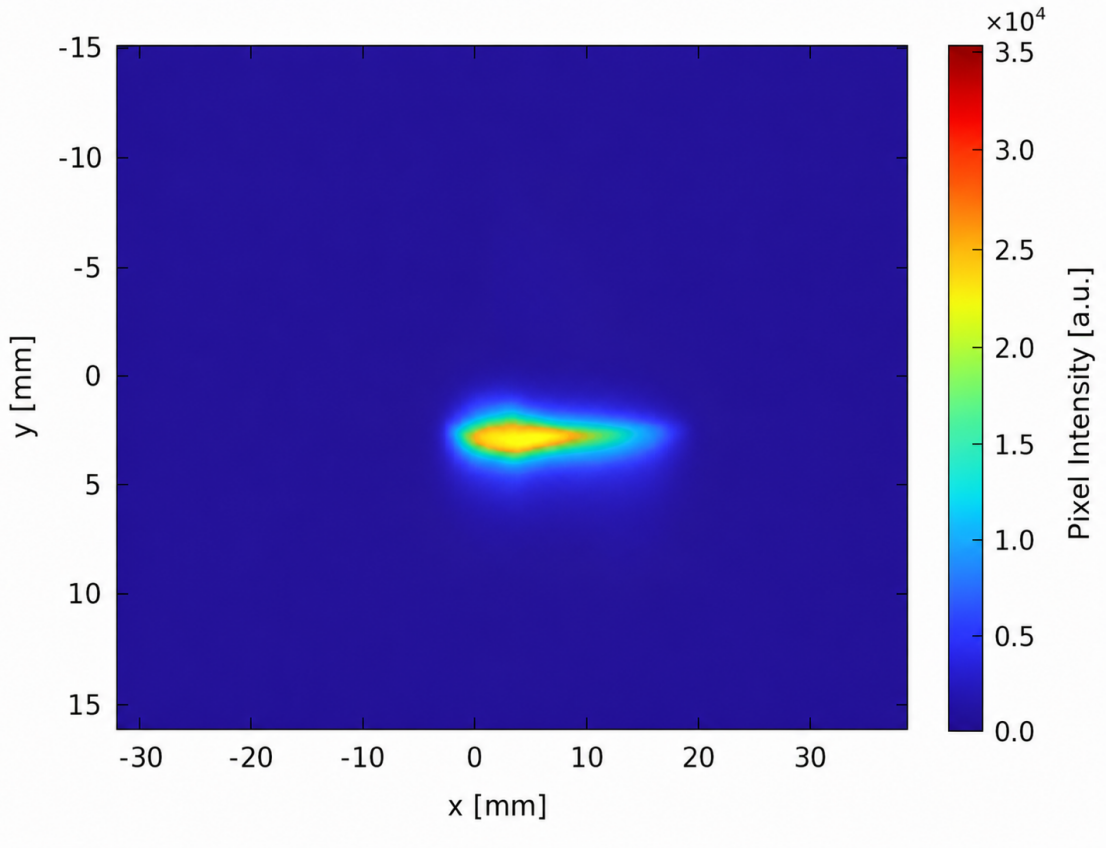



Figure 2.9: Beam profile obtained from the dipole spectrometer, through a fluorescent Chromox screen. Note the characteristic tail of the profile, proportional with the energy spread.

The dipole was essential for the CBS experiment as it allowed for the deflection of the electron beam from the X-rays, thus preventing charged particles from functioning as background for the X-ray detector.

### 2.1.5 Faraday cup

A Faraday cup installed at the beam dump on the gun axis is used for bunch charge measurements. Due to the small active area of a few millimetres, and to avoid beam losses, a special solenoid strength setting was used to focus the beam transversely on the Faraday cup. Nominal charges of 200 pC are used, while values of up to 800 pC have been measured. The nominal charge stability is within 2-5%.

### 2.1.6 Vacuum pumping port

ARTI presents a vacuum pumping port, housing a CF connector for attaching a rough and turbomolecular pump. Venting of the beamline is usually done by filling it with Nitrogen gas, before raising the pressure to the atmospheric level. The gun sector is typically kept under vacuum, while the downstream beamline is vented. To vacuum the sector, a rough pump is initially used up to a few millibars. Afterwards, the turbomolecular pump starts, bringing the vacuum down to $1 \times 10^{-5}$ mbar. The final pumping stage is performed by ion pumps, which can only be used under a moderate vacuum level. Several ion pumps are installed along the beamline, meant to bring the vacuum level down to its nominal value.

### 2.1.7 Electron beam characterisation

Diagnostics of the ARTI beamline were used to measure the stability of the electron beam parameters. Experimental results for the beam jitter in position, spot size, and bunch charge are shown in Fig. 2.10. An excellent shot-to-shot stability was obtained for both the position and size of the electron beam. A summary of the electron and laser beam jitter values at the CBS IP is provided in Table 2.2.

Fig. 2.10 presents the shot-to-shot stability of the electron beam position, beam size, and bunch charge. The horizontal and vertical beam positions measured on the OTR screen exhibit fluctuations around a stable mean value, with no significant long-term drift observed throughout the measurement period. The variations are generally limited to a few tens of micrometres, indicating good transverse beam pointing stability during operation of the injector.

The RMS beam sizes extracted from the OTR images also remain relatively stable over the course of the measurement. Although occasional excursions are

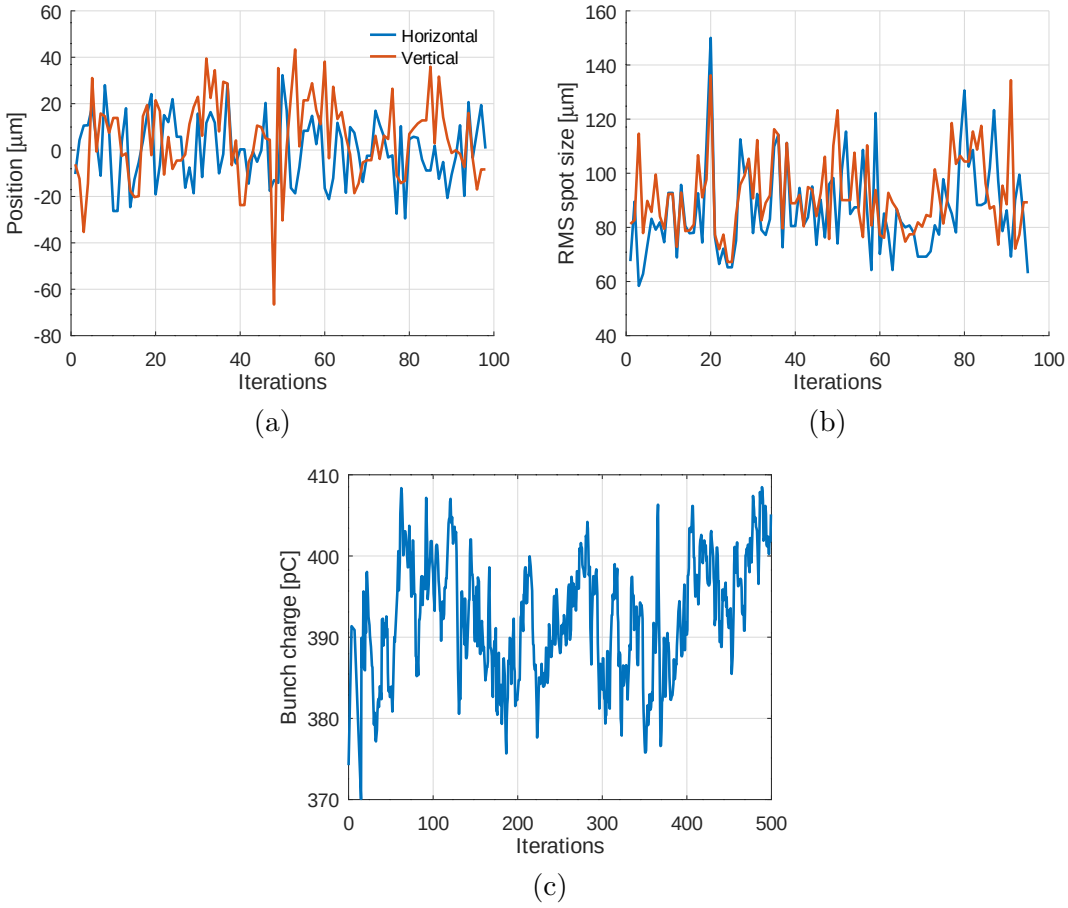



Figure 2.10: Sensitivity measurements of the electron beam. (a) Shot-to-shot stability measurements of the horizontal and vertical electron beam position, as seen on the OTR screen. (b) Shot-to-shot stability measurements of the horizontal and vertical RMS spot size of the electron beam, from the OTR screen. (c) Shot-to-shot stability measurement of the bunch charge, performed with the Faraday cup.

visible, the beam size does not exhibit any systematic trend, suggesting that the accelerator and focusing system operated under consistent conditions. The observed fluctuations are consistent with normal pulse-to-pulse variations in beam parameters and machine settings.

The bunch charge measurements obtained with the Faraday cup similarly show good stability. The charge fluctuates around an approximately constant average value with no evidence of significant drift over the duration of the measurement.

Table 2.2: Summary of Laser and Electron Beam Jitter Values at the CBS Interaction Point

| Parameter | Unit | Value |
|---|---|---|
| Horizontal/Vertical electron beam position | µm | 19/17 |
| Horizontal/Vertical electron beam size | % | 24/19 |
| Electron bunch charge | % | 2 |
| Electron beam energy | % | 0.1845 |
| Horizontal/Vertical laser spot position | µm | 14/11 |
| Laser spot size | % | 2.1 |
| Laser pulse energy | % | 0.2 |

Taken together, these results demonstrate that the injector provided a stable electron beam in terms of position, transverse size, and charge, thereby ensuring reproducible conditions for the Compton backscattering experiment.

## 2.2 Photoinjector laser

The electron bunches are generated using the fourth harmonic of a Light Conversion Pharos Laser System. The laser emits infrared pulses of 2 mJ, centred at 1030 nm, with a maximum repetition rate of 3 kHz [77]. The repetition rate of the electron beam is restricted to a maximum of 10 Hz due to the power and operational limitations of ARTI's klystron. The nominal extracted bunch charge is 400 pC, however up to 800 pC bunches have been measured for the smallest laser pulse length of 112 fs RMS with a 270 µm RMS spot size. A detailed schematic of the ARTI laser beamlines is shown in Fig. 2.11. Starting from the first second-harmonic generation (SHG) crystal, two beamlines are defined: the UV one, generating the electron bunches at the cathode, and the IR one, used to collide with the electron beam for the CBS experiment.

The pulse duration can be adjusted by chirping the IR pulse of the photoinjector laser. These changes affect both the IR and UV beamlines. A downside is the sub-optimal harmonic conversion efficiency, allowing for a reduced pulse duration tunability from 265 fs to 775 fs FWHM while keeping a pulse energy above 35 µJ. The longitudinal laser profile is measured using an autocorrelator. For the opera-

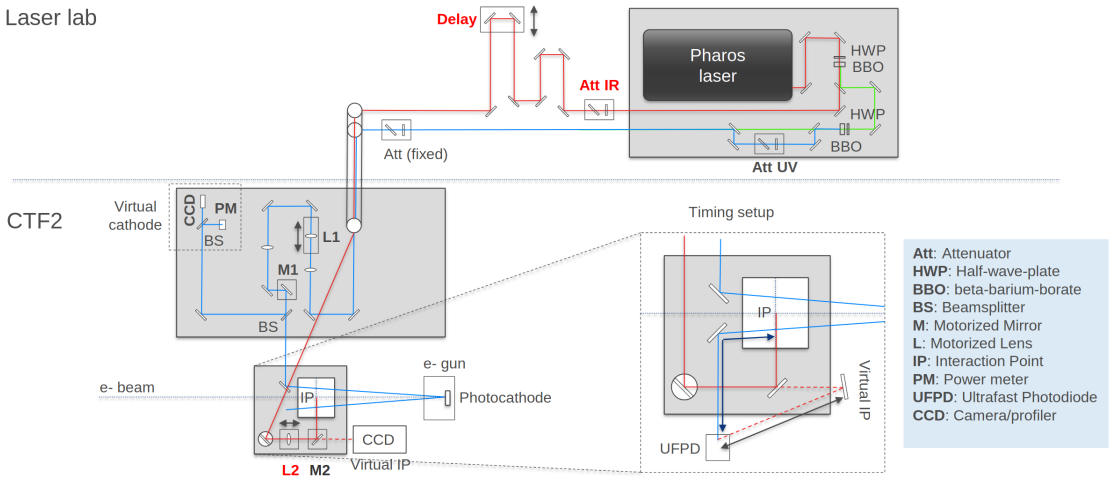
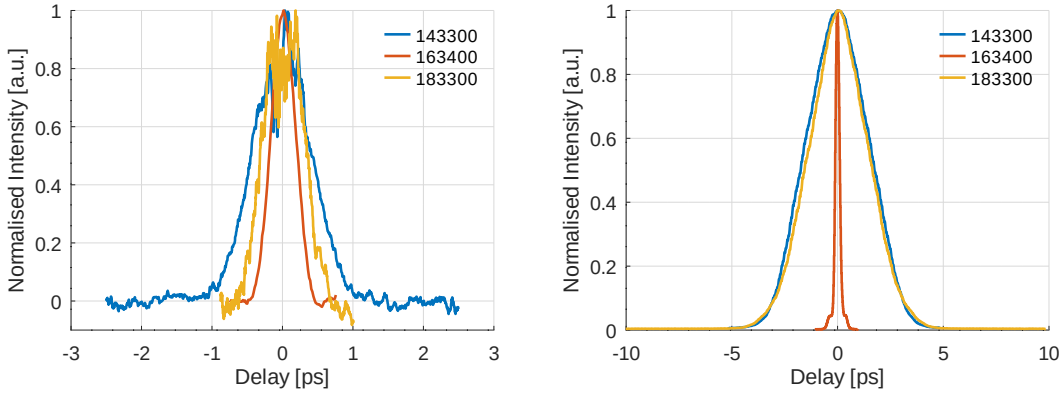



Figure 2.11: Schematic of the laser transport and timing systems installed at the ARTI beamline for the Compton backscattering experiment. The infrared (red) and ultraviolet (blue) laser beamlines originate from the Pharos laser system and are transported from the laser laboratory to the accelerator area. The UV beam is directed onto the photocathode for electron bunch generation, while the IR beam is delivered to the interaction point (IP) for Compton backscattering. The optical system incorporates attenuation, beam steering, focusing, and timing diagnostics to control the laser spot size, pulse energy, and temporal overlap between the laser and electron beams. (credit: Eduardo Granados)

tion of ARTI, three distinct longitudinal profiles were used, as shown in Fig. 2.12. The BBO crystals changed the duration of the UV pulse with respect to the IR pulse. Measurements of the three working points for the longitudinal distribution are provided in Table 2.3. One can see that there is a strong difference between the IR and UV laser pulse lengths for the same setting of the motor position. That is, while for the UV pulse duration of 265.5 fs, the corresponding value for the IR is 151 fs, for the UV pulse length of 540 fs, the IR pulse duration experiences a large increase to 2100 fs. Although the longer IR pulse length configuration yields a reduced flux, it increases the temporal overlap window between the laser pulse and the electron bunch, thereby relaxing the flux detection tolerance during the timing scan. Additionally, although not measured, RF-Track simulations indicated that the nominal electron bunch length was close to 2 ps, and, from Eq. 1.24, the convolution of the laser and electron pulse lengths ensures no significant gain in flux with a smaller pulse length.

Table 2.3: Pulse Duration Measurements of the UV and IR Beams. Pulse Duration Values are Deconvoluted and Provided in FWHM from Gaussian Fits.

| Motor Position | IR pulse duration | UV pulse duration |
|---|---|---|
| 163400 | 151 fs | 265.5 fs |
| 143300 | 2100 fs (negative chirp) | 540 fs |
| 183300 | 2310 fs (positive chirp) | 775.7 fs |



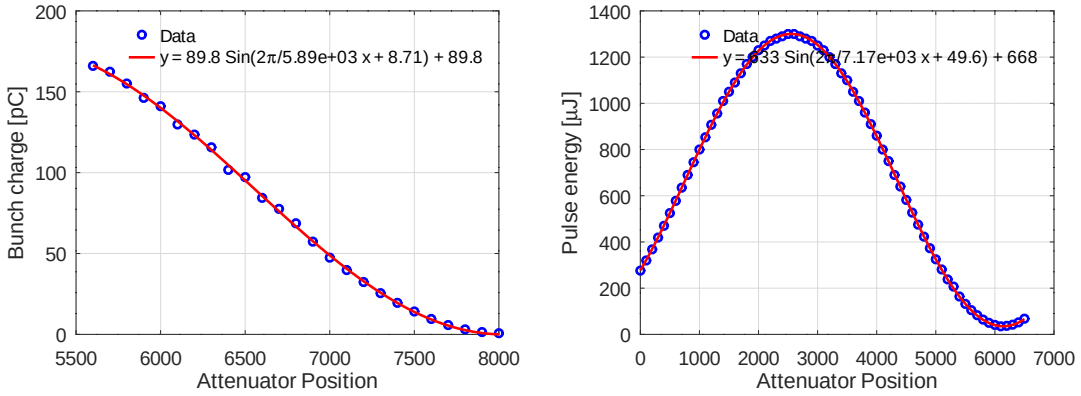

(a) (b)

Figure 2.12: Autocorrelation measurements of the longitudinal pulse profiles for the UV (a) and IR (b) laser systems at their respective working points. The normalised laser intensity is plotted as a function of the autocorrelator's temporal delay for different operating settings. High-frequency noise was reduced using a moving-average filter. The pulse duration was determined from the deconvoluted full width at half maximum obtained via a Gaussian fit to the autocorrelation traces. (credit data: Eduardo Granados)

#### 2.2.0.1 UV laser beamline

The output from PHAROS is first sent through two consecutive BBO crystals, in order to quadruple the laser frequency and match the photon energy to the copper work function of 4.6 eV. The first crystal is 2 mm thick, converting from 1030 nm to 515 nm with a 55% efficiency (1.2 mJ, 0.04% RMS fluctuation), the second, 0.5 mm thick, converting 515 nm to 257 nm with a 35% efficiency, leaving a total of 480 µJ for the UV, with a 0.09% RMS pulse energy stability. The frequency

doubling reduces the thermal emittance of the electron bunch, ensuring the highest quality beam at the cathode. The BBO crystals are followed by an attenuator, which allows for a motorised and automated control of the laser pulse energy. This is used to control the electron bunch charge. A typical experimental attenuation scan of the bunch charge is shown in Fig. 2.13a. Attenuation can reduce the bunch charge to a few pC. The reduction in charge from attenuation, as seen in Fig. 2.13, closely follows a sinusoidal function. The attenuator consists of a half-wave plate and a thin film polariser, exploiting beam polarisation to achieve the decrease in laser intensity.




(a) (b)

Figure 2.13: Representative attenuation scans of the UV (a) and IR (b) laser systems. For the UV laser, the attenuator setting is varied to control the emitted electron bunch charge, while for the IR laser the pulse energy is monitored as a function of attenuator position. In both cases, the measured data are fitted with a sinusoidal function, as indicated in the legend, reflecting the periodic transmission of the rotating attenuator.

Following its attenuation, the laser is directed towards the CTF2 experimental hall. Once in the hall, it passes through a two-mirror telescope, used to control the laser spot size on the cathode. The typical working range is between 0.2 and 0.5 mm in RMS spot size. The laser focus is followed by a motorised mirror, which allows for controlling the beam position on the cathode. This can provide an initial steering of the electron beam, along with an alignment of the laser on the gun axis, ensuring minimal emittance (the alignment technique is described in Chapter 4.6).

Lastly, before the UV laser enters the vacuum window, it passes through a beam splitter, taking a small energy laser component to a virtual cathode set-up. Virtual cathodes are regularly used in photoinjectors [78]. They consist of a camera system (for ARTI also a power metre), which is placed at a distance from the beamsplitter that is equal to the one travelled by the main beam to the cathode. This simple set-up allows for visualising the laser profile as it would appear at the cathode. A sample beam profile is shown in Fig. 2.14.

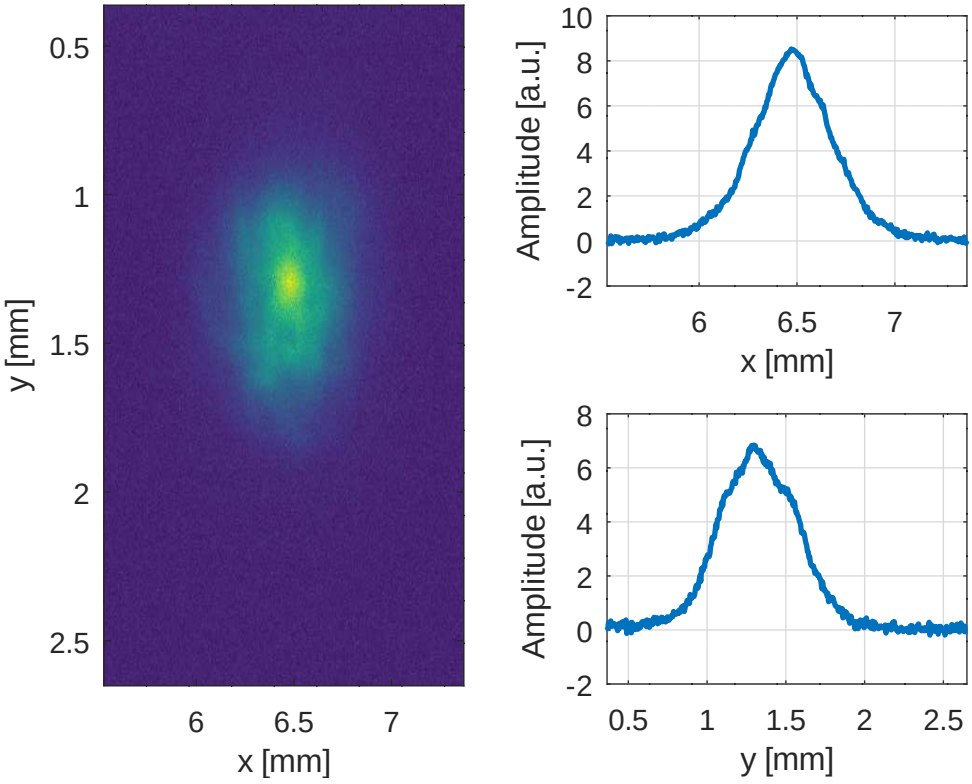



Figure 2.14: Typical image on the virtual cathode of the UV laser at the cathode location. The left plot corresponds to the UV laser profile, while the plots on the right correspond to horizontal (top) and vertical (bottom) projections of the 2D image data.

In regards to cathode physics, it should be noted that depending on the focus size and attenuation used, the charge emission can become saturated. Under these conditions, the bunch population can be controlled by other input parameters of

the UV laser. For example, increasing the laser spot size on the cathode in a saturated regime leads to an increase in bunch charge, since it effectively reduces the laser intensity past the saturation threshold. Studies, described in Chapter 2, have been performed at ARTI to evaluate the saturation limit and determine the quantum efficiency of the cathode.

Another relevant property of the laser beam is its stability, since it affects the electron bunch stability. As the UV beam was transported in air, cumulative nonlinear effects degrade its energy stability from 0.09% RMS at the quadrupler output to 1.04% at the input of the RF gun. One way to mitigate this for the CBS experiment was by stretching the pulse from 265 fs to 775 fs FWHM, which reduced the fluctuation of the RMS bunch charge from 5% to 1%.

#### 2.2.0.2 IR laser beamline

The IR laser beamline, constructed specifically for the CBS experiment, presents a similar structure to the UV laser's. It consists of the remnant pulse that is not converted from the first SHG, which amounts to a maximum pulse energy of 1.3 mJ. A typical IR attenuation scan is shown in Fig. 2.13b. The attenuator is motorised and was used to perform pulse energy scans for the CBS experiment. To allow for increased control, security interlocks, and a feasible data taking process, both the UV and IR beamline elements were automated.

One distinction from the UV beamline is the motorised delay stage, a staple of CBS experiments. The device consists of two 45 angled flat mirrors placed on a motorised linear stage. By shifting this stage, the total length of the IR laser beamline can be contracted or extended. The step size of the delay stage is equivalent to 1/60 ps. Delay stages are used to perform scans of the longitudinal position of the IR laser when searching for the CBS signal.

Following the delay stage, the laser is transported to the CTF2 experimental hall, passing through a fixed focusing lens, which reduces its RMS spot size to 20 µm. Before the laser enters vacuum through the fused silica vacuum window, it is reflected by a motorised mirror with a step size in the order of 5 µm. A photo of the last stage of the IR beamline is shown in Fig. 2.15. As shown in the schematic, the last stage of the beamline was also used for a preliminary timing alignment

of the electron and laser beams for the CBS experiment, which is described in Chapter 4.5.

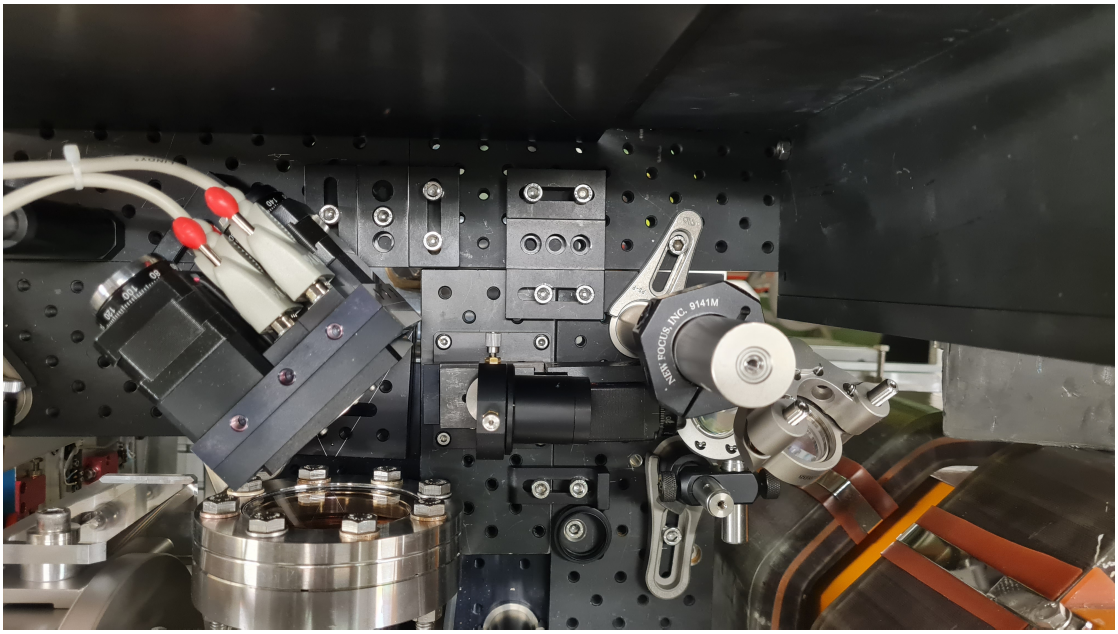



Figure 2.15: Photograph of the last section of the IR beamline, including the focus and motorised mirror.

One advantage of the 90° configuration for the CBS interaction is that both the laser and electron location at the IP can be easily imaged with a single digital camera, since the laser and light generated from the electron imaging screens travel in the same direction. However, given the high laser pulse energy, the actual laser beam was never used for imaging. Instead, the continuous amplified spontaneous emission (ASE) signal was employed, with a much lower intensity but nonetheless having the same position and focus size at the IP as the pulsed signal, a requirement for spatial alignment. The intensity of the ASE signal was controlled by a neutral-density (ND) filter wheel placed in front of the camera. A typical IR laser profile at the interaction point is shown in Fig. 2.16.

#### 2.2.0.3 Characterisation of the IR laser beam at the IP

As part of the CBS experimental study at ARTI, a correspondence between the predicted scattered photon flux from RF-Track and the measured number of pho-

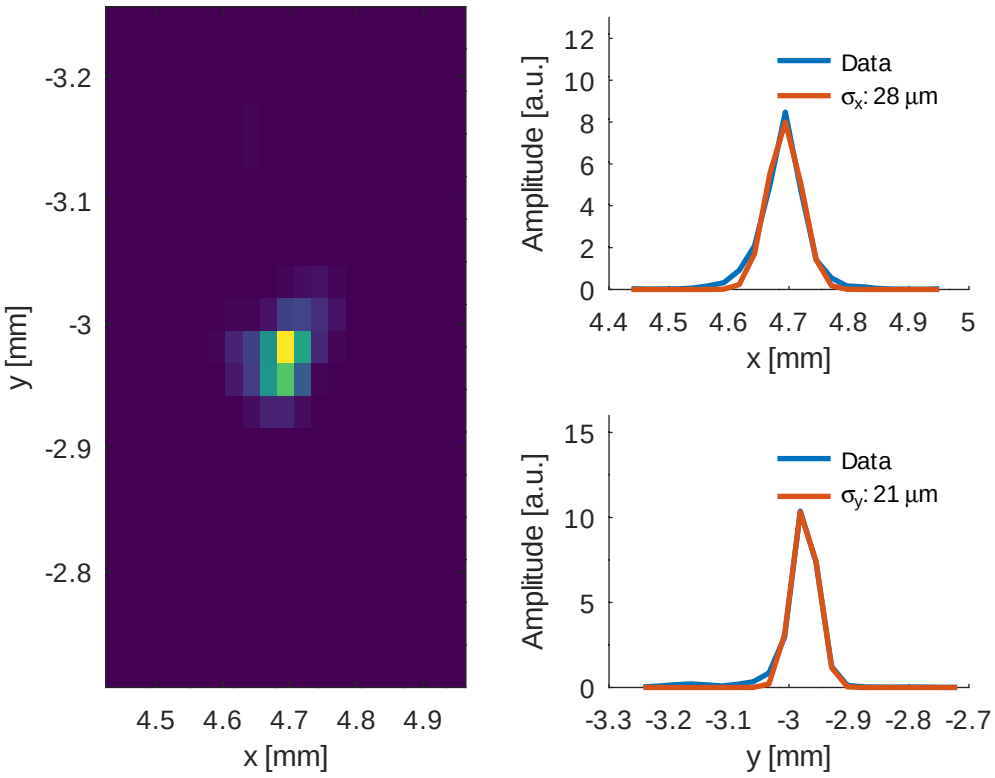



Figure 2.16: The measured IR laser profile at the interaction point, using the same digital camera used to observe the electron beam transverse distribution. Gaussian fits of the horizontal and vertical distributions are included. Note that the beam size measurement is limited by the camera pixel size.

tons from the X-ray detector was required. To achieve this, a set-up that mimics the virtual cathode was installed, this time applied with respect to the interaction point of the CBS experiment. The distance between the last motorised mirror and a laser beam profiler was matched to that from the mirror to the IP, as seen in the schematic in Fig. 2.11. The laser beam profiler was used to measure the beam parameters along with their stability. The impact of the drift in the delay stage on the IP parameters was also studied. Pulse energy measurements were taken with a laser power metre.

The results of the beam profiler measurements are shown in Fig. 2.17. Excellent beam conditions were achieved. The image profiler recorded snapshots of the laser

transverse distribution with a pixel size of 6.7 µm. An example profile is shown in Fig. 2.17f. An RMS spot size of 26.9 µm was measured. From Fig. 2.17a, one can see that the beam centroid is bounded by a 40 by 40 µm$^2$ ring. The laser pointing jitter can be attributed to vibrations affecting the mirror positions, thermal effects modifying the length of beamline elements, and air turbulence from thermal gradients. These effects are amplified by the long laser beamline, requiring a significant number of optical elements to steer it to the cathode and IP. The variation in the horizontal and vertical centroid position across 50 laser shots is shown in Fig. 2.17b. The RMS jitter in the horizontal position is 14.4 µm, and 11.4 µm in the vertical position. Dividing these values by the RMS spot size, a pointing instability of 53.5% and 42.4% is obtained in the horizontal and vertical, respectively. The stability of the peak pixel intensity across 50 shots is shown in Fig. 2.17c. An RMS variation of 3.2% was determined, which is proportional to the intensity of the IR laser. The variation in the $1/e^2$ beam diameter is shown in Fig. 2.17d. An RMS variation of the sigma spot size of 0.566 µm was measured. The variation in the radial spread of the centroid around the target area was plotted in Fig. 2.17e, showing good confinement.

The beam profiler measurements allowed for the estimation of core parameters of the IR beam at the IP (spot size, profile, and intensity), along with the variation and jitter in position, beam size, and peak intensity. Due to the small number of expected photons generated from CBS, a study of the beam jitter was necessary, in order to evaluate its impact on the photon flux. This study was reinforced by a simulated tolerance study before X-ray detection that was used to assess the realistic target parameters at the IP. A trade-off was needed given that a smaller beam spot size, although leading to a higher flux, also has a low tolerance to position jitter. Fortunately, simulations revealed that a very small RMS laser spot size of 20 µm could be feasibly used for the CBS interaction, given the low position jitter and the large electron spot size measured.

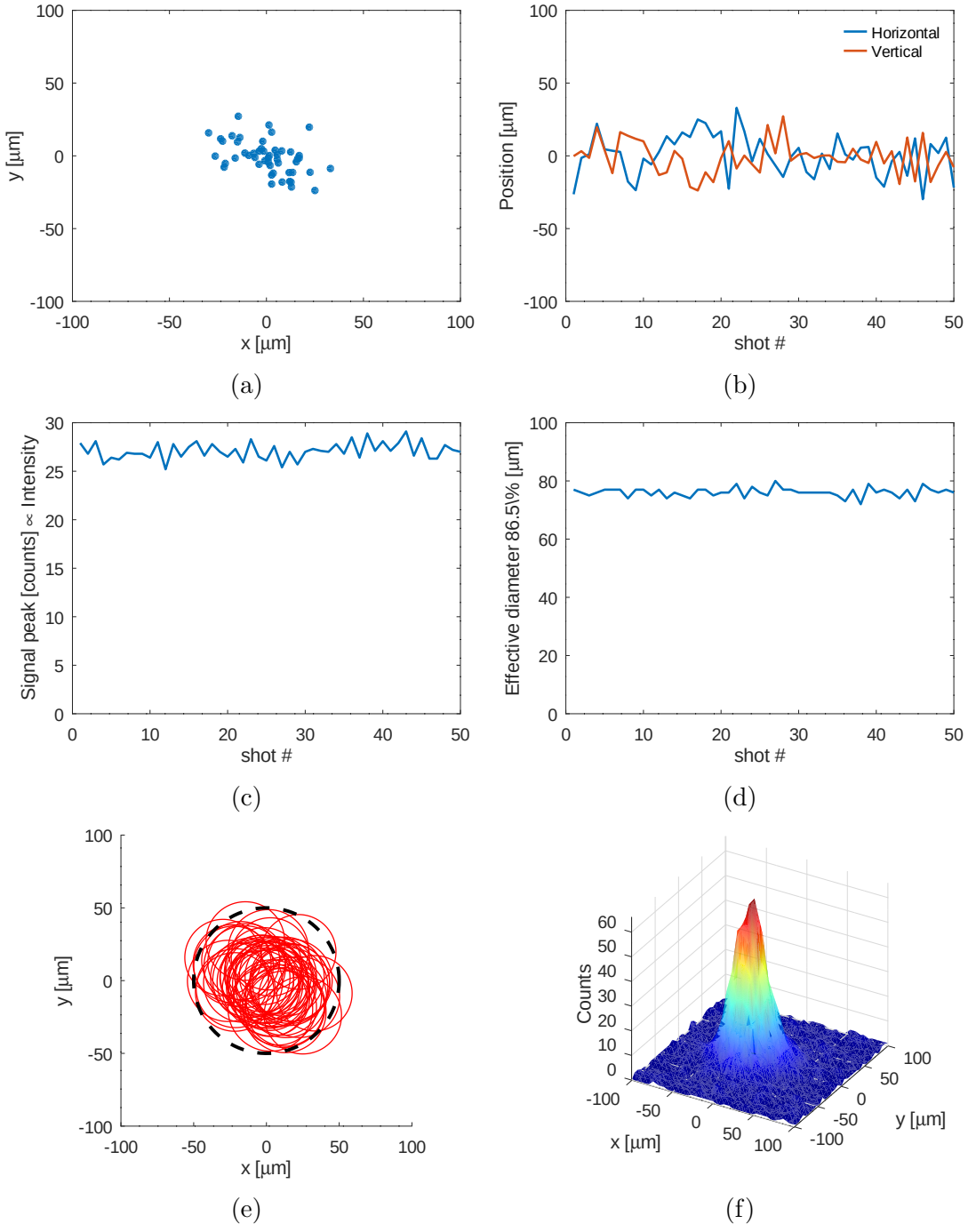
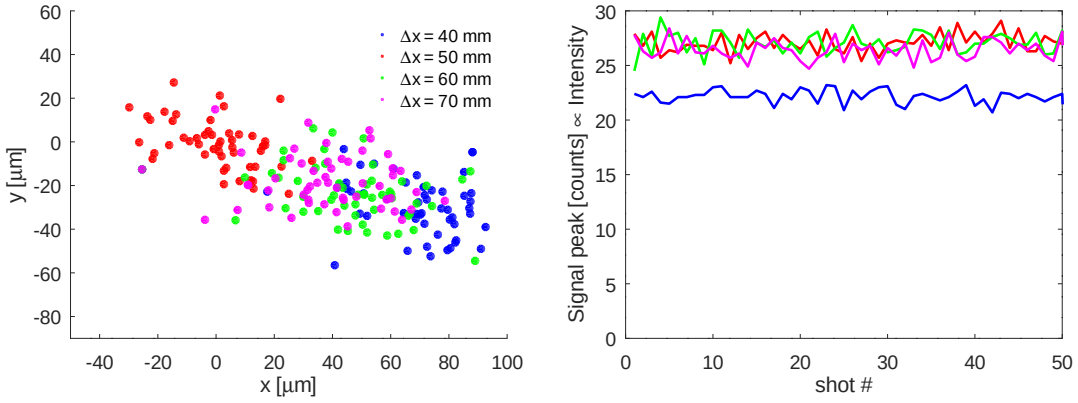



Figure 2.17: Experimental characterisation of the IR laser beam at the CBS interaction point. (a) Samples of the IR centroid in space. (b) Shot-by-shot stability measurement of the horizontal and vertical beam centroid. (c) Shot-by-shot stability measurement of the peak signal registered by the beam profiler, proportional to the beam intensity. (d) Shot-by-shot stability of the effective $1/e^2$ beam diameter. (e) Shot-by-shot variation of the IR $1/e^2$ diametral spread around the centroid. The black circle corresponds to the measurement average. (f) Sample of the transverse beam profile as measured by the beam profiler. (data credit: Eduardo Granados)

Since the delay stage is a movable component in the laser beamline, there is an associated risk of beam drift during the stage translation, due to the ingoing and outgoing laser beams from the delay stage not being exactly parallel to each other. Profiler measurements of the signal peak and beam position were made to study the impact of this misalignment. One can observe in Fig. 2.18a that for a displacement from 40 mm to 70 mm, in spite of a careful alignment of the laser, a noticeable beam drift of around 80 µm is present. Fortunately, during the CBS experimental campaign, a longitudinal spread of ±10 mm was explored, which minimised this drift. Nevertheless, to ensure reliability, systematic beam position measurements and corrections were made for every setting explored for the delay stage during the CBS experiment. Furthermore, one can see from Fig. 2.18b that the beam is clipped at the translation point, $\Delta x$ =70 mm. However, that position did not correspond to the temporal alignment of the electron and laser beam, nor to the range explored during the search for the CBS signal.




(a) (b)

Figure 2.18: Measurements of IR beam parameters at the IP for different positions of the delay stage. (a) Pointing stability for four different delay stage positions. (b) Shot-by-shot measurements of the beam intensity for the same four position settings, showing beam clipping at 40 mm. (data credit: Eduardo Granados)

Lastly, a laser power metre was used to investigate the IR laser pulse energy at the IP. One can see from the summary Table 2.4 that the laser pulse energy reaches an average value of 1.09 mJ at the IP, with an RMS stability of 0.205%.

The average pulse energy, spot size, and position jitter were used as input in RF-Track simulations at the IP.

Table 2.4: Summary of the Measured IR Beam Parameters at the IP

| Parameter | Unit | Value |
|---|---|---|
| RMS spot size | µm | 26.9 |
| RMS pulse length | fs | 2100 |
| RMS position stability x/y | µm | 14.4/11.4 |
| RMS intensity stability | % | 3.2 |
| RMS spot size stability | µm | 0.566 |
| Average pulse energy | mJ | 1.09 |
| Minimum pulse energy | mJ | 1.08 |
| RMS stability (200 shots) | % | 0.205 |
| Point-to-Point (PTP) stability | % | 1.182 |

The next chapter provides an account of the operation and optimisation of the ARTI gun, along with the establishing of an equivalent beam model in the CERN-developed particle tracking code, RF-Track.

# Chapter 3

# Optimisation of the ARTI Beamline

In order to provide the brightest possible CBS beam, optimisation of the ARTI beamline was essential. This required an alignment of the beamline elements and a thorough methodology for positioning the laser and electron pulses longitudinally and transversely at the CBS interaction point. In order to minimise the beam emittance and predict the electron beam parameters at the IP, a simulation model of the electron gun set-up was needed, able to track the electron bunch from the cathode, under the gun E-field, followed by the solenoid B-field and up to the IP squeeze. This model was made using RF-Track, a code which will be introduced in this chapter.

## 3.1 RF-Track

Most of the simulations presented in this thesis were obtained using a CERN-developed particle tracking code named RF-Track [79]. Standard Monte Carlo codes used for ICS simulations include CAIN [80] and COMPTON [81]. The latter has been benchmarked against experimental results from various ICS sources [82].

RF-Track is a fast and parallel particle-tracking code developed at CERN to simulate beam tracking in the presence of collective effects, such as space-charge and wakefields, in field maps as well as in conventional matrix-based elements. RFT has the ability to simulate the ICS process. RF-Track simulates ICS using a Monte Carlo method, where the electron-photon interaction is computed by taking

into account the scattering differential cross-section. RF-Track uses the Thomson cross-section at low photon energies, or the nonlinear Klein–Nishina cross-section at high photon energies [83, 84], to compute the parameters of the scattered photon as well as the electron recoil. The effects of linear laser polarisation are taken into account in both cases. All computations are performed in the electron's rest frame, through full 4-D Lorentz boosts from and to the laboratory frame. RF-Track allows the user to describe the laser beam using a set of realistic parameters: Gaussian vs uniform profile, polarisation, the $M^2$ parameter, the Rayleigh length, and the laser orientation in the 3-D space.

RF-Track also allows the user to select the minimum number of scattered photons generated per each integration step. Given the small value of the Compton scattering cross-section, this feature allows the user to generate arbitrarily large photon statistics, even for a low number of electron macro-particles. This particular feature makes the simulation of ICS in RF-Track orders of magnitude faster than similar codes [52].

As a code specialised in simulating beam transport through complex electromagnetic fields, RF-Track has been thoroughly benchmarked against other codes used to simulate particle injectors [52]. New features are continually added, and it is fostering a growing community of linac expert contributors. Since its inception in 2016, the code has been used in the design of proton-therapy linacs, CLIC, and a Very High Electron Energy (VHEE) linacs for FLASH therapy [85].

### 3.1.1 RF-Track CBS module

The CBS module for RF-Track was added as an alternative to popular CBS codes [86]. It seeks to offer a faster and more user-friendly alternative to established codes. RF-Track functions as a library that can be used in Python and Octave programming languages. The addition of the CBS module allows for creating single scripts for generating an electron bunch at a cathode, tracking its acceleration through a linac, followed by the beam squeeze through the final focus, the CBS interaction with the laser beam, and the tracking of the scattered X-ray beam up to the location of the detector, as well as its collimation.

#### 3.1.1.1 Implementation

The physics of the CBS interaction region is contained in the specialised lattice element "`LaserBeam`". It allows the user to define the key laser parameters: wavelength, pulse energy, pulse duration, incoming direction, $M^2$ parameter, aspect ratio, degree of linear polarisation, and whether the laser beam has a Gaussian or a uniform profile.

`LaserBeam`, as a time-dependent element, can be synchronised to the beam or to an absolute clock. It can also be misaligned in the lattice with offsets in angle and position. This allows for tolerance studies, such as assessing the impact of laser misalignments on flux. The element can have a finite length or can be infinitely thin. In both cases, the whole three-dimensional structure of the bunch is reconstructed during computation.

The scattering is computed in the rest frame of the charged particle as a Monte Carlo process. When the photon's energy is much lower than the particle's rest energy, its absolute momentum and wavelength remain unchanged during the collision. The resulting Thomson scattering is elastic. Compton scattering occurs for higher photon energies, when momentum transfer between the particle and the photon is reached, and the scattering is inelastic. After the CBS interaction the phase-space variables of particle and photon are recomputed and referred back to the laboratory frame. This allows for tracking both particle types further across the beamline.

Calculating the final state of the interacting particles requires knowledge of the total and differential cross-sections. The total cross-section is needed to determine $\lambda$, the particle's mean free path, that is, the distance a particle travels before it collides with a photon. The angular differential cross-section is needed to calculate the energy and deflection angle of the scattered photon and the recoil of the incident particle.

Since these cross-sections assume different expressions depending on whether the incoming photons are polarised, RF-Track effectively implements four scattering processes: Thomson or Compton, polarised or unpolarised input laser.

### 3.1.2 Algorithm

The CBS interaction between the electron and the laser beam is computed in RF-Track through a user-defined number of steps, $N$. Partitioning the interaction volume into slices according to $\Delta L = L/N$ enables the implementation of multiple scattering during collision. $L$ is the total length of the interaction volume.

For each slice and for each charged particle in the beam, RF-Track replicates the following seven steps until the colliding bunches no longer overlap:

1. Calculate the average density and direction of the incoming laser photon beam at the location of the particle.
2. Perform a Lorentz boost of the average photon into the rest frame of the scattered particle.
3. Compute whether the scattering is Thomson- or Compton-like. Based on the class of interaction, compute the total cross-section $\sigma$ and evaluate the particle's mean-free path $\lambda = 1/(\rho\sigma)$, with $\rho$ the volume number density of the photons.
4. Given $\lambda$ and $\Delta L$, compute the probability of scattering. If $\lambda \gg \Delta L$, force a scattering event and produce a weighted photon based on the weight of the charged particle.
5. Using Monte Carlo methods and the appropriate differential cross-section, evaluate the energy and 3D direction $(\theta, \varphi)$ of the scattered photon.
6. Given the direction and energy of the scattered photon, compute the kinematics of the scattering, update the particle's phase-space variables, and perform a Lorentz boost into the lab frame.
7. Add the scattered photon to the data structure of the beam and pass the electron and photon through to the next slice.

The computations are performed in parallel for all macroparticles of the incoming beam.

## 3.2 RF-Track benchmark against other codes

An RF-Track benchmark was performed against data from the literature and CAIN. The flux and brilliance of four ICS sources were determined in RF-Track,

and compared with values referenced in articles: CXLS [87], CBETA [66], ThomX [45], and ODU CLS [66]. This allowed for the study of the RF-Track output for several ICS designs. ODU CLS is a superconducting linac design, reaching the highest flux and brilliance known for any ICS source. CXLS is a linac-based source under commissioning at Arizona State University. ThomX is a storage ring source operating in Orsay. CBETA is an ERL design from Cornell with a focus on high-energy X-rays. Regarding the simulation codes used to derive properties of the output photon beam, ThomX used CAIN, ODU CLS used a programme developed by Erik Johnson [66], CXLS used COMPTON, and CBETA used both ICARUS [88] and ICCS3D [89]. Equations (1.24), (1.28) and (1.29) were used to compute the flux and average brilliance of the X-ray photon beam obtained from the simulation. Since RF-Track uses a Monte Carlo approach, the standard deviation of the results was computed from several runs of the code. Two configurations were considered for the ODU CLS, corresponding to laser spot sizes of $\sigma_{\text{laser}} = 3.2\,\mu\text{m}$ and $12\,\mu\text{m}$. The smaller spot size results in a significantly reduced Rayleigh length, and was used to assess the capability of RF-Track to accurately model the hourglass effect in the interaction region.

The comparison between the referenced and simulated results is shown in Fig. 3.1. RF-Track was found to accurately predict the flux and brilliance of ICS sources, including for set-ups with low $z_R$, such as the $\sigma_{\text{laser}} = 3.2\,\mu\text{m}$ configuration of ODU CLS.

Further benchmarks focused on comparing the performance of RF-Track against CAIN, since it represents the current standard for CBS simulations. In order to achieve this, sources with detailed technical reports were adapted, namely ThomX [90], which provided its own Technical Design Report, along with BriXSinO [91], and sources with publications detailing their simulations, e.g., the compact ERL (cERL) [50]. The input collision parameters used for the ThomX simulation are shown in Table 3.1.

Figure 3.2 displays a comparison of the plots obtained in RF-Track and in CAIN for the ThomX source [90]. Both codes derived the expected Compton edge of 45 keV. The size of the X-ray beam obtained in RF-Track, $\sigma_x/\sigma_y \sim 18/40\,\mu\text{m}$, and the divergence of the beam, ~4 mrad, also correspond to the CAIN results. The majority of the photons were concentrated in an opening angle of 2 mrad, as

Table 3.1: Input Collision Parameters Used for the ThomX Simulations

| **Parameter** | **Unit** | **Value** |
|---|---|---|
| Crossing angle | degrees | 2 |
| Electrons energy | MeV | 50 |
| Electrons energy spread | ‰ | 3 |
| Number of electrons | # | $6.25 \times 10^9$ |
| Laser pulse energy | mJ | 28 |
| Repetition rate | MHz | 17.84 |
| Laser pulse transverse dimension (RMS) | µm | 35 |
| Electron bunch transverse dimension (RMS) | µm | 70 |
| Laser pulse duration (RMS) | ps | 5 |
| Electron bunch length (RMS) | ps | 4 |

Table 3.2: Input Collision Parameters Used for the BriXSinO Simulations

| **Parameter** | **Unit** | **Value** |
|---|---|---|
| Electron beam energy | MeV | 22 - 45 |
| Bunch charge | pC | 50 - 200 |
| Repetition rate | GHz | 0.9286 |
| Energy spread (RMS) | ‰ | 5 - 15 |
| Electron Bunch length (RMS) | mm | 2.2 |
| Electron focal spot size (RMS) | µm | 30 - 60 |
| Laser pulse energy | mJ | 2.7 |
| Laser wavelength | nm | 1030 |
| Laser polarisation | | linear |
| Laser pulse length (RMS) | ps | 1.5 |
| Laser focal spot size x/y (RMS) | µm | 90/80 |
| Collision angle | degrees | 7 |

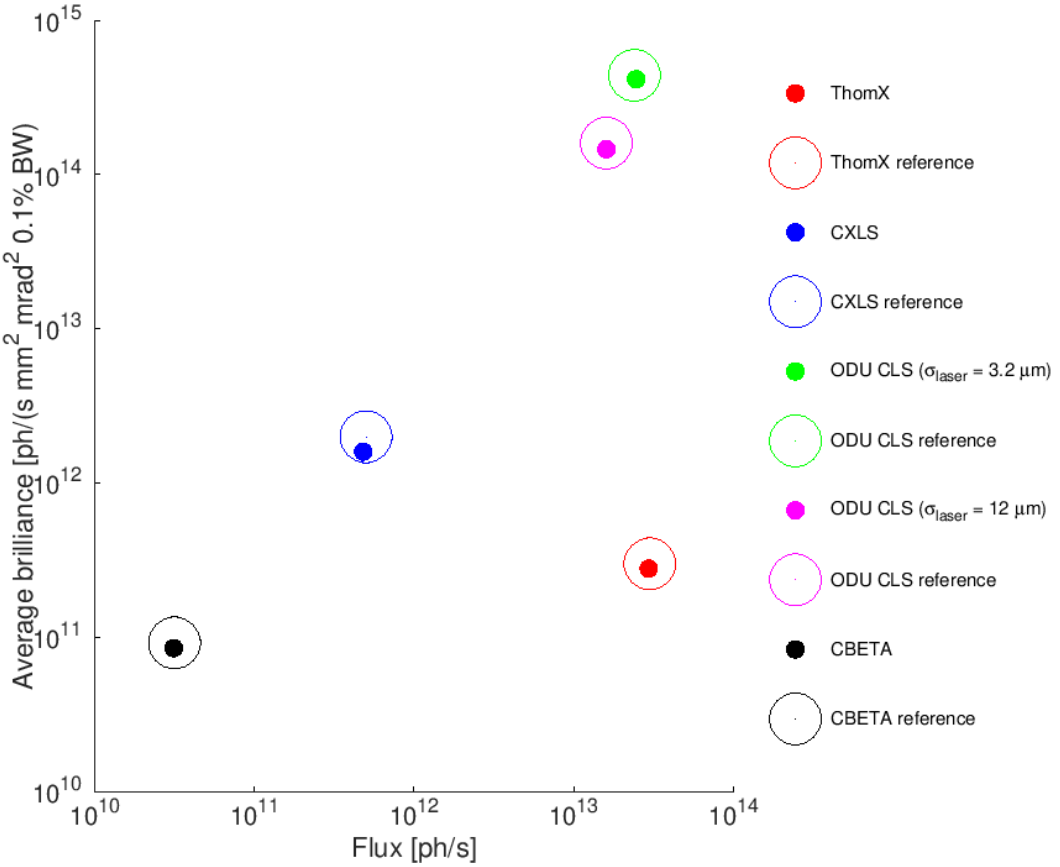



Figure 3.1: Comparison of total flux and average brilliance results from RF-Track with their corresponding referenced values. The errors obtained in RF-Track for both average brilliance and total flux are too small to be noticeable.

shown in Fig. 3.2d. The four plots in each subfigure represent figures of merit typically used to characterise a CBS source. First, the top-left plot shows the energy spectrum of the scattered photons for three different collection angles. Experimentally, the collection angle can be imposed through collimation, exploiting the CBS property of the photons being scattered at an angle dependent on their energy. From Eq. 1.25, a reduction in the collection angle is equivalent to a reduction in bandwidth. Concurrently, with collimation, the number of scattered photons is also reduced. Typically, an equilibrium must be achieved for the conditions of the highest flux for the lowest acceptable bandwidth. CBS energy spectra can be experimentally obtained through X-ray spectrometers, although the large bandwidth and ultra-short pulse length require the use of techniques such as attenuation to

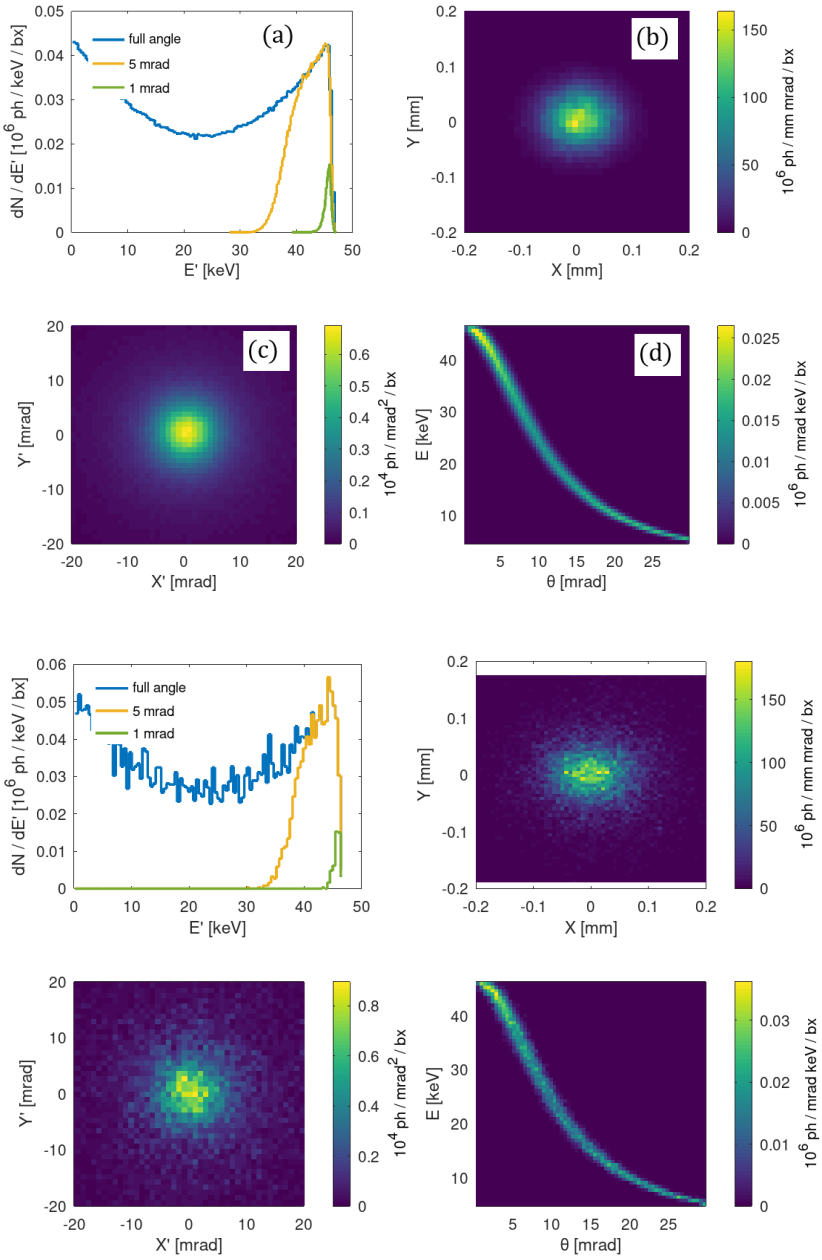



Figure 3.2: Comparison of plots from ThomX simulation using RF-Track (top) and CAIN (bottom). (a) The photon energy spectrum in a 1 mrad and 5 mrad collection angle, along with the full angle spectrum. (b) The transverse source size. (c) The angular emission distribution. (d) The number of photons/mrad$^2$/s against energy and collection angle.

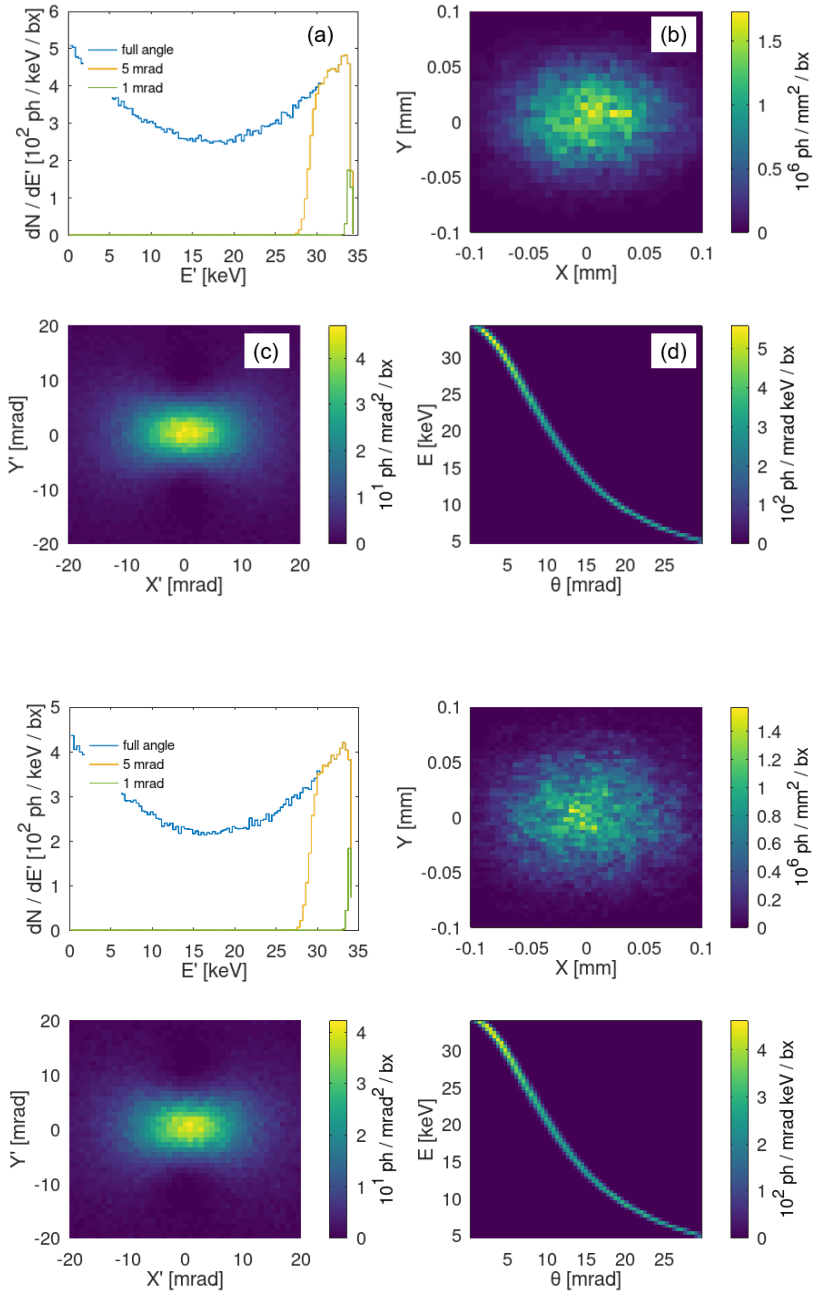



Figure 3.3: Comparison of plots from BriXSinO simulations using RF-Track (top) and CAIN (bottom), similarly to Fig. 3.2. An added contribution, showcased in RF-Track, is the CBS interaction with a linearly polarised laser.

single-photon events [92] or simulation-aided particle reconstructions in the detector [93]. In the upper right plot, the spatial beam profile is represented, showing the transverse span and distribution of the X-ray beam. The CBS beam size is computed through a convolution of the electron and laser spot sizes. As typically Gaussian electron beams interact with Gaussian laser pulses at the IP, the X-ray profile will also resemble a Gaussian distribution. X-ray image profilers are widely available for measuring the transverse profile, i.e. microchannel plates (MCPs) with phosphorous screens or multianodes. The bottom-left plot represents the transverse beam divergence, which determines the angular spread of the scattered photon beam. This profile cannot be measured directly. Lastly, on the bottom-right, the X-ray energy is plotted against the collection angle. The energy-angle distribution reveals the strong dependence of the X-ray energy on the collection angle (as indicated in Eq. 1.25) and can be used to determine the angular cut-off for the CBS collimation system. Note that the spread of this distribution is inversely proportional to the electron beam energy at the IP. The energy-angle plot can be reproduced using the combination of a collimation system and an X-ray spectrometer [94].

A similar benchmark was set for a proposed ERL-based CBS source, BriXSinO [51]. The input collision parameters used for the BriXSinO simulation are shown in Table 3.2. This source, as seen in the angular profile plots from Fig. 3.3, introduces the interaction with a linearly polarised laser. This leads to a beam distribution that exhibits an outer crown of X-ray photons. Note that only the outer rim of the beam profile is changed by the linear polarisation of the laser, and the properties of the beam core remain unchanged with respect to the unpolarised laser.

Table 3.3: Parameters Used to Compare the Performance of RF-Track Against CAIN Using the ThomX Input Parameters.

| **Parameter** | **CAIN** | **RF-Track** | **Analytic** |
|---|---|---|---|
| Electron macro-particles | $5 \times 10^7$ | $10^4$ | N/A |
| X-ray macro-particles | 12,700 | 1,350,311 | N/A |
| Runtime [s] | 2545 | 0.67 | N/A |
| Total flux [$10^{13}$ ph/s] | $2.65 \pm 0.02$ | $2.50 \pm 0.01$ | 2.54 |

The benchmark of RF-Track against CAIN also allowed for a comparison of the code's performance, summarised in Table 3.3. RF-Track computed the results from Figure 3.2 several orders of magnitude faster than CAIN. The difference in speed was due to RF-Track's ability to set the minimum number of scattered photon macro-particles per integration step, which effectively enhances the scattering cross-section. CAIN required $5 \times 10^3$ times more macro-electrons to generate photon macro-particles with sufficient statistics. The theoretical flux is noticeably closer to the value from RF-Track, rather than CAIN. The difference might be due to the fact that CAIN is handling more detailed models of beam polarisation than RF-Track, which only considers the linear polarisation of the photon beam. CAIN also implements models of photon-photon interactions. These effects would become relevant for higher laser-photon energies.

Another benchmark was the reproduction of cERL photon spectra, computed with CAIN [50]. The results, displayed in Fig. 3.4, indicate that RF-Track is able to reproduce characteristics such as the amplitude and bandwidth of the photon spectra at various collection angles, ranging from 1 mrad to the full angle spectrum. As expected from Eq. 1.25, as the collection angle decreases, the bandwidth decreases, along with the peak and area of the photon spectrum, corresponding to a decrease in flux through collimation. The plots also show the effect of the emittance term in Eq. 1.25. One can see from the top and bottom plots that reducing the collection angle does not necessarily guarantee a quasi-monochromatic spread of the scattered X-ray beam. Therefore, a minimisation of the electron beam emittance at the IP is essential in order to obtain a good CBS beam quality.

## 3.3 RF-Track Model of ARTI

Following the successful benchmark of the CBS module, an ARTI gun set-up model was built in RF-Track. As previously discussed, the code's ability to generate, track, and simulate CBS (all in one run) is greatly beneficial, as it allows for a direct optimisation of the whole beamline, with a merit function dependent on the actual flux. The RF-Track model was tested against beamline measurements, and the optimisation of the beamline offered guidelines for maximising the generated flux.

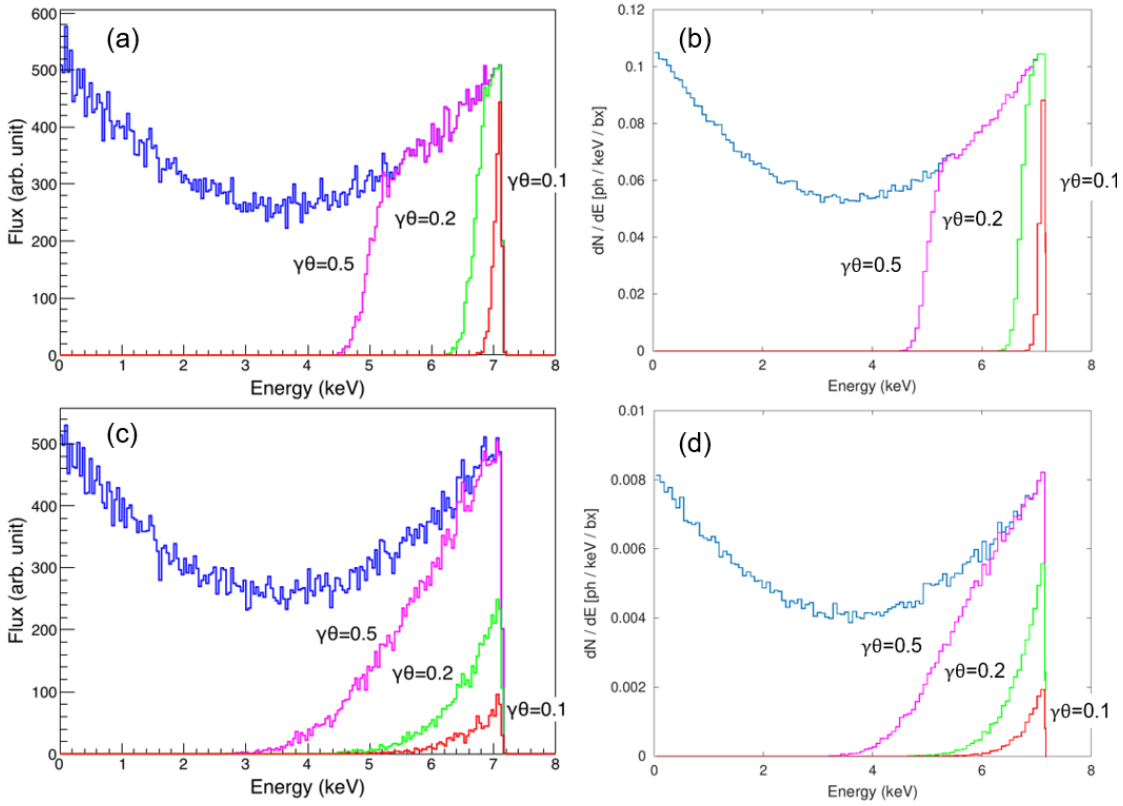



Figure 3.4: Comparison of cERL photon spectra computed in CAIN and RF-Track for different values of emittance. CAIN photon spectra at (a) $\epsilon^N = 1\,\text{mm mrad}$ and (c) $\epsilon^N = 5\,\text{mm mrad}$. RF-Track photon spectra at (b) $\epsilon^N = 1\,\text{mm mrad}$ and (d) $\epsilon^N = 5\,\text{mm mrad}$. Figures for three distinct collection angles are shown, along with the full energy spectrum. The data used for the plots corresponding to the CAIN simulation were taken from [50].

Additionally, efforts to align the lattice elements of the beamline were realised, which sought to minimise the beam emittance at the IP.

The RF-Track model developed for the CTF2 gun consisted of the implementation of its E-field, the B-field of the solenoid, and the location of the YAG screen (0.57 m). The EM fields are shown in Fig. 2.4. Following the implementation of the relevant beamline elements, several tuning parameters were established, summarised in Table 3.4.

At the cathode, the laser profile was chosen according to the one observed on the virtual cathode. A Gaussian pulse was chosen as the best approximation

Table 3.4: Summary of the RF-Track Gun Model Tuning Parameters

| **Cathode** | **Gun** | **Solenoid** |
|---|---|---|
| Bunch charge | RF phase | Field strength |
| Laser spot size | RF gradient | Field polarity |
| Laser pulse length | | |

of the observed profile. Other options provided by RF-Track include uniform, plateau, parabolic, and truncated Gaussian distributions, respectively. Similarly to ASTRA, there are no photocathode physics models implemented in the particle creation. The only cathode-dependent parameter used in RF-Track is the work function, as it determines, in combination with the laser photon energy, the thermal emittance, i.e., the minimum possible emittance obtainable from the cathode. In addition, the mirror charge contribution from the cathode on the space charge is implemented. One interesting feature is that, assuming a one-to-one profile matching of the laser on the cathode with the generated electron bunch, one can also adapt the virtual cathode image of the laser transverse profile directly as an input for the RF-Track bunch generator. The numerical input parameters to the cathode simulation include the bunch charge (controlled by the laser intensity on the cathode), along with the RMS laser spot size and pulse duration. The cathode parameters effectively define the electron bunch profile right at the cathode. The bunch is then accelerated by the electron gun, subject to the tuning parameters of gradient and phase. The gradient, measured in MV/m, depends on the power fed to the accelerating structure. The RF phase can be used to fine-tune the beam energy along with the overall particle distribution. Lastly, the solenoid field polarity and field strength were both considered for optimisation. The field strength was an essential parameter as it determined the beam focusing. The field polarities of plus-plus and plus-negative were studied, and it was seen that the plus-plus option led to the smallest spot size at the IP. Henceforth, the plus-plus configuration was considered both experimentally and in simulations.

## 3.4 ARTI optimisation in RF-Track

The RF-Track optimisation was performed using the Nelder-Mead algorithm, which uses a simplex to perform a direct search for the minimum of an objective function [95]. The overarching objectives included in the algorithm's merit function were:

1. Flux maximisation. Naturally, the main objective of the optimisation was to directly maximise the flux limited by the collection angle of the detector. Given the diameter of the X-ray detector and the distance from the IP and the detector, the collection angle of the X-rays is 21.5 mrad. Note that for previous CBS codes, the objective was typically to minimise the RMS electron spot size and pulse duration at the IP. However, as discussed in Section 3.4.2, this objective is flawed and does not necessarily guarantee maximum flux. By optimising for the flux directly, the electron beam is freely shaped to enable the maximum possible flux.
2. Background minimisation. There are some instances of flux maximisation that can inadvertently lead to a proportional increase in background. This constitutes an issue for detection, as it reduces the signal to noise ratio (indeed, one might note that the ultimate goal of the optimisation was to maximise the signal to noise ratio). This can translate into the reflection of UV laser photons from the cathode and reaching the detector, or the electron beam increasing in size so that it collides with the beam pipe walls (of 38 mm diameter), generating bremsstrahlung radiation. In order to attenuate these two effects, the conversion of the laser pulse to electron bunch at the cathode was maximised (the photoelectric conversion is limited by the saturation of the cathode surface), and the maximum RMS spot size across the tracking lattice was maintained to a value below 10 times the beam pipe radius, i.e., 1.7 mm.

Note that the Nelder-Mead method is not global. To compensate for this, 1000 randomised starting points were multithreaded for the optimisation, which enabled the exploration of a vast parameter space.

### 3.4.1 Optimised beam parameters

The optimised input parameters are shown in Table 3.5, together with the relevant electron beam parameters at the IP. The electron beam RMS spot, bunch length, transverse and 4D emittance are tracked in Fig. 3.5. The laser RMS spot size on the cathode and RF phase were reduced by simplex to minimise the emittance. In particular, the 200 pC case converged to a less off-crest RF phase, reflecting the trade-off between longitudinal compression and beam quality. The RF gradient was set to its maximum value in order to minimise the angular spread of the CBS photons. Lastly, the solenoid field was tuned to obtain a small electron beam waist size at the IP.

Table 3.5: Optimised Parameters of the Electron Beam from the Copper Cathode

| **Parameter** | **100 pC** | **200 pC** | **300 pC** | **400 pC** |
|---|---|---|---|---|
| RF phase [deg] | –19.5 | –11.5 | –21.0 | –26 |
| RF gradient [MV/m] | 120 | 120 | 120 | 120 |
| Solenoid field [T] | 0.350 | 0.355 | 0.350 | 0.336 |
| Laser RMS spot [µm] | 438 | 482 | 502 | 567 |
| Beam energy [MeV] | 5.77 | 5.84 | 5.77 | 5.75 |
| Emittance [mm mrad] | 1.88 | 2.77 | 4.00 | 6.14 |
| Max $e^-$ RMS spot [mm] | 1.27 | 1.68 | 1.78 | 1.80 |
| Min $e^-$ RMS spot [µm] | 42 | 46 | 61 | 94 |
| RMS bunch length [ps] | 0.4 | 0.6 | 0.8 | 1.1 |
| Total flux [$10^5$ ph/s] | 1.4 | 3.5 | 3.7 | 2.9 |

The laser spot was optimised to increase linearly with the bunch charge, which mitigated space charge effects by maintaining the bunch volume above the onset of strong space charge. The optimal RF phase ranges from −10° to −30° with respect to the on-crest phase. The emittance, RMS spot, and length of the electron bunch at the IP are proportional to the bunch charge. Note that the maximum photon flux is not obtained at the maximum bunch charge of 400 pC, but at 300 pC. This indicates that there is a space charge-induced limit on the achievable flux with respect to the bunch charge. Photons with a Compton edge of 630 eV are obtained. To reach the water window, the gun gradient can be slightly decreased; for optimisation, the maximum gun gradient was fixed to 120 MV/m.

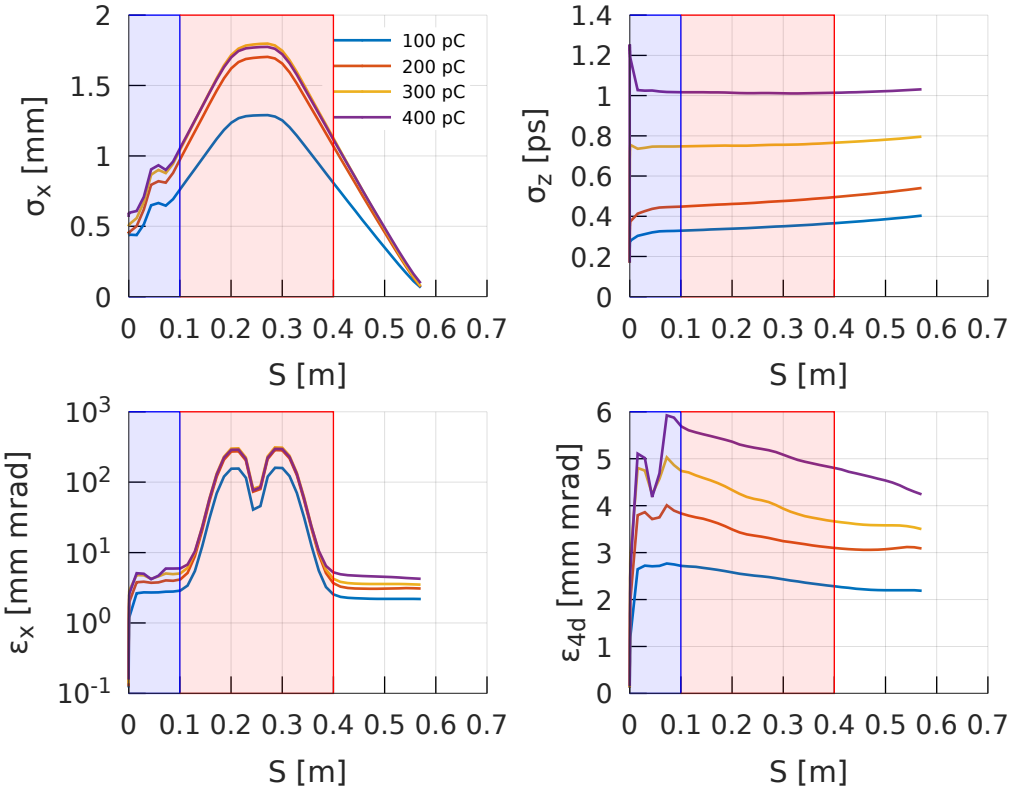



Figure 3.5: Tracking of the electron beam RMS spot size, bunch length, transverse emittance, and 4D normalised emittance along the ARTI beamline for beam configurations optimised for the Compton backscattering experiment. The optimisation was performed independently for four distinct bunch charges. The blue and red shaded regions indicate the longitudinal locations of the electron gun and solenoid magnet, respectively.

The transverse normalised emittance shown in Fig. 3.5 exhibits a sharp increase within the solenoid region before decreasing and stabilising downstream. This behaviour is attributed primarily to strong space-charge forces at low beam energy, which generate nonlinear distortions and beam halo during the initial stages of acceleration. Additional contributions arise from transverse coupling introduced by the solenoid, which can temporarily increase the projected emittance. The fact that the final emittances reported in Table 3.5 remain at only a few mm mrad suggests that the large intermediate values are dominated by halo particles rather than representing the emittance of the beam core, indicating that the optimisation

successfully preserves the quality of the central beam despite significant phase-space distortion during transport.

In the early stages of the experiment, an exchange of the Cu cathode with a CsTe one was considered because it allowed for multibunch operation. To compare the two set-ups, the optimisation was also performed for the CsTe configuration, where the input laser is replaced by a OneFive laser system with a pulse energy of 15 µJ. One notable difference between the CsTe and Cu cathode configurations is the electron bunch length, which is increased to 3 ps RMS for CsTe due to the longer pulse length of the OneFive laser system. Due to the 100 times smaller laser pulse energy, and given similar electron bunch charges generated, the number of photons scattered per bunch at the IP is reduced to a few hundred. However, the OneFive laser and CsTe cathode allow for multi-bunch electron operation. For a nominal value of 80 bunches per train, the photon flux corresponds to the values obtained in the copper configuration. The two configurations are therefore equivalent in terms of CBS performance.

The multibunch operation also allows for the implementation of a Fabry-Pérot optical enhancement cavity at the interaction point [96]. Assuming 80 electron bunch trains, limiting the cavity finesse to 1000, and using 20000 laser pulse bursts, a maximum circulating laser energy available for the ICS interaction, or effective energy, of 0.5 J could be obtained, using the optimisation described in [97]. The cavity finesse was limited in order to ease the requirements for laser matching and mirror tuning. By comparison, the configuration without an FPC, where each electron bunch interacts with only one laser pulse, had an effective energy of $7.5 \times 10^{-4}$ J. The addition of an FPC leads to an increase in the total photon flux to the order of $10^8$ photons per second, which corresponds to typical requirements for water window imaging [72].

Concerns related to the feasibility of the implementation led to the use of the original copper cathode configuration for the experiment. In particular, the requirement to install a load-lock system for cathode swapping, to reconfigure the entire laser beamline to suit the OneFive laser, along with increased requirements on vacuum, which would have required the installation of an additional gate valve between the dipole and detection chamber. Vacuum baking would have also been

required to bring the ARTI beamline from its current pressure of $4 \times 10^{-7}$ mbar to the ultra-high vacuum of $1 \times 10^{-12}$ mbar needed for the CsTe cathode.

### 3.4.2 *q*-Gaussian beam shaping at the interaction point

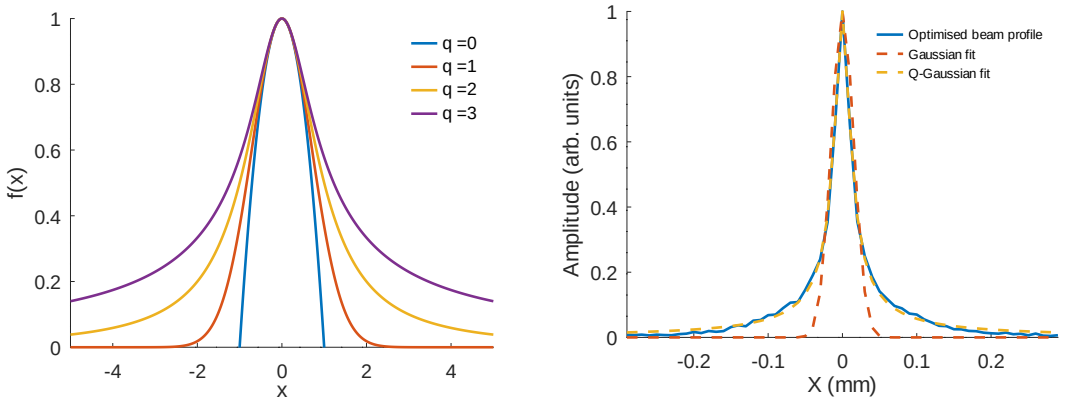
One notable outcome of the electron beam optimisation was the formation of a non-Gaussian transverse beam profile at the IP. As shown in Fig. 3.6b, the maximum scattered photon flux was obtained for an electron distribution with pronounced transverse tails rather than a conventional Gaussian profile. The optimised distribution is well described by a $q$-Gaussian function [98], which generalises the normal distribution through the introduction of an additional shape parameter, $q$. This parameter controls the tails of the distribution, a large $q$ being equivalent to a heavy-tailed distribution, while a smaller $q$ being equivalent to a tail cut-off. For $q \to 1$, the Gaussian distribution is recovered. The $q$-Gaussian distribution can be expressed as

$$f(x) = \left[1 - (1-q)\beta x^2\right]^{1/(1-q)}, \tag{3.1}$$

where $\beta$ is a parameter that describes the variance of the distribution [99]. A sampler of $q$-Gaussian distributions is shown in Fig. 3.6a.

RF-Track simulations show that the $q$-Gaussian profile at ARTI is mainly caused by space-charge forces. This was confirmed by turning off space charge effects in the simulation, which led to the reshaping of the beam profile at the IP to a smooth Gaussian distribution. The space charge therefore generates a beam halo that envelops the Gaussian core. The space charge-induced beam halo was also observed experimentally at the IP, as detailed in Section 3.8.1. The photon flux was maximised in RF-Track by increasing the electron beam core density through beam shaping under space charge forces.

The transverse profile of the optimised bunch exhibits pronounced long tails, as shown in Fig. 3.6b, which are characteristic of a significant beam halo component. To distinguish between the halo and the core, the tails of the distribution were fitted with a Gaussian function, while the central peak was fitted with a separate Gaussian. The superposition of the two fits enabled a clear separation of the core and halo contributions. A comparison of the integrated areas of the two Gaussian




(a) (b)

Figure 3.6: Sampler of $q$-Gaussian distributions (a), and a Gaussian and $q$-Gaussian fit of the optimised electron beam distribution at the IP (b). Note that for $q \to 1$, the distribution is equivalent to a Gaussian. $q > 1$ define heavy-tailed distributions, while $q < 1$ generate tail cut-offs. The $q$-Gaussian fit parameters from Eq. 3.1 in (b) are $q = 2.6$ and $\beta = 6117$.

components revealed that the halo accounts for approximately 20% of the total transverse charge distribution.

The extended tails of the halo increase the effective RMS spot size of the bunch. According to the standard flux expression given in Eq. 1.24, which assumes purely Gaussian beam distributions, such an increase in spot size would imply a reduction in the predicted photon flux. However, the core of the bunch remains highly concentrated at the interaction point, resulting in a region of significantly enhanced particle density. This observation suggests that, for the optimisation of a CBS source, maximising the flux cannot be reduced to minimising the overall RMS electron spot size. Instead, the electron beam distribution that yields the highest local interaction density should be sought.

In practice, optimisation of the Gaussian-based flux formula for the ARTI beamline resulted in a predicted scattered photon flux that was approximately a factor of two lower than that obtained through direct flux maximisation in simulation. Under these conditions, it is therefore preferable to employ particle-tracking codes such as RF-Track to maximise the photon yield directly, rather than optimising the parameters of the analytical flux expression independently.

To assess the impact of a realistic bunch on the CBS output, the flux formula [36] was modified to correspond to a head-on collision of a $q$-Gaussian beam with a Gaussian one,

$$N_\gamma = \frac{\sigma_T N_e N_l \sigma^{-4k-1}}{2\pi^2 \beta \sqrt{k} \Gamma\left(k-\frac{1}{2}\right)^2} \times \left[ k^{k-1/2} \beta^{2k-1} \Gamma\left(\frac{1}{2}-k\right) \Gamma(k)\, {}_1F_1\left(k; k+\frac{1}{2}; \frac{k\beta^2}{\sigma^2}\right) + \sqrt{\pi}\sigma^{2k-1} \Gamma\left(k-\frac{1}{2}\right) {}_1F_1\left(\frac{1}{2}; \frac{3}{2}-k; \frac{k\beta^2}{\sigma^2}\right)\right]^2, \tag{3.2}$$

where $k = 1/(q-1)$, ${}_1F_1$ is the confluent hypergeometric function, $\Gamma$ is the gamma function, $\sigma$ is the RMS transverse size of the Gaussian beam, and $\beta$ and $q$ are the fit parameters of the $q$-Gaussian distribution. The equation was obtained by retracing the derivation of the standard luminosity formula, Eq. 1.24, but replacing one of the input Gaussian beams with a $q$-Gaussian one. The formula corresponds to $1 < q < 3$, for which the heavy tails observed in simulations and experiment are obtained. Note that for head-on collisions, there is no contribution from the longitudinal distribution. By comparing the result of the modified flux formula with simulations, a difference of less than 9% was observed between the two methods, significantly smaller than for the standard formula.

From the RF-Track-based optimisation, it should be noted that even for a perfect alignment of the lattice elements, the total flux is far from the typical value expected for CBS sources, which is higher than $10^8$ ph/s. Using the location of the CBS photon detector with respect to the IP, it was determined that an average number of photons of 170 per bunch would reach the detector, while around 1000 photons would be generated at the IP. This is due to the inverse proportionality of the CBS photon emission angle against the electron beam energy. A low-energy beamline, such as ARTI, would therefore scatter CBS flux at a large angle, and most of the particles would hit and be absorbed by the beam pipe walls instead of reaching the X-ray detector.

## 3.5 Quantum efficiency study of the photoinjector cathode

A relevant experimental campaign that aided the optimisation of the ARTI beamline for the CBS experiment was the derivation of the quantum efficiency (QE) of ARTI's Cu photocathode. The study of the quantum efficiency was relevant to the CBS experiment as it allowed for defining the values for the laser spot size on the cathode outside the saturation limit. Beyond that limit, a nonlinear dependence between the input pulse energy and the output bunch charge arises. Since this effect is not reproduced in the RF-Track simulations, the onset of this effect impedes the ability to provide accurate predictions for the output CBS photon flux.

The quantum efficiency is calculated from

$$QE = \frac{N_e}{N_{ph}}, \tag{3.3}$$

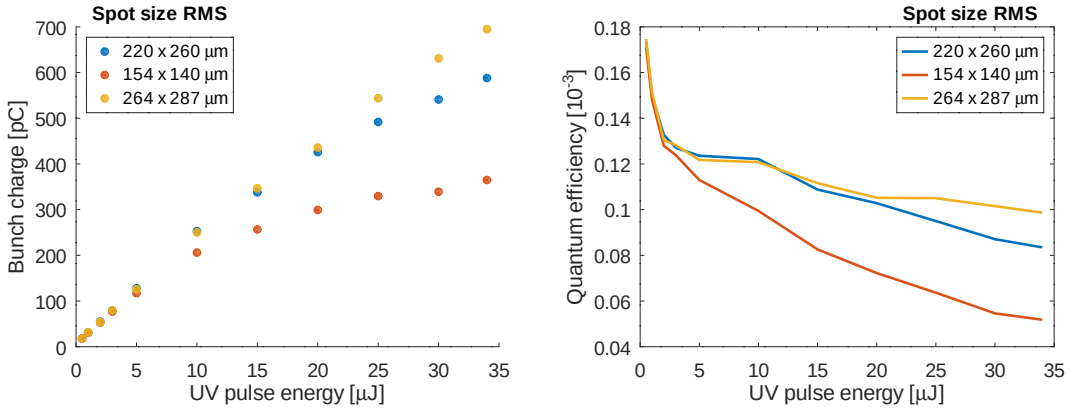
where $N_e$ is the number of electrons generated from the photoelectric effect on the photocathode, and $N_{ph}$ is the number of photons in the incident laser pulse [100]. The laser fluence, $F$, a relevant figure of merit for this study, is defined as

$$F = \frac{E}{\pi w^2/2}, \tag{3.4}$$

where $E$ is the laser pulse energy and $w$ the $1/e^2$ laser radius.

As part of the QE study, the impact of the input UV pulse energy on the bunch charge was measured for different values of the laser spot size on the cathode. The main results are shown in Fig. 3.7. Note that for the bunch charge scan in Fig. 3.7a, a maximum charge of 700 pC was achieved. The saturation effect was shown to emerge at 100 pC. Beyond this point, a linear dependence between the UV pulse energy and the bunch charge occurred only for the larger spot size of 264 by 287 µm$^2$ RMS. The other two spot-size configurations reached a plateau in the extracted bunch charge, indicating the onset of saturation.

The plots from Fig. 3.7a were used to determine the smallest laser spot size within the saturation limit, 264 by 287 µm$^2$ RMS in horizontal and vertical, respectively. The telescope focus setting corresponding to this spot size was used




(a) (b)

Figure 3.7: Characterisation of the quantum efficiency of the copper photocathode installed at ARTI for three UV laser spot sizes. (a) Measured bunch charge as a function of incident UV pulse energy, showing the onset of charge saturation at higher laser energies. (b) Corresponding quantum efficiency as a function of UV pulse energy for each laser spot size.

throughout the CBS experiment. A high QE also prevents a larger amount of background radiation from reaching the detector, since the UV photons reflected by the cathode are sensitive to the X-ray detector used for the CBS experiment.

From Fig. 3.7b, one can see that the dependence of the quantum efficiency on the UV pulse energy is not constant. For larger laser spot sizes, QE decreases from a peak at small UV pulse energies, reaching a plateau at $1.1 \times 10^{-4}$, while in the saturated regime, QE continues to linearly decrease.

Lastly, to identify the laser settings that would cause damage to the cathode, the fluence was calculated against QE, as shown in Fig. 3.8. From the linearity of all plots under the three different laser spot size configurations, one can deduce that the ablation threshold for the cathode was not reached, which made the laser safe to use for a large parameter range. This study was performed for a typical laser pulse length of 776 fs RMS. Shorter pulse lengths were available to use with PHAROS, with a more restrictive parameter able to leave the cathode undamaged; however, they were not used for the CBS experiment.

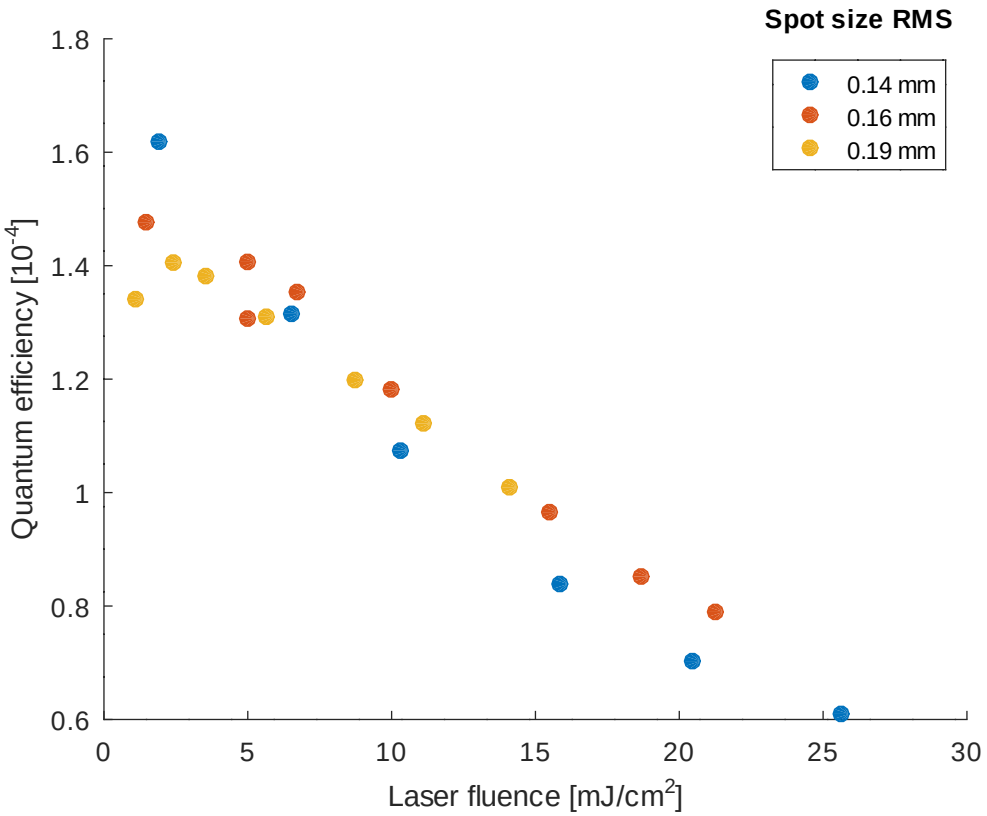



Figure 3.8: Quantum efficiency of the copper photocathode as a function of the incident laser fluence for three different RMS laser spot sizes. The data demonstrate an approximately linear dependence of the quantum efficiency on fluence within the investigated range, with variations arising from the different transverse spot size configurations.

## 3.6 Beam-based alignment of the ARTI beamline

As part of the commissioning and routine operation of an accelerator beamline, precise alignment of the lattice elements is essential. Mechanical misalignments introduce deviations from the ideal machine configuration assumed in simulations and can significantly affect beam dynamics. These imperfections give rise to systematic orbit distortions and beam quality degradation. In particular, transverse misalignments cause the beam to deviate from its reference trajectory, which may result in particle losses and consequently reduced charge transmission along the

beamline. To accurately reproduce such effects in simulations, virtual apertures must be implemented in order to account for charge losses.

In operational machines, orbit distortions are mitigated through the installation of beam position monitors (BPMs) and corrector magnets distributed along the beamline. The resulting beam steering can be categorised into several strategies, including orbit correction, dispersion-free steering, and wakefield-free steering. In addition to orbit distortions, lattice misalignments also lead to beam quality degradation, most notably through emittance growth. This effect is particularly pronounced in the low-energy sections of the accelerator, where the beam is more sensitive to transverse kicks and focusing errors. Consequently, strict alignment tolerances are required, especially in the injector region, to preserve beam quality.

Since misalignments occur during the installation phase of the beamline elements, various metrology techniques (such as laser metrology) have been employed for the initial survey, before obtaining the first beam from the accelerator [101]. Nevertheless, these measurements are only able to limit misalignments to within a millimetre-level range. Further fine-tuning is typically done by placing select beamline elements on movable girders. Since it is not possible to probe all parameters of an accelerator beamline across its entire length, beam-based alignment (BBA) procedures have been widely used in accelerators. Namely, by tracking the electron beam parameters as seen on the ARTI YAG screen against the properties of the beamline elements, i.e., the RF phase and gradient, or the solenoid magnetic strength, and comparing them with simulations (where the impact of various offsets on the electron beam can be studied), the misalignment of the lattice elements can be quantified and corrected.

To ensure a sufficiently high signal-to-noise ratio, a thorough experimental campaign of beam-based alignment was conducted, which corrected the spatial offset of the solenoid and of the UV laser on the cathode. Both of these misalignments contribute greatly to the increase in emittance, as seen in Fig. 3.9. Displacements of the order of 10 mm in critical lattice elements such as the RF gun can lead to an 85% increase in the normalised emittance. Angular offsets were not considered, as the common girder supporting the beamline provided a high degree of mechanical stability, making relative rotations between components negligible.

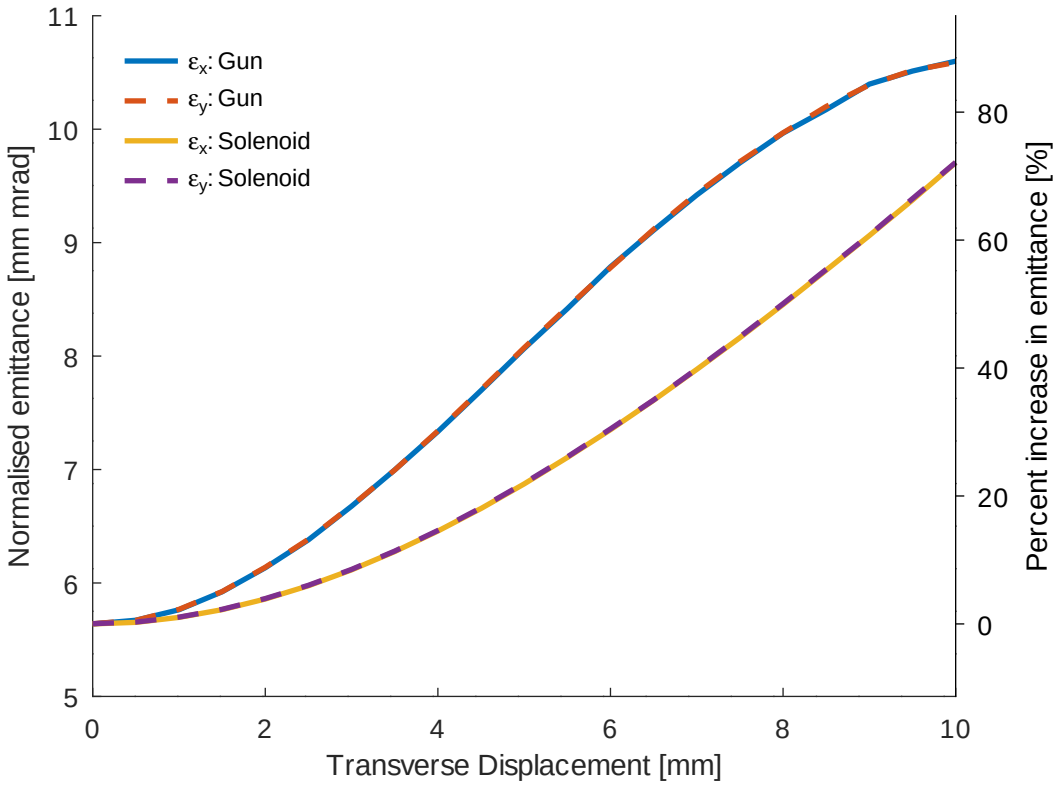



Figure 3.9: Evolution of the transverse normalised emittance as a function of transverse displacement for the gun and solenoid sections. The horizontal and vertical emittances are shown separately. The secondary axis indicates the corresponding relative increase in emittance with respect to the nominal aligned configuration. The results illustrate the sensitivity of beam quality to transverse misalignment in both elements.

### 3.6.1 A novel offset inference method

For the purposes of ARTI, a way to infer the value of the offsets was needed so that the beamline model in RF-Track could be constructed as accurately as possible. The methodology for the inference method was as follows:

1. Measurements of the beam parameters are taken, under different magnet/RF settings.
2. Assembly of a preliminary accelerator model in RF-Track, using already known lattice element parameters (i.e. magnet position/strength, gun RF

gradient, gun/magnet fields, screen location). Unknown values are left as free parameters, i.e., the misalignment values of the lattice elements.

3. The measured parameters are inserted into the beamline model to match the conditions used for the measurements in step 1.
4. Using a numerical optimiser and the misalignment values as free parameters, the simulated model is matched to the measured results.
5. The simulated model is compared to the measured parameters. If needed, the free-parameter bounds are readjusted and fixed input parameters converted into free-parameters. Both measures would lead to an increase in the parameter space.
6. Once a satisfactory match is reached, the misalignments are corrected experimentally. If needed, the process can be repeated until the lattice elements are perfectly aligned.

Prior iterations of studies trying to derive the misalignments also used simulated beamline models, but were restricted to manual tunings of the beamline model's misalignments, requiring an iterative process of alignment upstream from the cathode, in order to remove coupling effects (an uncorrected downstream misalignment affecting the correction of an upstream element) [102]. This novel method assumes fully randomised offsets of the lattice elements and is able to derive each independent value of the misalignments from beam parameter measurements. In the case of ARTI, the alignment only needed to be restricted to the position of the laser on the cathode and the transverse position of the solenoid. The laser position on the cathode affects interaction of the electron bunch with the accelerating E-field generated by the gun, while the solenoid misalignment impacts the orientation of the field affecting the electron bunch. No other principal field components were present up to the interaction point for the CBS experiment. Note that the solenoid alignment was limited to the transverse plane since that was the only range allowed by the piezo-motorised baseplate.

Beam measurements were limited by the diagnostics available. To account for potential calibration errors that would have led to systematic errors, only one of the available screen set-ups was used, the one located at the IP. In the absence of a spectrometer, measurements were limited to tracking the beam position and size against changes in the input parameters. Solenoid strength scans were taken, along

with recordings of the beam profile in the smallest focus setting, as seen in Fig. 3.10 and Fig. 3.11. Scans of the RF phase could have also been performed; however, the exact input value of the RF phase in RF-Track was uncertain, because of occasional phase drifts. Moreover, the solenoid provided a well-calibrated reference field that only impacted the beam position and size, i.e., the actual observables. Tracking the beam position was relevant for the solenoid scans because it is a direct consequence of beamline offsets, which leads to multipole contributions in the beam dynamics. Transverse beam profiles were also taken to try to reproduce the observed beam halo in RF-Track. The experimental RMS spot size values were measured by taking the horizontal and vertical pixel lines passing through the beam peak, and calculating the full width at half maximum (FWHM). The FWHM value was then converted to RMS. To ensure consistency, the same method was applied for the RF-Track simulations, replicating the image set-up under the appropriate pixel size.

The RF-Track beamline model was made using the field maps of the RF gun and the solenoid (shown in Fig. 2.4). The exact locations of the solenoid and diagnostic screen were taken from the technical drawings of the beamline; the screen was located 0.5675 m from the cathode. In terms of inputs, an RMS laser pulse length of 327 fs and an RMS laser spot of 160 µm by 230 µm were measured during the scans. A bunch charge of 53 pC was set in order to minimise space charge effects. From a phase scan, an RF phase of $-20°$ was measured, relative to the maximum energy value. The RF gradient was inferred to be 112 MV/m by fitting the curvature of the measured energy phase scan to simulated phase scans of different gradients. This surpassed issues related to the calibration of the spectrometer. The gradient estimate was reasonable given that the maximum gradient for the gun is 120 MV/m. The gradient inference method is shown in Fig. 3.12. The input parameters required for the simulation are summarised in Table 3.6.

In the initial stage of the inference, the gradient was set as a free variable, bounded from 110 to 115 MV/m. However, since a small change in the gradient led to a significant change in energy, the convergence for matching the simulated solenoid scan to the measured one was significantly hampered. The remaining free variables were the horizontal and vertical position offsets of the solenoid, along with

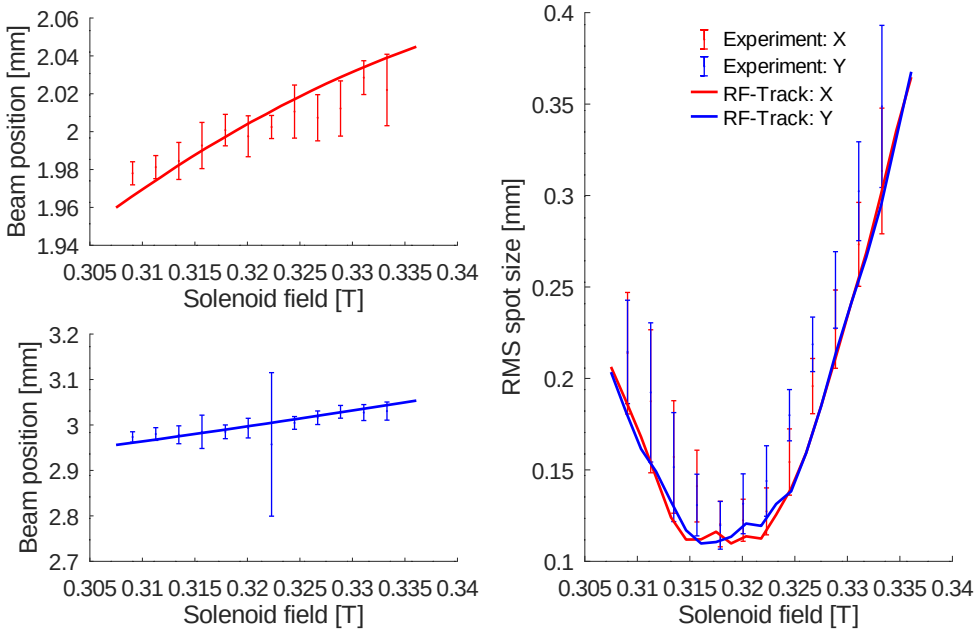



Figure 3.10: Comparison of measured and simulated beam response in a solenoid scan. The beam centroid position in the horizontal and vertical planes (left) and the RMS transverse spot size (right) are shown as functions of the solenoid magnetic field. Experimental data are compared with RF-Track simulations performed using the offset parameters obtained from the simplex-based inference procedure.

the horizontal and vertical position offsets of the laser position on the cathode. A small boundary range was also given for the pitch and yaw angles of the solenoid. Angle offsets were neither measurable nor correctable. The roll angle was not considered because the solenoid field map is symmetric, providing no change in the forces that impact the particle beam.

The Nelder-Mead algorithm was used to match the results of the simulated solenoid scan to the experimental one. Observing the progress of the optimisation also led to insights into the tuning procedure. The laser position was used by the optimiser to tune the electron spot size, since the position offset leads to changes in the electric field experienced by the electron bunch, which changes the beam energy. The solenoid offset also affected the spot size, but at a reduced rate.

It is well known that the Nelder-Mead algorithm tends to converge to local minima. In order to assimilate features of a global optimisation, it was run on

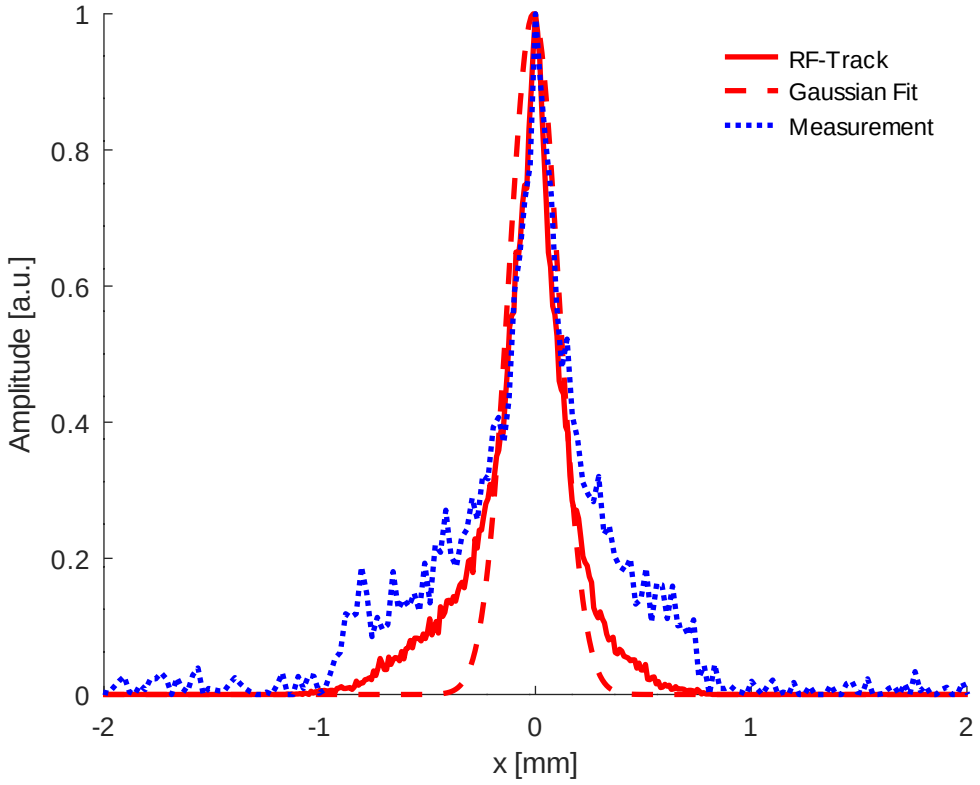



Figure 3.11: Comparison between the measured transverse beam profile and RF-Track simulation. The measured distribution is shown together with the corresponding simulated profile and a Gaussian fit.

a CERN computer cluster with 1000 threads, each with a different randomised starting point. The output file containing the iteration of the free parameters and the value of the merit function was constantly read by the scripts and updated whenever a lower merit value was found. The communication between the parallel-running scripts and the randomised starting points ensured a non-localised optimisation. The merit function was set to match the simulated data with the measured one.

The results of the offset inference method are shown in Fig. 3.10. It can be seen that the simulation was able to match the measured parameters within less than one $\sigma$ experimental uncertainty. The curvature of the solenoid scan was maintained in RF-Track for both the beam size and its position. RMS spot sizes

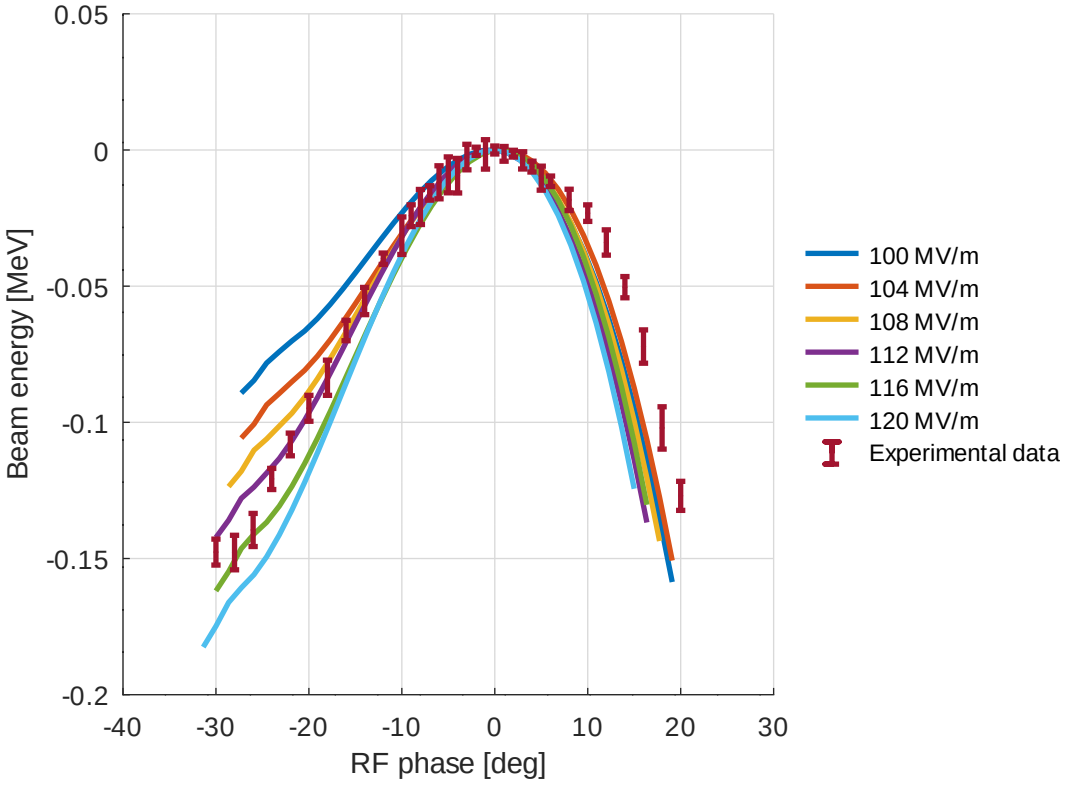



Figure 3.12: Normalised measured phase scan compared with RF-Track simulations performed for different accelerating gradients. The experimental data are overlaid with simulated phase scans corresponding to gradients between 100 and 120 MV/m. The best agreement is obtained for an accelerating gradient of 112 MV/m, indicating this value as the effective operating gradient.

as small as 0.11 mm were obtained from the YAG. The offset inference outputs enabled the simulation of the particle trajectory in the ARTI gun. The highly curved trajectory, along with the one $\sigma$ beam size envelope, is shown in Fig. 3.13.

Similarly, from Fig. 3.11 it can be seen that the simulation was able to accurately predict the transverse beam profile. As evidenced by the Gaussian fit, the simulated beam profile presents a notable beam halo that manifests itself as long tails in the transverse distribution. A slightly larger halo intensity in the measured value was explained by the saturation of the YAG screen, suppressing the peak intensity. Furthermore, note that the asymmetry in the halo distribution was successfully reproduced by the RF-Track simulation. The beam profiles were

Table 3.6: Input and Output parameters obtained from the offset inference method

| Offset | Value | Unit |
|---|---|---|
| Bunch charge | 53 | pC |
| RF gradient | 112 | MV/m |
| RF phase | –20 | ° |
| Laser pulse length (RMS) | 327 | fs |
| Laser spot size x (RMS) | 160 | µm |
| Laser spot size y (RMS) | 230 | µm |
| Solenoid offset x | 2.66 | mm |
| Solenoid offset y | 3.19 | mm |
| Solenoid pitch | 0.625 | mrad |
| Solenoid yaw | 0.770 | mrad |
| Cathode laser offset x | 2.30 | mm |
| Cathode laser offset y | 1.33 | mm |

best fitted to a heavy-tailed $q$-Gaussian, and the halo accounted for approximately 80% of the total bunch population.

Finally, the resulting inferred values, noted in Table 3.7, were corrected. However, it was found that the new beamline configuration did not correspond to the one with the smallest emittance . In hindsight, after the OTR screen was installed, it was found that the YAG screen did not provide a realistic representation of the beam profile. The YAG enlarged the actual spot size at the waist by a factor of two. Assuming linearity with respect to the offsets, this would explain the factor of two difference between the measured and inferred offsets. The difference between YAG and OTR measurements is detailed in Section 3.8.1.1. Due to the initially inconclusive results from the inference method, a purely experimental misalignment correction method was later implemented.

### 3.6.2 Experimental correction of the ARTI beamline offsets

Standardised methods were used to correct the offset of the laser on the cathode and of the solenoid. The alignment was also beam-based, but less reliant on a detailed simulation model than the inference-based method. Iteratively, the

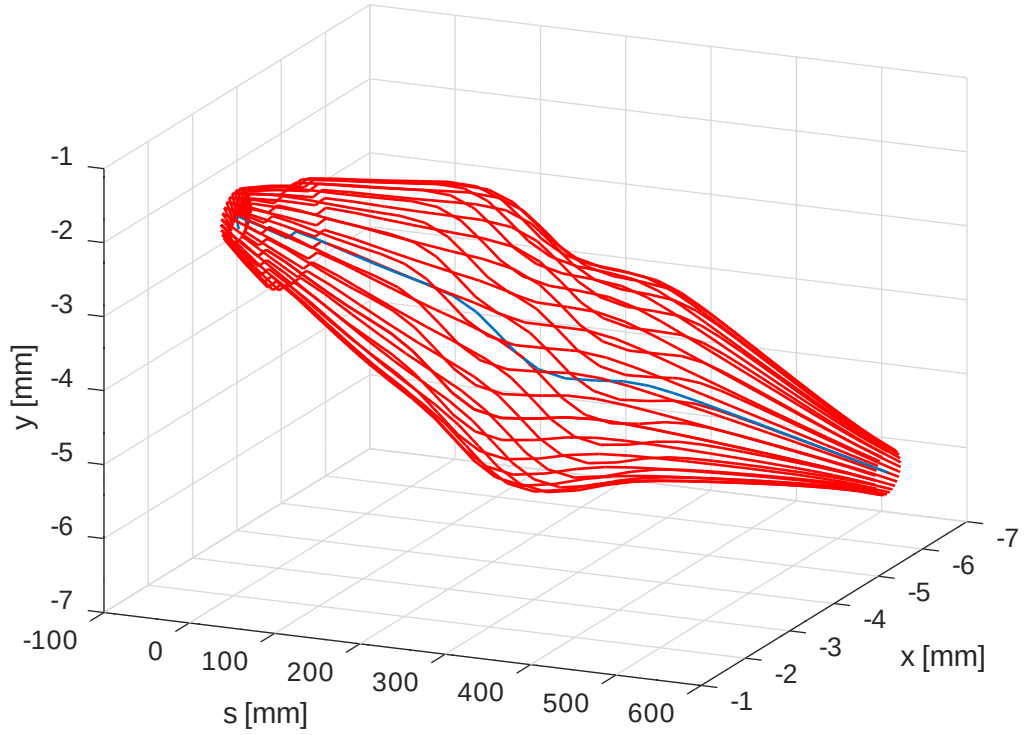



Figure 3.13: RF-Track simulations of the beam trajectory from cathode to the interaction point, provided the derived offsets are implemented. The red lines define the beam envelope at $1\sigma$.

position of the laser on the cathode was first corrected, followed by the one of the solenoid.

#### 3.6.2.1 Alignment of the laser position on the cathode

From Fig. 3.9, the misalignment of the laser position on the cathode has the largest impact on the beam emittance. To ensure excellent beam quality for the CBS experiment, correction of this misalignment was required.

The alignment methodology was based on the technique described in [102]. The additional diagnostics required were the virtual cathode set-up and a remotely controlled movable mirror, which were already installed during the commissioning of the electron gun. This allowed for scanning the laser position on the cathode,

and for tracking its path.

The alignment is done through the use of RF focusing. Solenoids and all other magnets are turned off during the alignment, to prevent any coupling between the electric and magnetic fields. For accurate position measurements, the electron beam must be contained on the YAG screen, located 0.57 m from the cathode. To achieve this, a low RF gradient and bunch charge are required. The low RF gradient reduces the beam energy for RF focusing. Since a lower beam energy requires a smaller magnet focusing strength to reach the waist, a configuration with no magnets would require a very low energy to achieve focusing. Indeed, for the ARTI alignment, a beam energy of 0.7 MeV was reached, measured with the dipole spectrometer. Additionally, the low energy also improves the resolution of the beam-based alignment. A moderately high beam energy is still needed; otherwise, the beam becomes highly sensitive to external fields, which significantly increases the position jitter, complicating the alignment process. A low charge of 10 pC was used to prevent beam expansion due to space-charge forces, and contain the beam on the YAG. This translated into low beam visibility. Unfortunately, multi-bunch operation is not available at ARTI, so 10 shots at 10 Hz were integrated to mitigate this effect. In this set-up, the transverse fields of the RF gun cavity perform the RF focusing. An example beam profile is shown in Fig. 3.14. Due to the large RMS spot size of 0.5 mm, and the reduced space-charge force, the transverse profile is highly Gaussian-like.

Once the electron beam is RF focused on the YAG screen, the current laser position on the cathode is recorded using the virtual cathode set-up. Following this, the RF phase is scanned from 160° to 178° (absolute value of the RF phase). Under the influence of the multipolar fields of the RF gun, the electron beam position on the YAG drifts linearly. The initial trajectory is fitted to $a_1x + b_1y = c_1$. Afterwards, the laser position on the cathode is displaced horizontally or vertically by a few millimetres. The relative laser displacement is denoted by $\vec{\Delta} = (\Delta_x, \Delta_y)$. The RF phase scan is then repeated and a new linear fit of $a_2x + b_2y = c_2$ is made. If feasible, a displacement of the laser spot that allows for a beam drift orthogonal to the first one is recommended. This allows for the best resolution for finding the field axis. The point where the two fits cross corresponds to the gun axis. From

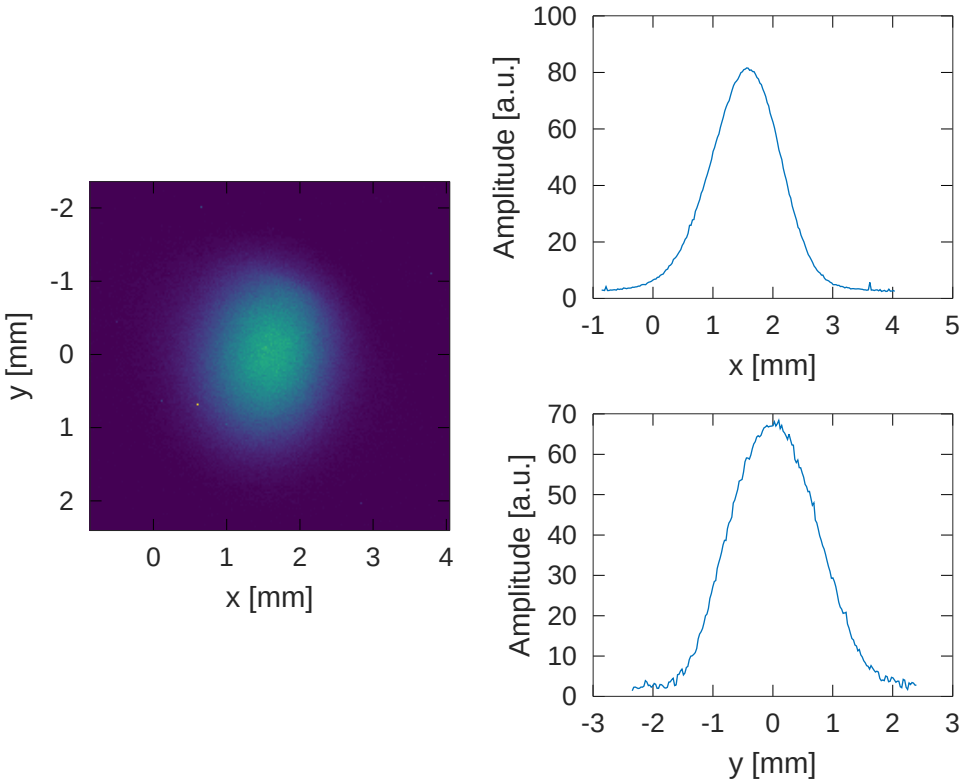



Figure 3.14: Transverse electron beam profile under RF focusing at ARTI. This configuration was employed to align the laser on the photocathode with respect to the gun axis. The two-dimensional intensity distribution is shown together with the corresponding horizontal and vertical projections. The beam was recorded on a YAG screen positioned 0.57 m downstream of the photocathode.

the fit coefficients, one can determine the relative displacement, $\vec{V}$, for the centring of the current laser position on the cathode using

$$\vec{V} = \begin{pmatrix} V_x \\ V_y \end{pmatrix} = \frac{a_1\Delta_x + b_1\Delta_y}{a_1 b_2 - a_2 b_1} \begin{pmatrix} -b_2 \\ a_2 \end{pmatrix}. \tag{3.5}$$

By applying the calculated laser shift, the UV laser can be centred on the gun axis. As the centring process continues, the beam drift during a phase scan is minimised. However, a remnant beam offset was observed even after the alignment process was completed. This can be explained by non-homogeneous cavity fields in the RF gun occurring for on-crest phases, and by the influence of the Earth's magnetic field

for extreme phases, which correspond to lower beam energies. The first cause can be addressed through an RF gun design made to prevent distortions of the accelerating E-field.

An example plot showing the alignment process of the UV laser position on the cathode to the gun axis is shown in Fig. 3.15. Due to the small span of the YAG screen, the shifted laser position could not be adjusted to reach an orthogonal secondary beam drift under a phase scan. Nevertheless, the distance between the electron beam positions under the two iterations was greater than the $3\sigma$ uncertainty. As seen in the plot, the two instances of the photocathode laser position corresponded to a strongly linear drift in the electron beam position. The fit crossing was accurate enough to allow for finding the optimal laser position within one run of the alignment process, as exemplified in the "after laser alignment" data points. A subsequent phase scan performed for the optimal laser position indicated micrometre displacement of the electron beam under changes in energy.

Note that the initial beamline misalignments were such that in the first iteration of the correction process, the gun axis was found to be placed outside of YAG screen span. The vacuum chamber housing the YAG and OTR screens was therefore moved by a few milimetres to bring the gun axis towards the centre of the screen set-ups.

The next step following the alignment of the laser on the cathode was the alignment of the solenoid with respect to the gun axis.

#### 3.6.2.2 Alignment of the solenoid

As shown in Fig. 3.9, the misalignment of the solenoid with respect to the beam axis leads to a significant increase in the beam emittance, albeit smaller than for the laser position offset on the cathode. When the beam axis is not aligned with the solenoid's, multipolar magnetic fields affect the travelling bunch, leading to changes in the beam position against the solenoid strength, along with the aforementioned emittance degradation.

The alignment of the laser on the cathode represents a one-dimensional problem, due to its use of RF phase scans. The solenoid alignment is markedly two-dimensional, involving a coupling of the horizontal and vertical misalignments. Moreover, the tilt angles of the solenoid (pitch and yaw) also contribute to the

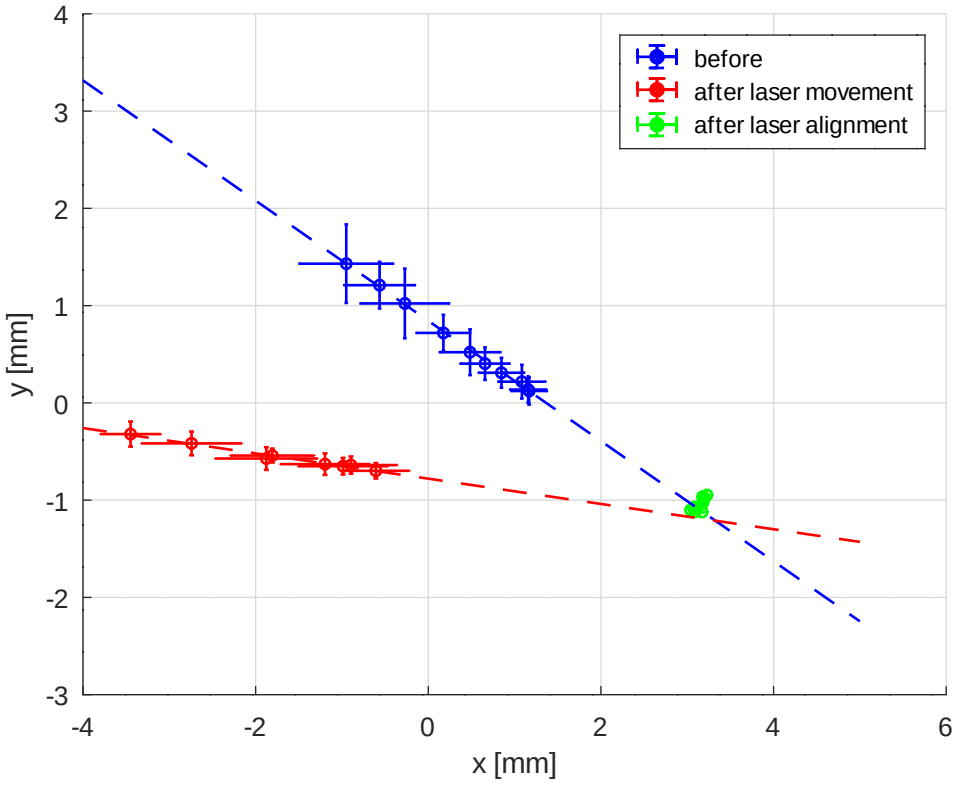
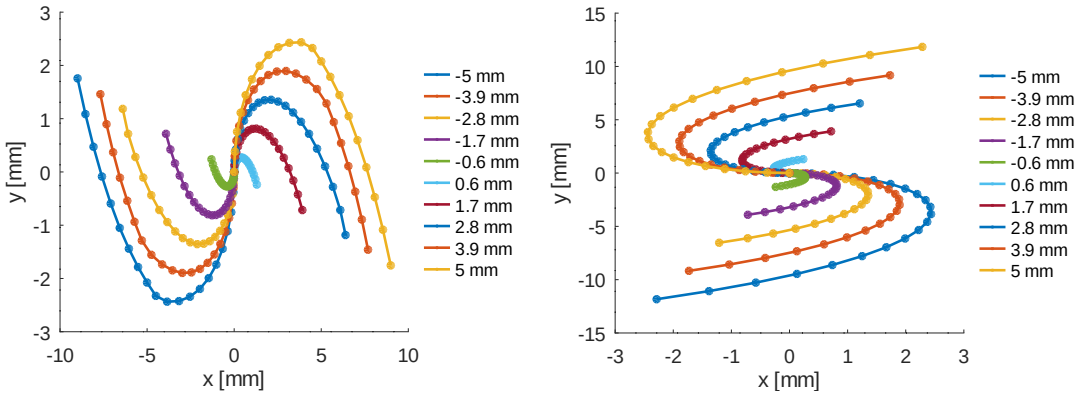



Figure 3.15: Beam-based alignment of the ARTI photocathode laser to the gun axis. The electron beam position under an RF phase scan is shown for three different iterations of the alignment: before the alignment process, after the initial laser shift (required in order to deduce the optimal position), and after the alignment. The lack of beam drift under a change in beam energy, as seen in the post-alignment data, indicates that the laser has been centred on the gun axis.

coupling and, in the case of ARTI, cannot be easily corrected. Indeed, the alignment was restricted to the horizontal and vertical positions, since the two were controlled through a motorised baseplate. The tuning range of the solenoid movers is 6 mm (which proved to be insufficient for alignment), and the step size is in the micrometre level.

The beam-based alignment was aided by RF-Track simulations to deduce the transverse offsets of the ARTI solenoid. Using RF-Track, plots were made showing the tracking of the electron beam position at the location of the YAG screen against the solenoid magnetic strength, starting from 0 T. They are exemplified

in Fig. 3.16, for horizontal and vertical misalignments. It can be seen that the polarity, modulus, and direction of the solenoid misalignment directly affect the trajectory of the beam position, in particular the orientation and magnitude of its curvature.




(a) (b)

Figure 3.16: Simulated dependence of the transverse beam position on solenoid strength for a range of imposed horizontal (a) and vertical (b) offset values. The evolution of the beam trajectory with magnetic field is shown for different initial misalignments. These simulations were used to identify the dominant transverse offset component during the solenoid alignment procedure by comparison with the measured beam response.

By experimentally replicating the solenoid scan starting from 0 T, and comparing its trajectory with the one obtained in RF-Track, the dominant offset component can be identified and corrected; the process is repeated until a change in solenoid strength no longer has an impact on the electron beam position. A typical measurement of the evolution in beam position under a solenoid scan is shown in Fig. 3.17. To perform the solenoid alignment experimentally, the gun was set to RF focusing, to determine the beam position at 0 T. A solenoid scan was then performed from 0 T to 0.0233 T, which kept the electron beam contained on the YAG screen. The electron beam position was tracked, and the resulting trajectory superimposed on the simulated values. An example plot comparing the measured trajectory to the simulated one is shown in Fig. 3.18.

The measured trajectory was compared with the simulated ones from RF-Track, based on the beamline model developed during commissioning. One can see

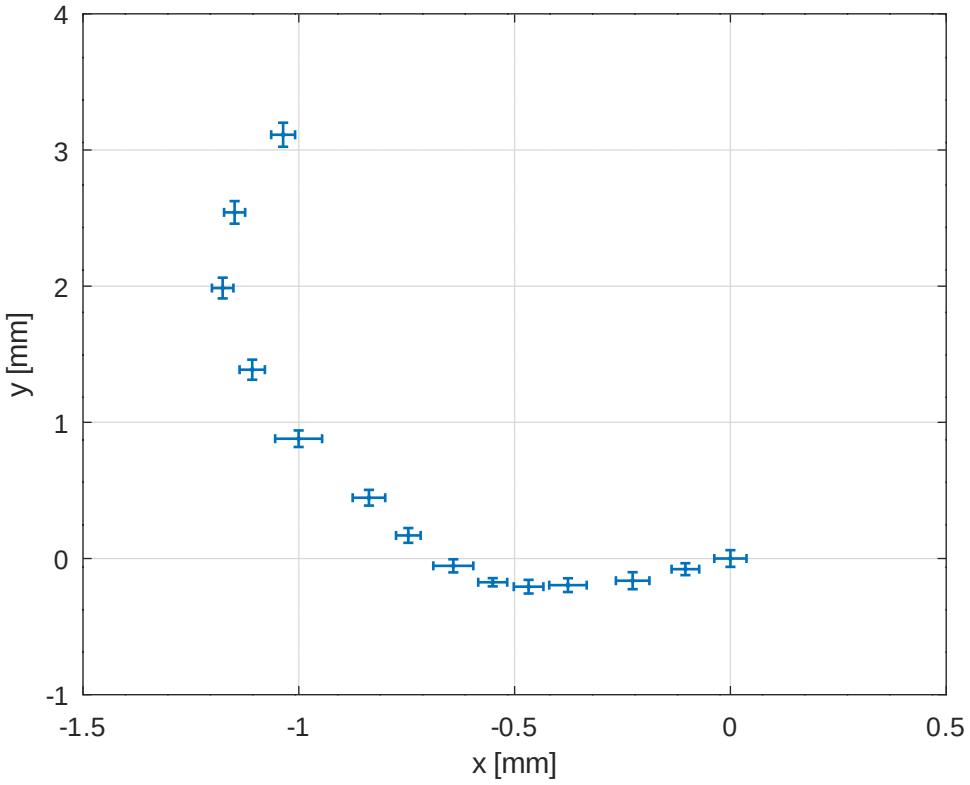



Figure 3.17: Measured transverse electron beam position for different values of the solenoid magnetic field strength. Each data point represents the beam centroid position recorded at a fixed solenoid setting, illustrating the field-dependent trajectory of the beam during the solenoid scan.

that radius of the trajectory is directly proportional to the magnitude of the offset, while the orientation of the traced orbit is dependent on whether the horizontal or vertical offsets are dominant, along with the offset's polarity. Using this method, the magnitude and orientation of the solenoid offset were successfully identified and corrected.

Although helpful in assessing the original offset values, a slightly different methodology was used to verify the inferred offset values. This new method also provided a shorter execution runtime. As part of it, a small solenoid strength is input; based on the possible trajectories shown in Fig. 3.16, the dominant transverse component of the solenoid misalignment is identified, along with its polarity.

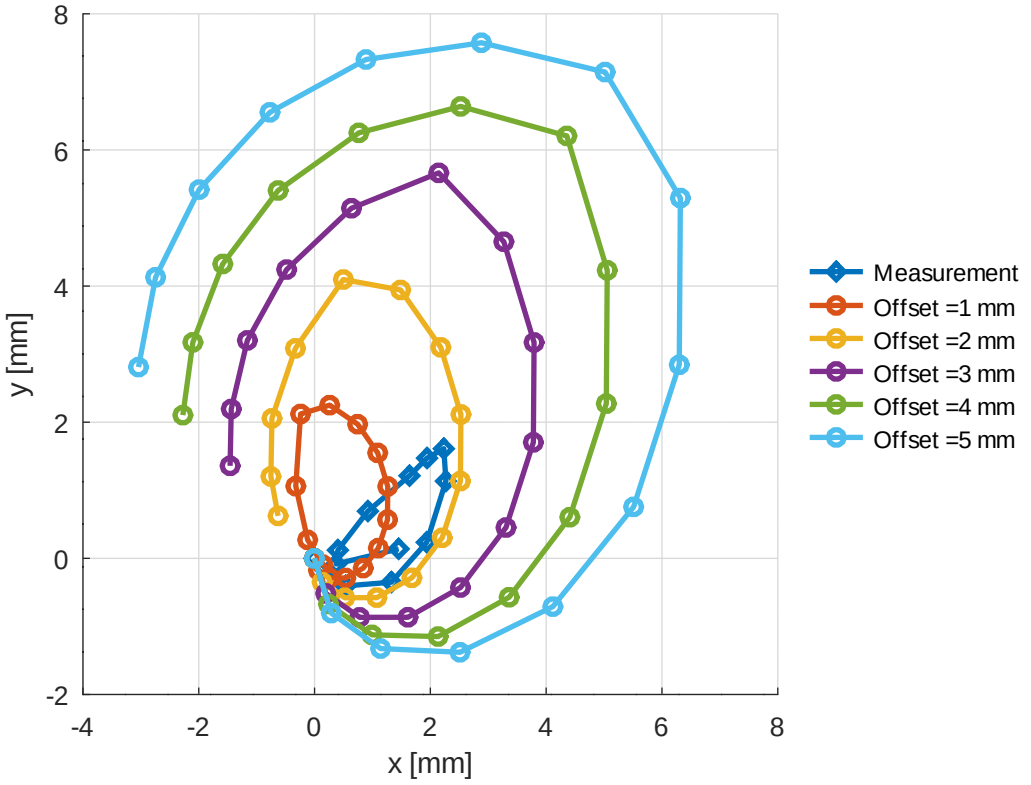



Figure 3.18: Measured electron beam trajectory obtained from a solenoid strength scan, overlaid with RF-Track simulations for a range of assumed transverse solenoid offset values. The simulated trajectories correspond to increasing horizontal and vertical offsets, allowing direct comparison with the experimental data to determine the effective solenoid misalignment.

Following this, the solenoid is moved to correct that particular offset, until the electron beam is brought back to its original position at 0 T. The process is repeated until the solenoid is centred on the gun axis and the beam position is no longer influenced by changes in the solenoid strength.

Unfortunately, although the offsets were ultimately inferred using the technique exemplified in Fig. 3.18, the alignment of the solenoid was not finalised. This was due to the fact that the solenoid base plate has a tuning range of around 3 mm. The solenoid was originally placed in the middle of the tuning range, and the magnitude of both the vertical and horizontal offsets was larger than the tuning range. At the time of the experiment, the corrected configuration was deemed sufficient for

the purposes of the CBS experiment. In order to finish the alignment, the solenoid would have needed to be reinstalled on the base plate and reintegrated into the functioning beamline.

### 3.6.3 Results from the lattice element alignment

The main goal of the ARTI lattice element alignment was to minimise the beam emittance at the interaction point for the CBS experiment. Although the alignment of the solenoid was not finalised, the emittance still significantly decreased, as seen in Fig. 3.19. One can see a subsequent reduction by 30.6% of the minimum electron spot size on the YAG screen following the alignment of the critical beamline elements. The change in emittance is also reflected in the narrower curvature of the solenoid scan plot after alignment.

No diagnostics were installed to enable emittance measurements at ARTI. The placement of the YAG screen and solenoid installation prevented the use of traditional quadrupole scans. Given the lower energy exhibited by the injector, a pepper-pot mask, which uses beamlet formation to derive phase space components at the respective location [103], would have been recommended. However, it was not installed at ARTI.

The experimental correction of the beamline offsets was also used to evaluate the performance of the offset inference method described in a previous section. The experimentally-derived offsets are collected in Table 3.7, along with values obtained from the novel inference method. It can be seen that the misalignment values inferred using the RF-Track model consistently predicted offsets that were twice larger than the actual offsets of around 1.5 mm.

Table 3.7: Offsets measured and inferred from RF-Track using the Simplex-based method. Note that the alignment of the solenoid was not completed.

| Offset | Inferred | Measured | Unit |
|---|---|---|---|
| Cathode Laser x/y | 2.30 / 1.33 | 1.27 / 0.85 | mm |
| Solenoid x/y | 2.66 / 3.19 | 1.64 / 1.63 | mm |

The difference between the measured and inferred offsets in the case of the solenoid was explained by the tuning range limit of ±1.5 mm, which prevented

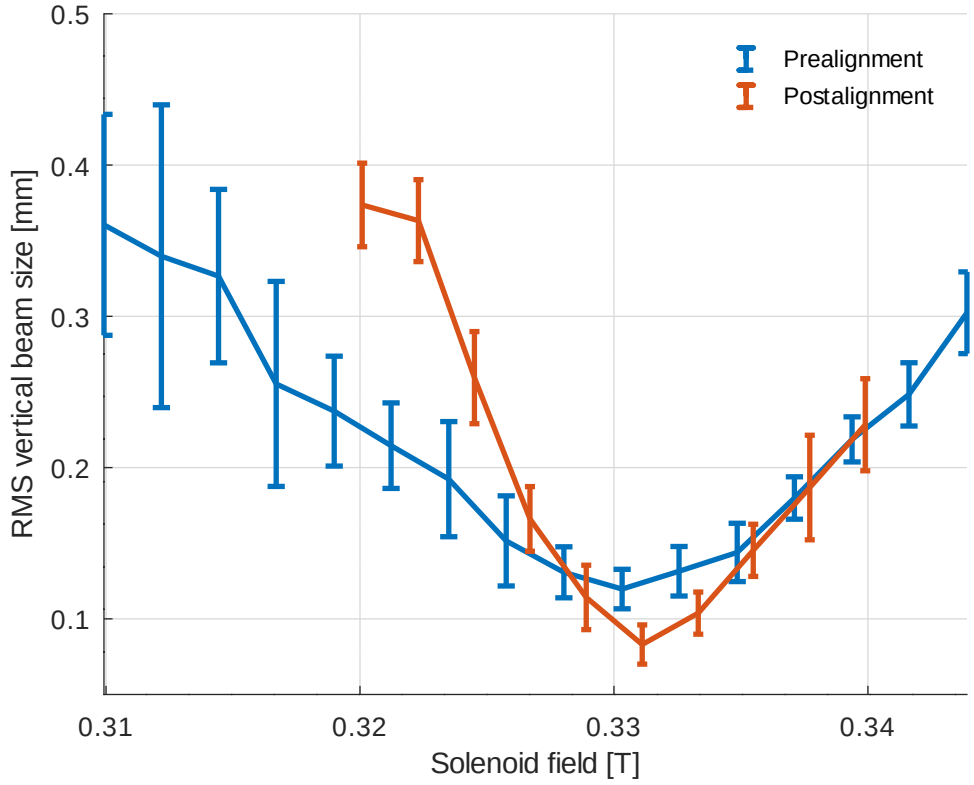



Figure 3.19: RMS vertical electron spot size at the interaction point as a function of solenoid magnetic field strength, measured before and after beamline alignment. The post-alignment scan exhibits a more symmetric dependence and a reduced minimum spot size. The beam profile was recorded on a YAG screen.

larger corrections from being made. According to the simulated results, a further correction of 1 mm in both the horizontal and vertical directions was required.

In regards to the laser position offset on the cathode, the discrepancy between the measured and inferred values can be explained by the choice of imaging screen. As detailed in Section 3.8.1.1, the YAG screen proved to be inadequate in realistically representing the electron beam profile at focus. Studies done at other beamlines [75] have shown that YAG screens tend to saturate for charge densities greater than $1.5\,\mathrm{nC\,mm^{-2}}$. Assuming a nominal bunch charge of 200 pC and RMS spot size of 100 µm, one obtains a charge density of $6.36\,\mathrm{nC\,mm^{-2}}$, which far exceeds the quoted threshold value. This saturation effect leads to a plateau in the

solenoid scan of the electron spot size, as reproduced in Fig. 3.20. This prevents realistic measurements of the electron spot size at the magnet focus point. This effect is inherent to the YAG:Ce material and can only be avoided by changing the actual screen. The beam imaging can also be affected by multiple scattering in the YAG screen, but this should have been minimised given that the one used is ultra-thin (100 µm thick).

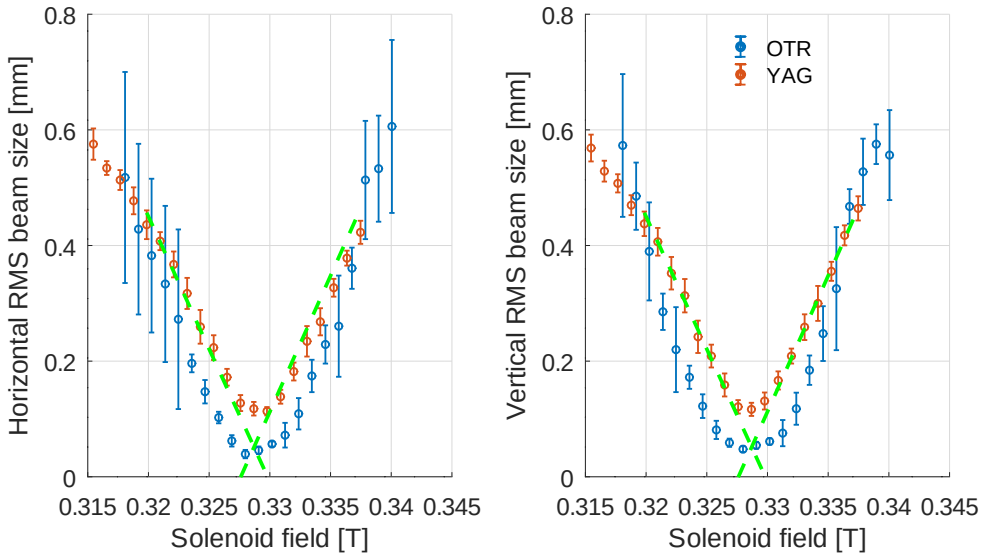



Figure 3.20: Comparison of solenoid scans measured with a YAG screen and an OTR screen, illustrating saturation effects at high charge densities near the beam focus. The RMS horizontal (left) and vertical (right) beam sizes are shown as a function of the solenoid magnetic field strength. Around the focal point, the YAG measurement exhibits a plateau due to scintillator saturation, leading to an overestimation of the minimum beam size. Linear fits to the low- and high-field regions are included to indicate the apparent waist position and to highlight the discrepancy between the saturated YAG profile and the unsaturated OTR measurement.

After installing an OTR screen (consisting of a high purity silicon wafer coated on one side with 100 nm thick), the saturation effect no longer occurred and henceforth 50% smaller electron spot sizes have been measured. As shown in RF-Track simulations of the impact of the lattice element offsets, a large misalignment of the position of the laser on the cathode leads to a correspondingly large increase

in emittance. This in turn increases the electron spot at focus. The inference script, taking the YAG-measured solenoid scan as realistic, tried to reproduce its curvature as accurately as possible. Given the large spot size measured (compared to reality), the inference overestimated the offset required to reproduce the equivalent emittance degradation. Assuming a direct proportionality, the two-fold larger inferred offsets can be explained by the two-fold larger spot size as seen on the YAG screen compared to reality (as seen on the OTR reference screen).

Due to this notable discrepancy, the OTR screen was exclusively employed during the development of the CBS experiment. One disadvantage of OTR screens is their significantly lower yield compared to scintillating screens. However, their reduced material price made them more expendable, which allowed them to be used for a high precision spatial alignment scheme for the laser and electron beam at the IP of the CBS experiment (details discussed in Section 4.6).

Lastly, given the identification of the offsets present in the critical beamline elements, a corresponding RF-Track simulation model was built. This model was benchmarked against parametric scans of the beam parameters, which were used to define the optimal electron gun settings for maximising the scattered CBS photon flux.

## 3.7 Parametric scans of the beam parameters

The low energy ARTI set-up and its laser system were such that they only allowed for a limited number of photons to be generated via CBS. Both the electron and laser beam intensities were severely limited compared to typical CBS sources. To counteract these limitations, the other parameters in the flux equation needed to be optimised to provide the maximum possible performance. This was done with the aid of an RF-Track model of the beamline. The model was first independently optimised to maximise the output flux, as described in the previous chapter, and define the target parameters for the electron gun and solenoid. Following alignment of the ARTI beamline elements, the RFT model was updated and tested against measurements taken using the YAG screen. Due to the discrepancy between the YAG and OTR measurements of the beam spot size, the spot size measurements presented in this section have a correction factor equivalent to 50% (both for

the horizontal and vertical components), to match them to the realistic OTR measurements.

The tuning parameters of the ARTI beamline at the time of the CBS experiment were: the RF phase and gradient of the electron gun, the position and spot size of the UV laser on the copper photocathode, and the position, magnetic strength, and polarity of the focusing solenoid. The positions of the solenoid and cathode laser were fixed following the alignment process. The RF-Track model showed that lower electron spot sizes can be obtained at the IP using a plus-minus polarity for the solenoid. The polarity was therefore fixed to the respective setting throughout the CBS experiment. Lastly, the RF gradient was set to maximise the electron beam energy, as the collection angle of the scattered photon beam is inversely proportional to the relativistic gamma factor.

The parameters used for the 2D parametric scan were therefore the RF phase, the solenoid magnetic strength, and the laser spot size on the cathode. These parameters can be used to tune various observables given by the electron beam, namely the beam energy, energy spread, beam profile distribution, and spot size. The first two values were fixed during the CBS experiment and not directly correlated to the scattered photon flux. The spot size is integral to the flux formula, and a setting needed to be found that ensured its smallest possible value. Nevertheless, the Gaussian profile is subject to change from nonlinear beam effects, notably space charge [104]. Under strong space-charge effects, the beam profile can be reshaped to a $q$-Gaussian-like distribution, with heavy tails encompassing the so-called "beam halos". The CBS flux formula is strictly defined for the collision of two Gaussian beams (an extension for the collision of a Gaussian and a $q$-Gaussian beam was derived and included in this thesis), but nevertheless, the maximisation of the CBS photon flux is conditioned by the presence of a highly dense bunch at the IP.

An optimisation of the ARTI beamline to provide a highly dense electron bunch at the IP by tuning the RF phase and solenoid strength was done. Given the limited automation of the ARTI beamline, the optimisation used heatmaps of the tuning parameters colour-coded by the RMS electron spot size measured with the YAG. The heatmaps were first obtained using the updated RF-Track model of the ARTI beamline. The simulated heatmaps defined the limits and step sizes of the

parameter space. Measurements were then performed at the ARTI beamline, using the same parameter input as for the simulation. The heatmaps were measured via solenoid scans for each RF phase or laser spot size. Experimentally, the RF phase and laser spot size can also affect the amount of charge extracted from the photocathode.

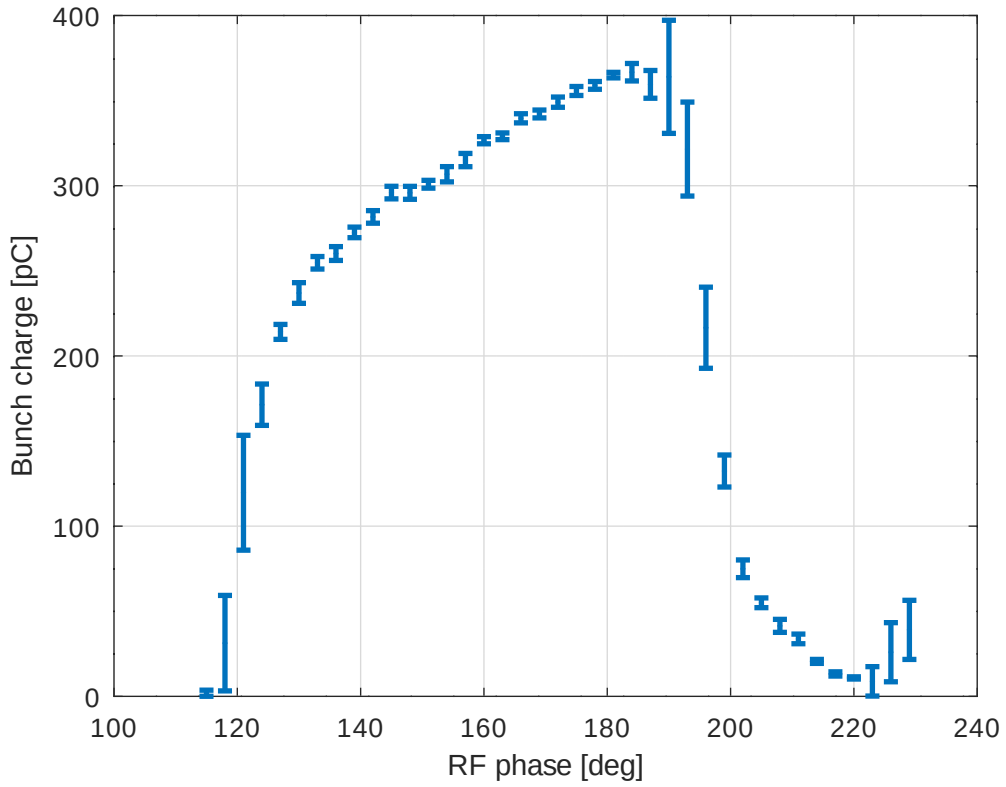



Figure 3.21: Experimental measurement of the bunch charge as a function of RF phase, performed at ARTI.

Since the bunch charge was a fixed parameter in the RF-Track simulation, the evolution of the bunch charge against the RF phase was studied, and the laser intensity energy was tuned throughout the measurement process to provide the same bunch charge of 400 pC. An example plot showing the nonlinear dependence of the bunch charge on the RF phase is shown in Fig. 3.21. It can be seen from the plot that the bunch is defined for a range of 100°, with a peak in charge located a few degrees following the on-crest phase (corresponding to the maximum energy).

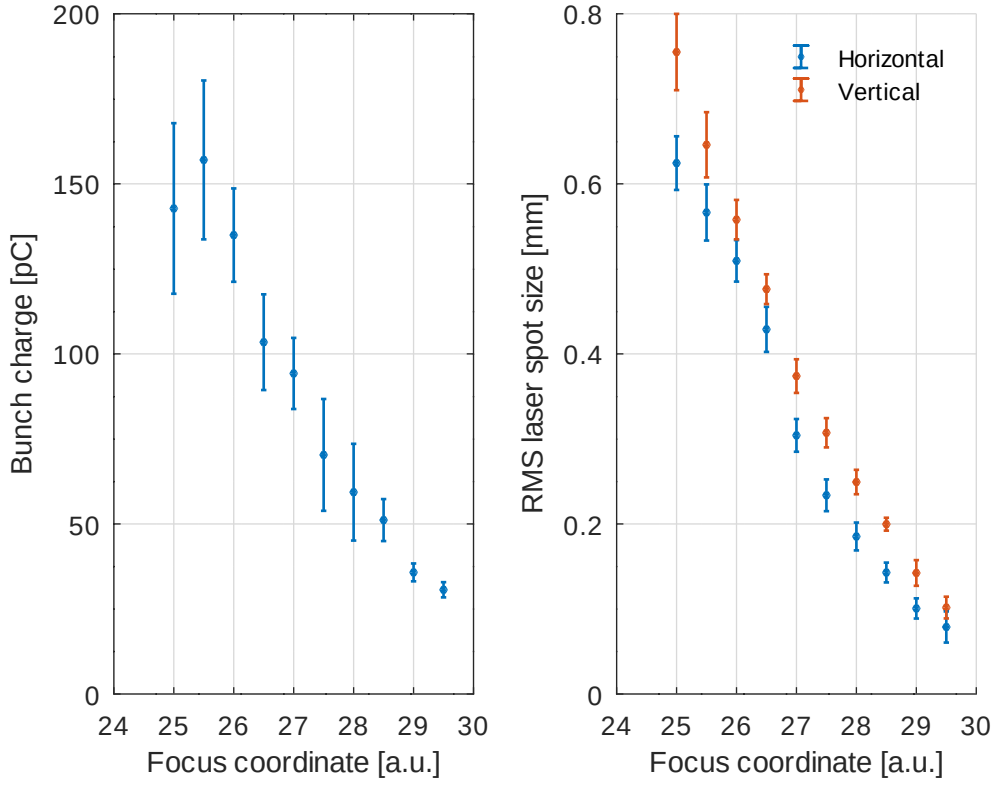



Figure 3.22: Experimental scan of the laser focus motor coordinate against the bunch charge (left), along with the measured RMS laser spot size on the cathode against the focus motor coordinate (right). The later plot was used to calibrate the first. Outside the saturation effect of the cathode (occurring for small enough spot sizes), the dependence of the extracted bunch charge against the laser spot size appears strictly linear. Bunch charge measurements were taken using a Faraday cup, while the laser spot size measurements were taken using the virtual cathode set-up.

The typical phase tuning range was selected to ensure a linear charge distribution against the RF phase, spanning 50°. A similar effect occurred for the cathode laser spot size on the bunch charge, as seen in Fig. 3.22. As the number and spread of the emitted photoelectrons is determined by the incident laser intensity, the laser spot size on the photocathode can be used to control both the bunch charge and the transverse emittance. However, quantum efficiency measurements of the photocathode under UV illumination revealed the onset of saturation at sufficiently

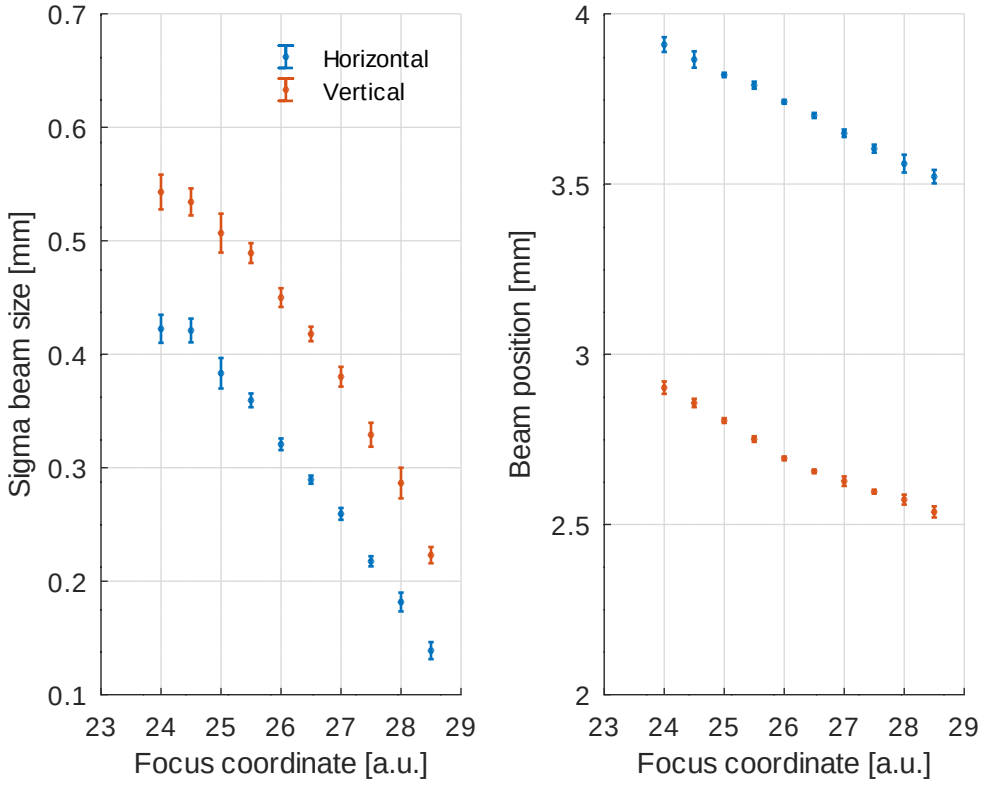



Figure 3.23: The dependence of the cathode laser spot size (left) and position (right) on the motorised focus setting. Note the noticeable drift in the laser beam position under a change in focus, indicating a misalignment of the lenses in the focusing telescope. The measurement was taken using the virtual cathode set-up at ARTI.

small laser spot sizes. In this regime, further increases in the local laser intensity do not result in a proportional increase in the emitted charge, thereby limiting the number of additional photoelectrons that can be generated.

The resulting parametric scans are shown in Fig. 3.24. The solenoid scans are pictorially represented by the heatmap's columns. The darker colours correspond to the optimal setting of small spot sizes achieved for the CBS interaction. It can be seen from the RF phase maps of Fig. 3.24a and Fig. 3.24b that a band-like region of minimal electron spot sizes is defined. Although a notably small spot size was expected for each solenoid scan, the band's shape reveals that the solenoid strength corresponding to the smallest electron spot sizes varies with the

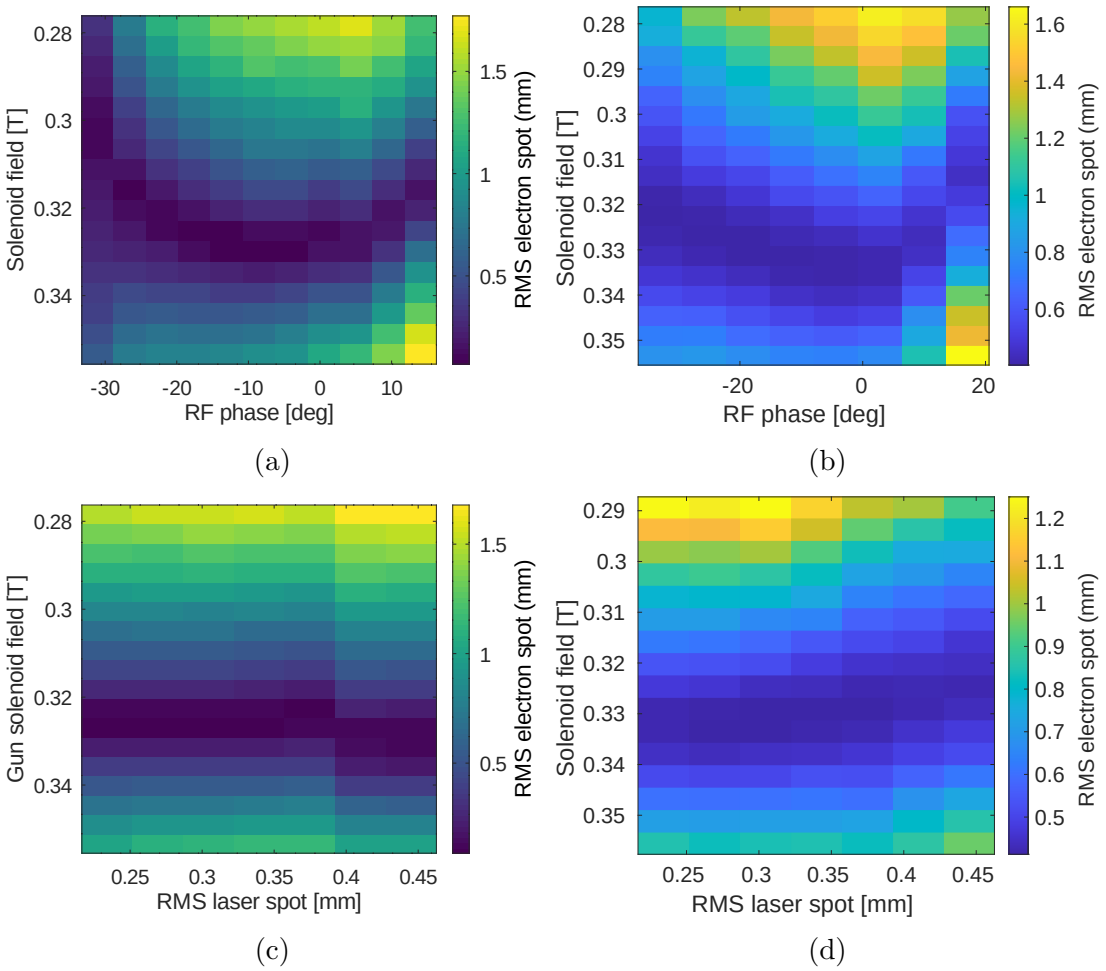



Figure 3.24: Comparisons between simulations (left) and measured data (right) of electron beam size as a function of the solenoid strength with respect to the RF phase (top) and laser spot size (bottom).

RF phase. This can be explained by the strong dependence of the RF phase on the beam energy, as observed in Fig. 2.8. The change in RF phase triggers a change in beam energy, which shifts the focusing strength required to reach a beam waist, thus achieving the distinct band shape seen in both the RF-Track simulation in Fig. 3.24a and the experiment in Fig. 3.24b. Furthermore, the on-crest phase, corresponding to the highest beam energy, can be identified in the heatmap from the minimum of the band curve (where the solenoid strength required to focus the electron beam is the strongest).

A similar study was performed for the effect of the cathode laser spot size on the beam emittance at the IP. With respect to the RF phase study, there is an observable difference between the simulated and measured heatmaps. In contrast with Fig. 3.24a and Fig. 3.24b, the band corresponding to the minimal electron spot size recorded appears as a horizontal line, constant with respect to the solenoid field. This is expected, given that a change in the cathode laser spot size in itself would not change the energy gain of the bunch in the RF gun. Nevertheless, for the experimental results of Fig. 3.24d, the band has a slight gradient, corresponding to a change in the optimal solenoid strength against the laser spot size. This suggests that during the measurement there was a change in the beam energy. From Fig. 3.23, the laser beam position actually shifts under a change in the focus settings. The change in the laser beam position on the cathode affects the accelerating E-field seen by the beam as it travels through the RF gun. Assuming a displacement with respect to the gun axis, the energy of the electron bunch will notably decrease, as seen in the RF-Track simulation from Fig. 3.25. Even with a laser spot size tuning range of 0.25 mm, a change in the beam energy is significant enough to be observed in the heatmap from Fig. 3.24d.

The holistic representation of the optimisation carried out for the ARTI beamline was followed by a targeted study of the electron beam size evolution within the heatmaps' band structure. Therefore, for each solenoid scan, the minimum electron spot size was extracted, and the resulting array was plotted. The resulting 1D plots are shown in Fig. 3.26.

For the RF phase scans, at values larger than those of the on-crest phase, the electron beam experienced a significant emittance degradation, with a corresponding increase in beam size. The spot size decreased linearly, reaching a minimum in a relative phase of $-10°$, followed by a plateau observed up to $-30°$. Both the measured and the simulated spot sizes followed the same pattern. For the CBS experiment, a relative RF phase of $-10°$ was used.

For the cathode laser spot size scan, the electron spot size followed a linear descent from 0.45 mm to 0.3 mm RMS, followed by a plateau in the region corresponding to laser spots smaller than 0.3 mm RMS. The experimental data and the RF-Track data followed a similar pattern. For the CBS experiment, to ensure sta-

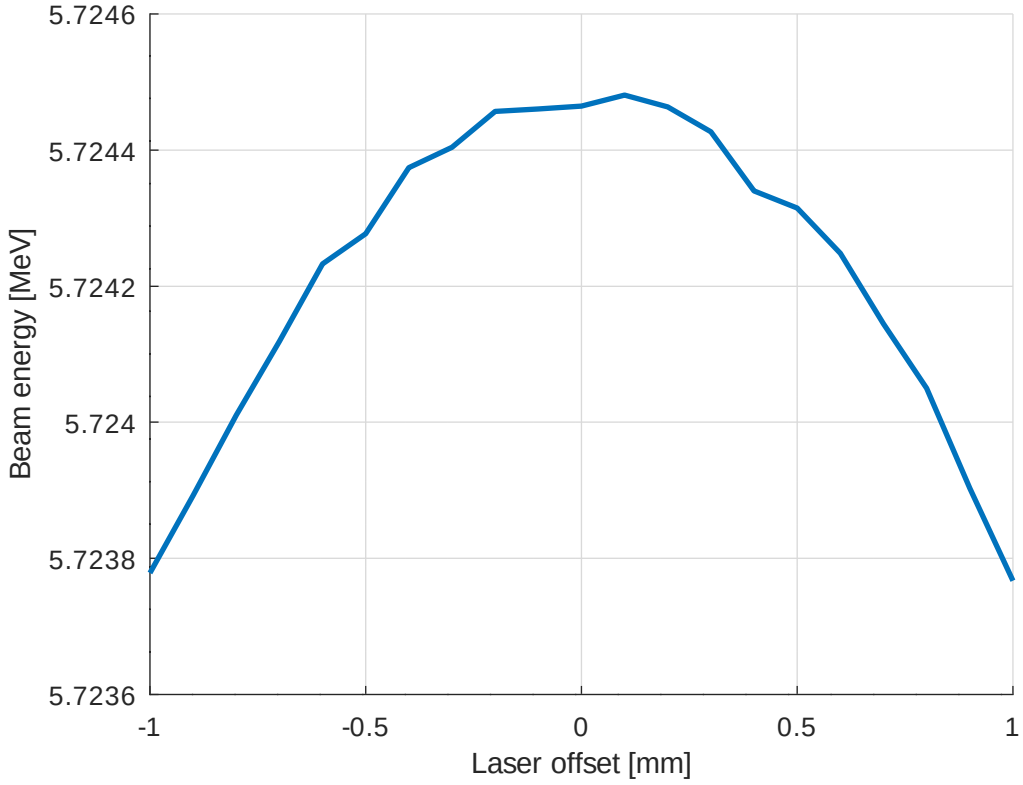



Figure 3.25: RF-Track-simulated dependence of the beam energy on the laser offset.

bility in the electron spot, a small laser beam size of 0.25 mm RMS was therefore used.

The heatmap analysis allowed for the selection of the optimal RF phase and laser spot size on the cathode that minimised the electron beam size at the IP. Furthermore, the analysis allowed for the benchmark of the RF-Track beamline model against a variation of measured data. The confidence gained from the benchmark allowed for the safe deployment of the RF-Track code for further beamline studies. In particular, for the purposes of the CBS experiment, it ensured that a realistic expectation for the number of scattered CBS photons can be obtained.

As mentioned in a previous section, the electron beam size had to be optimised while also considering the beam profile at the IP. This entailed an investigation of the beam halo observed at ARTI, to find its source of formation, and to be able

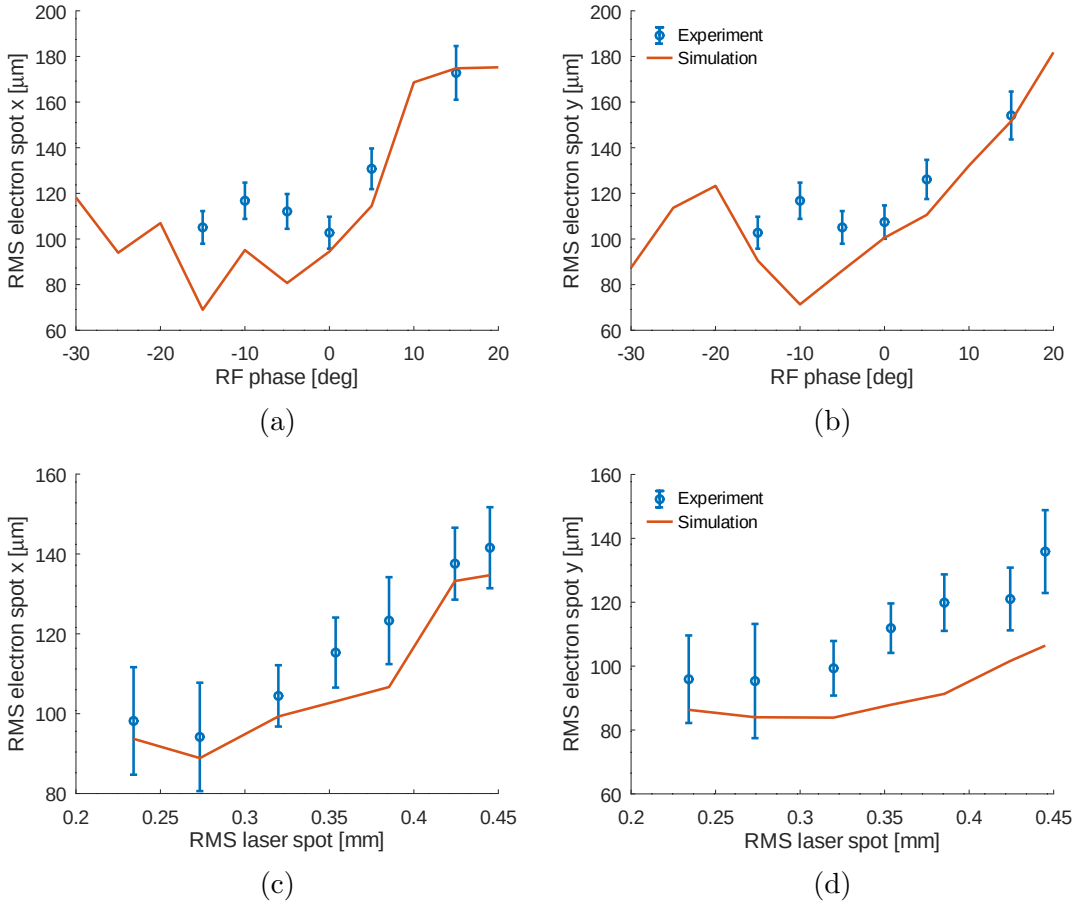



Figure 3.26: Comparisons between simulated and measured data corresponding to the minimum electron spot size sigma in the horizontal and vertical, against the RF phase (top) and laser spot size on the cathode (bottom) for the horizontal (left) and vertical (right) axes.

to model it in RF-Track.

## 3.8 Novel beam halo source studies at ARTI

Beam halos inevitably affect the performance of high-intensity accelerators. The halo is defined as a region of low particle density surrounding a highly dense beam core. Due to the large span of the halo, it can interact with the beam pipe walls, leading to beam loss and vacuum degradation. The mechanisms of halo formation depend on the type of accelerator involved [105]. Whatever the

mechanism, the sources of beam halos need to be well understood to prevent halo formation, minimise beam loss, and ultimately improve machine performance.

Insofar as the CBS experiment is concerned, the study of potential halo sources in photoinjector guns was required for ARTI. Halos at the gun level are typically attributed to space charge forces due to a high-intensity beam. As part of the experimental investigation of the beam halo at ARTI, a novel halo formation method in photoinjectors was identified. The subsequent matching of the experimental beam profile with the simulated one is detailed in this section.

As described in Section 3.6.1, a significant halo was observed from the YAG screen installed at the IP. This was particularly concerning, given that the initial simulations were not able to predict the intensity of the measured halo, and because a notable percentage of the bunch population would spread out in the halo volume and, therefore, not able to interact with the laser pulse in the CBS interaction. An accurate estimate of the halo population was therefore required along with an accurate representation of the experimental beam profile. Lastly, the cause of the beam halo was sought, as it allowed for replicating the exact beam profile at the IP through RF-Track.

### 3.8.1 Measurement of the beam halo

The beam halo was first observed using the YAG:Ce screen. The thin screen of 100 µm was placed orthogonally to the beam, coated on the upstream side with 100 nm Aluminium, and the scintillating light reflected on the in-air digital camera by a 45°mirror. This design was deemed reliable for measurements of low energy electron beams [74]. However, from initial measurements at ARTI, the ability of the screen set-up to accurately measure beam profiles was questioned.

#### 3.8.1.1 Benchmark of the YAG screen imaging set-up against the OTR screen set-up

A two-fold difference was observed between the beam size measured from the YAG screen and the simulated one. Initial measurements deemed it to be even higher, but this was caused by the projection method used to compute the 1D beam profiles. The method constructed the horizontal and vertical beam profiles

by summing the intensity of the rows and columns of the image matrix. This approach is useful for removing outliers and for its ease of computation. However, it also masks the halo profile, as seen in Fig. 3.27b. As anticipated from the central limit theorem, the summation of the image pixel lines amounts to a Gaussian approximation of the beam profile [106]. However, the beam's 2D profile is non-Gaussian-like, as seen in Fig. 3.27a. The high intensity beam "core" is encircled by a uniform disc comprising the beam halo. Using the initial projected method, the measured beam size was four times larger than the one simulated using the RF-Track model. A new measurement method of the electron beam profile was required.

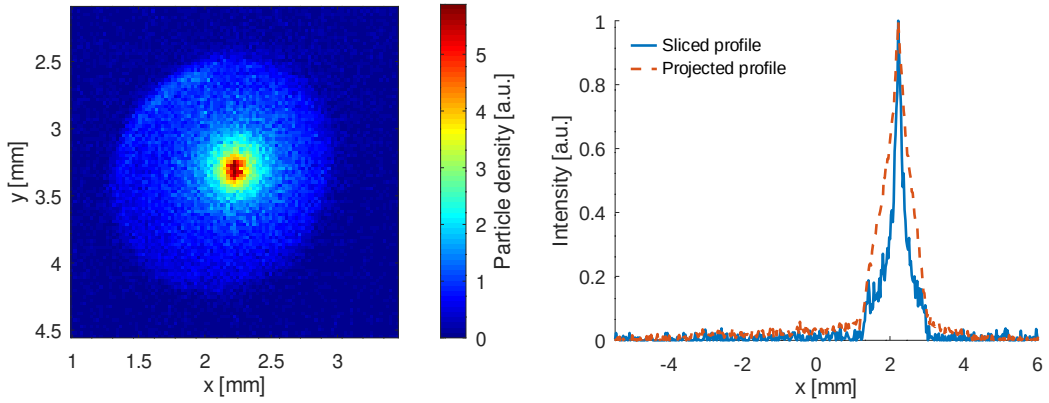



Figure 3.27: Measured transverse electron beam distribution on the YAG screen at the solenoid focal point (a). Comparison of the corresponding horizontal beam profile obtained from the two primary analysis methods used at ARTI, namely the sliced profile and the projected profile (b).

To provide an accurate 1D assessment of the beam profile, the peak coordinates of the horizontal and vertical projected profiles were extracted, and the single pixel row and column passing through the beam peak was plotted. This image "slicing" method provided a non-averaged profile, subject to background outliers and dead pixels, but nonetheless an accurate representation of the actual beam shape. As seen in Fig. 3.27, although the projected profile was able to accurately predict the beam size of the halo, the beam core is significantly narrower in shape. Gaussian

fits of the 1D profiles show that the actual beam size is half of the one initially measured using the projection method.

The RMS beam size was measured by calculating the FWHM of the "sliced" profile and converting it to its sigma value. In the case of the projection method, the non-Gaussian halo would bias the Gaussian fit and enlarge the spot size prediction. The FWHM was therefore used throughout the thesis to compute the RMS spot size.

To obtain an accurate measurement of beam size, an OTR screen was installed in place of the 1 inch diameter mirror slot of the motorised actuator (shown in Fig. 2.5). There were two designs of OTR screen used at ARTI; this section presents measurements taken with the initial OTR screen, pictured in Fig. 2.6a. The first OTR screen consisted of a 0.6 mm thick silicon wafer coated with 100 nm thick aluminium.

To provide a detailed comparison of the YAG and OTR screen performance, scans of the solenoid magnetic strength were made to measure the electron beam spot size. The results for both the horizontal and vertical planes are shown in Fig. 3.28. The YAG and OTR measurements were then matched with those from the RF-Track beamline model. It can be seen that the YAG measurements are consistently larger than the ones from RF-Track and the OTR screen. In fact, the OTR screen result is matched with that of RF-Track within one sigma. This confirmed that the beam size discrepancy was indeed caused by the screen set-up choice.

#### 3.8.1.2 Halo-Core Percentage

The OTR screen was therefore used to characterise the beam halo. One relevant question in regards to the CBS experiment was the actual amount of bunch charge involved in the CBS interaction. Beyond the Faraday cup measurements, one needed an estimate of the percent of the bunch population occupying the beam core, and vice versa. Once these were known, the charge corresponding to the beam core could be used as an input in the RF-Track simulations of the interaction point.

To evaluate the core-halo percentage, a small spot beam profile was analysed, as shown in Fig. 3.29. The horizontal and vertical "sliced" beam profiles were

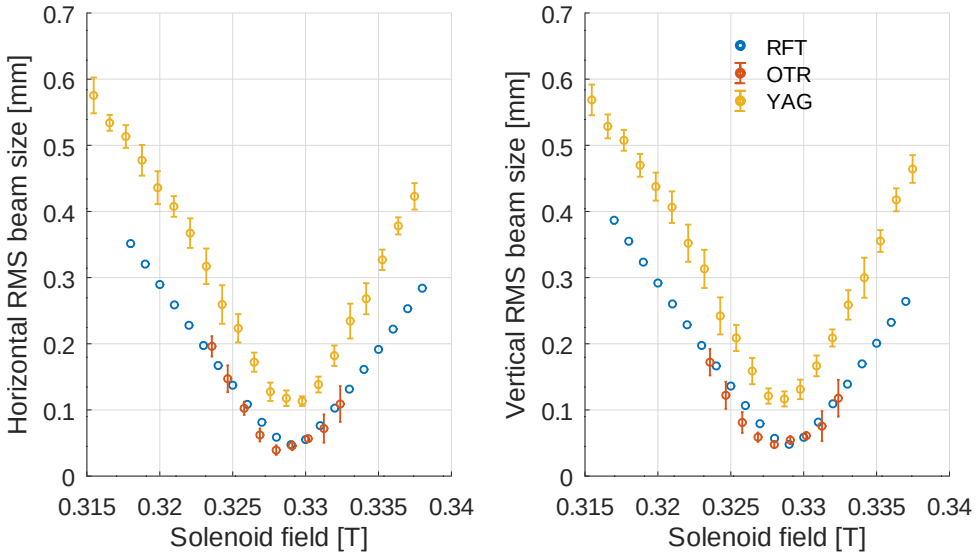



Figure 3.28: Comparison of YAG and OTR screen measurements of a solenoid scan at ARTI, against RF-Track simulations. The scans tracked both the horizontal (a) and vertical (b) spot sizes. The measured RMS electron spot size is plotted against its corresponding solenoid magnetic field value. Note that the YAG measurement predicts consistently higher values for the RMS beam size measurement than the OTR. The OTR and RF-Track beam size measurements match within less than one sigma.

computed. The halo and core profiles were identified by fitting the Gaussian distribution to the appropriate section of data: for the halo, the tails of the profile, and for the core, the centre peak. The halo/core percentage was calculated by taking the integral of the halo/core Gaussian fit and dividing it by the integral of the 1D profile data. This was done for both the horizontal and vertical distributions.

For the horizontal distribution, a halo percentage of 31.1% was obtained, while for the vertical distribution, a halo percentage of 20.0% was obtained. This corresponds to a mean of 25.6% for the halo percentage. This result confirmed that despite the large spatial spread of the beam halo, a reduced halo amounting to a quarter of the bunch population was present.

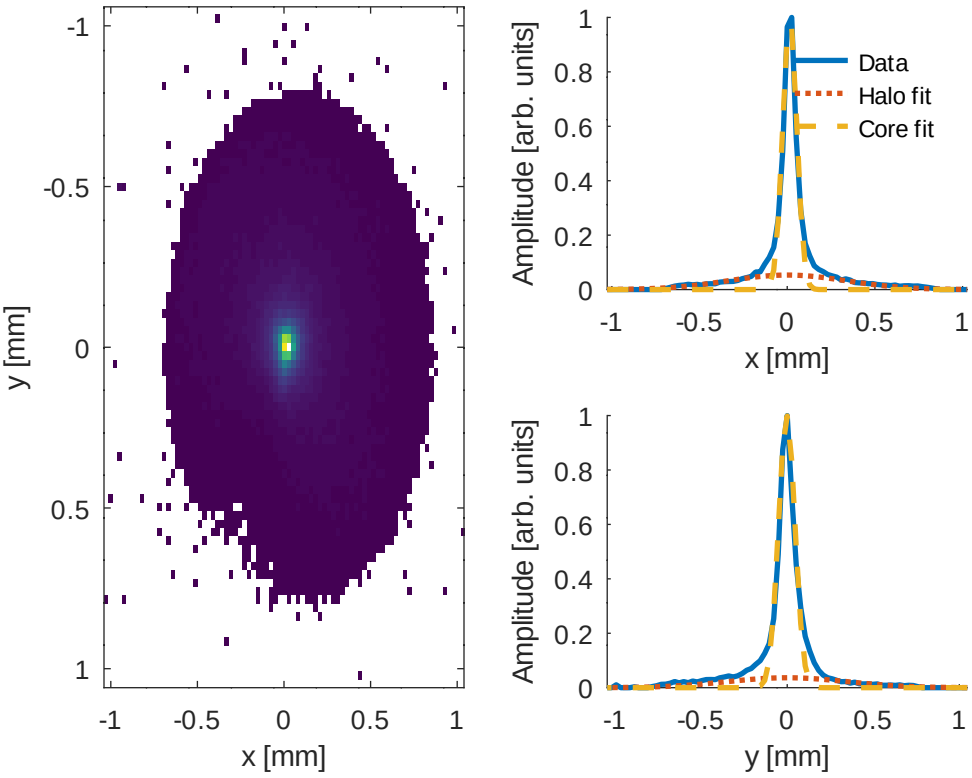



Figure 3.29: The measured profile of the electron beam, optimised for the smallest spot size. Gaussian fits of the beam core and halo are shown for the horizontal and vertical distributions.

### 3.8.2 Mechanism for the halo generation at ARTI

Initial RF-Track simulations of the beam profile at the interaction point (shown in Fig. 3.36b) revealed a less significant beam halo than the one measured. Space charge effects, a common cause of beam halos [107], were included in the simulation. Due to the single bunch emission, wakefields and beam loading would have had no notable impact. The simulated beam profile also included the misalignments measured for the solenoid and laser position on the cathode, which could have led to beam halos [105]. Nonlinear effects related to the cathode material were excluded, as metallic cathodes have an instantaneous response, preventing the emergence of a longitudinal bunch tail, which was shown to have caused a significant beam halo in cERL [108]. Due to the high vacuum level and relatively low

bunch charge used at ARTI, Coulomb scattering in the beam or with a residual gas could also be ruled out [109]. The lack of explanation for the pronounced tail distribution observed at ARTI motivated the study of a potentially novel source of halos in photoinjectors.

#### 3.8.2.1 Observation of a different energy bunch at ARTI

The indication of the presence of a novel halo source came from the observation of a bump in the spectrometer beam profile under a specific RF phase range, shown in Fig. 3.30. This result was corroborated with a scan of the bunch charge against the spectrometer dipole current, where a similar bump was detected, as seen in Fig. 3.31. This indicated that a separate bunch, of different energy, was being generated following the main bunch.

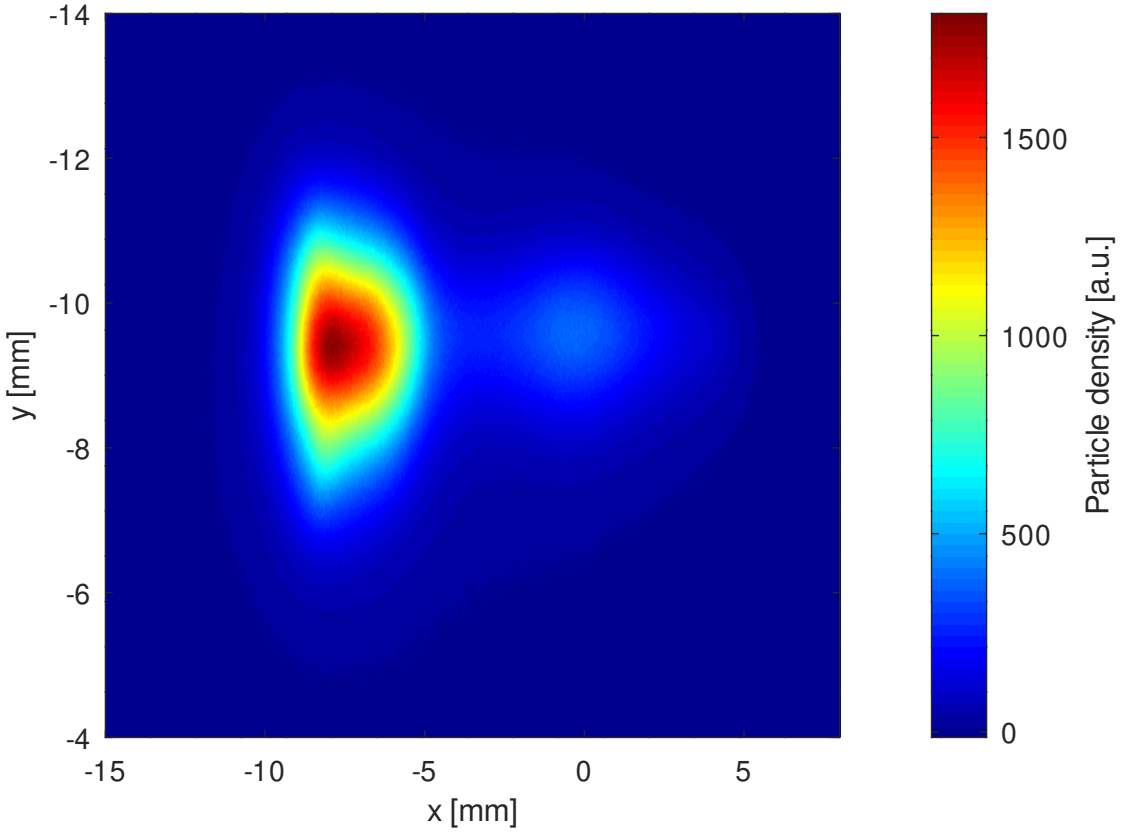



Figure 3.30: Two-dimensional beam profile taken from the ARTI dipole spectrometer, showcasing the separation of the core and halo bunches.

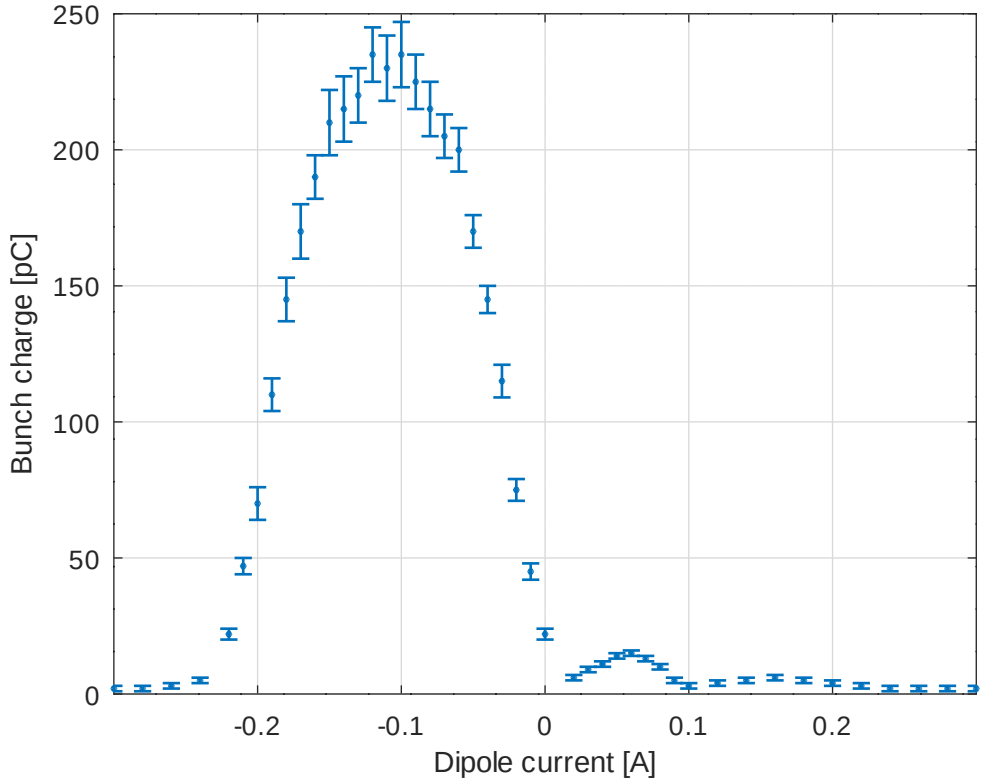



Figure 3.31: Measurement of the bunch charge versus the spectrometer dipole current. The dipole current is quoted in Ampere units. Besides the Gaussian distribution observed for the main electron bunch, there is an additional "bump" in charge observed for a dipole current in the range 0-0.1 A. The additional distribution would correspond to an additional bunch different in energy and charge to the main one.

Comparing Fig. 3.31 with the halo/core percentage calculated in the previous section, it seemed that the Faraday cup measurement underestimated the halo component by a large margin. However, the nonlinear trajectory of the electron bunch through the ARTI beamline, along with the presence of sectors with a low beam diameter, allowed for a significant reduction of the halo population at the location of the Faraday cup via direct interaction with the beam pipe walls.

The findings from the Faraday cup measurement were supplemented by those from the spectrometer diagnostics, i.e., the Chromox and digital camera installed at the end of the spectrometer line. As visible in Fig. 3.30, a distinct lower energy

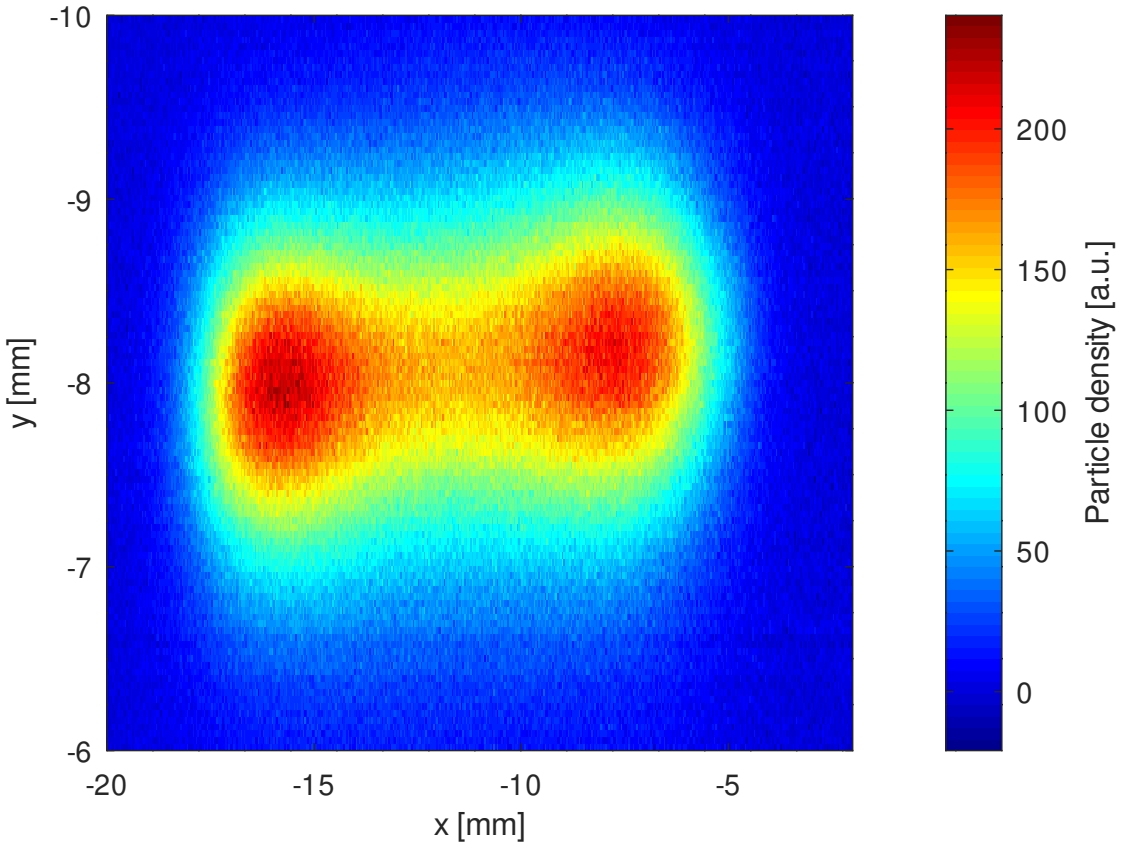



Figure 3.32: Spectrometer beam profile obtained for an RF-phase corresponding to an equal bunch charge for both the halo and core profiles.

bunch could be observed on the spectrometer line. The profile was not compatible with the typical tailed distributions produced under the dispersion generated by the dipole bend. The clear separation between the two bunches enabled a dedicated study of the properties of the two bunches. It was found that for the nominal RF phase, the charge of the secondary bunch was significantly smaller compared to that of the primary. Nevertheless, for very low RF phases, the two bunches could be brought to a similar charge, as shown in Fig. 3.32.

The distributions of the two bunches were fitted with two Gaussians, similarly to the analysis done with the YAG screen at the IP. The resulting plots are shown in Fig. 3.33. The two distributions were found to be Gaussian-like, and by integrating the two fits and dividing the integral to the one corresponding to the full data, a share percentage of 78.6% was obtained for the dominant bunch and 22.9% for

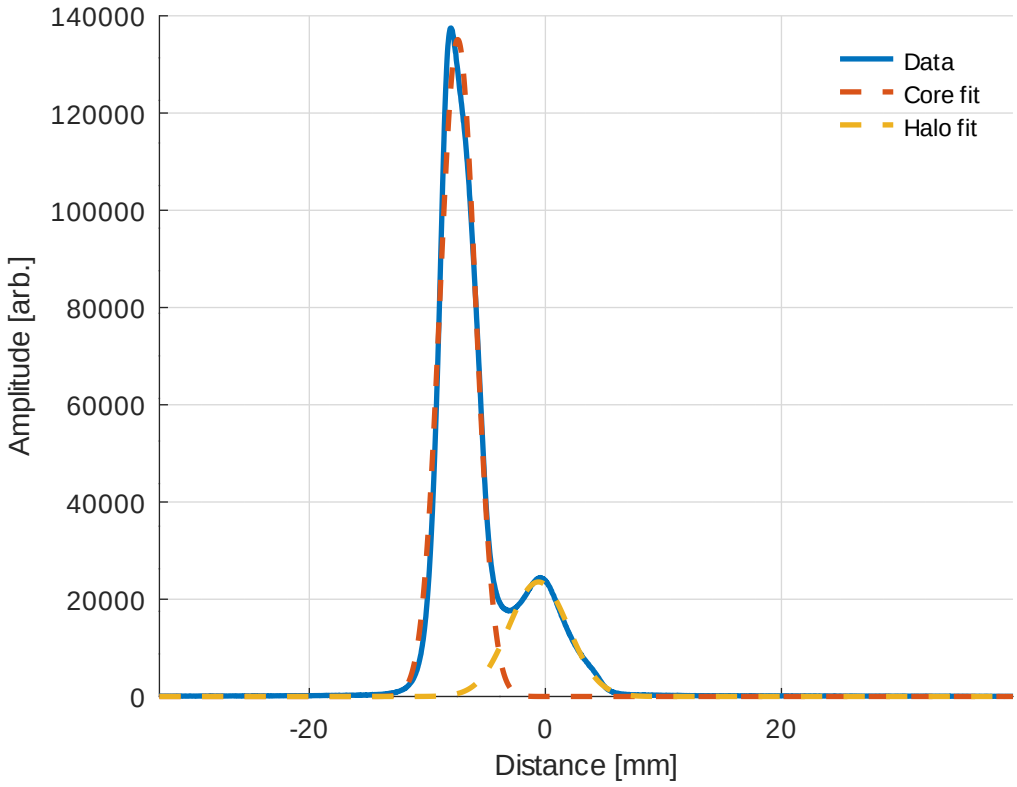



Figure 3.33: Gaussian fits of the beam core and halo from the horizontal distribution, measured using the dipole spectrometer.

the other, respectively. These findings corroborate previous core-halo percentage calculations done at the IP with the installed YAG screen. This indicated that the halo population was contained within the secondary bunch observed on the spectrometer.

These findings led to the proposal of a novel source of beam halos in photoinjectors.

#### 3.8.2.2 Photoinjector halo generation via ps-delayed laser pulses generating additional bunches in the same RF pulse

Photoinjectors are among the most common electron sources. They are based on the photoelectric effect enabled by the interaction of a laser pulse with a photocathode under vacuum. This mechanism enables the generation of high charge

and low emittance bunches, or even trains of bunches [110, 111]. Currently, commercially available lasers can be used to drive standard photoinjectors [112, 113]. Along the laser path, a series of optical elements (mirrors, lenses, waveplate, thin film polariser, etc.) are installed, guiding the beam and modifying its properties before reaching the cathode target. A schematic of the laser beamline for ARTI is shown in Fig. 2.11. Each of these optical elements has an associated thickness (in the case of mirrors, determined by the substrate). As the laser interacts with these elements, it undergoes both reflection and refraction, due to the difference in the index of refraction between the entry laser medium and the material of the optical element. Given large enough angles of incidence, the laser beam experiences total reflection. The angle of incidence $\theta_c$ that allows for total internal reflection from the entry medium of refractive index $n_1$ to the exit medium $n_2$ can be determined from Snell's law,

$$\theta_c = \arcsin \frac{n_2}{n_1}. \tag{3.6}$$

Provided the conditions for internal reflection are satisfied, the laser beam, instead of passing through the optical medium, is reflected within it. For angles close to the internal reflection one, the beam can become split, so that a majority of it is transmitted, while the other travels through the optical material. When the reflected laser reaches the medium boundary again, it splits again, one part being transmitted back to air, while the other remains inside the material. This internal reflection process is visualised in Fig. 3.34.

In practice, this mechanism leads to the generation of additional laser pulses of a smaller intensity, delayed by a few picoseconds to the main pulse. The exact value of the delay depends on the thickness of the optical material involved. This delay is small enough to be able to allow the insertion of two (or more) laser pulses within the same RF pulse provided by the S-band klystron of the electron gun. Given a high enough quantum efficiency of the photocathode and a significant enough secondary laser pulse energy, additional electron bunches can be generated in the same RF pulse. Because the RF pulse is non-uniform, the RF phase of each bunch is distinct. Again, the extent of the difference in RF phase experienced by the additional bunch is dependent on the time delay between it and the main pulse. The additional bunch will therefore be generated with a different energy

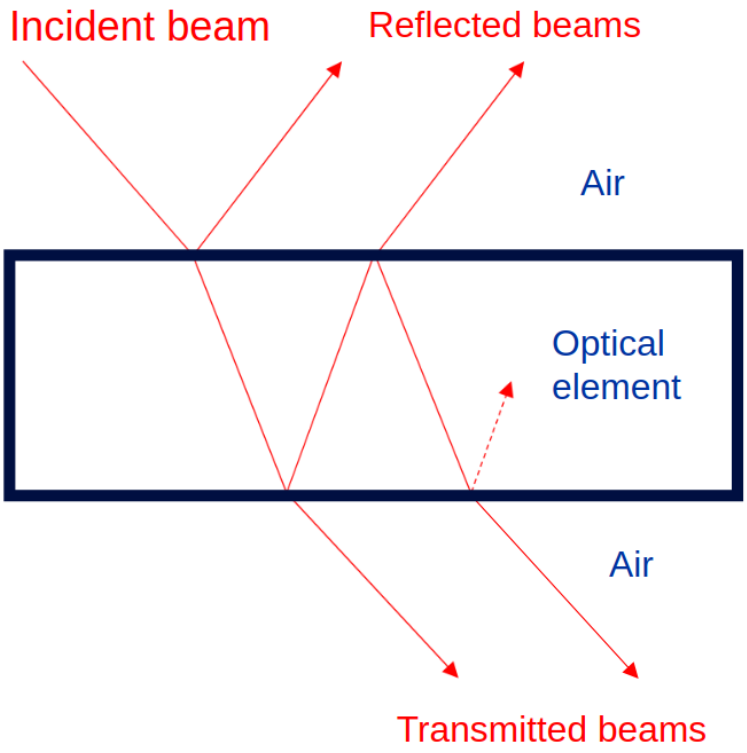



Figure 3.34: Schematic showing the generation of secondary time-delayed laser pulses through multiple reflection.

and chromatic variation in the solenoid focusing. The dipole-bended trajectory will also be different with respect to the main pulse.

The supposed mechanism presented would have a high degree of occurrence among photoinjectors, leading to the generation of intense halos that were not predicted by simulation. This novel halo source was able to explain the observations at ARTI and allowed for a detailed characterisation of the two bunches.

### 3.8.3 Characterisation of the novel halo source observed at ARTI

There are several methods to show that the beam halo is caused by a picosecond time-delayed laser pulse. Given the difference in energy between the halo and core bunches, the two would be displaced on a dipole spectrometer. Additionally, by tuning the focusing strength, a regime would exist where the beam core is tightly

focused, while the halo is visibly defocused. An RF phase scan of the electron gun can then be used to determine the difference in RF phase between the two bunches. This, in turn, would lead to the calculation of the difference in time between the two laser pulses and, therefore, the necessary thickness of the optical element. Once the optical element causing multiple reflections is identified, it can be removed from the beamline (or replaced with an alternative of a different thickness) to prevent halo formation.

#### 3.8.3.1 Experimental derivation of the time delay between the two laser pulses

The UV laser pulse, which was used to generate the core bunch, had a FWHM pulse length of 770 fs and an RMS spot size of $241 \times 308$ µm$^2$. The total pulse energy of the two pulses was measured as 15 µJ. Using the percentages derived from the Gaussian fits of the beam distribution, the primary pulse would have 11.16 µJ, while the secondary pulse, 3.84 µJ [77].

As shown in Fig. 3.33, the horizontal beam profile taken with the spectrometer camera presented two peaks, which were fitted to two separate Gaussian functions. An RF phase of $-17°$ relative to the on-crest was used to obtain the spectrometer profile. From the spectrometer calibration, a difference in energy between the two distribution peaks of 70 keV was measured [76]. The measurement was performed following a scan of the RF phase against the measured energy, shown in Fig. 3.35. This scan showed that the 70 keV difference in energy corresponded to a $13.2 \pm 0.1°$ difference in RF phase between the core and the halo bunches. From Fig. 3.35, it can be seen that due to the time delay and the difference in phase, the halo bunch would nominally have a higher energy than the core bunch. This corroborates with the spectrometer profile, Fig. 3.30, where the lower intensity halo bunch is shown to have had a lower bend, and therefore higher energy, with respect to the core bunch. It should also be noted that based on the RF phase scan curvature, it is possible to have configurations where the core bunch has a higher energy than the halo and even one specific case where the two bunches are equal in energy. A similar statement can be made with respect to an RF phase scan against the measured bunch charge, and indeed a configuration where the charge of the two bunches is equal was found, as seen in Fig. 3.32.

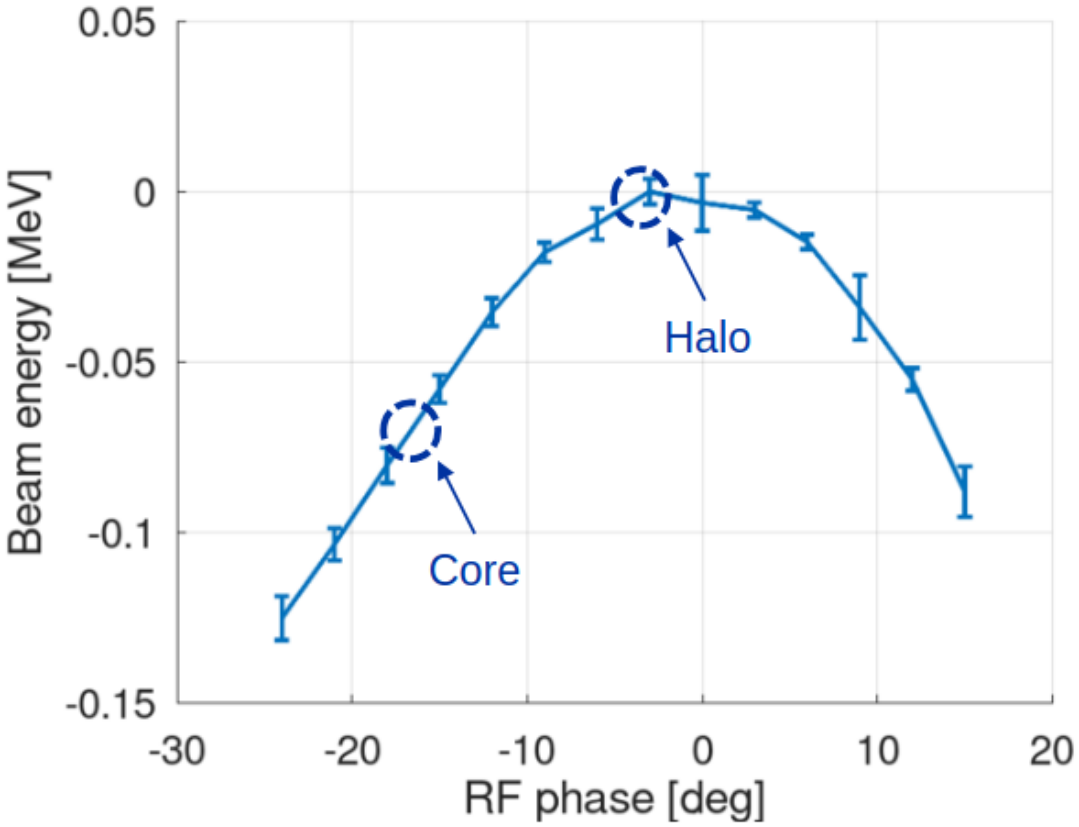



Figure 3.35: Normalised experimental RF phase scan showing the beam energy as a function of RF phase. The circled regions highlight the energy difference between the core and halo components of the bunch, illustrating their distinct phase-dependent energy response.

The difference in RF phase between the two bunches was used to calculate their time delay. The frequency of the ARTI electron gun is 3 GHz, which corresponds to a 0.9259 ps/deg conversion factor. Using the RF phase difference computed earlier, the time difference between the laser pulses that generate the core and the halo bunches was calculated to be $12.2 \pm 0.9$ ps. Given that the most likely substrate material for optical materials is fused silica, its refractive index was used to derive a predicted thickness of $2.43 \pm 0.30$ mm for the optic generating secondary laser pulses. Incidentally, this value corresponded to the 3 mm width of the thin film polariser installed on the beamline as part of the laser attenuator.

The polariser causing the secondary laser pulse could not be removed, as the

laser energy in the absence of an attenuator would have been high enough to cause ablation to the cathode surface. The quoted width is standardised, so there were also no alternative filters readily available to replace the installed one.

Following the experimental campaign, a final benchmark was performed in order to show that a secondary laser pulse was indeed causing the experimentally-observed halo. This entailed a matching of the RF-Track simulation with the measurements made at ARTI.

### 3.8.4 RF-Track reconstruction of the measured beam profile

With a clearer understanding of the potential cause for the beam halo, the core and halo bunches were simulated using RF-Track. To this end, a reconstruction of the beam profile measured using the OTR screen in Fig. 3.29 was sought. In order to achieve this, the bunch population and the difference in energy between the two bunches was used.

The two bunches were simulated in RF-Track using Gaussian transverse and longitudinal profiles corresponding to the measured UV pulse properties at the cathode. The initial beam conditions are summarised in Table 3.8. Using the measured solenoid strength from ARTI and the energy difference calculated from the phase scan, both the core and halo bunches were then tracked under space-charge effects to the screen position. Nominal parameters were used, measured during the halo source study, and the measured beamline element misalignments were included in RF-Track. The bunch charge was split according to the population distribution observed on the spectrometer camera, as it provided a clear distinction between the two bunches.

The RF-Track simulations showed that despite the minimal change in beam energy due to the RF phase, the difference in output beam profiles was significant. As seen in Fig. 3.36a, the halo bunch was shaped into a uniform distribution at the interaction point. This was a curious find, as the expected beam profile would have been expected to resemble a Gaussian for both the core and halo profiles. By comparison, the profile corresponding to the core bunch was distinctly Gaussian.

Table 3.8: Initial Beam Conditions Used as RF-Track Input for the Novel Halo Source Study

| **Parameter** | **Unit** | **Value** |
|---|---|---|
| RF phase (Core/Halo) | deg | –17 / –4 |
| RF gradient | MV/m | 112.5 |
| Solenoid field | T | 0.321 |
| Laser RMS spot (X/Y) | µm | 212 / 269 |
| Laser RMS pulse length | fs | 327 |
| Bunch charge | pC | 400 |

The profile also contained a non-negligible long tail, corresponding to a space-charge-generated halo. The core profile is visibly smaller in size compared to the halo bunch. To reproduce the beam at the OTR, the camera setup conditions were replicated. That is, given the large exposure time of 0.5 s, the two beam profiles would blend from the camera's perspective. Therefore, to match the real conditions, the two distributions were summarised. The resulting beam profile, shown in Fig. 3.36c, accurately matched the one measured on the OTR. The combination of the halo's uniform profile and the core's Gaussian profile resulted in a long-tailed $q$-Gaussian distribution with a high-amplitude halo.

### 3.8.5 Halo mitigation strategies

As previously stated, the novel halo source observed at ARTI would be a common occurrence in electron photoinjectors. Nevertheless, there are mitigative procedures that can be employed. Namely, the generation of secondary laser pulses through internal reflections in an optical material can be prevented by: minimising the number of optical elements used for the laser beamline, placing the emission laser as close as possible to the photoinjector, using optical materials with ultra-thin substrates, or with anti-reflective coatings (which increase throughput and reduce back-reflections). The latter additions imply an increase in material expenditure. The mitigation measures can also be applied after the beamline is already operational. Using the diagnostics previously described, the optical material that causes the secondary laser pulse can then be identified and replaced.

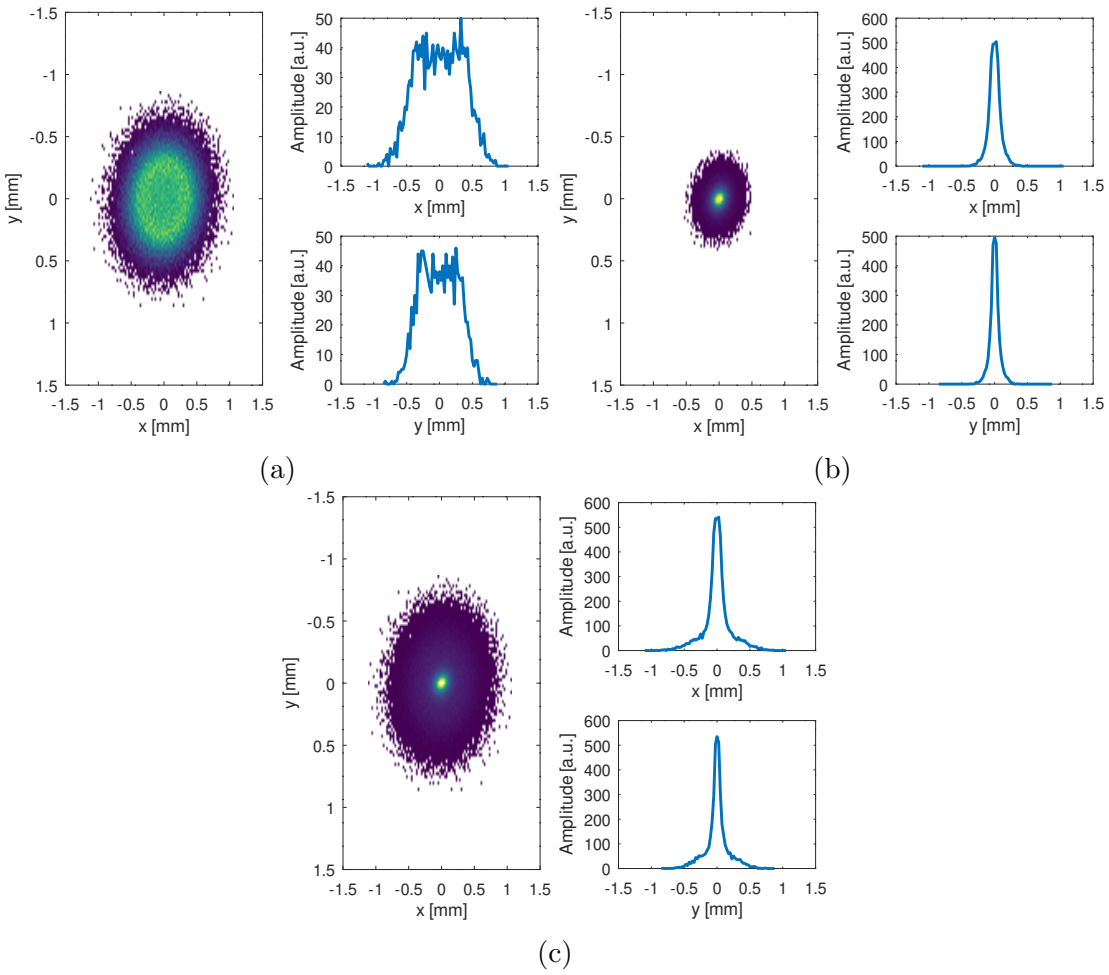



Figure 3.36: Beam profiles generated with RF-Track, showing the halo (a), core (b), and reconstructed beam profile (c). For each plot, the 2D beam profile is shown on the left, while the right contains the horizontal (top) and vertical (bottom) projections, respectively.

## 3.9 Conclusions from the optimisation of the ARTI beamline

This chapter presented the optimisation of the ARTI beamline for the Compton backscattering experiment. To achieve this, a start-to-end model of the injector was developed in RF-Track, enabling the generation, transport, and interaction of the electron bunch to be simulated within a single framework.

To set-up the RF-Track model of ARTI, the field maps of the electron gun and

solenoid were used as input. The goals of the optimisation were the maximisation of the scattered photon flux and the minimisation of background. In practice, the first implied the delivery of a high density electron bunch at the IP comparable in size to the profile of the interaction laser at the IP, while the second imposed a maximum threshold for the electron beam envelope across the length of the beamline, to avoid the collision with the beam pipe walls, which would generate secondary radiation.

The RF-Track optimisation of the beamline defined target parameters for the laser on the cathode, electron gun, and solenoid. An interesting feature of the optimised bunch was that its transverse profile at the IP resembled a $q$-Gaussian distribution, which allowed for the highest density profile at the IP under space charge effects.

Experimentally, the optimisation was supported by a beam-based alignment campaign. The UV laser position on the cathode and the transverse position of the solenoid were aligned with respect to the gun axis through dedicated RF phase and solenoid field scans. The measured corrections were consistent with offsets predicted by the RF-Track model and led to a substantial reduction in the electron beam size at the interaction point.

Following alignment, systematic scans of the RF phase, solenoid field, and laser spot size on the cathode were performed to identify the operating conditions that minimised the beam size at the interaction point. The measurements confirmed the trends predicted by simulation and demonstrated that the smallest beam sizes were obtained for relatively small laser spot sizes and RF phases.

Finally, the optimised beam was found to exhibit a pronounced halo containing approximately 25% of the bunch charge. Through a combination of experimental measurements and simulations, this halo was attributed to secondary laser pulses generated by multiple reflections within the optical transport system. The resulting secondary electron bunches acquired different energies during acceleration and subsequently formed a halo through chromatic effects during beam transport.

The next chapter describes the Compton backscattering experiment performed at the ARTI beamline. The optimisation of the electron beam presented in this chapter enabled the delivery of a sufficiently high signal-to-noise ratio for the successful observation of the CBS signal.

# Chapter 4

# A Soft X-ray CBS Experiment at CTF2

The optimisation of the ARTI electron beamline culminated in the implementation of a Compton backscattering experiment for the generation of soft X-rays in the water window. To this end, a dedicated laser beamline was constructed to deliver the laser pulse to the interaction point, and a vacuum chamber equipped with a microchannel plate detector for the detection of the scattered X-rays was integrated into the beamline. Following the commissioning of the modified beamline, a detailed spatial and temporal alignment of the electron and laser beams was carried out in order to maximise the yield of Compton backscattered photons. The detection and optimisation of the resulting X-ray beam were subsequently completed through a full characterisation of the CBS signal and a quantitative comparison with predictions from the RF-Track model of the beamline.

## 4.1 The Electromagnetic Water Window

The water window represents a region of the electromagnetic spectrum, defined for the photon energies between 282 eV and 533 eV, where the water is transparent, while carbon and its organic compounds is opaque. This allows for high-resolution imaging of live hydrated samples [114]. Developments in water window imaging have led to 3D soft X-ray microscopy of cryo-fixed cells, providing 3D images of nearly intact cells in their natural environment and the classification of different intracellular structures (i.e., nuclei, mitochondria, vacuoles) [115–118]. Examples

of images taken using water window imaging with a laboratory source are shown in Fig. 4.1.

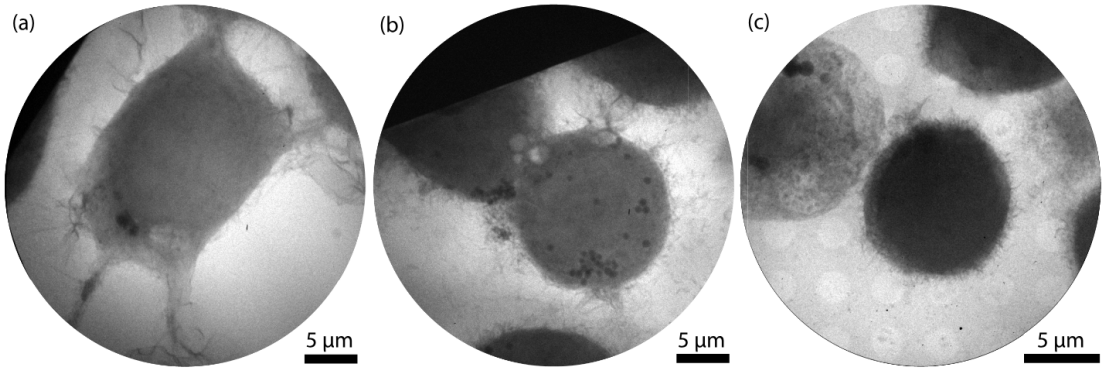



Figure 4.1: Samples of 2D cryo imaging performed with a laboratory water window X-ray source. Taken from [72].

Most water window imaging is performed at large-scale synchtrotrons or FELs. Amplified by an increased demand from biologists, limited beamtime availability in light source facilities has contributed to an overall push towards laboratory soft X-ray sources. Other advantages of such laboratory sources include: easier integration with other laboratory analysis instruments, a more cost-effective and feasible pathway to biological research, and the possibility of conducting longer-running scans of the biological sample. Emerging technologies and growing interest have encouraged the development of table-top soft X-ray sources in the water window [72]. Among the current types of laboratory sources considered for water window imaging include: discharge [119, 120], laser-plasma [121, 122], electron-impact [123], coherent (such as high harmonic generation [124, 125], plasma-based X-ray lasers [126, 127], or betatron radiation through laser-wakefield acceleration [128]), and Compton backscattering [129]. The feasibility of using CBS sources for water window imaging is currently being investigated. Due to their increased energy tunability and small footprint, CBS sources can be used as a driver for table-top water window microscopes.

## 4.2 X-ray detector set-up

As part of the CBS experiment, a detector capable of measuring the X-rays generated in the laser-electron collision was required. Since such a diagnostic was not present as part of the initial design of ARTI, a suitable vacuum chamber was required to be designed, installed, and commissioned as part of the experiment.

The location and already existing equipment of ARTI imposed a series of constraints on the detector used to count the scattered CBS photons. The decision on the most suitable X-ray detector was made according to several factors:

1. **Vacuum compatibility**. As seen in Fig. 4.2, the 200 eV soft X-rays generated by CBS would be fully absorbed once in air. The X-rays therefore needed to be detected under vacuum, a challenging medium for detectors. Coincidentally, having the detector under vacuum also allowed it to be closer to the IP, increasing the number of detectable X-ray photons.
2. **Size**. Given the placement in the beamline vacuum, the detector needed to be small enough to fit in a diameter approximate to the beampipe's 30 mm. However, the detector active area needed to be large enough to detect as much of the outgoing X-ray cone as possible. Additionally, since the beam dump consisted of the Faraday cup, the detector needs to be light enough to be able to be lifted if one wants to clear the path for the electron beam and measure the bunch charge.
3. **Rise time**. The X-ray signal was expected to have an RMS pulse length of 2 ps. To avoid background detection, a gated or otherwise low rise time would be beneficial for the detector.
4. **Detection efficiency**. Given the high absorption rate of soft X-rays, and the small number of them generated in the experiment, a reasonably high detection efficiency was required from the detector.
5. **Gain**. Given the low number of X-rays expected to be detected, a sufficiently high gain would be required to ensure the outgoing signal is detectable. The gain provided should also be adjustable.
6. **Availability**. Given that the focus of the thesis was to benchmark CBS measurements to simulations and not develop a new detection method for soft X-rays, a commercially available detector was sought.

7. **Dark current**. A systematic and permanent source of background, the dark current represents a parasitic signal created by the detector itself. Its minimisation is desired for the CBS experiment.
8. **Output linearity**. A detector with a high saturation threshold would be desired, along with a linear response to the number of detected particles.

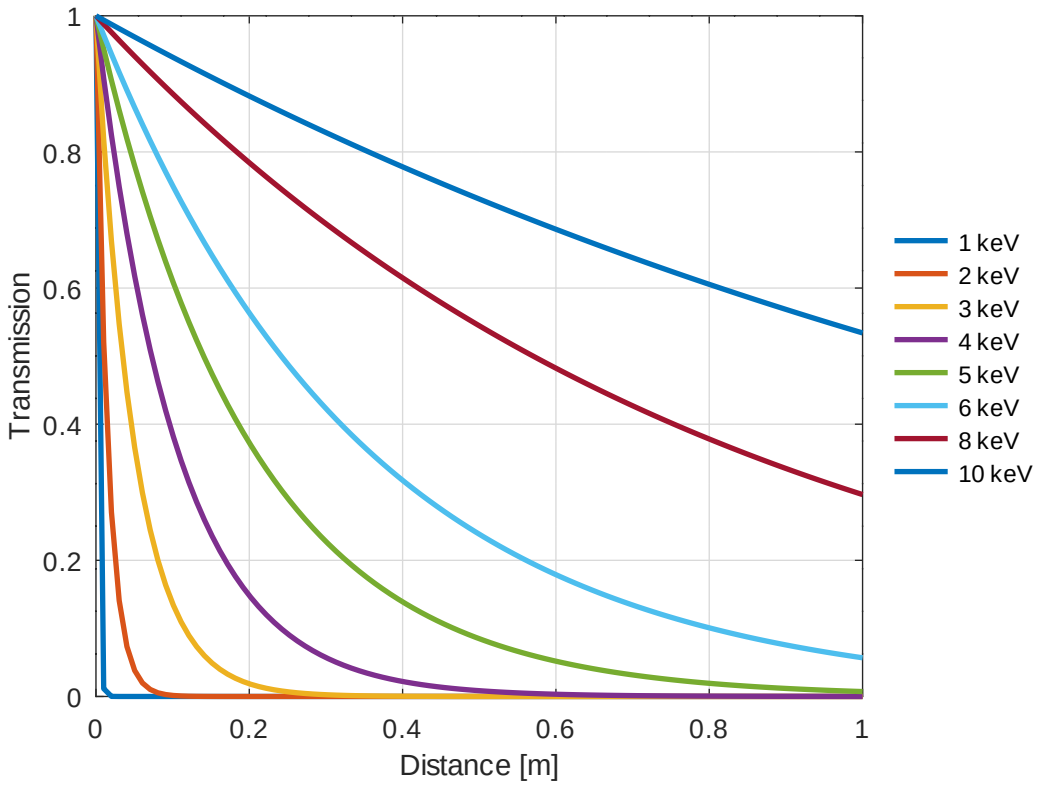
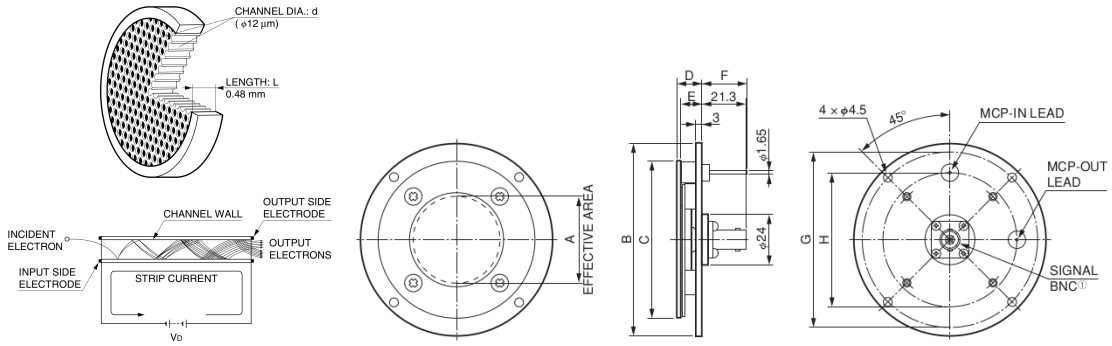



Figure 4.2: Calculated X-ray transmission in air as a function of propagation distance for photon energies between 1 and 10 keV. The horizontal axis shows the distance travelled in air, while the vertical axis represents the transmitted fraction of the initial intensity. For photon energies below 1 keV, such as the 200 eV X-rays generated in the CBS experiment, the attenuation length in air is on the order of millimetres, resulting in nearly complete absorption over very short distances.

### 4.2.1 The microchannel plate

Given all the requirements, a Hamamatsu microchannel plate model F9890-13 was chosen for the experiment. A schematic of the MCP model is shown in Fig. 4.3b. The basic structure of an MCP is shown in Fig. 4.3a. MCPs consist of a two-dimensional array of microscopic glass capillaries, referred to as channels, arranged in a disc-shaped structure. Each channel acts as an independent electron multiplier, effectively functioning as a miniature photomultiplier tube. When an incident photon strikes the wall of a channel, a photoelectron may be emitted and accelerated along the channel by the electric field generated by the voltage applied across the MCP. To increase the probability of interaction between the electrons and the channel walls, the channels are inclined with respect to the surface normal by a bias angle, typically between 5° and 15°. As the electron travels through the channel, repeated collisions with the walls produce secondary electrons, resulting in an avalanche multiplication process. The amplified electron cloud exits the channel and is collected at the anode. In the Hamamatsu F9890-13 detector, the output from all channels is summed onto a single anode and extracted through an SMA connector. The resulting signal is transmitted via an SMA vacuum feedthrough to a 2 GHz oscilloscope, where waveforms such as that shown in Fig. 4.4 are recorded. The oscilloscope is triggered using the laser input signal, which provides a stable and reproducible timing reference.




(a) (b)

Figure 4.3: Structure and operating principle of an MCP (a) and a schematic of the MCP used for the CBS experiment, model F9890-13 (b). (credit: Hamamatsu)

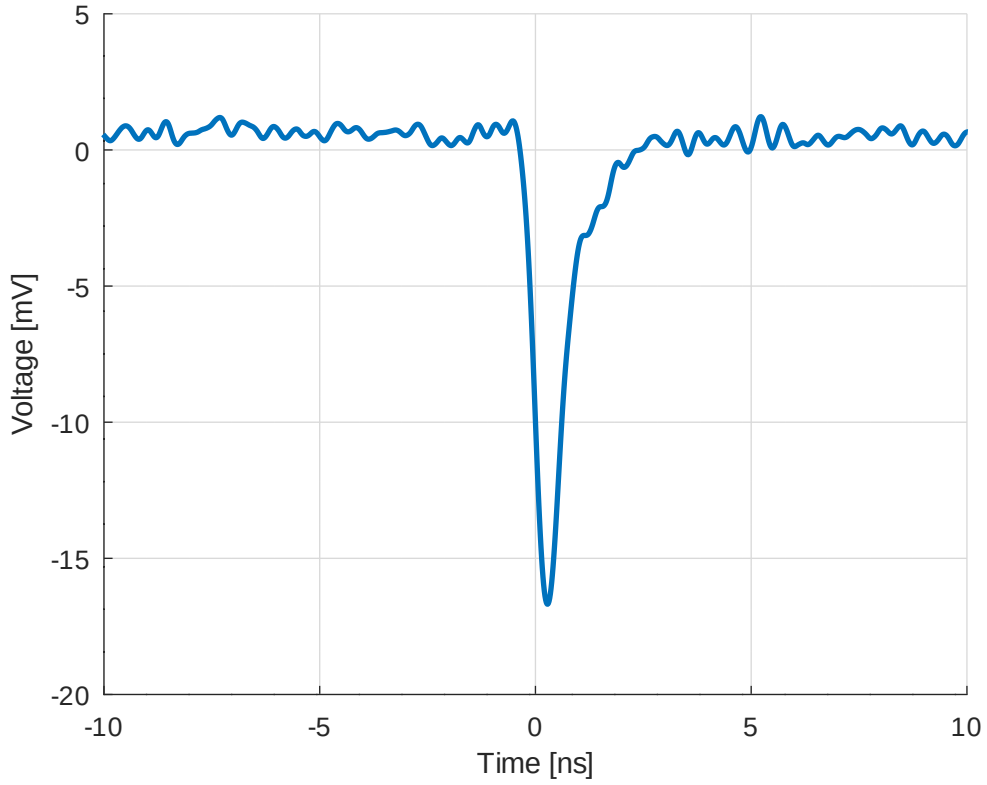
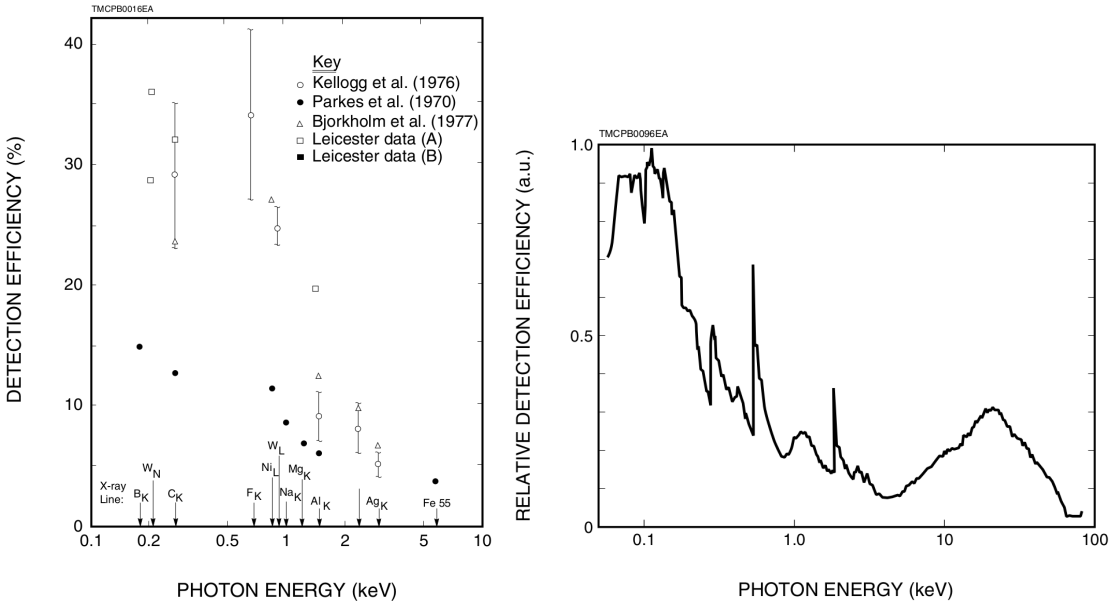



Figure 4.4: Measured voltage waveform from the microchannel plate detector corresponding to a single X-ray event. The horizontal axis shows the time relative to the trigger in nanoseconds, while the vertical axis represents the measured voltage in millivolts. The pulse has a full width at half maximum of approximately 900 ps.

The MCP model used could only operate under a vacuum of $1.3 \times 10^{-4}$ Pa [130]. Weighing just 200 g and with a total diameter of 72 mm, the detector was easily able to fit into the detection chamber and be manipulated vertically. Its time response is determined by the channel length, which for a two-stage assembly is typically 0.5 mm. This translates into a pulse width of 900 ps FWHM, as observed in Fig. 4.4. The detection efficiency is proportional to the open area ratio (the ratio of the combined hole areas to the disc area), the angle of incidence, and whether the MCP surface is coated. The open area ratio for the MCP used in the CBS experiment is 0.6. Note that there have been newer channel designs implemented for MCPs, shaped to form a funnel, which increased the open area ratio from 0.6




(a) (b)

Figure 4.5: Measured absolute (a) and relative (b) X-ray detection efficiency for a microchannel plate, versus the incident photon energy. The MCP configuration used for the CBS experiment corresponded to the one used for the Parkes et al. study from 1970. (credit: Hamamatsu)

to 0.9.

The model used has a reasonable detection efficiency of Carbon K-line photons of 12.5%, from Fig. 4.5a. Note that the Carbon K-line is 277 eV, which corresponds to the 267 eV photon energy generated by the CBS experiment. The MCP's X-ray detection efficiency varies considerably with the photon energy, as seen in Fig. 4.5b. The detection efficiency of X-rays can be significantly increased by coating the surface with photoelectric materials such as CsI. However, this coating requires careful handling and minimal exposure to air. An advantage for the detection efficiency is that the MCP is invisible to IR and has a value for UV photons of less than 1‰, which ensured that the laser itself would be a minimal contributor to background. The detection efficiency of 5 MeV electrons from the gun is non-negligible, which required the use of the dipole spectrometer to deflect the electron beam away from the MCP. The synchrotron photons subsequently emitted from the dipole bend would reach a maximum energy equivalent to IR, making them

invisible to the MCP.

The gain of the MCP is tunable, up to $10^7$. The approximate gain is obtained from

$$g = \exp(G \cdot \alpha), \tag{4.1}$$

where $G$ is the gain factor, determined by the secondary emission characteristics of the channel wall, and $\alpha$ is the length-to-diameter ratio of the channel. The gain is obtained by applying a high voltage difference between the open channel ends, which also makes it highly tunable. Gain curves were measured for a range of input voltages. Since $g$ also depends on the length of the MCP assembly, the overall gain can be increased by stacking multiple MCPs in a chevron shape, allowing for good electron transport. The model used for the CBS experiment was a two-stage MCP.

The dark current in MCPs originates from electric field emission from the channel walls, ionisation of residual gas, local high E-field discharges, and photoelectron emission from E-field scintillation in the MCP components. Nevertheless, MCPs exhibit a very low dark current compared to other signal intensifiers, such as silicon-based photomultipliers. For model F9890-13, the maximum dark count is $3\,\mathrm{s^{-1}\,cm^{-2}}$, under a supply voltage of 1 kV per MCP, a vacuum pressure of $1.3 \times 10^{-4}$ Pa, and an operating temperature of 25 °C.

Lastly, the MCP has a relatively high dynamic range. If a large output current is extracted from the MCP, its channel walls are charged by a large amount of secondary electrons. This leads to a weakening of the electric field intensity, which suppresses electron multiplication. The charging effect is neutralised by the strip current of the channel walls. The decrease in gain defines the saturation effect and usually occurs when the output current reaches 5% to 6% of the strip current. Due to low background and signal events, this effect was not reproduced during the CBS experiment.

Another relevant aspect of the MCP is its electrical circuitry. An example of wiring from the supplier's technical documentation, shown in Fig. 4.6, was reproduced for the ARTI installation. One difference from the figure was the SMA signal output used (instead of BNC), which allowed for a higher-frequency signal transmission. To transmit the output signal, an in-vacuum kapton cable with SMA endings was used to connect the MCP to the vacuum chamber's SMA feedthrough.

In-air, an ultra-low-loss cable was used to transport the signal from the vacuum feedthrough to the oscilloscope, installed in the laser room above the experimental hall. Due to the use of a low-loss cable of around 10 m, the signal was strong enough to not require an amplifier. The power supply used to drive the MCP was an ISEG SHR 4260, a Switchable High Precision AC/DC Desktop High Voltage Power Supply. The power supply did not offer the option for floating operation. Therefore, a divider circuit was created that split the signal from the HV power supply into an 80% and 20% component using an ensemble of parallel resistors. For example, if one supplied 2.5 kV, 2 kV would reach the MCP-In HV connector, while 0.5 kV would reach the MCP-Out connector.

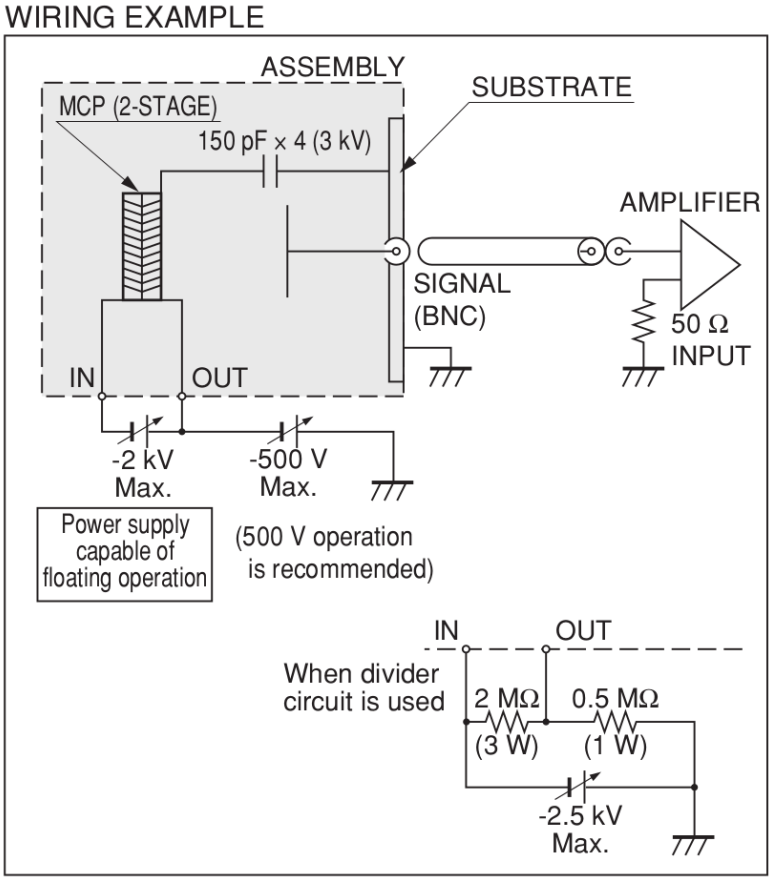



Figure 4.6: Wiring example of the MCP, that was used during its operation at ARTI. (credit: Hamamatsu)

### 4.2.2 The vacuum detection chamber

In order to allow for the in-vacuum operation of the microchannel plate, a custom-made detection chamber was commissioned and installed at ARTI. A photo and CAD drawing of the chamber are shown in Fig. 4.7. The detection chamber consists of a CF cube of 100 mm nominal diameter (ND 100), a CF straight connector of ND 100, two high voltage vacuum feedthroughs, one double-sided SMA vacuum feedthrough, and a linear drive. The CF cube houses the MCP in a compact volume and is connected directly to the rest of the beamline through two zero length reducer flanges. The CF straight connector allowed enough space to vertically manipulate the MCP. The high voltage feedthroughs were used to interface the MCP lead pins to a power supply located in the lab upstairs. Up to −2.5 kV have been applied to the MCP, and nominally −1.9 kV. The linear drive is motorised, has micrometre-level step size, and an excellent repeatability, thanks to the implementation of an optical encoder. All connectors are attached to a standardised feedthrough flange with four ports. To connect the MCP to the feedthrough flange, two kapton high voltage compatible cables were used due to their low outgassing.

### 4.2.3 Measurement of the MCP's electrical continuity

An initial step in the commissioning of the MCP detector for the experiment was determining its electrical continuity, along with its internal resistance. The reference resistance value provided by the supplier is between 13.4 MΩ and 66.6 MΩ [131]. After reaching the target vacuum level, the MCP-In feedthrough was wired to the high voltage power supply. An ammeter was then connected to the MCP-Out feedthrough and ground (i.e., the vacuum chamber casing) to measure the MCP's resistance. The power supply voltage was subsequently increased from 100 V to 500 V in steps of 100 V. The resulting strip current flowing through the MCP was recorded by the ammeter.

The data obtained from the electrical continuity test is shown in Fig. 4.8. An excellent linear response was obtained for the change in strip current versus the input voltage.

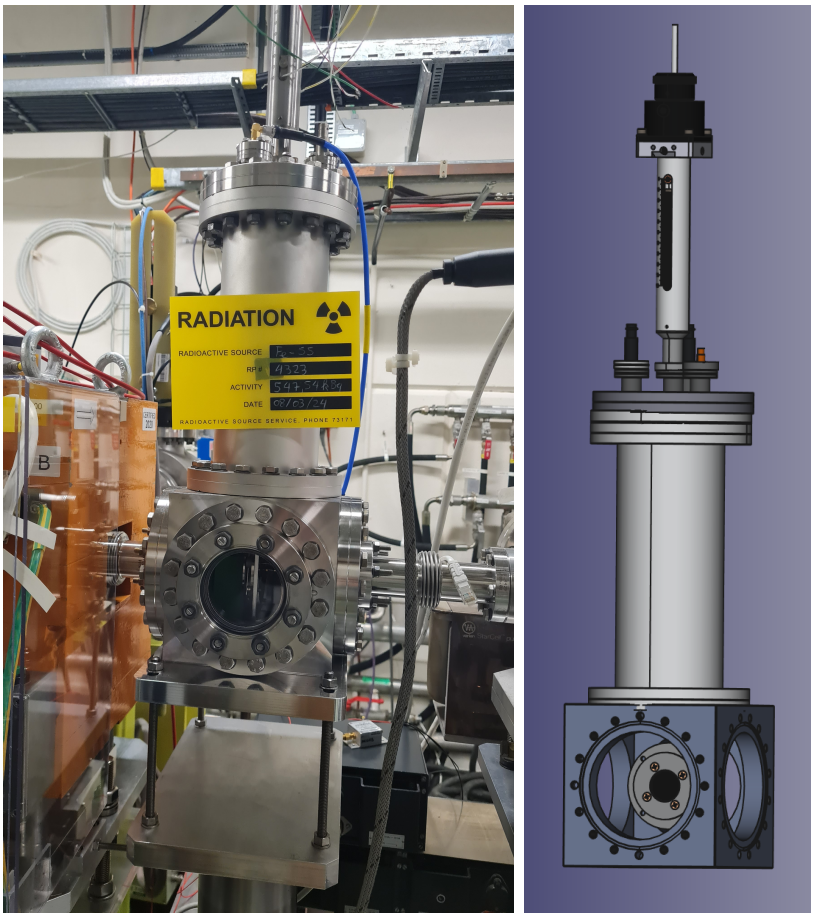



Figure 4.7: The integrated vacuum chamber housing the microchannel plate detector (left), and a CAD sketch of the detection chamber (right).

The strip current, $I_s$, passing through the MCP is given by

$$I_s = \frac{V}{R_1 + R_2}, \tag{4.2}$$

where $V$ is the input voltage provided by the power supply, and $R_1$ and $R_2$ are the resistances of the MCPs stacked in the assembly used for ARTI. The electrical continuity measurement was used to measure the total resistance. The difference in resistance between the two MCPs is between 10%. From the linear fit and using Ohm's law, a total resistance of $52.10 \pm 0.27\,\mathrm{M\Omega}$ was obtained, which corresponded to the given range provided by the manufacturer, $13.4\,\mathrm{M\Omega}$ to $66.6\,\mathrm{M\Omega}$.

The electrical continuity test showed that the MCP response was linear and that no damage was done to the MCP prior to its installation at ARTI.

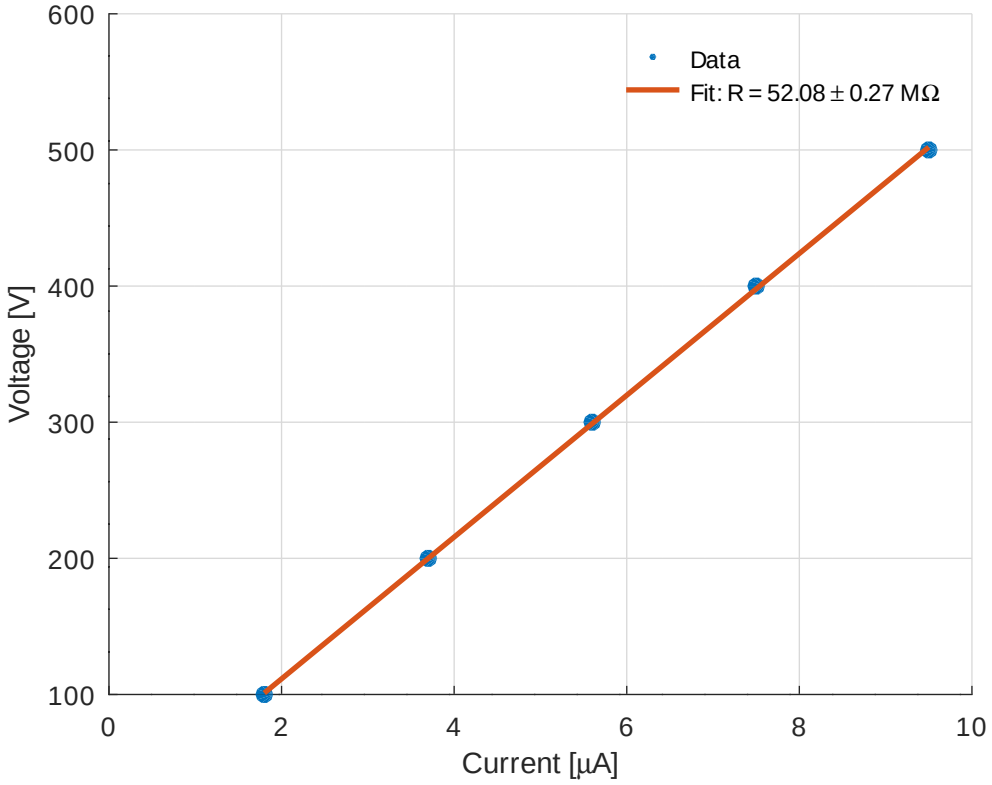



Figure 4.8: Measurement of the linearity response of the MCP used for the CBS experiment. The input MCP voltage is plotted as a function of the induced strip current. The linear fit of the data was used to derive the MCP internal resistance of $52.08 \pm 0.27\,\mathrm{M\Omega}$.

### 4.2.4 Detector calibration

Following its electrical continuity check, the MCP detector was calibrated using an Iron-55 (Fe-55) radioactive source. Fe-55 is an isotope that decays via electron capture, emitting manganese K-shell X-rays with an energy of approximately 6 keV. The source has an emission probability of 24.4% and a half-life of 2.737 years [132]. This radiation source was selected because of its compact size, vacuum compatibility, monoenergetic emission, and the proximity of its X-ray energy to that expected from the CBS photons. Furthermore, comparison of the measured detector response with the manufacturer's specifications at 6 keV provided a validation of the quoted MCP efficiency, increasing confidence in the use of the

manufacturer's efficiency data at the lower photon energies relevant to the CBS experiment.

A schematic of the capsule housing the radioactive source is shown in Fig. 4.9. The active spot (i.e., the radioactive source) was electrochemically deposited onto a copper plate and sealed in a welded monel capsule. On top of the source, a brazed beryllium window was placed, through which the radiation is emitted. The relevant dimensions of the capsule include: the outer diameter of $7.925 \pm 0.025$ mm, the window diameter of $4.0 \pm 0.1$ mm, and the capsule height of $5.0 \pm 0.2$ mm, with the uncertainties as specified by the manufacturer.

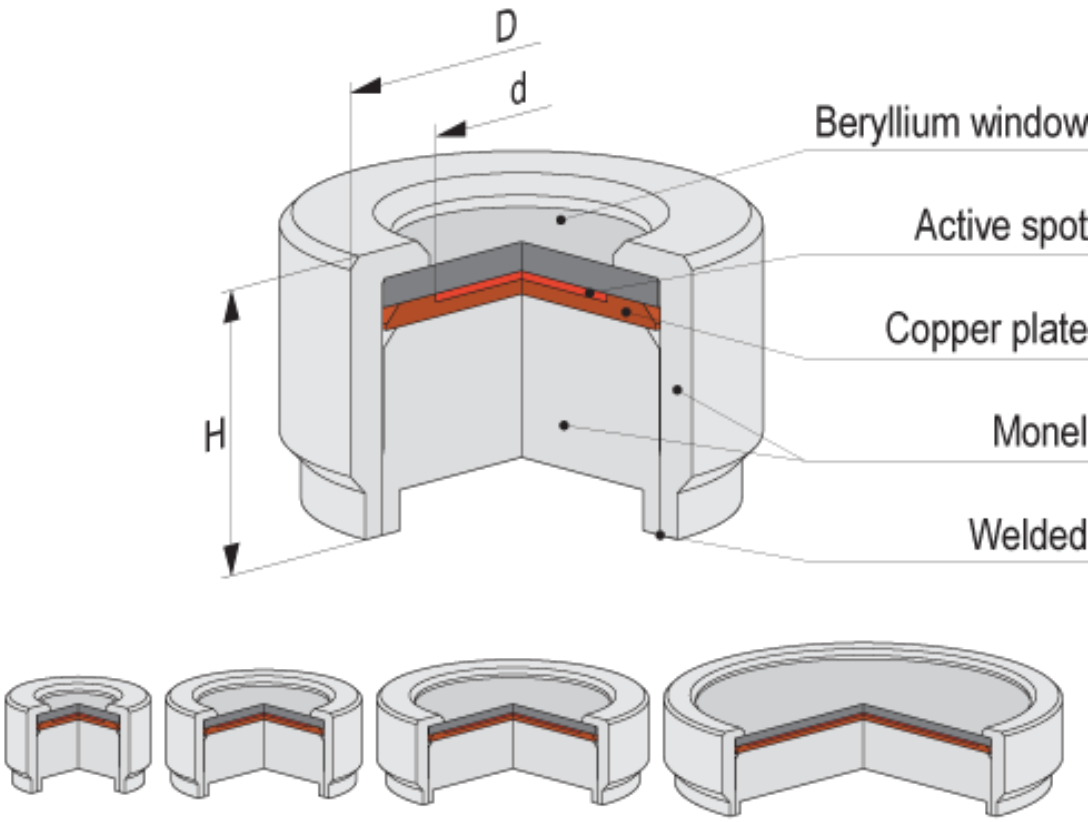



Figure 4.9: Schematic of the Fe-55 radioactive source used in the MCP calibration experiment. The source was electrochemically deposited on a copper plate and sealed in a welded monel metal capsule with a brazed beryllium window. The outer diameter $D$ is $7.925 \pm 0.025$ mm, the window diameter $d$ is $4.0 \pm 0.1$ mm, and the capsule height $H$ is $5.0 \pm 0.2$ mm.

There were two main goals to the calibration of the MCP detector: a measurement of the detector efficiency and gain response. In order to achieve this, a holder for the radioactive source suitable for vacuum operation was needed. Using available equipment from CERN, the holder was 3D printed along with a screw-in mask to secure the radioactive source in place while still leaving an open space for its active area. A photo of the holder with the source inserted is shown in Fig. 4.10. There were some concerns initially related to the out-gassing of the plastic material (polylactic acid) used for the source holder. Fortunately, given the low requirement for vacuum operation of the MCP of $1.3 \times 10^{-6}$ mbar, the holder was deemed suitable.

The radioactive source holder was placed right in front of the MCP assembly to simplify the estimates for the number of incident photons on the MCP's active area.

#### 4.2.4.1 Measurement of the MCP's detection efficiency

The quantum efficiency of the MCP detector is determined by its material component, glass. Damage to the MCP's surface can lead to a non-uniformity of the QE distribution. To ensure an accurate measurement of the CBS photons, a QE measurement of the MCP was performed.

With the oscilloscope already connected to the MCP, the device was also used to count the number of detected particles. Ideally, a frequency counter would have been used to accurately measure the number of counts; however, such a device was not available during the experiment. An example of a typical oscilloscope trace showing particle events is shown in Fig. 4.11. An in-built detection algorithm was used to get the number of signal events per sweep.

The timing domain was increased to ±5 ms in order to capture as many events as possible in a single sweep. Based on the number of events recorded per sweep and knowing the time scale involved (10 ms), the number of photons detected per second was calculated. Twenty-five sweeps were recorded, from which the average number of events per second was determined, along with the measurement uncertainty. Given the MCP assembly used, a reference dark current value of $3\,s^{-1}\,cm^{-2}$ was used. Given the active diameter of 2.7 cm of the MCP, a dark current flux of $17.2\,s^{-1}$ was calculated. By subtracting the contribution from the




Figure 4.10: Photo of the 3D-printed holder for the Fe-55 radioactive source used to calibrate the MCP detector. The Fe-55 source is shown placed in the holder, with a mask screwed in to hold it in place.

dark current contribution, a measured photon flux of $395.30 \pm 42.16\,\mathrm{s}^{-1}$ was obtained ($42.16\,\mathrm{s}^{-1}$ is the standard deviation on the mean). The significant uncertainty in the measurement is explained by the measurement method used. If the timing sweeps had been extended to 1 s instead of 10 ms, a more precise evaluation of the number of counts recorded per second could have been obtained. This experimental

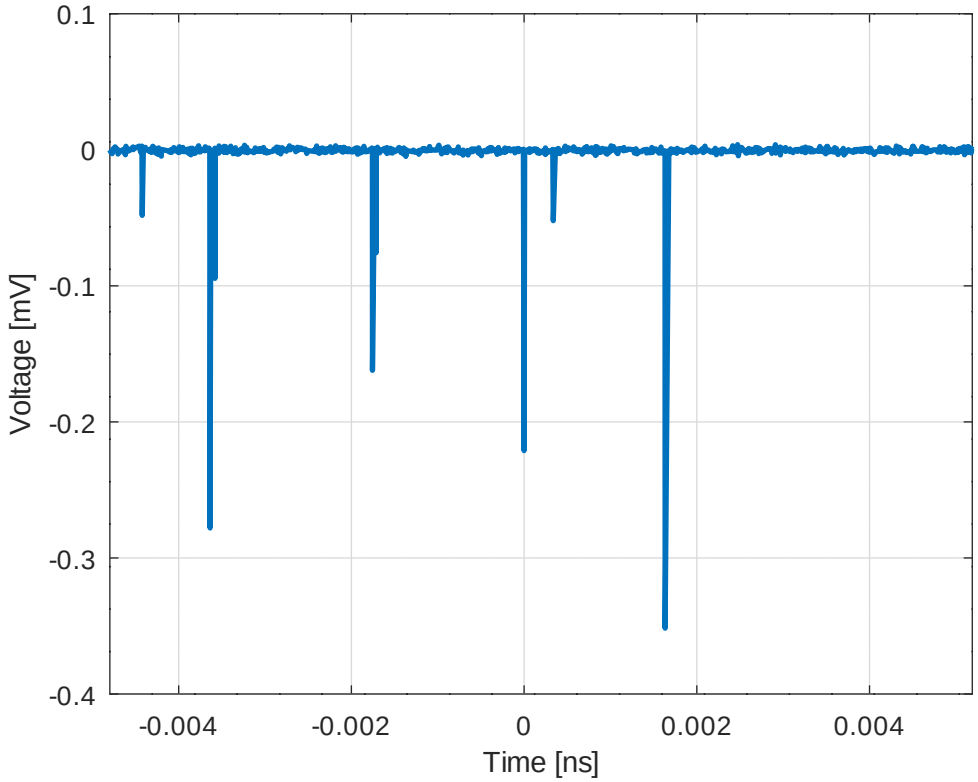



Figure 4.11: Example of a typical oscilloscope trace made during the measurement of the MCP's detection efficiency. The measured waveform voltage is plotted as a function of the time relative to the oscilloscope trigger.

result was compared with a theoretical one.

The theoretical detection efficiency of the MCP was selected from the literature displayed in Fig. 4.5a. Given that the Fe-55 source naturally radiates isotropically, considerations for the detection geometry needed to be taken. In particular, the limited emission area from one face of the cylinder housing the Fe-55 material, along with the steradian encompassing the volume of radiation reaching the MCP's active area. The expected photon flux $N_{\mathrm{exp,ph}}$ was calculated using the formula

$$N_{\mathrm{exp,ph}} = A \times (DE \times P_{\mathrm{emission}}) \times T_{\mathrm{Be}} \times R_{\mathrm{SD}}, \tag{4.3}$$

where $A$ is the source activity, $DE$ the X-ray detection efficiency at ≈5 keV, $P_{\mathrm{emission}}$ the X-ray emission probability, $T_{\mathrm{Be}}$ the transmission probability from Beryllium,

and $R_{\mathrm{SD}}$ the ratio of radiation impinging on the MCP over the radiation emitted over the total radiation emitted. The source activity was provided by the radioprotection (RP) unit at CERN, and was calculated to be $486.39 \times 10^3$ Bq given the source's half-life, activity at creation, and time passed since. Based on measurements from [133], shown in Fig. 4.5a, the detection efficiency of Fe-55 radiated photons is 4%. The X-ray emission probability is determined by the radioactive source type; for Fe-55, it is 0.2725. The transmission through the beryllium window for Fe-55 X-rays is $0.668285 \pm 0.000167$. Lastly, $R_{\mathrm{SD}}$ was calculated from

$$R_{\mathrm{SD}} = \frac{\Omega_D}{\Omega_S}, \tag{4.4}$$

where $\Omega_S = 4\pi$ accounts for the isotropically emitted radiation, and $\Omega_D = 2\pi(1 - \cos\theta_{\mathrm{max}})$ is the effective radiation volume reaching the MCP. The maximum angle that subtends the effective volume is determined from $\theta_{\mathrm{max}} = \arctan\frac{d}{2D_{\mathrm{MCP}}}$, where $D_{MCP}$ =2.5 mm is the distance from the source to the MCP.

Using all factors discussed previously, the expected measured flux was determined to be $388.19\,\mathrm{s}^{-1}$. Compared with the actual flux of $395.30 \pm 42.16\,\mathrm{s}^{-1}$, one can see that a good degree of correspondence was achieved. This provided confirmation on the use of the detection efficiency studies from Fig. 4.5a. The predicted detection efficiency of 12.5% was then attributed to the soft X-rays generated via CBS, and used for the subsequent analysis.

#### 4.2.4.2 Measurement of the gain response

During the calibration, single photon events were recorded, while for the CBS experiment, the incoming X-ray pulse was too short in longitudinal length to have allowed the MCP to discriminate between photons. For the oscilloscope, this translates into a signal trace encompassing a larger area, proportional to the number of photons present in the X-ray pulse. Knowing the area (or peak value) of a signal trace under a signal photon event, the number of photons in the X-ray pulse (that were detected by the MCP) can be deduced. However, the signal area also depends on the gain applied to the MCP. A study of the impact of the applied gain on the signal area and peak voltage was required to accurately determine the number of photons recorded by the MCP within a single pulse.

The gain response was measured by recording a number of signal events from the Fe-55 source for a range of gain settings of the MCP. From the recorded signals, the area and peak-to-peak voltage was determined, averaged, and fitted with respect to the amount of supply voltage (which determined the gain). Although not strictly necessary for the CBS experiment itself, the MCP gain value associated with a particular supply voltage was also determined. Note that the supply voltage represents the voltage provided by the HV power supply to the MCP, divided into the MCP-In and MCP-Out electrical feedthroughs.

The gain for a particular supply voltage was calculated from the area of the signal trace on the MCP, measured in pV s. Dividing it by the oscilloscope's 50 Ω resistance, the electric charge in pC was obtained. To find the gain, the signal charge was divided by the elementary charge, $1.602\,176\,63 \times 10^{-7}$ pC. For the MCP working range of 1600 V to 2700 V, gain values from $2 \times 10^5$ to $4 \times 10^7$ were obtained, as shown in Fig. 4.12. Although some form of gain degradation would have been expected given the continued use of the MCP, the gain values matched very well with those expected from a double-stack MCP [131]. The gain versus supply voltage plot follows an exponential fit.

The gain response of the MCP, characterised by the dependence of the signal area and peak-to-peak voltage on the MCP supply voltage, is shown in Fig. 4.13. The signal parameters were measured across the full operational voltage range of the MCP, from 1600 V to 2700 V, in increments of 50 V. At voltages below 1600 V, the signal amplitude was insufficient to be reliably distinguished from noise, while operation above 2700 V was avoided to prevent potential damage to the detector. The measured response exhibits an exponential dependence on the applied supply voltage, with the signal area and peak-to-peak voltage following nearly identical trends. As the measurements correspond to single-photon events, both quantities provide a suitable basis for estimating the number of X-ray photons produced in the Compton backscattering interaction. However, owing to its simpler extraction and reduced sensitivity to outliers compared with the integrated signal area, the peak-to-peak voltage was selected as the primary observable for the subsequent analysis of the CBS photon yield.

An additional observation from the gain response measurements was that the jitter in the area and peak-to-peak measurements increases with the gain. This

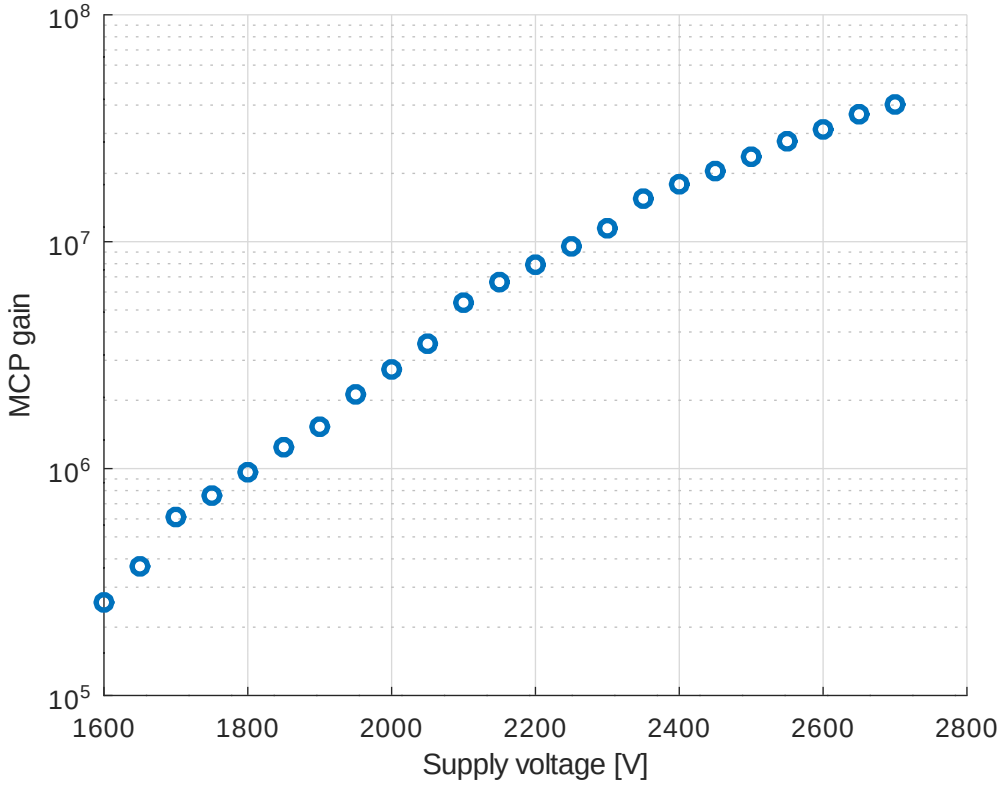
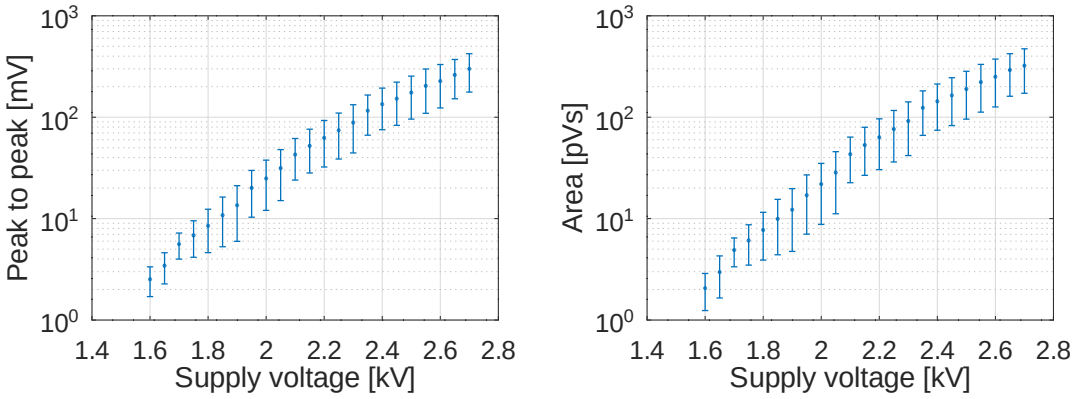



Figure 4.12: The gain of the microchannel plate used for the CBS experiment, plotted as a function of the input supply voltage.

phenomenon is clearly seen in the pulse height distributions pictured in Fig. 4.14, obtained from measuring the Fe-55 X-ray signal. Pulse height distributions represent histograms of the peak-to-peak signal voltage at a given gain. For the analysis below, the histogram was computed for the signal area since the two signal features are proportional to each other. One can see that for a low supply voltage of 1600 V, the pulse height distribution is well defined as a narrow-width Gaussian. However, as the gain increases, the distribution broadens, making analysis of the CBS signal more challenging. In addition, for supply voltages above 1800 V, the gain becomes sufficiently large for the dark current to exceed the detection threshold. This accounts for the pronounced fluctuations observed in the histograms at higher supply voltages in Fig. 4.14.

An optimal supply voltage was needed to ensure that the CBS signal was dis-




(a) (b)

Figure 4.13: Gain calibration curves obtained with an Fe-55 source from the MCP. The peak-to-peak (a) and area (b) of the signal waveform is shown as a function of the input supply voltage.

tinguishable while also minimising the pulse height resolution. The pulse height resolution (PHR) is a critical parameter of the pulse height distribution, representing the ratio of the full width at half maximum of the pulse-height distribution to its peak position. A plot for the PHR as a function of the MCP supply voltage is shown in Fig. 4.15.

Figure 4.15 shows the dependence of the pulse-height resolution on the MCP supply voltage. Between 1600 V and 1850 V, the pulse-height resolution increases linearly with the supply voltage. At higher voltages, it fluctuates between 100% and 250%, indicating increased gain variations within the detector. Although single-photon events were already clearly distinguishable at 1600 V, operating at higher voltages provides increased gain and consequently larger signal amplitudes, which is advantageous given the low photon flux expected from the CBS experiment. However, excessive gain can lead to detector saturation and an increase in dark-current-induced signals. A supply voltage of 1900 V was therefore selected for operation, as it provided a gain of approximately $1.5 \times 10^6$ while maintaining a pulse-height resolution of about 150%, representing a suitable compromise between signal amplification and detector performance.

In conclusion, the calibration of the MCP detector was successful in measuring the detection efficiency and gain response. The detection efficiency allowed us to

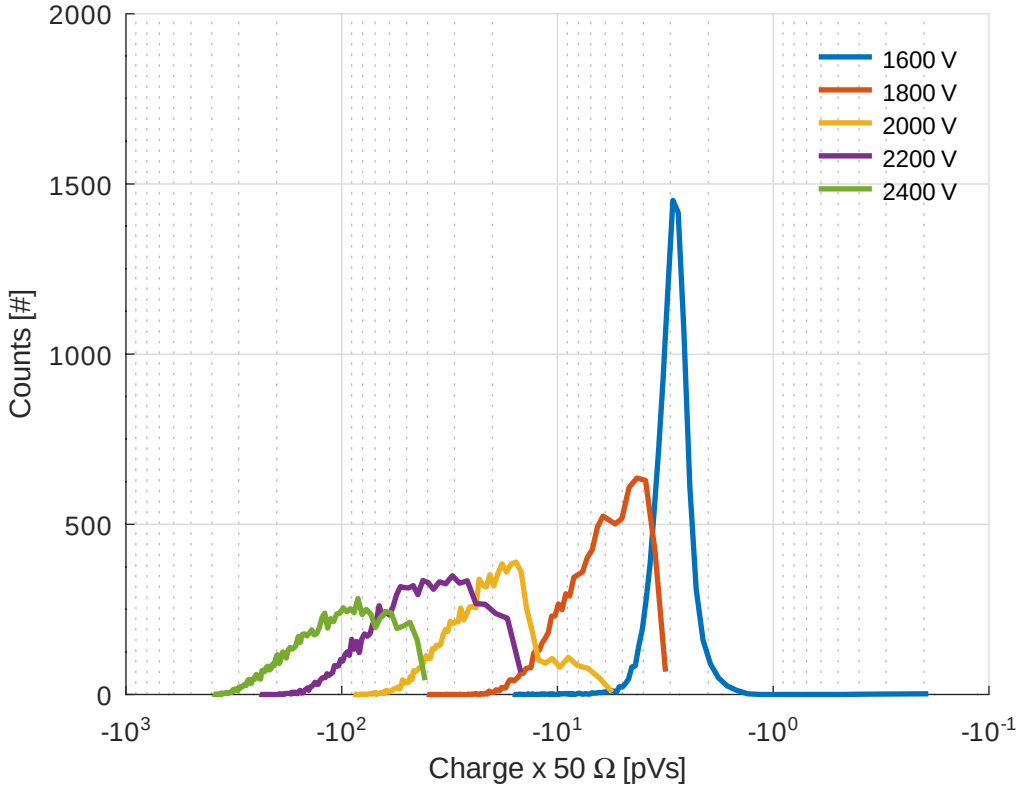



Figure 4.14: Pulse height distributions (PHDs) of the microchannel plate (MCP) detector for supply voltages between 1600 V and 2400 V. The horizontal axis shows the waveform area (or the integrated pulse charge multiplied by 50 Ω) in units of pVs, while the vertical axis represents the number of recorded events. As the supply voltage increases, the distribution shifts towards larger pulse areas and exhibits a broader spread, indicating increased gain and a corresponding rise in measurement fluctuations.

deduce the number of X-ray photons in the pulse from the number of detected photons, a value that can then be used to benchmark the CBS interaction simulations done in RF-Track. The gain calibration was used to calculate the number of X-ray photons detected by the MCP.

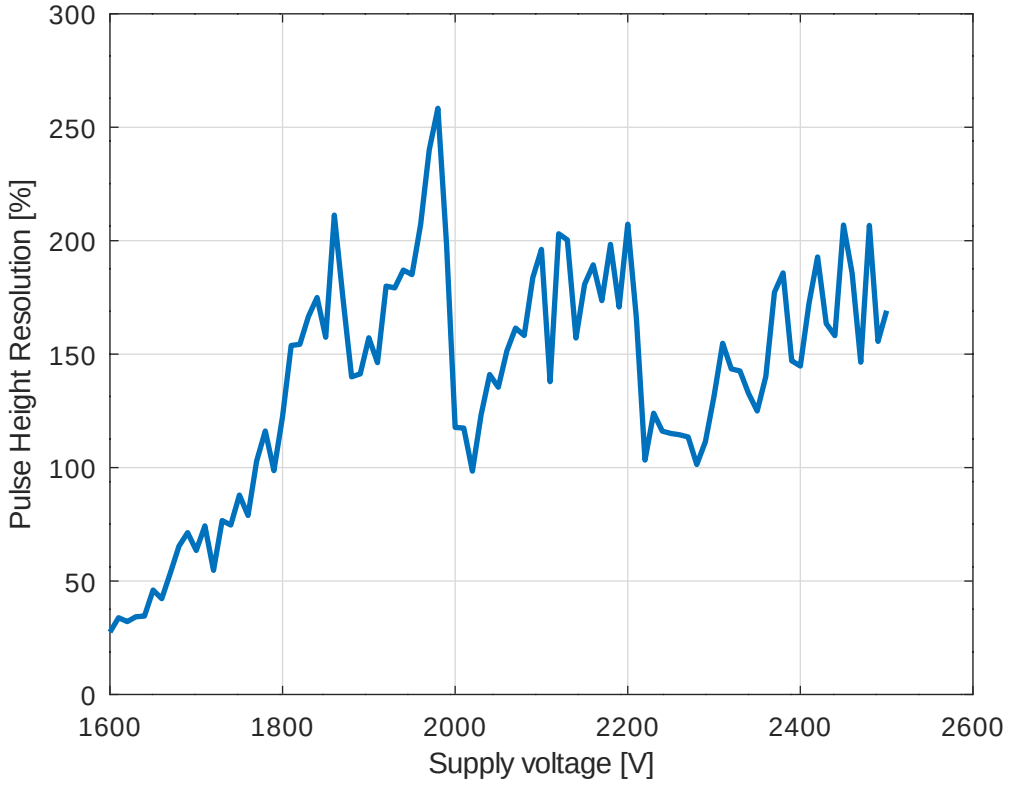



Figure 4.15: Pulse height resolution versus the applied supply voltage, as measured for the MCP.

## 4.3 Background mitigation for the MCP

Microchannel plates are sensitive to a select range of particles, a minority of which was present at ARTI as background. The MCP model used was able to detect ultraviolet photons, X-rays, alpha particles, charged particles, neutrons, electrons, and ions. Their respective detection efficiencies are tabulated in Table 4.1. As referenced in Fig. 4.5a, the detection efficiency of the soft X-ray signal ranges from 5% to 15%. The low signal detection efficiency competed with several particle types comprising the MCP background, most of which being bremsstrahlung photons from the interaction of the electron beam with the beam pipe walls, UV laser photons reflected from the copper cathode, and dark current generated by the RF system. For the 250 nm UV photons from the PHAROS laser, the detection

efficiency is less than 0.01%, as shown in Fig. 4.16.

Table 4.1: Detection Efficiency of MCP (Credit: [134])

| **Types of Radiation** | **Energy or Wavelength** | **Detection Efficiency** |
|---|---|---|
| Electron | 0.2 keV to 2 keV | 50% to 85% |
| | 2 keV to 50 keV | 10% to 60% |
| Ion ($H^+$, $He^+$, $Ar^+$) | 0.5 keV to 2 keV | 5% to 58% |
| | 2 keV to 50 keV | 60% to 85% |
| | 50 keV to 200 keV | 4% to 60% |
| UV | 300 Å to 1100 Å | 5% to 15% |
| | 1100 Å to 1500 Å | 1% to 5% |
| Soft X-ray | 2 Å to 50 Å | 5% to 15% |
| Hard X-ray | 0.12 Å to 0.2 Å | 1% |
| High energy particle | 1 GeV to 10 GeV | to 95% |
| Neutron | 2.5 MeV to 14 MeV | 0.14% to 0.64% |

From Table 4.1, the MCP is particularly sensitive to low energy electrons. In the ARTI beamline, background electrons would be present either from the generated bunches or from the RF dark current. Most of the electrons comprising the bunch are deflected by the spectrometer dipole before reaching the MCP. However, once in the spectrometer line, some electrons may hit the beam pipe walls. Furthermore, the RF dark current (comprising a few picoCoulombs) presents a very broad energy spectrum, leading to a large bending dispersion by the spectrometer, and additional electrons colliding with the beam pipe walls. These electrons are subject to the creation of secondary radiation, an additional source of background for the MCP. The main mechanism for the generation of secondary radiation is bremsstrahlung, i.e., photons generated from the deceleration of a charged particle from being deflected by another charged particle.

To block bremsstrahlung radiation generated in the dipole bend from reaching the MCP, the spectrometer beamline was covered in lead sheets, along with the region between the detection chamber and the dipole. This did not noticeably affect the main background pulse; however, it did remove a signal bump that appeared slightly earlier in time on the oscilloscope. Any attempts to place blocking

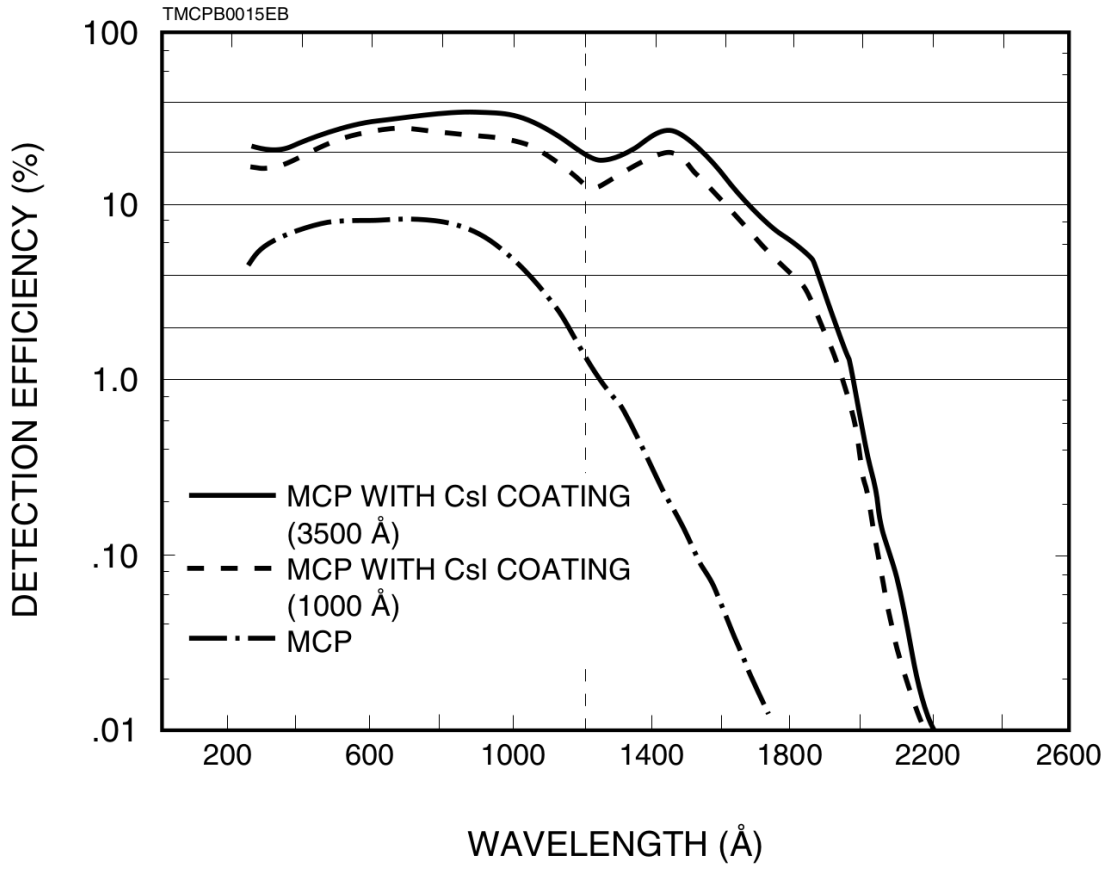



Figure 4.16: Detection efficiency of the MCP versus the UV wavelength. (Taken from: [134])

material inside the beam pipe would have resulted in outgassing, beam impedance, and the possibility of generating additional secondary radiation. To mitigate this, the beam transport was optimised to minimise any losses across the beamline.

Another significant source of background in the microchannel plate originated from reflections of the laser beam at the cathode. Owing to the MCP detection efficiency of less than 0.01% for 250 nm photons, UV reflections from the cathode were initially expected to contribute negligibly to the overall background. Contrary to this expectation, the ultraviolet laser was found to be the dominant background source in the Compton backscattering experiment, as illustrated in Fig. 4.17. When the UV laser reflects from the metallic cathode and the RF is turned off, a low noise signal is observable on the MCP. Since the RF is off, there is

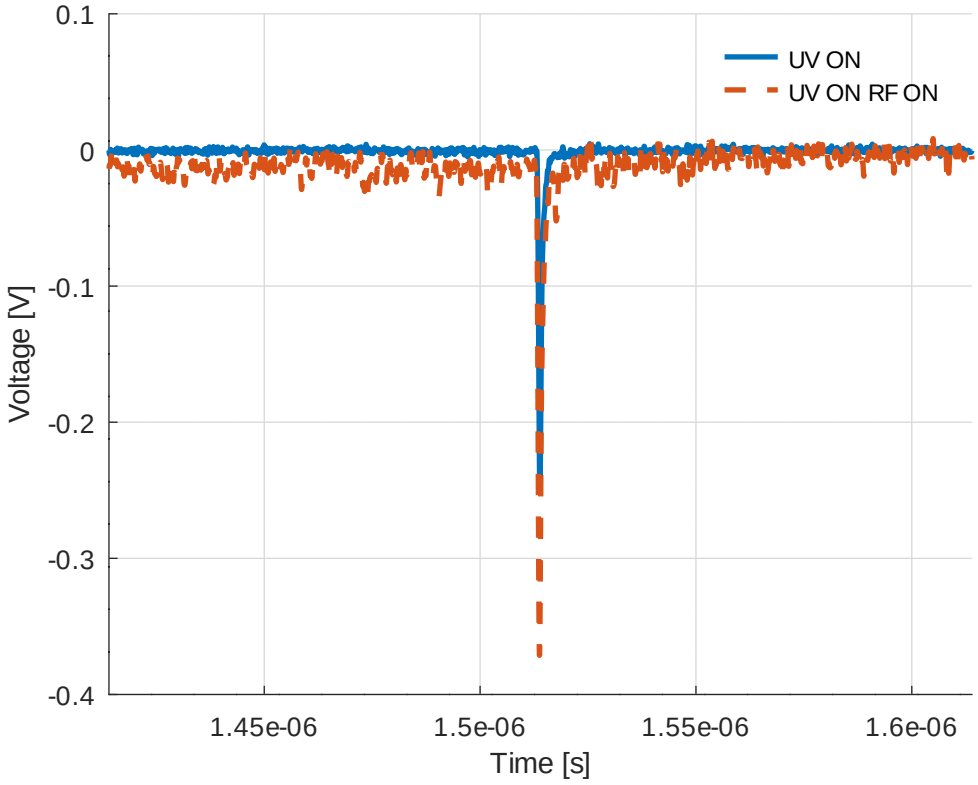



Figure 4.17: Comparison of the MCP voltage waveforms recorded under two operating conditions: with the ultraviolet (UV) laser incident on the cathode and the RF system inactive ("UV ON"), and with both the UV laser and RF field active ("UV ON, RF ON"). The horizontal axis shows time after trigger in seconds, and the vertical axis represents the measured signal voltage in volts.

no dark current or electron bunch impinging on the detector. If both UV and RF are off, there is no observable signal. Once the RF is on, the background waveform increases in area, a sign that both the laser and the secondary radiation reach the MCP within its rise time, 300 ps. The noise level also increases then, which can be explained by the presence of the continuous dark current, or electrical pick-ups by the signal cable. From Fig. 4.18, the background waveform area and peak-to-peak voltage directly depend on the laser attenuation. This provided confirmation that the MCP is indeed detecting UV photons reflected from the cathode.

Mitigating the UV background proved to be challenging. Thin foils were initially considered to cover the MCP surface. However, because of the low energy of

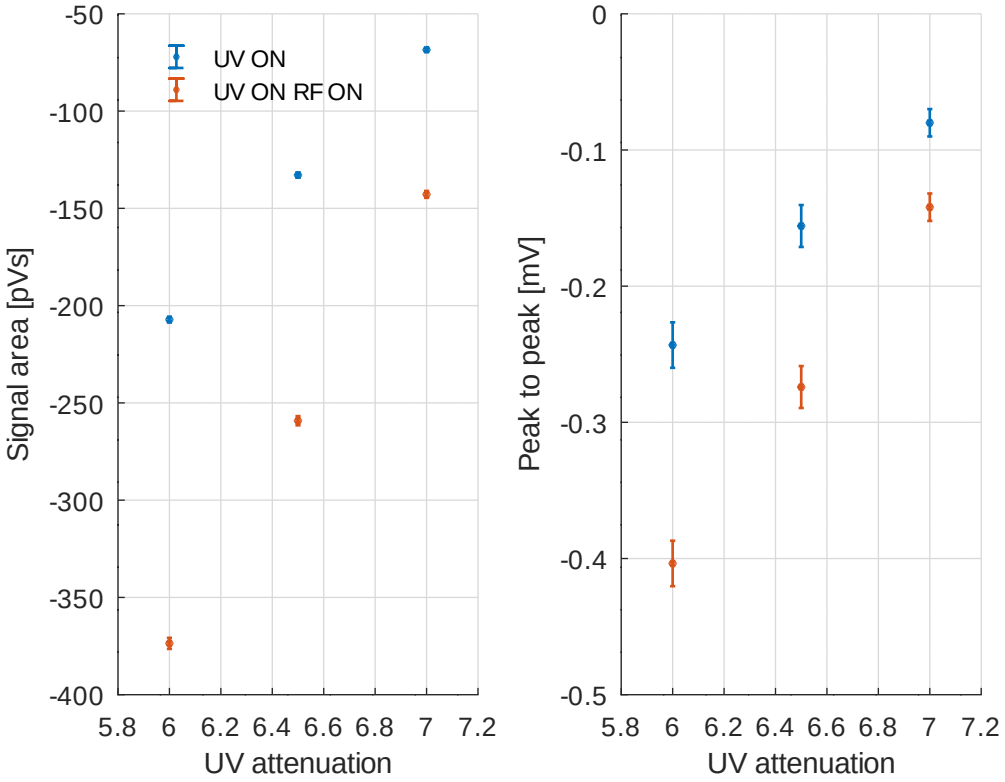



Figure 4.18: The MCP waveform area (left) and peak-to-peak (right) shown as a function of the motor coordinates of the UV laser intensity attenuator. The setting corresponding to the absence of RF signal and presence of the UV laser on the cathode is shown is included, along with the setting where the RF signal is active and the UV laser reaches the cathode. The plots indicate that there is a significant background detected by the MCP from the reflection of the UV laser from the cathode.

the soft X-rays, this would also have involved a significant degradation of the CBS signal. Attenuating the laser was not an option, as it proportionally decreased the potential CBS signal. The UV photons were instead partially blocked using the actuator-attached screen frame. To achieve this, the lower frame of the YAG screen was lowered up to the edge of the electron beam. Although only able to block one half of the area through which the UV beam passes, this method proved nevertheless quite effective, reducing the waveform area from −3.86 nVs to −3.03 nVs, and peak-to-peak voltage from 1 V to 0.66 V. The optimal actuator position could be

quickly identified by scanning the background against the actuator position.

The remaining background mitigation was the tuning of the solenoid and dipole magnetic strengths to provide low-loss transport from the cathode to the spectrometer end. A scan of the waveform area against the solenoid current is shown in Fig. 4.19. Note that the solenoid current is proportional to its magnetic strength. For low current values, the absolute signal area increases dramatically, which is ex-

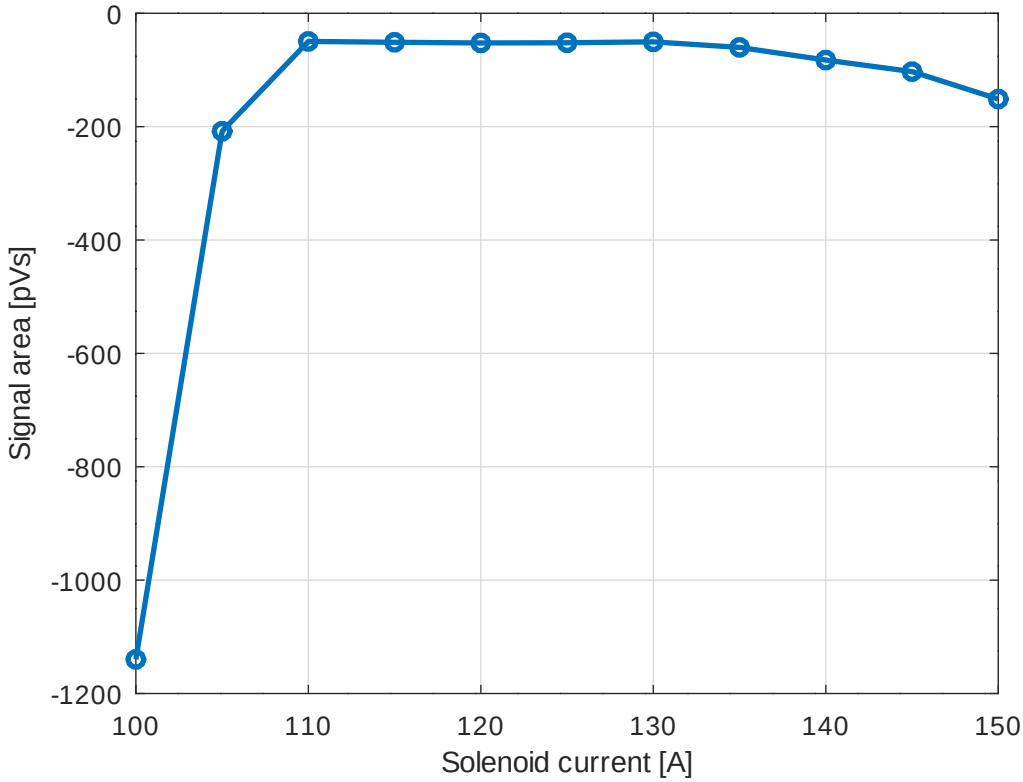



Figure 4.19: Scan of the MCP signal area versus the magnetic strength of ARTI's solenoid, in the background-only case.

plained by the increase in beam size and subsequent collision of the halo electrons with the beam pipe walls. The forward travelling bremsstrahlung radiation resulting from the collision could then form a background on the MCP. For the typical solenoid strengths used, between 120 A and 130 A, the waveform area reaches a plateau. For larger solenoid strengths, the absolute signal area slightly increases, corresponding to the interaction of the beam with the beam pipe walls between

the solenoid and the actuator's location. The solenoid scan provided a suitable range for the magnetic strength where the background was minimal.

Similar considerations were made for the dipole magnet. Again, the signal area was plotted against the dipole current, as shown in Fig. 4.20. As for the solenoid, the dipole current is proportional to its magnetic strength. For dipole currents

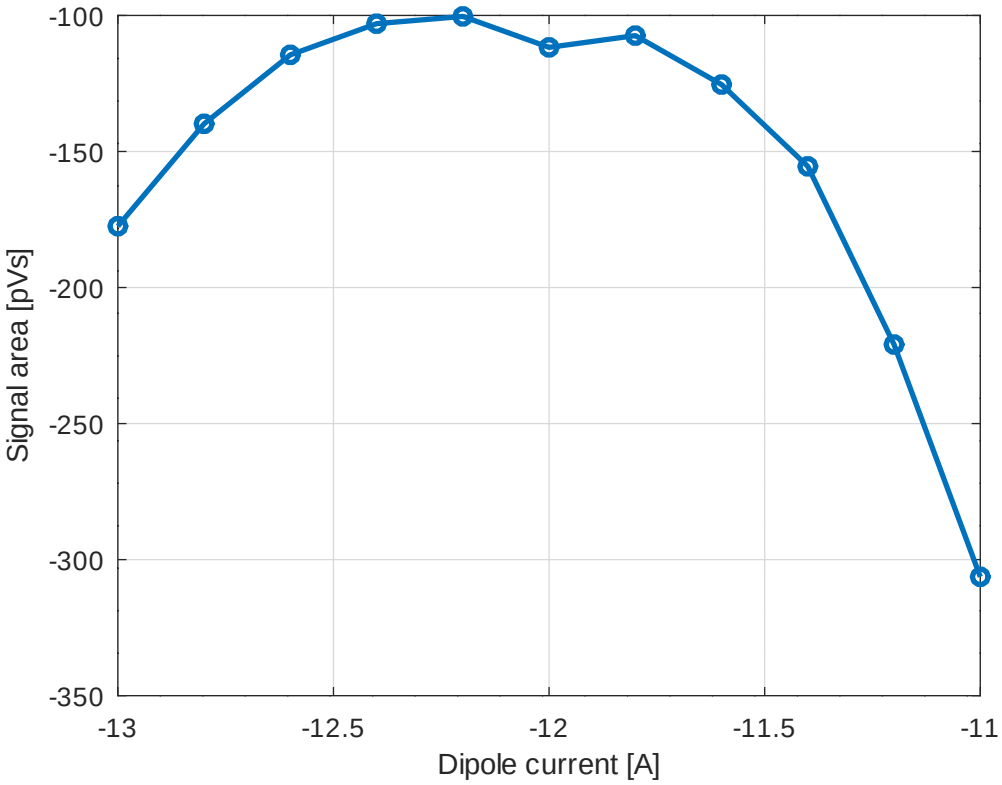



Figure 4.20: Scan of the MCP signal area versus the magnetic strength of ARTI's dipole, in the background-only case.

between −13 A and −12.5 A, the absolute waveform area increases. In this setting, the electron beam is strongly bended, leading to a collision with the pipe walls in the spectrometer line, or with the beam-splitting chamber inside the dipole. Since the radiation generated in the spectrometer beamline would be blocked from reaching the MCP by the lead sheets, and the bremsstrahlung generated in the dipole chamber would be forward moving towards the spectrometer line, the slight increase in signal area was expected. At −12.25 A, the absolute signal area is

minimised. This setting corresponds to the centring of the electron beam on the spectrometer line. This trajectory minimises the interaction of the electron beam with the pipe walls, leading to the smallest background, and was used for the CBS experiment. Between −12 A and −11 A, the electron beam is bent towards the MCP, allowing high energy electrons to reach the detector, which leads to a significant increase in the absolute signal area.

Following the background mitigation, the final step before the temporal and spatial alignment of the electron and IR laser beam could commence was the centring of the X-ray beam on the MCP. The installation and commissioning of the IR laser beamline was detailed in Chapter 2.2.0.2.

## 4.4 Alignment of the CBS X-ray to the MCP detector

Prior to spatially aligning the laser and electron beams, the Compton backscattered X-ray beam was aligned with the microchannel plate detector. This preliminary alignment maximised the number of detected photons and facilitated a simplified and more reliable simulation set-up. Owing to the large angular divergence of the scattered X-ray beam, significant photon losses can occur if the beam is not properly centred on the detector. Consequently, precise centring of the X-ray beam on the MCP was required to mitigate these losses.

From CBS theory, the angle between the scattered X-ray beam axis and the electron beam axis outgoing from the CBS interaction is ~0° [135]. Therefore, one can assume that, notwithstanding magnetic effects, the electron beam travels after the IP in the same direction as the X-ray beam. The electron beam at ARTI could therefore be used to centre the X-ray beam on the MCP detector.

This property was investigated using RF-Track simulations. For the interaction of 5.44 MeV electrons with an infrared laser beam at a crossing angle of 90°, the resulting scattering angles between the outgoing X-ray and electron beams were found to be 0.3523° in the horizontal plane. The resulting tilt of the X-ray beam is therefore sufficiently small to be considered negligible for the purposes of this study.

Prior to the use of the electron beam scheme, the MCP was aligned to the centre of the beamline axis using an industrial alignment laser. Since the CF cube housing the MCP presented an optical viewport on one of its faces, the alignment laser could be used to orient the MCP so that its active area was aligned to the centre of the beam pipe.

Following the rough alignment with the industrial laser, the electron beam position was scanned two-dimensionally on the MCP's surface. In order to prevent damage to the MCP, the maximum possible attenuation was used for the electron beam (~2 pC). The resulting parametric scan is shown in Fig. 4.21. The location

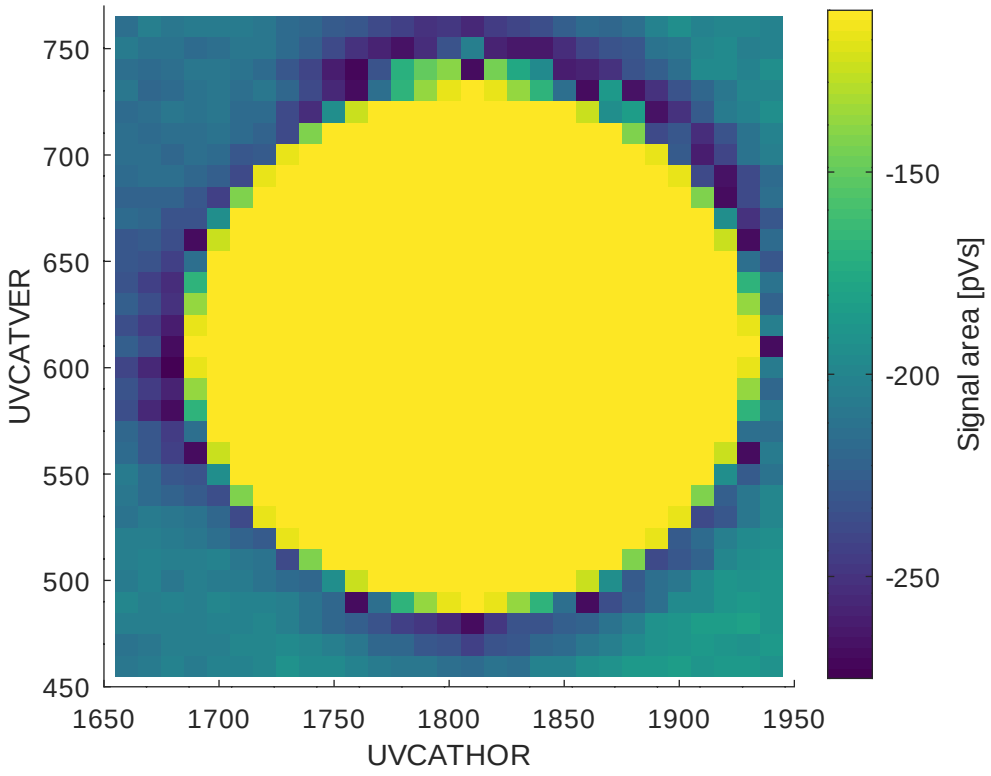



Figure 4.21: Two dimensional scan of the signal area against the position of the electron beam impinging on the MCP. The shape of the MCP's active area is clearly distinguishable as the maximum signal area plateau. UVCATHOR and UVCATVER represent the controls for the horizontal and vertical position of the UV laser on the cathode, respectively.

of the electron beam on the MCP was scanned by modifying the position of the

UV laser on the cathode. The displacement in the position of the two beams was proportional to each other. For each beam position, MCP waveforms were recorded, from which the signal area was computed. The entire MCP's active area was covered during the 2D scan, and a heatmap colour-coded by the signal area was plotted. The detector's centre was identified from the heatmap's horizontal and vertical projections.

This alignment study also served as a means to check the uniformity of the MCP's quantum efficiency. Under the incidence of a large number of input particles, a high supply voltage, low vacuum, or contamination of its active area, the detector can be subject to electrical discharge, which defines regions with reduced QE within the MCP's active area. As seen in Fig. 4.21, such features were not observed in the 2D scan.

## 4.5 Temporal alignment of the laser and electron beams

The alignment of the electron and laser beams at the IP was critical to the CBS experiment. Given the low expected number of detectable photons from the CBS interaction, the accuracy of the alignment needed to be within a few micrometres in space and a few picoseconds in time. To achieve this, the temporal alignment was performed by tuning the longitudinal position of the IR laser with a delay stage, as shown in Fig. 2.11, with a step size of 17 fs.

Most CBS experiments measure the temporal delay by aligning the laser pulse and the OTR signal from the electron bunch on a streak camera. However, such a diagnostic was not available at ARTI. An alternative method was therefore conceived, in which the UV beam reflected from the cathode was used instead of the electron bunch, and the streak camera was replaced with an ultrafast photodiode (or beam splitter). This methodology was enabled by the high reflectivity of the metallic cathode and the availability of an exit port for the reflected ultraviolet beam. By reproducing the geometry of a Mach–Zehnder interferometer, which splits light into two independent paths before recombining the beams at a common location, the reflected ultraviolet beam was directed to intersect the infrared beam at the location of an ultrafast photodiode (or beam splitter), as illustrated

in Fig. 4.22. By arranging the IR and UV beam paths downstream of the CBS interaction point to form a parallelogram, any additional transverse offset between the two beams introduced after the interaction point was eliminated. The temporal delay between the ultraviolet and infrared pulses was then measured using an ultrafast photodiode positioned at the point of intersection.

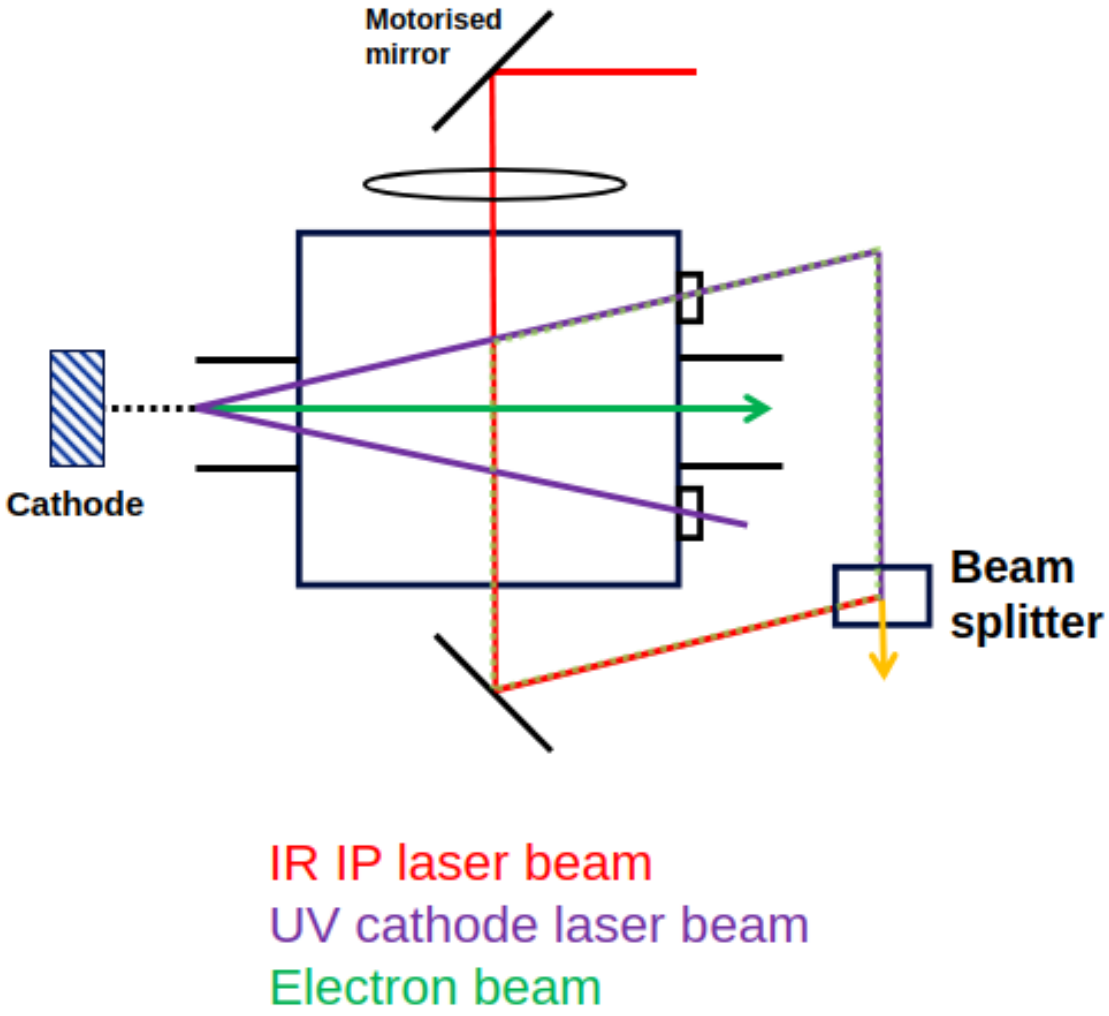



Figure 4.22: Schematic of the set-up used to align the UV and IR laser beams.

An initial consideration when using the UV beam instead of the electron was that the speed of the laser beam is higher than the speed of the electron beam. Additionally, the speed of the IR beam is constant, whereas the speed of the electron beam increases as it passes through the gun field. Lastly, the UV beam

travels at an angle with respect to the electron bunch. All of these effects change the measured time delay of the UV beam with respect to the electron beam. Using the beamline design of Fig. 2.1 to determine the angle between the UV beam and the electron beam (2.55°), and simulating in RF-Track the difference in time due to the electron beam's acceleration, a 42 ps – 2 ps = 40 ps difference in time between the electron beam and the UV beam was calculated. This timing correction was applied during the alignment of the two laser beams.

The low rise time of the ultrafast photodiode required the use of a high frequency oscilloscope. For the CBS experiment, 10 GHz MSO64-10 provided a sampling rate large enough to be able to discriminate between the rise time of the two pulses. Nevertheless, the initial study performed with the 10 GHz oscilloscope was the calibration of the delay stage's step size. The calibration was performed by tracking the offset in time of one of the laser pulses against the set position of the delay stage. The results are shown in Fig. 4.23. Five distinct positions were recorded, and the entire data set was linearly fitted, along with its two extrema. A good degree of correspondence between the two fits was observed, and the data points strictly followed a linear curve.

The next step was the actual alignment, performed using the 10 GHz oscilloscope interface. The results are shown in Fig. 4.24. The two laser beams were focused on the small active area of the ultrafast photodiode. The two pulses were also severely attenuated to prevent the saturation of the photodiode. Once this was achieved, two well-defined waveforms could be observed, as shown in Fig. 4.24a. The locations of the peaks in the two distributions were recorded, and the delay stage was adjusted to compensate for this distance. A representation of the combined waveforms after alignment is shown in Fig. 4.24b.

Using this set-up, a preliminary temporal alignment was readily achieved, with the temporal resolution limited by the 40 ps rise time of the photodiode. To compensate for this limitation during the search for the CBS signal, the optical delay stage was scanned over a temporal window of 100 ps in steps of 0.5 ps. Both the delay stage and the oscilloscope were operated through automated control scripts.

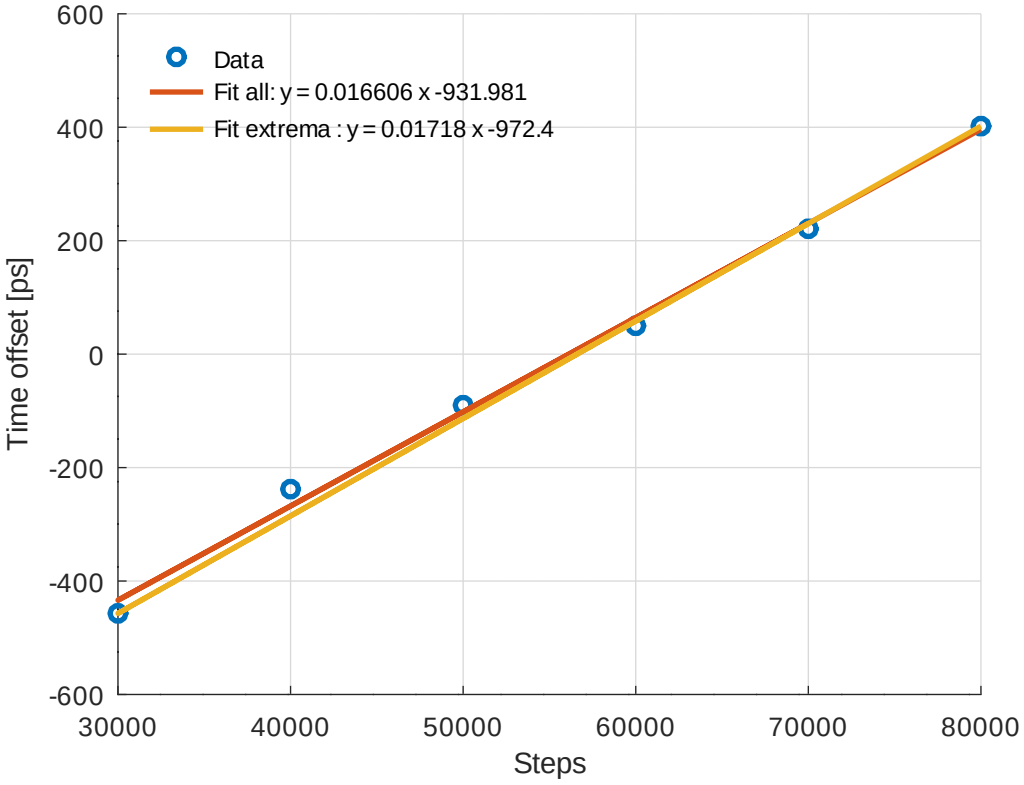
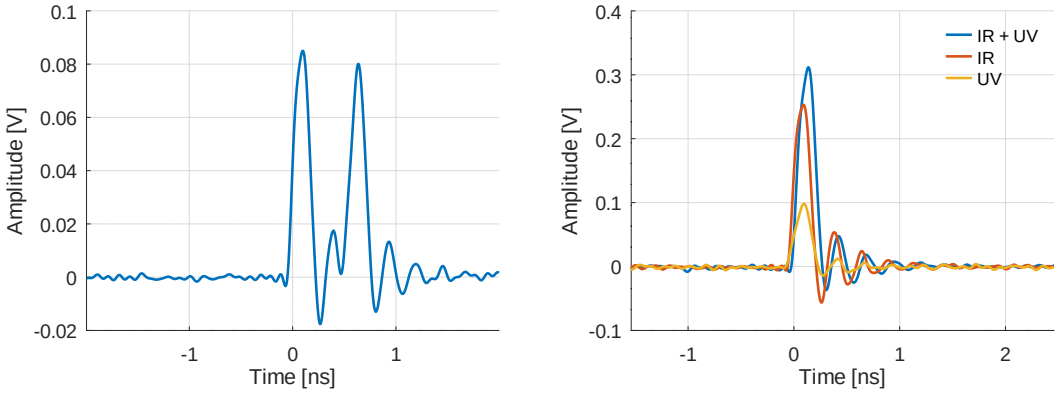



Figure 4.23: Calibration plot for the motorised delay stage installed at ARTI. The temporal offset between the IR and UV laser beams (measured in picoseconds) is shown versus the position coordinate of the delay stage. The motor's step position was correlated to the time offset of the laser beam measured by an ultrafast photodiode using a 10 GHz oscilloscope.

## 4.6 Spatial alignment of the laser and electron beam

Following the establishment of a baseline temporal alignment between the laser pulse and the electron beam, the spatial alignment procedure was performed. This process was constrained by the approximately 20 µm RMS spot size of the infrared laser beam, which limited the permissible transverse offsets in order to avoid a further reduction of the Compton backscattering flux. RF-Track simulations indicated that the CBS photon yield decreases to approximately half of its maximum value for vertical offsets exceeding 130 µm.




(a) (b)

Figure 4.24: Waveform traces recorded with the 10 GHz oscilloscope during the temporal alignment of the UV and IR laser pulses for the CBS experiment. The measured voltage amplitude (V) is shown as a function of time relative to the trigger (ns). The signals prior (a) and after (b) the temporal alignment are displayed.

The spatial alignment was performed using an OTR screen installed at the IP. Two designs of the OTR screen have been used. The first, shown in Fig. 4.25, consisted of a silicon substrate with a 100 nm thick aluminium coating on one side. A series of holes arranged on a diagonal were drilled through the screen using a laser cutter and used for the spatial alignment.

Since the OTR light is emitted in the same direction as the interaction laser (due to the 45° tilt of the screen with respect to the electron beam), the laser and electron beams can be simultaneously observed on the digital camera facing the IP. However, the alignment of the images of the electron and laser beams on the camera is not equivalent to their actual alignment. To ensure that this was indeed the case, the two beams were arranged to pass through a delimited interaction zone. The vertical position of the OTR screen was scanned until the hole through which the electron beam passed was identified. The IR laser was then directed to pass through that same hole. Due to the large laser pulse energy, PHAROS' alignment sensing and control (ASC) signal was used throughout the spatial alignment, which provided a continuous and lower intensity laser beam, typically used for the laser alignment feedback loop.

Following the alignment of the IR laser on the interaction zone, the set position

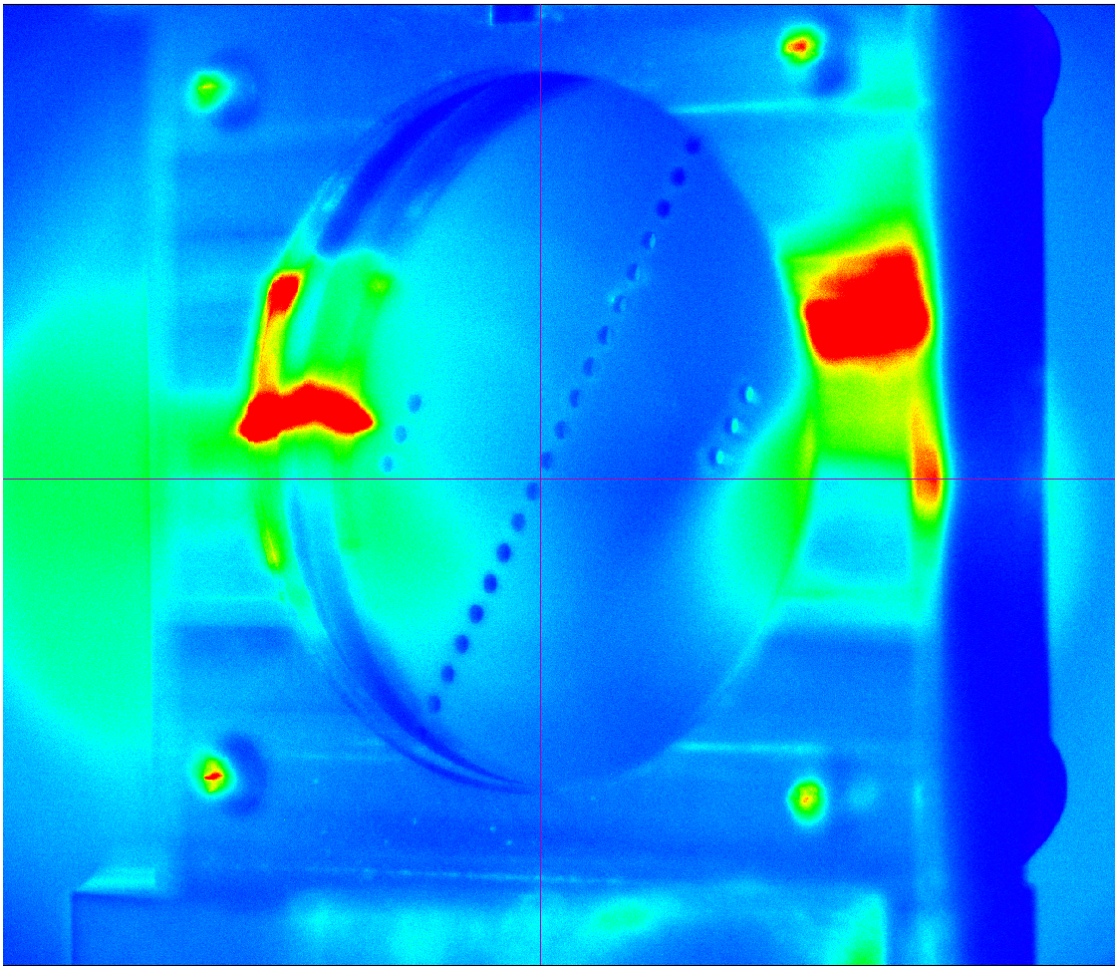


Figure 4.25: The first design of the OTR screen, as seen installed under vacuum. The holes placed diagonally across the screen's surface were made using a laser cutter, and subsequently used for the spatial alignment of the laser and electron beams.

of the screen actuator was recorded, the IR laser's position was scanned around the hole's area, and the sum of the camera's pixel intensities was calculated for each step. The resulting heatmap (shown in Fig. 4.26) was used to identify the position settings for the motorised mirror corresponding to the centring of the IR laser. This procedure was then replicated using the OTR light from the electron beam. The electron beam position was scanned by displacing the UV laser on the cathode. The resulting two-dimensional plot made for the electron beam is shown in Fig. 4.27. The optimum beam position was identified from the minimum value

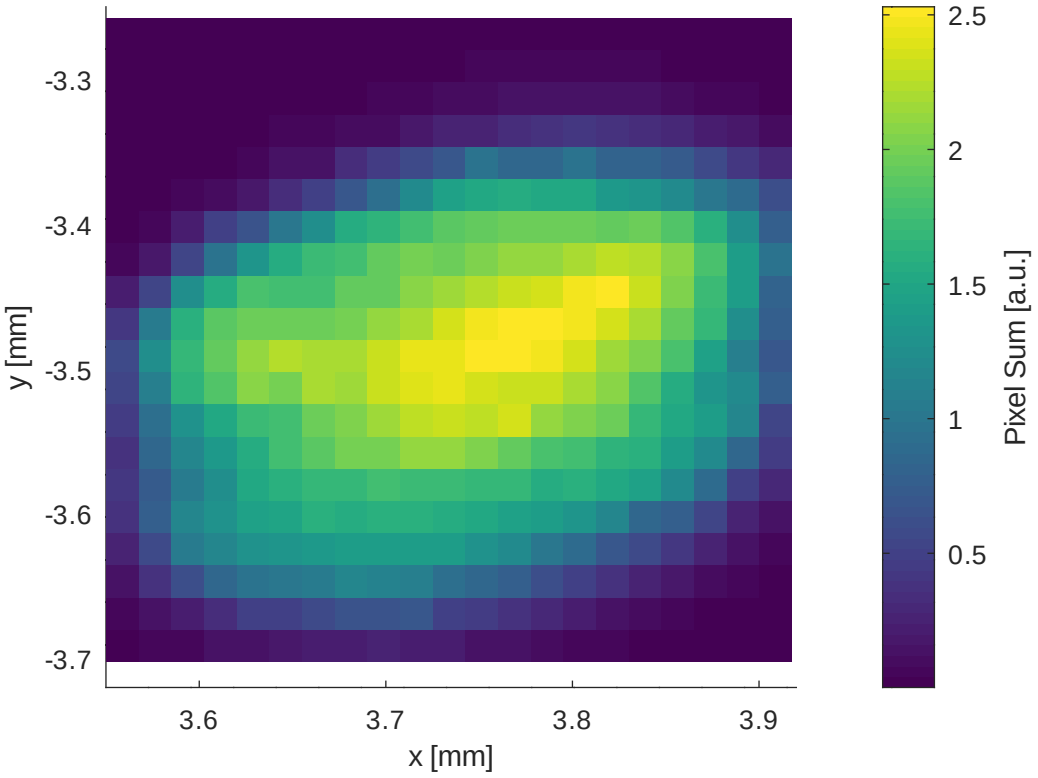



Figure 4.26: Spatial alignment scan used to centre the IR laser beam on one of the apertures of the OTR screen. The measurement was performed using the first design iteration of the OTR screen. The horizontal and vertical axes represent the transverse displacement of the mirror directing the IR beam towards the IP, while the colour scale shows the integrated pixel intensity (a.u.) corresponding to the laser signal transmitted through the aperture.

of the scanning heatmap, corresponding to the location for which the electron beam core passes through the hole's centre, and hence where the light scattered from the interaction of the electron beam with the OTR screen is minimal.

The pixel light intensity captured by the installed camera was complemented by charge measurements from the Faraday cup. If the electron beam is centred on the hole, a majority of electrons can travel through it and reach the Faraday cup, leading to an increase in the measured charge. Because the Faraday cup measurement has higher precision and lower noise compared to the camera, it could be used successfully as a confirmation of the predicted centre coordinates.

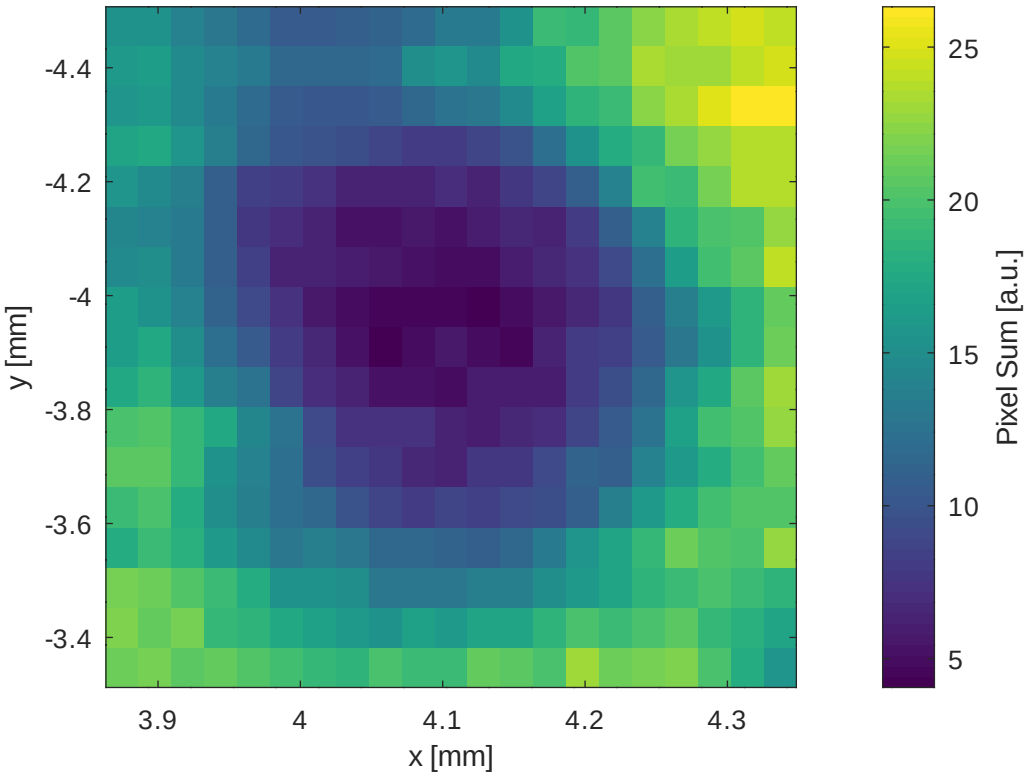



Figure 4.27: Two-dimensional spatial scan used to align the electron beam with the centre of an aperture in the first-generation OTR screen. The horizontal and vertical axes show the transverse displacement of the UV beam on the cathode in millimetres, while the colour scale represents the integrated pixel intensity in arbitrary units. The minimum in the pixel sum corresponds to the beam passing through the aperture, thereby identifying the optimal alignment position.

The IR laser traced an elliptical heatmap across the circular hole, as shown in Fig. 4.26. This can be explained by the 45° tilt of the OTR screen with respect to the IR laser, which reduced the horizontal diameter observed on the camera by $\sqrt{2}$. From both the electron and laser heatmaps, it can be seen that the projected diameter of 620 µm of the screen hole was reproduced. The size of the laser-drilled holes was ultimately too large to allow for a precise determination of the IP. To mitigate this effect, a new OTR screen was designed and installed.

A more simplified approach was taken for the second design of the OTR screen. Similarly to other CBS experiments [136], a 25 µm thick high-purity (99.5%) Alu-

minium foil was used. The updated heatmap corresponding to the electron beam in this new configuration is shown in Fig. 4.28. To ensure the smallest possible

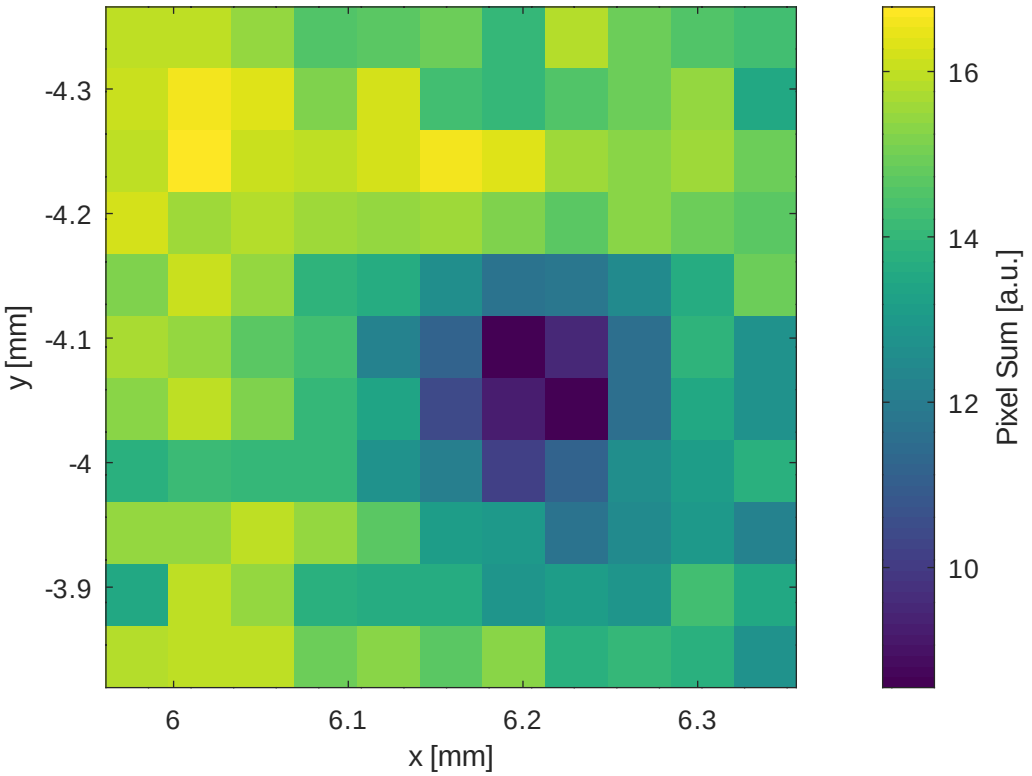



Figure 4.28: Two-dimensional spatial scan used to align the electron beam with the laser-bored aperture in the second-generation OTR screen. The horizontal and vertical axes indicate the transverse displacement of the UV beam on the cathode in millimetres, while the colour scale represents the integrated pixel intensity in arbitrary units. Compared to the initial OTR design, the central minimum corresponding to the beam passing through the aperture is confined to a significantly smaller region, demonstrating the improved localisation and alignment sensitivity of the modified OTR screen.

interaction area for the spatial alignment, a few IR laser pulses at maximum intensity were shone on the OTR screen, which created a hole approximately in size to the laser beam. The scanning region thus became considerably smaller than the initial design. Using this method, the alignment of the IR laser no longer needed to be performed. Coupled with the alignment of the electron beam within a smaller

region, the alignment process sped up considerably. Finally, this was the design that allowed for the detection of the CBS photons.

## 4.7 Measurement of the CBS signal

Once a precise spatial alignment between the laser and electron beams was obtained, the search for the CBS signal commenced. Based on the temporal alignment described in a previous section, the delay stage position was scanned along a range of 60 ps, in steps of 0.5 ps. When a gradual increase in the voltage output from the MCP was registered on the connected oscilloscope, a finer rescan of the target area was performed. If the signal decreased according to a Gaussian distribution against the longitudinal scan, horizontal and vertical scans of the IR laser's position were then performed to narrow down the settings that maximised the observed signal. If a Gaussian distribution was observed across all three scans and the signal vanished when the IR laser was blocked from reaching the IP, the oscilloscope reading could be interpreted as corresponding to CBS photons with a high degree of confidence. To map out the interaction point and ensure that a three-dimensional reconstruction was possible in RF-Track, two-dimensional scans of pairs of the three coordinates were done, along with a full three-dimensional scan tracing the entire interaction region. The 2D and 3D scans performed at ARTI represent the first full mapping of the CBS interaction region in the literature.

For the measurements presented in this section, the relevant electron and IR laser beam parameters at the IP are tabulated in Tab. 4.2. To ensure high beam stability and minimise the collection angle of the Compton backscattered radiation, the electron beam energy was maximised by operating the electron gun at the highest achievable RF gradient. The RF phase was set to an optimum value of $-10°$, as determined in Chapter 3.7, corresponding to the minimum normalised transverse emittance. According to Eq. 1.24, maximisation of the CBS photon flux requires minimisation of the electron beam spot size at the interaction point, which was achieved using the solenoid magnet. The bunch charge was set to 150 pC, representing a compromise between reduced space-charge effects and a sufficient number of electrons participating in the CBS interaction.

Table 4.2: Parameters of the electron and laser beam at the interaction point

| **Parameter** | **Unit** | **Value** |
|---|---|---|
| Beam energy | MeV | 5.44 |
| Electron RMS spot size (x/y) | µm | 54.5/77.7 |
| Bunch charge | pC | 150 |
| RMS bunch length | ps | 2 |
| Laser RMS spot | µm | 18 |
| Pulse energy | mJ | 1.1 |
| RMS pulse length | ps | 1 |
| Laser wavelength | nm | 1030 |

Owing to the limited availability of diagnostics, the electron bunch length was not measured directly; however, RF-Track simulations indicated that space-charge effects would increase the bunch length to approximately 2 ps RMS at the interaction point. The laser spot size was minimised to 18 µm at the interaction point in order to further enhance the scattered photon flux, while the laser pulse energy was set to its maximum available value of 1.1 mJ. Finally, to maximise the data acquisition rate, the repetition rates of both the electron beam and the laser system were set to 10 Hz.

An image of the beam used for the CBS interaction is shown in Fig. 4.29, as seen from the OTR screen. The beam core's tilt was explained by the significant misalignment of the solenoid magnet position, which was made in order to centre the electron beam on the MCP.

A plot of an example waveform showing both the signal and background is shown in Fig. 4.30. The signal appeared as an increase in the area of the main background pulse, which was expected given that the 300 ps rise time of the MCP was not large enough to be able to discriminate between the arrival time of the background and of the actual signal. To obtain an accurate measurement of the CBS signal, 100 waveforms were recorded for each point of analysis.

### 4.7.1 Parametric scans of the CBS signal

Following the observation of the Compton backscattering signal, a comprehensive measurement campaign was undertaken to map the interaction region and per-

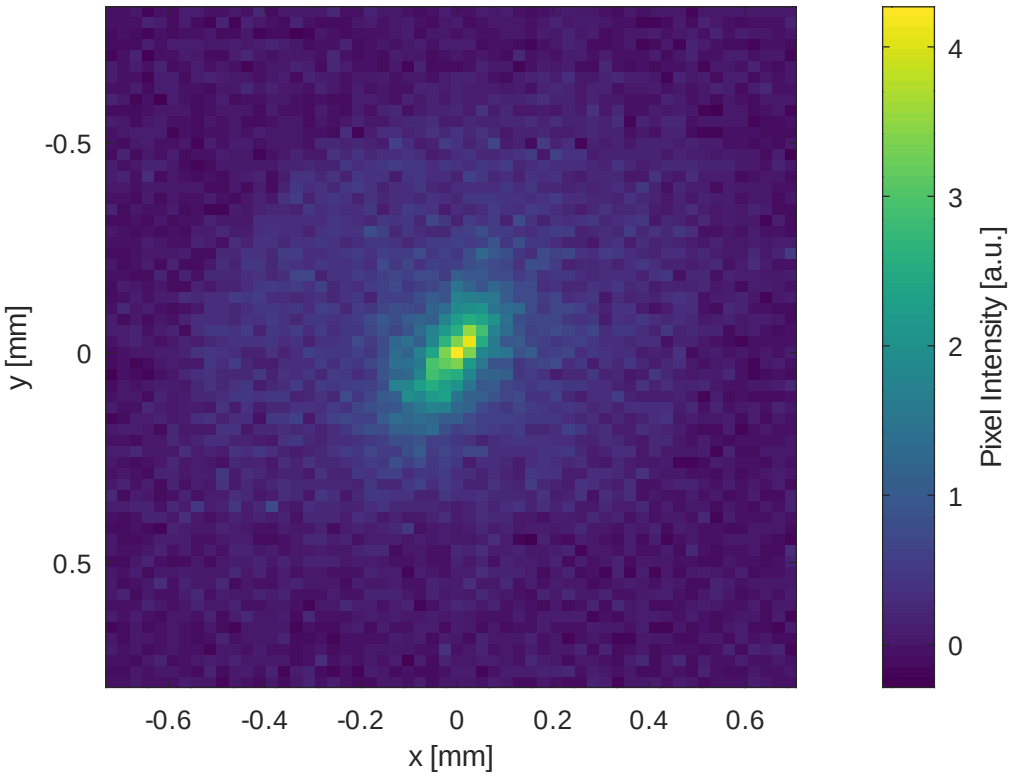



Figure 4.29: Two-dimensional image of the electron beam profile at the interaction point (IP), recorded using the OTR screen. The horizontal and vertical axes represent the transverse beam coordinates in millimetres, while the colour scale indicates the integrated pixel intensity in arbitrary units. The image reveals a tightly focused beam core with a slight tilt in the transverse plane.

form parametric scans of the input beam parameters. The experimental results were subsequently compared with RF-Track simulations. To minimise systematic uncertainties, each point in a parameter scan was accompanied by an independent background measurement, obtained by blocking the infrared laser upstream of the interaction region. The area and peak-to-peak voltage of the resulting background waveform were evaluated and subtracted from the corresponding signal waveform. The background-corrected signal parameters, together with the gain response shown in Fig. 4.13, were then used to determine the number of CBS photons detected by the microchannel plate. Finally, the number of photons incident on the detector was inferred by correcting the detected photon count for the soft

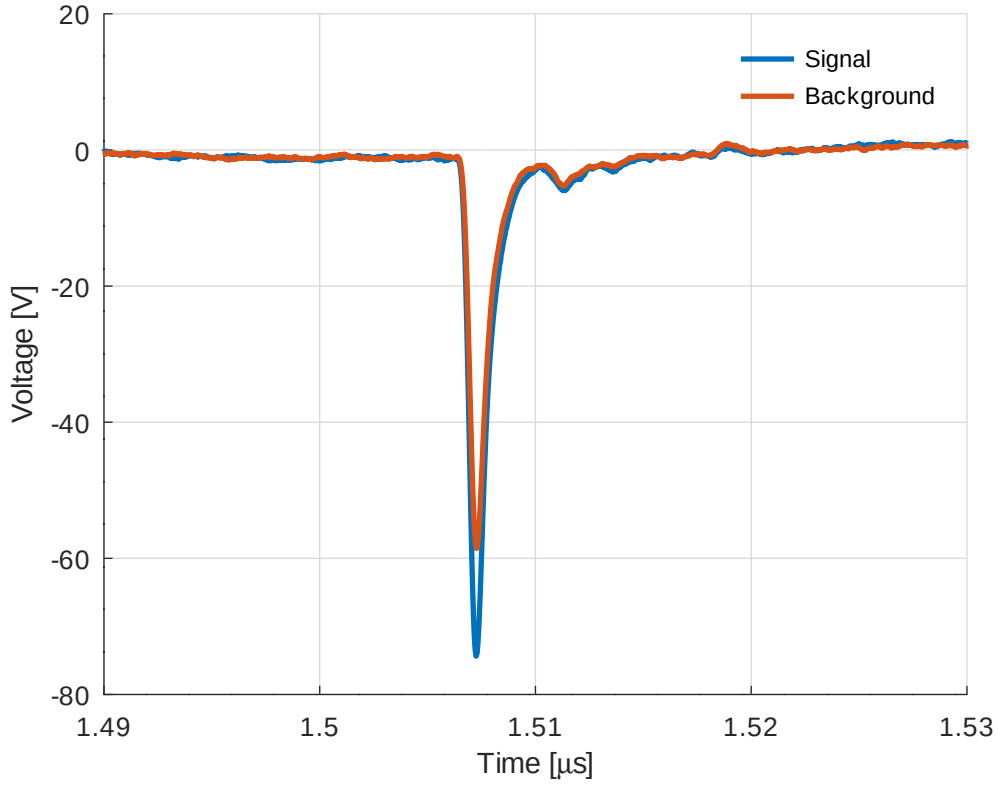



Figure 4.30: Averaged CBS signal and background response from the MCP. The measured voltage (Volts) is plotted as a function of time relative to the trigger (µs).

X-ray detection efficiency determined in Chapter 4.2.4.

Using this methodology, 15 soft X-ray photons per electron bunch were found to be incident on the detector. From the detection efficiency of 12.5%, this amounted to 120 photons incident on the detector. To ensure a sufficiently high signal-to-noise ratio, a large number of waveforms were collected per data point. Due to excellent stability in beam parameters and low MCP dark current, the standard on the mean could be decreased as such to be able to clearly distinguish the CBS signal from the background.

#### 4.7.1.1 Realistic simulations of the output photon flux from the CBS interaction

The experimental results obtained from the Compton backscattering experiment at ARTI were complemented by interaction-point simulations performed using RF-Track. The detailed beamline modelling effort described in Chapter 3.3 enabled a direct benchmark of the RF-Track CBS implementation against experimental measurements. In order to provide the most accurate possible representation of the interaction point, a one-to-one reconstruction of the electron beam profile was implemented within RF-Track.

Measurements acquired with the optical transition radiation screen revealed a tightly focused electron beam at the interaction point, exhibiting a core tilted in the horizontal–vertical plane, as shown in Fig. 4.29. This image was used to reconstruct the transverse electron beam distribution at the interaction point in RF-Track. The longitudinal profile was taken from the established beamline model. Although the reconstruction is inherently limited by the pixel resolution of the input image, this effect was considered negligible in the present case, given the 54.5 µm RMS electron beam size relative to the 4.8 µm pixel size.

Before detailing the profile reproduction process, some considerations of the bunch creation process in RF-Track are required. In RF-Track, particle bunches tracked in space are created from the following line of code (in Octave),

```
B = Bunch6d( [ X XP Y YP T P MASS Q N ] );
```

where `Bunch6d` is the structure encompassing the bunch, `X` the column vector of the horizontal coordinates (in mm units), `XP` the column vector of the horizontal angles (in mrad units), `Y` the column vector of the vertical coordinates (in mm units), `YP` the column vector of the vertical angles (in mrad units), `T` the column vector of the arrival times (in mm/$c$ units), `P` the column vector of the total momenta (in MeV/$c$ units), `MASS` the column vector of particle masses (in MeV/$c^2$ units), `Q` the column vector of single particle charges (in units of $e$), and `N` the column vector of numbers of single particles per macro particle. This last parameter was relevant to the profile reconstruction. To save considerable running time, packets of single particles can be bundled in macro particle structures in RF-Track. The choice for

the number of macro particles is made based on the balance of desired simulation running time and targeted model accuracy.

The first step in reproducing the electron beam profile consisted of generating a Gaussian bunch in RF-Track using the input parameters listed in Table 4.2. The total number of macroparticles was chosen to be equal to the sum of the pixel intensities of the reference image. The `N` attribute of each macroparticle was then employed to populate each corresponding pixel area with a number of particles proportional to the pixel intensity, while maintaining equal macroparticle weights throughout the distribution. The transverse positions and angles of the particles were assigned using a random number generator, with values constrained to the spatial extent of each pixel area.

The accuracy of this reconstruction method was verified by simulating an electron bunch in RF-Track, performing the CBS interaction, deriving the total scattered photon flux, and comparing it with the value obtained from the pixelated beam profile reconstructed from the transverse distribution of the original bunch. A difference of less than 1% was obtained between the two flux values, confirming the accuracy of this methodology.

The beam jitter experimentally measured at the IP (and included in Table 2.2) was included in the RF-Track flux estimate. In the RF-Track script, the jitter amplitudes were sampled using a random number generator, and the simulation was run for 1000 different configurations. The resulting flux histogram is shown in Fig. 4.31. Note that the distribution peaks at 13 photons per bunch, and the mean and standard deviation of the simulated data set is $13.98 \pm 2.72$ photons per bunch. The predicted variation in the photon flux was therefore noticeably small, which provided an advantage to the reliability of the experimental results.

#### 4.7.1.2 Main results of the CBS experiment at ARTI

The experimental results obtained from the MCP installed at ARTI allowed for a comprehensive benchmark against the RF-Track CBS model. The first recorded scan of the CBS photon parameters was a longitudinal one. The results are shown in Fig. 4.32. Excellent agreement was observed between the experimental measurements and the corresponding RF-Track predictions. The slightly larger peak observed in the experimental data was identified as a systematic effect specific

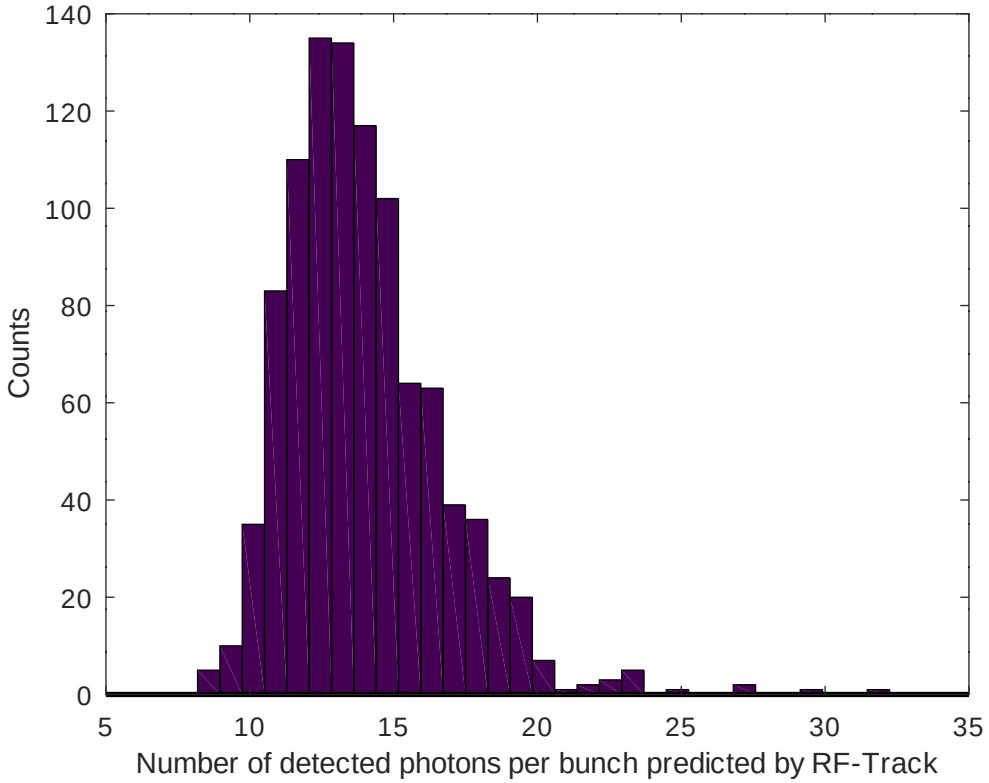



Figure 4.31: Histogram of the number of detected photons by the MCP, as predicted by RF-Track. The histogram was obtained from 1000 samples, and the laser and electron beam jitter parameters at the interaction point were included. The distribution peaks at 13 photons per bunch.

to the longitudinal scan. The experimental longitudinal distribution exhibited an RMS width of 2.1 ps, in good agreement with the 2 ps RMS electron bunch length predicted by RF-Track. The comparatively large scan width is attributed to the convolution of the longitudinal profiles of the electron bunch and the laser pulse, as described by Eq. 1.24. Consequently, both the photon yield and the effective longitudinal extent of the interaction region are governed by the longer of the two pulse durations.

Convolution was also present in the scan of the horizontal position of the IR laser against the number of detected CBS photons. A plot of the scan is shown in Fig. 4.33. The scan was characterised by a large spread of 0.667 mm. The

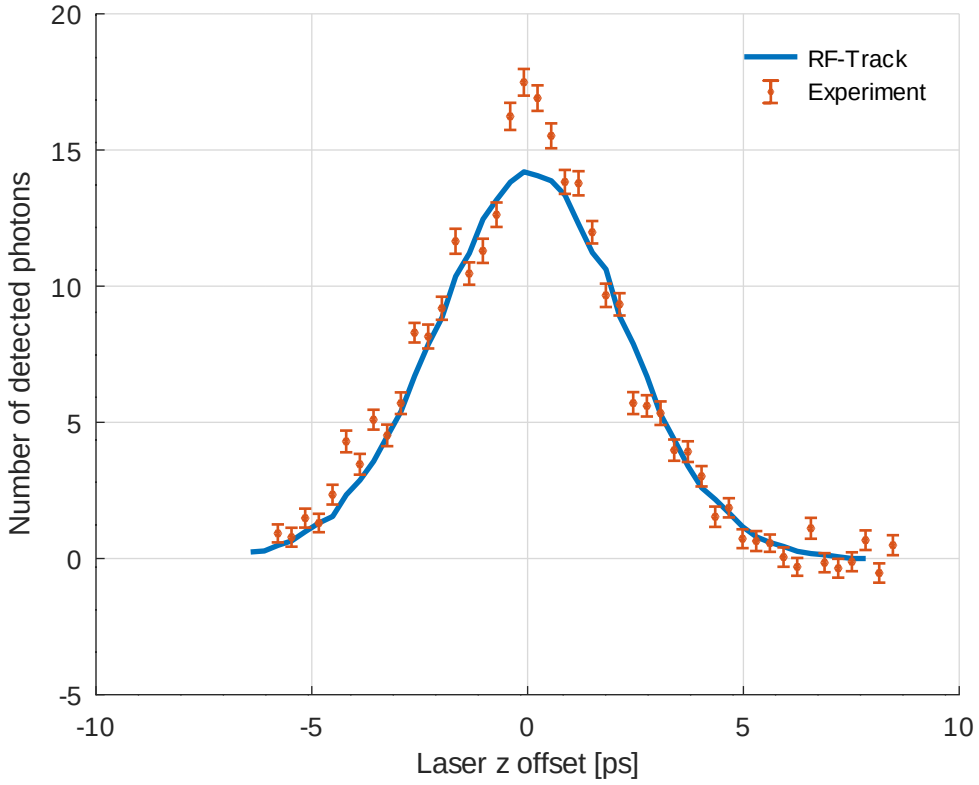



Figure 4.32: Scan of the number of CBS photons detected by the MCP against the arrival time of the IR laser at the IP. Experimental measurements (red) are compared with simulations performed in RF-Track (blue). The error bars in the experimental data correspond to the standard error on the mean.

performance in terms of peak scattered photon flux was a result of the convolution of the laser and electron's horizontal spot size, as shown in Eq. 1.24. Due to the geometry of the laser-electron interaction, the horizontal scan was effectively a convolution of the horizontal and longitudinal planes, i.e., a movement of the laser along the horizontal axis is equivalent to a time delay (one main difference being that the time delay excludes a change in the crossing angle). Therefore, the trace of the horizontal scan was a convolution of both the horizontal spot size and the longitudinal length of the two pulses. Since the electron RMS pulse length reaches 0.60 mm (much larger than the electron RMS spot size of 0.10 mm), the scan's trace width extended to a comparable value of 0.667 mm RMS.

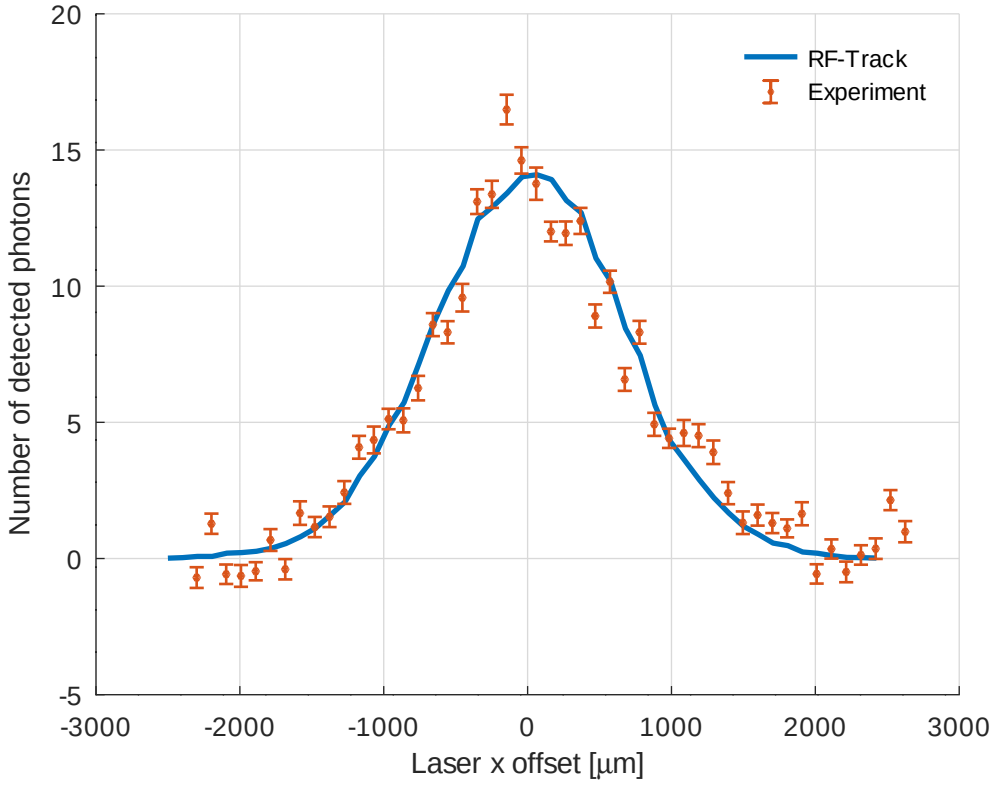



Figure 4.33: Scan of the number of CBS photons detected by the MCP against the horizontal position of the IR laser at the IP. Experimental measurements (red) are compared with simulations performed in RF-Track (blue). The error bars in the experimental data correspond to the standard error on the mean.

The last 1D spatial scan was performed for the vertical displacement of the laser position at the IP. The results are shown in Fig. 4.34. For the vertical scan, the only convolution present was the one between the vertical laser and electron spot sizes. The width of the vertical distribution corresponded to the larger of the two values, i.e., the electron RMS spot size. This resulted in a significantly narrower distribution than the longitudinal and horizontal ones. There were notable inconsistencies between the experimental and simulated results, in particular, a non-Gaussian experimental trace. This can be explained by the very fine scan of the laser position, which was more subject to errors of the motor controlling the laser mirror angle.

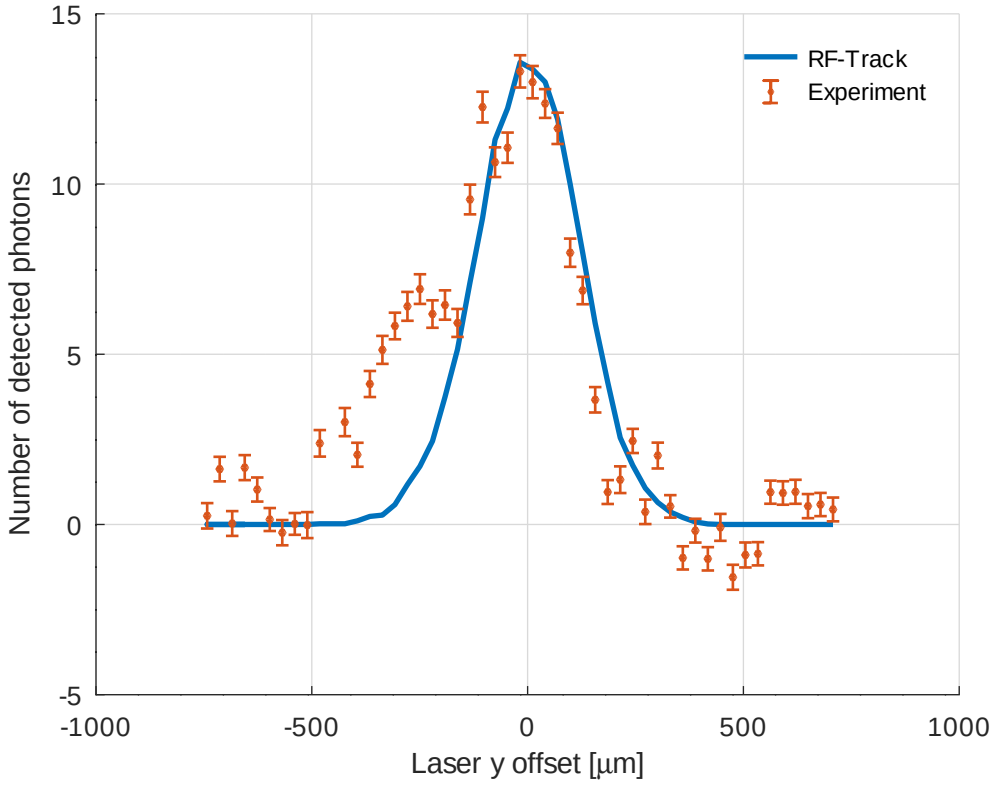



Figure 4.34: Scan of the number of CBS photons detected by the MCP against the vertical position of the IR laser at the IP. Experimental measurements (red) are compared with simulations performed in RF-Track (blue). The error bars in the experimental data correspond to the standard error on the mean.

The rest of the 1D scans studied the impact of tuning the intensity of the electron and laser signals against the scattered photon flux. For instance, the number of detected CBS photons was tracked against the bunch charge, as shown in Fig. 4.35. The charge was varied by changing the attenuation of the UV pulse energy on the cathode. A linear distribution was obtained for both the RF-Track and the experimental measurements. However, for bunch charges under 20 pC, the number of detected photons remained constant. This could be explained by noting that the lower bunch charge values failed to pass the noise threshold, making the signal invisible to the background. Note that the quoted charge does not correspond to the one measured by the Faraday cup. As shown in Section 3.8, the

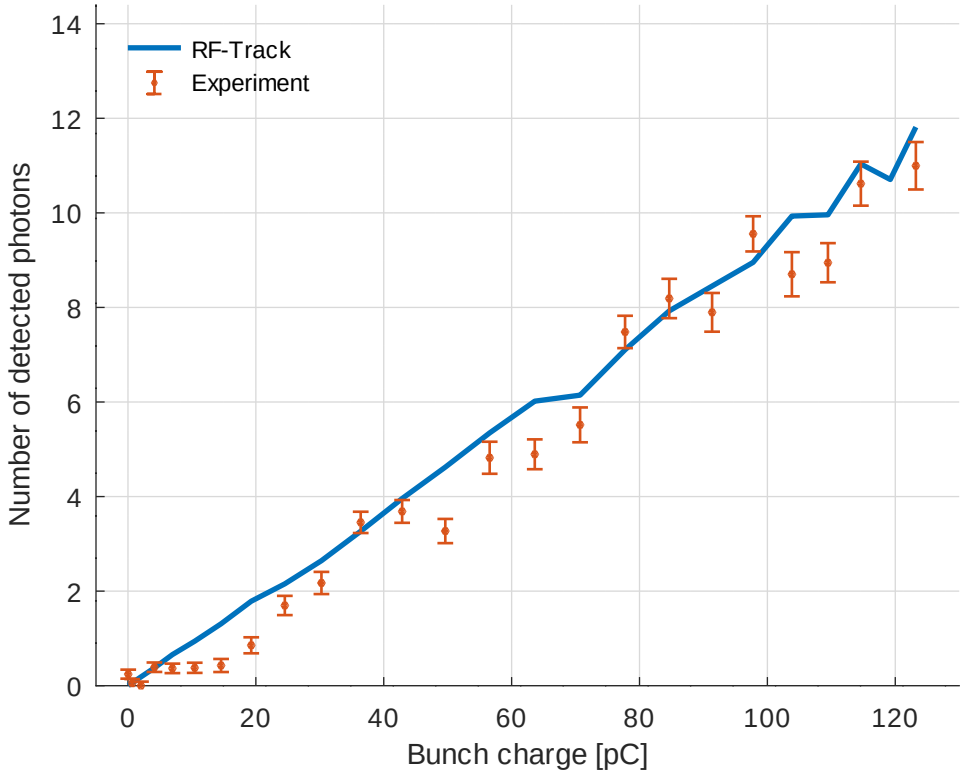



Figure 4.35: Scan of the number of CBS photons detected by the MCP against the electron bunch charge at the IP. Experimental measurements (red) are compared with simulations performed in RF-Track (blue). The error bars in the experimental data correspond to the standard error on the mean. Note that from the experimental dataset, the 25% contribution from the halo was removed.

electron beam presented a separate halo bunch, delayed by a few picoseconds with respect to the main bunch. Since the halo bunch encompasses approximately 25% of the charge recorded by the Faraday cup, its contribution had to be removed to equate the RF-Track result with the experimental one.

The second intensity scan performed was for the IR laser energy. The outcome is shown in Fig. 4.36. The scan was obtained by varying the attenuation of the IR laser pulse, thus reducing the laser pulse energy at the IP. A linear distribution was again obtained for both the experimental and RF-Track data. A discrepancy between the two datasets in the lower intensity ranges can be attributed to the absence of a strong enough signal to pass the MCP's detection threshold. In the

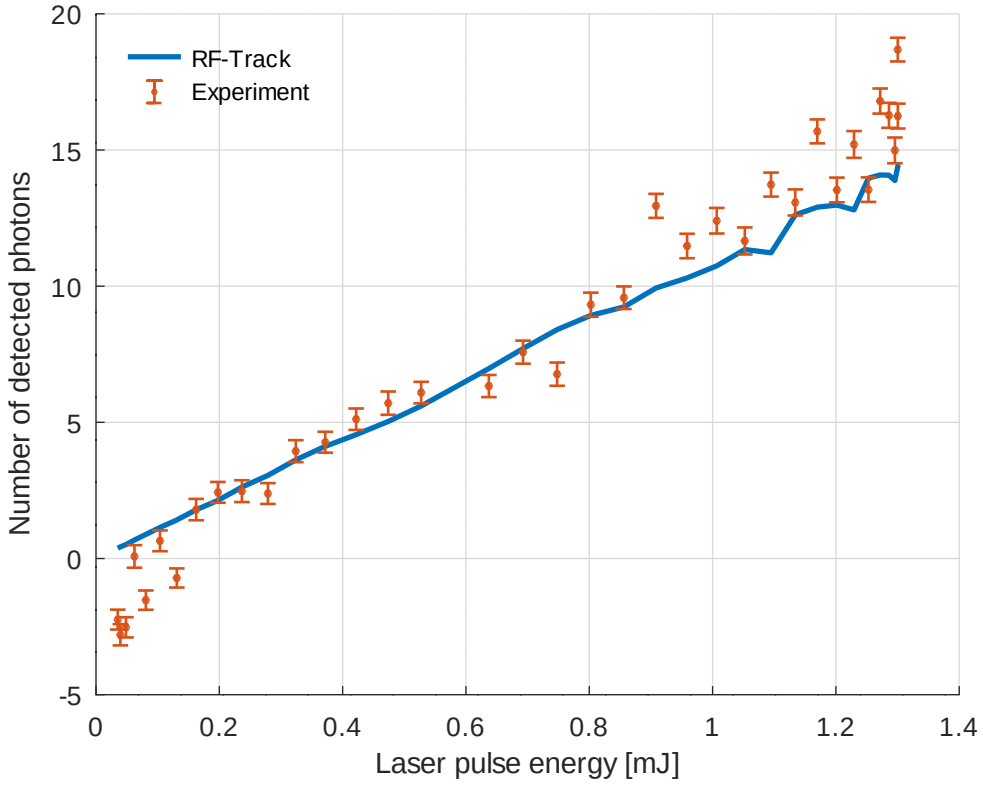



Figure 4.36: Scan of the number of CBS photons detected by the MCP against the laser pulse energy at the IP. Background-subtracted experimental measurements (red) are compared with simulations performed in RF-Track (blue). The error bars in the experimental data correspond to the standard error on the mean.

higher energy range, the discrepancy can be explained by an increase in the laser pulse energy jitter.

The one-dimensional scans were followed by the two-dimensional scans, which sought to map the CBS interaction region. To account for all present axes, horizontal-vertical, horizontal-longitudinal, and vertical-longitudinal scans were measured and reproduced in RF-Track.

The first scan performed was for the horizontal and vertical planes, shown in Fig. 4.37. As expected from the previous 1D scans, the horizontal component of the distribution, subject to the horizontal-longitudinal convolution, exhibited a larger width compared to the vertical component. In 2D, this translates into an elliptical

distribution, reproduced for both the experimental and RF-Track datasets.

For the 2D scan in the vertical and longitudinal planes, a similar shape to the one observed for the horizontal-vertical map was obtained, as seen in Fig. 4.38. Again, the convolution between the horizontal and longitudinal widths led to a widening of the longitudinal component of the distribution, while the vertical component was, as for the 1D scan, much narrower. An elliptical shape was obtained for both the experimental datasets and the RF-Track datasets.

The last 2D map, shown in Fig. 4.39, comprised a scan of the horizontal and longitudinal planes of the interaction region. An interesting feature can be observed for this particular scan. Whereas for the previous two heatmaps, the plot was strictly elliptical, a constant strip was observed for Fig. 4.39. The signal band exhibits a constant signal peak at its centre, with the edges decreasing in intensity under a Gaussian-like distribution. These features were observed for both the experimental and RF-Track studies. The signal distribution can be explained by considering the geometry of the CBS interaction. A scan of the horizontal laser position at the IP can be conceived as equivalent to a temporal (or longitudinal) delay of the laser pulse, and vice-versa. Therefore, if one shifted the laser position to reach the electron axis at a position closer to the cathode, the effect can be compensated by delaying the time at which the laser arrives at the said position, thus ensuring that the electron and laser pulses will still collide. In practice, the band's centre will eventually lower in intensity because of the electron's increase in beam size around the focus point. However, simulations showed that the increase in beam size was only in the order of 15%, with no noticeable impact on the CBS flux within the explored range.

The last scan performed as part of the CBS experiment was a full three-dimensional scan mapping of the entire interaction region. In order to visualise the scan, isosurfaces were plotted for both the experimental and RF-Track measurements, as seen in Fig. 4.40. In order to plot isosurfaces, a constant value was needed to be provided [137], which for the given dataset was 50% of the peak recorded CBS flux. This value provided an equilibrium between the background onset and the unit value equivalent to the peak amplitude. One can see from the plotted figure that a tubular surface defined the interaction region. The tubular geometry was explained as a 3D projection of Fig. 4.39. Since the horizontal-longitudinal

2D scan presented the largest number of peak flux data points, its dominance over the projection of the other 2D scans was expected. It should be noted that the cross-section of the tubular surface was not circular, but elliptical, in accordance with the shape obtained for the horizontal-vertical and vertical-longitudinal 2D scans.

The scans in this section were achieved due to an excellent RF stability of the modulator installed at ARTI, and an excellent pointing stability provided by the PHAROS laser (documented in Chapter 2.2).

## 4.8 Conclusions and achievements of the CBS experiment

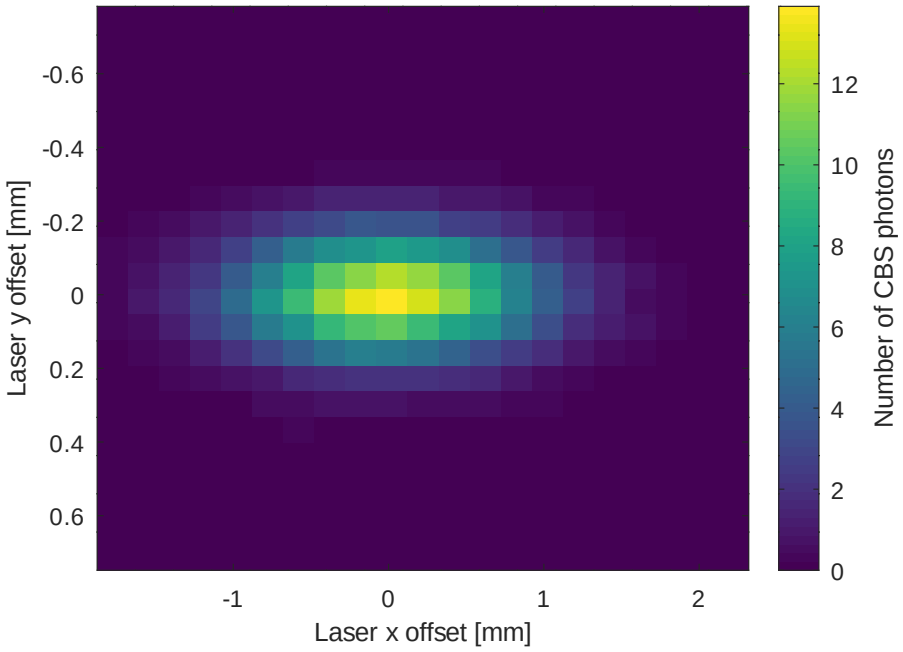
This chapter presented a comprehensive description of the Compton backscattering experiment performed at ARTI. Following the optimisation of the electron beamline to maximise the detected CBS photon flux and the consolidation of the RF-Track model of the gun beamline, a custom-designed vacuum chamber housing a microchannel plate detector was installed. After integration into the beamline, the MCP was calibrated using an Fe-55 radioactive source, which emits photons of energies comparable to those produced in the CBS interaction.

The spatial and temporal alignment of the electron and laser beams was achieved using a custom optical transition radiation screen, enabling fine control of the relative beam displacement. The CBS signal was subsequently identified during a longitudinal offset scan, after which a series of systematic scans was performed. These measurements fully mapped the interaction region and characterised the dependence of the detected CBS photon yield on a range of tunable input parameters. The experimentally measured results were then compared with simulations performed using the RF-Track code, yielding excellent agreement and thereby validating the newly implemented CBS module.

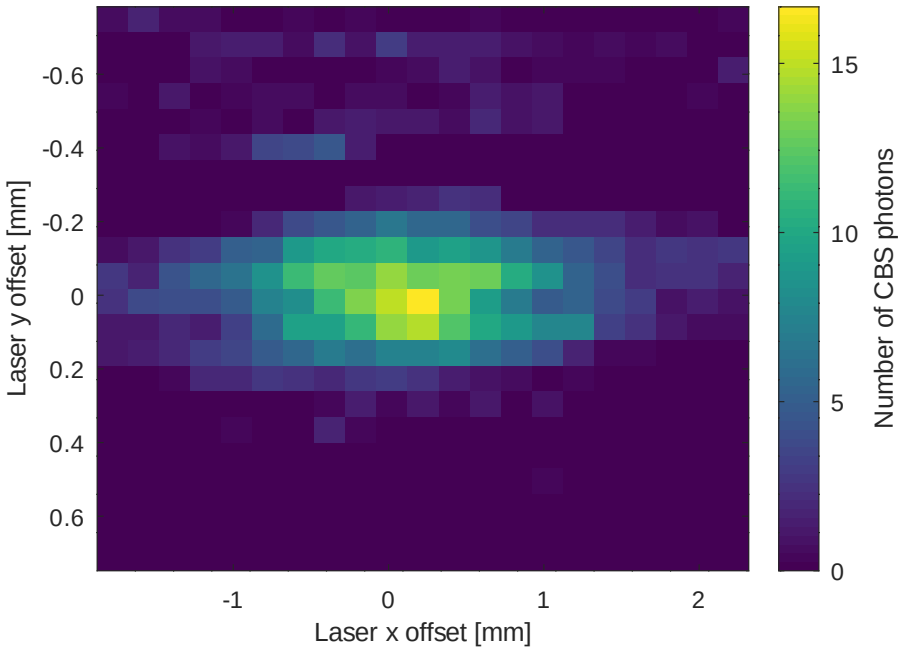
In addition to providing a thorough benchmark of RF-Track against experimental CBS data obtained at a CERN facility, the experiment demonstrated the feasibility of generating narrow-bandwidth soft X-ray photons using the smallest RF-based CBS set-up reported in the literature at the time of writing. Furthermore, the two- and three-dimensional scans performed in this work represent, to

the author's knowledge, the first experimental attempt to map the spatial extent of the CBS interaction region.

Despite these achievements, the detection of the CBS signal proved challenging. Owing to the large angular divergence of the scattered photons, the majority of the generated X-rays were absorbed by the beam pipe walls, with only a small fraction reaching the active area of the MCP detector. No practical mitigation strategy was identified within the constraints of the existing beamline. The detector was therefore positioned as close as possible to the dipole spectrometer at which the electron and X-ray beams were separated. While the use of X-ray optics could, in principle, improve photon collection for higher CBS yields, significant losses would still be expected during transport through X-ray capillaries [138]. Moreover, such optics could only be installed downstream of the dipole magnet, as placement closer to the interaction point would result in electron–optics interactions, producing bremsstrahlung and additional background on the MCP. With a sufficiently stronger CBS signal, the installation of an X-ray imaging detector or spectrometer in place of the MCP would have enabled a more detailed characterisation of the X-ray beam profile.

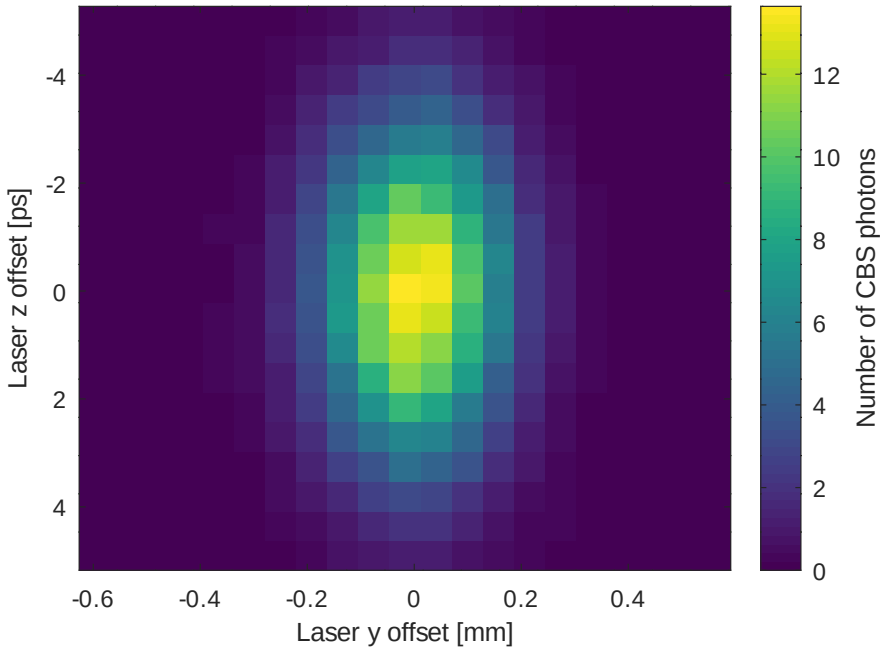



(a)

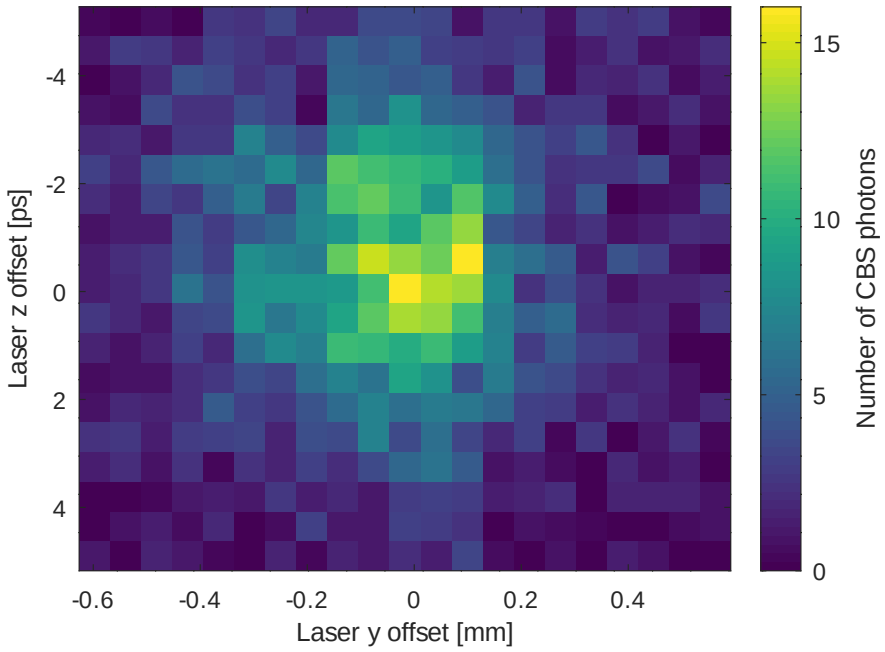



(b)

Figure 4.37: Two-dimensional scan of the horizontal and vertical position of the IR laser around the IP, against the number of CBS photons detected by the MCP in the RF-Track simulation (a) and experimental measurement (b).

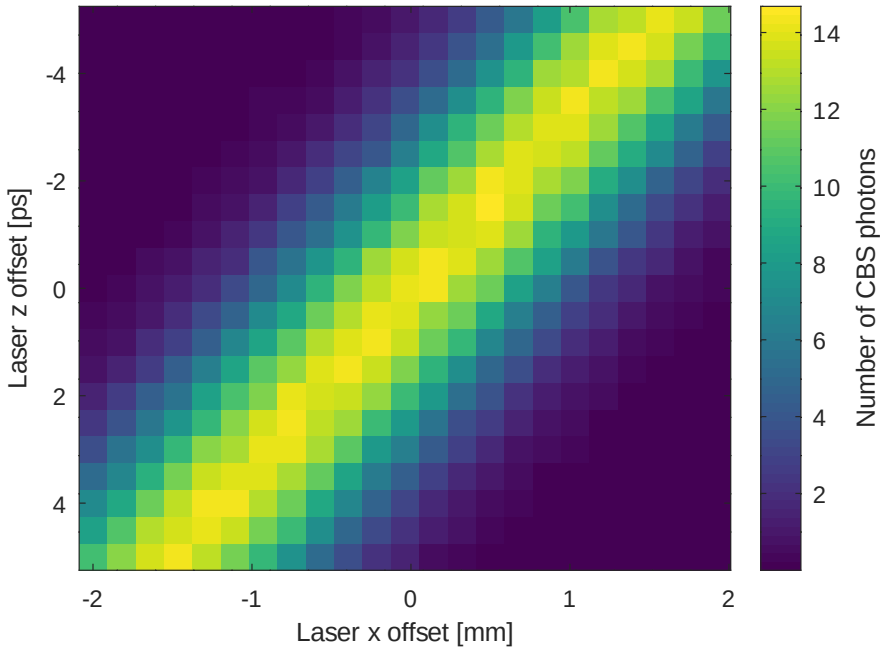



(a)

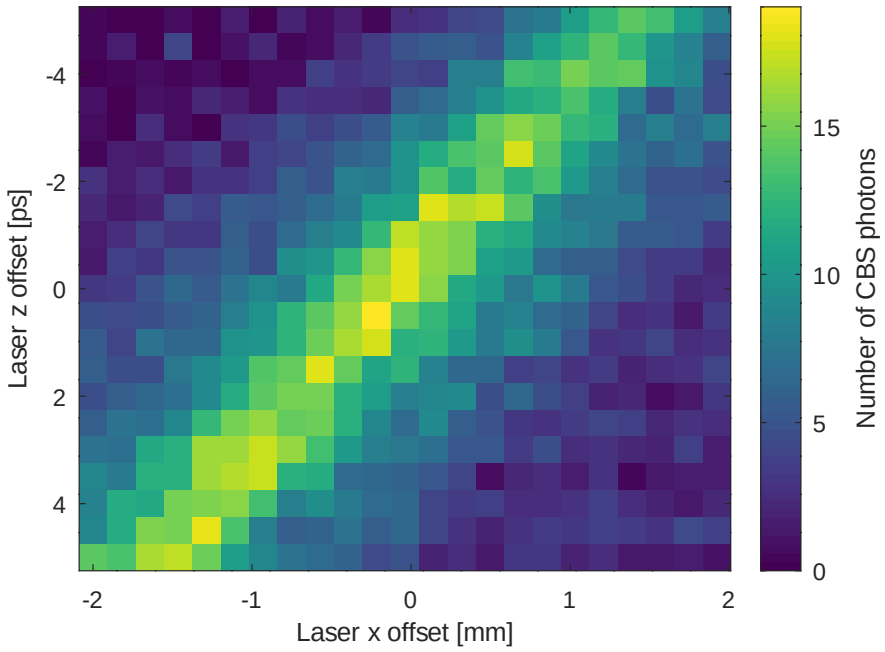



(b)

Figure 4.38: Two-dimensional scan of the vertical position and arrival time of the IR laser around the IP, against the number of CBS photons detected by the MCP in the RF-Track simulation (a) and experimental measurement (b).

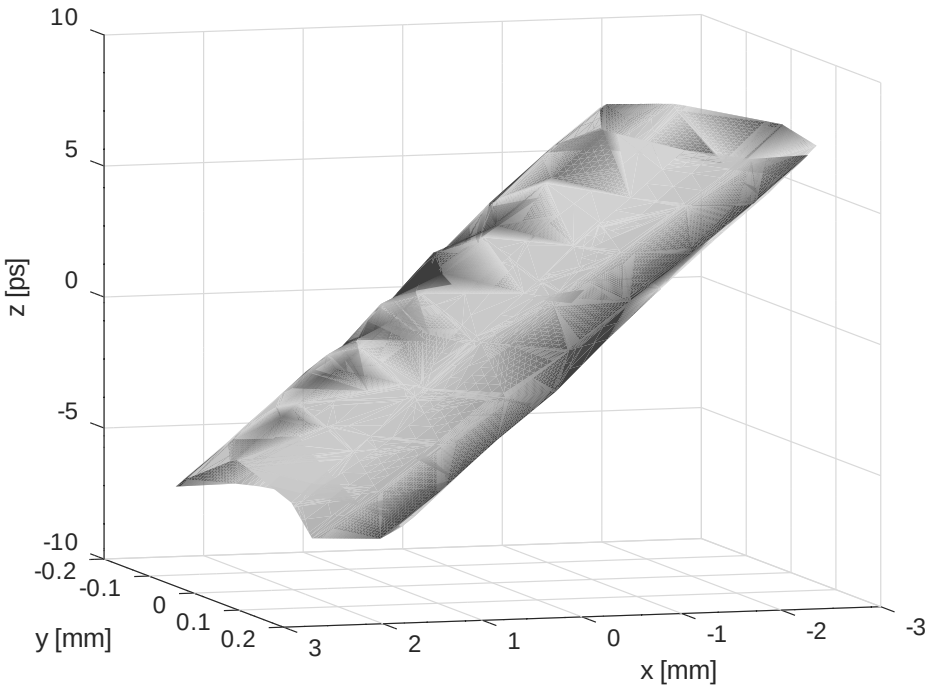



(a)

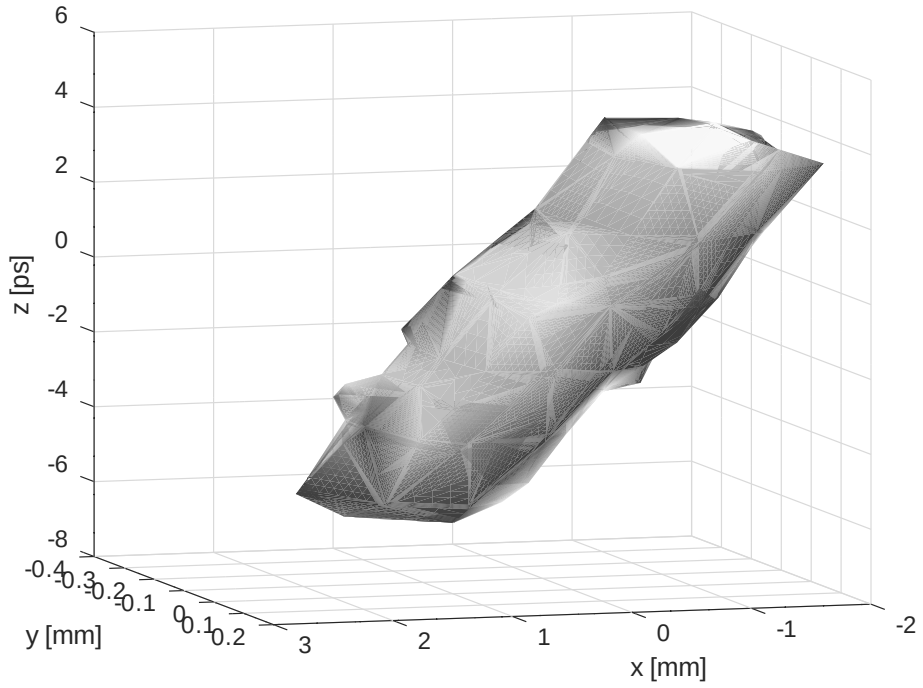



(b)

Figure 4.39: Two-dimensional scan of the horizontal position and arrival time of the IR laser around the IP, against the number of CBS photons detected by the MCP in the RF-Track simulation (a) and experimental measurement (b).




(a)




(b)

Figure 4.40: Three-dimensional scan of the horizontal and vertical position of the IR laser around the IP, along with the laser's arrival time, against the number of CBS photons detected by the MCP in the RF-Track simulation (a) and in the experimental measurement (b). The 3D plots represent isosurfaces, with an amplitude threshold set as 40% of the maximum flux value.

# Chapter 5

# Conclusions and Further Work

A Compton backscattering experiment was performed at the AWAKE Run 2 Test Injector, resulting in one of the most compact RF-based CBS sources reported in the literature at the time of writing, with a cathode-to-detector distance of 1 m. The system demonstrated the generation of soft X-rays in the water window regime within a compact RF accelerator configuration. A dedicated RF-Track model of the beamline was developed to predict the scattered photon flux at the location of a vacuum-compatible X-ray detector. To enable experimental validation, a custom vacuum chamber housing a microchannel plate (MCP) detector was designed, manufactured, and integrated into the beamline. A detailed calibration campaign was conducted using an Fe-55 radioactive source in order to determine the detector response and accurately infer the number of CBS photons from the measured signals.

Prior to the CBS experiment, the ARTI beamline was optimised to provide a high quality electron beam at the IP by tuning the input parameters of the photocathode laser, electron gun, and solenoid magnet. Beam-based alignment measurements were performed to correct transverse offsets and validate the model predictions, resulting in a significant reduction of the electron beam size at the interaction point. Subsequent scans of the RF phase, solenoid field, and laser spot size confirmed the simulated trends and identified the operating conditions that produced the smallest beam sizes. The study also revealed the presence of a beam halo containing approximately 25% of the bunch charge, which was traced to secondary laser pulses generated by reflections in the optical transport system.

Overall, the optimisation campaign provided the beam quality and signal-to-noise ratio required for the successful observation of Compton backscattering at ARTI.

The experimental measurements of the CBS photon yield and interaction region were benchmarked against RF-Track simulations, yielding excellent agreement and thereby validating both the beamline model and the CBS implementation within RF-Track. Prior to the CBS campaign, the injector beamline was commissioned and optimised to deliver a high-density, low-emittance electron beam at the interaction point. During this process, a previously unreported source of injector beam halo was identified, originating from multiple reflections of the cathode laser within upstream optical components. The halo-to-core fraction was quantified, and dedicated mitigation procedures were developed to suppress this contribution, thereby improving beam quality and stability at the interaction point.

With regard to future developments, the CBS module of RF-Track should be validated in a high-energy beamline, as this regime is representative of the majority of existing and proposed Compton backscattering sources. Such an experimental campaign would provide a stringent benchmark of the module under conditions where recoil effects and beam–laser interaction dynamics become more pronounced. Following successful validation, RF-Track could be employed for the comprehensive design of a high-energy CBS source, including start-to-end optimisation studies.

To ensure compactness while maximising photon flux, such a source could integrate advanced accelerator and laser technologies, such as X-band accelerating structures developed for CLIC and burst-mode-operated Fabry-Pérot optical enhancement cavities. The combination of high-gradient acceleration and enhanced optical power offers a promising route toward compact, high-brightness CBS facilities.

Although the CBS module was successfully benchmarked against the experimental results presented in this work, it currently models only the linear Compton regime. It does not account for nonlinear CBS effects [139, 140], which arise at high laser intensities where a single electron can absorb multiple photons within a single scattering event. Extending the module to include nonlinear Compton processes would significantly broaden its applicability, particularly in view of the growing interest in strong-field QED phenomena [141]. Such an implementation

would position RF-Track as a versatile tool for both applied photon-source development and fundamental high-field physics studies.

# Appendix A

# RF-Track Example Code

This appendix presents an example GNU Octave script used to simulate Compton backscattering in RF-Track. The code demonstrates the definition of an electron bunch and laser pulse, the implementation of the interaction geometry, and the calculation of the resulting scattered photon distribution.

```
RF_Track;
%% Define beam-laser IP parameters
L_FP = 0.0; % m, length of the IP region
IP_beta = 0.1; % m, beta star
IP_Lstar = L_FP/2; % m
X_angle = 2; % deg, crossing angle
%% Define beam parameters
Pref = 50; % MeV/c
Pspread = 3; % permil, momentum spread
sigma_t = 5 * RF_Track.ps; % mm/c
Q_pC = 1000; % pC, bunch charge
%% Define Twiss parameters
Twiss = Bunch6d_twiss();
Twiss.emitt_x = 5; % mm.mrad, normalized emittances
Twiss.emitt_y = 5; % mm.mrad
Twiss.beta_x = IP_beta + IP_Lstar^2 / IP_beta; % m
Twiss.beta_y = IP_beta + IP_Lstar^2 / IP_beta; % m
Twiss.alpha_x = IP_Lstar / IP_beta; % converging beam
Twiss.alpha_y = IP_Lstar / IP_beta; %
Twiss.sigma_t = sigma_t; % mm/c
Twiss.sigma_pt = Pspread; % permil
%% Create the bunch
B0 = Bunch6d(RF_Track.electronmass, Q_pC*RF_Track.pC, -1, Pref,
    Twiss, 10000);
E0 = B0.get_phase_space();
%% Define laser-beam IP region
FP = LaserBeam(); % Fabry-Perot resonator
```

```
FP.pulse_energy = 28; % mJ, laser pulse energy
FP.pulse_length = 5; % ps, laser pulse length
FP.wavelength = 1030; % nm, laser wavelength
FP.set_direction(sind(180-X_angle), 0, cosd(180-X_angle)); % 2
    degrees crossing angle
FP.length = L_FP;
FP.set_position(IP_Lstar); % m
FP.R = 0.035; % mm, laser rms radius at waist, Gaussian profile
FP.M2 = 1; %
FP.min_number_of_gammas_per_slice = 10;
FP.set_nsteps(20);
%% Define lattice
L = Lattice();
L.append (FP);
%% Tracking
B1 = L.track(B0);
%% Post-processing
M1 = B1.get_phase_space('%x %xp %y %yp %t %Pc %m %N %Vz');
M1_w = M1(:,7)==0.0; % pick the photons
E1 = M1(~M1_w,:); % electrons
P1 = M1( M1_w,:); % gammas
%% Total number of gammas produced
Nw_RFT = sum(P1(:,8))s
```

Listing A.1: Example script for simulating the CBS interaction between an electron bunch and laser pulse.

The script begins by defining the interaction point geometry, including the beta function at the interaction point, the interaction region length, and the laser–electron crossing angle. The electron bunch parameters are then specified through the reference momentum, momentum spread, bunch length, bunch charge, and transverse Twiss parameters. Using these inputs, a six-dimensional electron bunch is generated with the `Bunch6d` class.

The laser pulse is subsequently defined using the `LaserBeam` class, where the pulse energy, pulse duration, wavelength, spot size, crossing angle, and interaction region are specified. The laser is modelled as a Gaussian beam and configured to calculate the Compton scattering process over a series of longitudinal integration steps. The interaction point is then inserted into an RF-Track lattice, after which the electron bunch is tracked through the interaction region. During tracking, RF-Track computes the Compton scattering process and generates the corresponding scattered photons.

Finally, the output phase-space distribution is analysed to separate the scattered photons from the electron macroparticles. The total number of generated photons is obtained by summing the statistical weights of all photon macroparticles, providing an estimate of the Compton backscattering yield for the specified beam and laser parameters. This example illustrates the simplicity of the RF-Track framework, which enables the complete simulation of a Compton backscattering interaction within a compact script.

The simplicity of the RF-Track framework enables the definition of an electron bunch and laser pulse, together with the calculation of their Compton backscattering interaction, in fewer than 50 lines of code.

# Bibliography


[1] S. Navas et al. (Particle Data Group). "Review of Particle Physics". *Physical Review D* 110 (2024), p. 030001. DOI: 10.1103/PhysRevD.110.030001.

[2] J. J. Thomson. "XL. Cathode Rays ". *The London, Edinburgh, and Dublin Philosophical Magazine and Journal of Science* 44 (1897), pp. 293–316. DOI: 10.1080/14786449708621070. URL: https://doi.org/10.1080/14786449708621070.

[3] S. H. Neddermeyer and C. D. Anderson. "Note on the Nature of Cosmic-Ray Particles". *Physical Review* 51 (1937), pp. 884–886. DOI: 10.1103/PhysRev.51.884.

[4] E. D. Bloom et al. "High-Energy Inelastic e-p Scattering at 6° and 10°". *Physical Review Letters* 23 (1969), pp. 930–934. DOI: 10.1103/PhysRevLett.23.930.

[5] J. J. Aubert et al. "Experimental Observation of a Heavy Particle J". *Physical Review Letters* 33 (1974), pp. 1404–1406. DOI: 10.1103/PhysRevLett.33.1404.

[6] M. L. Perl et al. "Evidence for Anomalous Lepton Production in e+e- Annihilation". *Physical Review Letters* 35 (1975), pp. 1489–1492. DOI: 10.1103/PhysRevLett.35.1489.

[7] S. W. Herb et al. "Observation of a Dimuon Resonance at 9.5 GeV in 400-GeV Proton-Nucleus Collisions". *Physical Review Letters* 39 (1977), pp. 252–255. DOI: 10.1103/PhysRevLett.39.252.

[8] D. P. Barber et al. "Discovery of Three-Jet Events and a Test of Quantum Chromodynamics at PETRA". *Physical Review Letters* 43 (1979), pp. 830–833. DOI: 10.1103/PhysRevLett.43.830.

[9] G. Arnison et al. "Experimental observation of lepton pairs of invariant mass around 95 GeV/c2 at the CERN SPS collider". *Physics Letters B* 126 (1983), pp. 398–410. DOI: 10.1016/0370-2693(83)90188-0.

[10] S. Abachi et al. "Observation of the Top Quark". *Physical Review Letters* 74 (1995), pp. 2632–2637. DOI: 10.1103/PhysRevLett.74.2632.

[11] G. Aad et al. "Observation of a new particle in the search for the Standard Model Higgs boson with the ATLAS detector at the LHC". *Physics Letters B* 716 (2012), pp. 1–29. DOI: https://doi.org/10.1016/j.physletb.2012.08.020. URL: https://www.sciencedirect.com/science/article/pii/S037026931200857X.

[12] H. Haber. "The search for supersymmetry: Probing physics beyond the standard model". *Physics Reports* 117 (1985), pp. 75–263. DOI: 10.1016/0370-1573(85)90051-1.

[13] M. S. Livingston. "Early History of Particle Accelerators**Work done under the auspices of the U.S. Department of Energy." Ed. by L. Marton and C. Marton. Vol. 50. Advances in Electronics and Electron Physics. Academic Press, 1980, pp. 1–88. DOI: https://doi.org/10.1016/S0065-2539(08)61061-6. URL: https://www.sciencedirect.com/science/article/pii/S0065253908610616.

[14] J. Maldacena. "The large N limit of superconformal field theories and supergravity". *Advances in Theoretical and Mathematical Physics* 2 (1998), pp. 231–252. DOI: 10.4310/ATMP.1998.v2.n2.a1.

[15] S. Chatrchyan et al. "Observation of a new boson at a mass of 125 GeV with the CMS experiment at the LHC". *Physics Letters B* 716 (2012), pp. 30–61. DOI: https://doi.org/10.1016/j.physletb.2012.08.021. URL: https://www.sciencedirect.com/science/article/pii/S0370269312008581.

[16] G. Moortgat-Pick et al. "Polarized positrons and electrons at the linear collider". *Physics Reports* 460 (2008), pp. 131–243. DOI: 10.1016/j.physrep.2007.12.003.

[17] P. C. Rowson, D. Su, and S. Willocq. "Highlights of the SLD Physics Program at the SLAC Linear Collider". *Annual Review of Nuclear and Particle Science* 51 (2001), pp. 345–412. DOI: 10.1146/annurev.nucl.51.101701.132413.

[18] D. Schulte. "Beam-beam effects in linear colliders". *CERN Yellow Reports: School Proceedings*. Vol. 3. 2017. DOI: 10.23730/CYRSP-2017-003.431.

[19] M. Jeitler. "The European Strategy for Particle Physics and its Update in 2020". *Proceedings of ALPS 2019 An Alpine LHC Physics Summit — PoS(ALPS2019)*. Trieste, Italy: Sissa Medialab, 2021, p. 002. DOI: 10.22323/1.360.0002.

[20] H. Abramowicz et al. "A linear collider vision for the future of particle physics". *The European Physical Journal Special Topics* (2026). DOI: 10.1140/epjs/s11734-026-02153-w.

[21] E. Adli et al. “CLIC readiness report”. *The European Physical Journal Special Topics* 234 (2026), pp. 6473–6652. DOI: 10.1140/epjs/s11734-025-02016-w.

[22] M. Aicheler et al. *A Multi-TeV Linear Collider Based on CLIC Technology*. CERN Yellow Reports: Monographs. Geneva: CERN, 2012. DOI: 10.5170/CERN-2012-007. URL: https://cds.cern.ch/record/1500095.

[23] T. K. Charles et al. “The Compact Linear Collider (CLIC) - 2018 Summary Report” (2019). DOI: 10.23731/CYRM-2018-002.

[24] E. Adli et al. “The Compact Linear e+e- Collider (CLIC)” (2025).

[25] L. Wroe et al. “Compact Electron Linacs for Research, Medical, and Industrial Applications”. *Proceedings of 42nd International Conference on High Energy Physics — PoS(ICHEP2024)*. Trieste, Italy: Sissa Medialab, 2025, p. 831. DOI: 10.22323/1.476.0831.

[26] L. Wroe et al. “Electron-driven, pulsed neutron source”. *The European Physical Journal Special Topics* (2025). DOI: 10.1140/epjs/s11734-025-01827-1.

[27] J. O. Herrador et al. “Feasibility of High-Intensity Electron Linacs as Drivers for Compact Neutron Sources”. *IEEE Transactions on Nuclear Science* 73 (2025), pp. 2–11. DOI: 10.1109/TNS.2025.3637190.

[28] E. Gschwendtner et al. “AWAKE, The Advanced Proton Driven Plasma Wakefield Acceleration Experiment at CERN”. *Nuclear Instruments and Methods in Physics Research Section A: Accelerators, Spectrometers, Detectors and Associated Equipment* 829 (2016), pp. 76–82. DOI: 10.1016/j.nima.2016.02.026.

[29] E. Adli et al. “Acceleration of electrons in the plasma wakefield of a proton bunch”. *Nature* 561 (2018), pp. 363–367. DOI: 10.1038/s41586-018-0485-4.

[30] E. Adli and P. Muggli. “Proton-beam-driven plasma acceleration”. *Reviews of Accelerator Science and Technology*. Vol. 9. 2017. DOI: 10.1142/S1793626816300048.

[31] J. S. Schmidt et al. “The AWAKE electron primary beam line”. *6th International Particle Accelerator Conference, IPAC 2015*. 2015.

[32] H. Wiedemann. *Particle Accelerator Physics*. Berlin, Heidelberg: Springer Berlin Heidelberg, 2007. DOI: 10.1007/978-3-540-49045-6.

[33] E. D. Courant and H. S. Snyder. "Theory of the alternating-gradient synchrotron". *Annals of Physics* 3 (1958), pp. 1–48. DOI: https://doi.org/10.1016/0003-4916(58)90012-5. URL: https://www.sciencedirect.com/science/article/pii/0003491658900125.

[34] E. Wilson. *An Introduction to Particle Accelerators*. Oxford University Press, 2001. DOI: 10.1093/acprof:oso/9780198508298.001.0001. URL: https://doi.org/10.1093/acprof:oso/9780198508298.001.0001.

[35] J. Liouville. "Note sur la Théorie de la Variation des constantes arbitraires." fre. *Journal de Mathématiques Pures et Appliquées* (1838), pp. 342–349. URL: http://eudml.org/doc/234417.

[36] G. A. Krafft and G. Priebe. "Compton Sources of Electromagnetic Radiation". *Reviews of Accelerator Science and Technology* 03 (2010), pp. 147–163. DOI: 10.1142/S1793626810000440.

[37] E. Feenberg and H. Primakoff. "Interaction of Cosmic-Ray Primaries with Sunlight and Starlight". *Physical Review* 73 (1948), pp. 449–469. DOI: 10.1103/PhysRev.73.449.

[38] R. H. Milburn. "Electron Scattering by an Intense Polarized Photon Field". *Physical Review Letters* 10 (1963), pp. 75–77. DOI: 10.1103/PhysRevLett.10.75.

[39] F. Arutyunian and V. Tumanian. "The Compton effect on relativistic electrons and the possibility of obtaining high energy beams". *Physics Letters* 4 (1963), pp. 176–178. DOI: 10.1016/0031-9163(63)90351-2.

[40] P. Sprangle et al. "High-power lasers for directed-energy applications". *Applied Optics* 54 (2015), F201. DOI: 10.1364/AO.54.00F201.

[41] S. Kulpe et al. "K-edge subtraction imaging for coronary angiography with a compact synchrotron X-ray source". *PLOS ONE* 13 (2018). Ed. by R. Zhang, e0208446. DOI: 10.1371/journal.pone.0208446. URL: https://dx.plos.org/10.1371/journal.pone.0208446.

[42] R. Gradl et al. "Propagation-based Phase-Contrast X-ray Imaging at a Compact Light Source". *Scientific Reports* 7 (2017), p. 4908. DOI: 10.1038/s41598-017-04739-w.

[43] Y. Du et al. "Generation of first hard X-ray pulse at Tsinghua Thomson Scattering X-ray Source". *Review of Scientific Instruments* 84 (2013). DOI: 10.1063/1.4803671.

[44] H. R. Weller et al. *Research opportunities at the upgraded HI$\gamma$S facility*. 2009. DOI: 10.1016/j.ppnp.2008.07.001.

[45] K. Dupraz et al. “The ThomX ICS source”. *Physics Open* 5 (2020). DOI: 10.1016/j.physo.2020.100051.

[46] W. S. Graves. “The CXFEL Project at Arizona State University”. *Proc. 67th ICFA Adv. Beam Dyn. Workshop Future Light Sources (FLS'23)*. ICFA Advanced Beam Dynamics Workshop. JACoW Publishing, Geneva, Switzerland, 2024, pp. 54–57. DOI: 10.18429/JACoW-FLS2023-TU1C4. URL: http://jacow.org/fls2023/papers/tu1c4.pdf.

[47] P. Cardarelli et al. “BriXS, a new X-ray inverse Compton source for medical applications”. *Physica Medica* 77 (2020). DOI: 10.1016/j.ejmp.2020.08.013.

[48] A. Bacci et al. “The STAR project”. *IPAC 2014: Proceedings of the 5th International Particle Accelerator Conference*. 2014.

[49] A. Bacci et al. “Status of the STAR project”. *IPAC 2016 - Proceedings of the 7th International Particle Accelerator Conference*. 2016.

[50] T. Akagi et al. “Narrow-band photon beam via laser Compton scattering in an energy recovery linac”. *Physical Review Accelerators and Beams* 19 (2016), p. 114701. DOI: 10.1103/PhysRevAccelBeams.19.114701.

[51] I. Drebot et al. “Brixsino high-flux dual X-ray and THz radiation source based on energy recovery linacs”. *Proc. IPAC'23*. International Particle Accelerator Conference. JACoW Publishing, Geneva, Switzerland, 2023, pp. 2123–2126. DOI: 10.18429/JACoW-IPAC2023-TUPL162.

[52] V. Mușat, A. Latina, and G. D'Auria. “A High-Energy and High-Intensity Inverse Compton Scattering Source Based on CompactLight Technology”. *Photonics* 9 (2022), p. 308. DOI: 10.3390/photonics9050308.

[53] S. Kulpe et al. “K-edge Subtraction Computed Tomography with a Compact Synchrotron X-ray Source”. *Scientific Reports* 9 (2019). DOI: 10.1038/s41598-019-49899-z.

[54] R. Gradl et al. “In vivo Dynamic Phase-Contrast X-ray Imaging using a Compact Light Source”. *Scientific Reports* 8 (2018). DOI: 10.1038/s41598-018-24763-8.

[55] M. Jacquet and P. Suortti. “Radiation therapy at compact Compton sources”. *Physica Medica* 31 (2015), pp. 596–600. DOI: 10.1016/j.ejmp.2015.02.010.

[56] A. C. Dombrowsky et al. “A proof of principle experiment for microbeam radiation therapy at the Munich compact light source”. *Radiation and Environmental Biophysics* 59 (2020), pp. 111–120. DOI: 10.1007/s00411-019-00816-y.

[57] S. Bartzsch et al. “Technical advances in x-ray microbeam radiation therapy”. *Physics in Medicine & Biology* 65 (2020), 02TR01. DOI: 10.1088/1361-6560/ab5507.

[58] J. Bourhis et al. “Clinical translation of FLASH radiotherapy: Why and how?” *Radiotherapy and Oncology* 139 (2019), pp. 11–17. DOI: 10.1016/j.radonc.2019.04.008.

[59] P. Montay-Gruel et al. “X-rays can trigger the FLASH effect: Ultra-high dose-rate synchrotron light source prevents normal brain injury after whole brain irradiation in mice”. *Radiotherapy and Oncology* 129 (2018). DOI: 10.1016/j.radonc.2018.08.016.

[60] J. Abendroth et al. “X-ray structure determination of the glycine cleavage system protein H of Mycobacterium tuberculosis using an inverse Compton synchrotron X-ray source”. *Journal of Structural and Functional Genomics* 11 (2010), pp. 91–100. DOI: 10.1007/s10969-010-9087-6.

[61] S. R. Byrn, G. Zografi, and X. ( Chen. *Solid State Properties of Pharmaceutical Materials*. Wiley, 2017. DOI: 10.1002/9781119264408.

[62] P. Walter et al. “A new high quality X-ray source for Cultural Heritage”. *Comptes Rendus. Physique* 10 (2009), pp. 676–690. DOI: 10.1016/j.crhy.2009.09.001.

[63] J. Dik et al. “Visualization of a lost painting by Vincent van Gogh using synchrotron radiation based X-ray fluorescence elemental mapping”. *Analytical Chemistry* 80 (2008), pp. 6436–6442. DOI: 10.1021/ac800965g.

[64] R. Hajima et al. “Proposal of nondestructive radionuclide assay using a high-flux gamma-ray source and nuclear resonance fluorescence”. *Journal of Nuclear Science and Technology* 45 (2008), pp. 441–451. DOI: 10.1080/18811248.2008.9711453.

[65] M. Jacquet. “Potential of compact Compton sources in the medical field”. *Physica Medica* 32 (2016), pp. 1790–1794. DOI: 10.1016/j.ejmp.2016.11.003.

[66] K. E. Deitrick et al. “High-brilliance, high-flux compact inverse Compton light source”. *Physical Review Accelerators and Beams* 21 (2018), p. 080703. DOI: 10.1103/PhysRevAccelBeams.21.080703.

[67] O. Klein and Y. Nishina. “Über die Streuung von Strahlung durch freie Elektronen nach der neuen relativistischen Quantendynamik von Dirac”. *Zeitschrift für Physik* 52 (1929), pp. 853–868. DOI: 10.1007/BF01366453.

[68] V. Petrillo et al. “Photon flux and spectrum of $\gamma$-rays Compton sources”. *Nuclear Instruments and Methods in Physics Research, Section A: Accelerators, Spectrometers, Detectors and Associated Equipment* 693 (2012), pp. 109–116. DOI: 10.1016/j.nima.2012.07.015.

[69] C. Curatolo et al. “Analytical description of photon beam phase spaces in inverse Compton scattering sources”. *Physical Review Accelerators and Beams* 20 (2017), p. 080701. DOI: 10.1103/PhysRevAccelBeams.20.080701.

[70] J. M. Arnesano and S. Doebert. “Design of an X-band bunching and accelerating system for the AWAKE Run 2”. *Proceedings - Linear Accelerator Conference, LINAC*. 2022, pp. 458–461. DOI: 10.18429/JACoW-LINAC2022-TUPOPA24.

[71] D. Alesini et al. “Design, realization, and high power test of high gradient, high repetition rate brazing-free S-band photogun”. *Physical Review Accelerators and Beams* 21 (2018), p. 112001. DOI: 10.1103/PhysRevAccelBeams.21.112001.

[72] M. Kördel et al. “Laboratory water-window x-ray microscopy”. *Optica* 7 (2020), pp. 658–674. DOI: 10.1364/OPTICA.393014.

[73] F. Tuinstra and J. L. Koenig. “Raman Spectrum of Graphite”. *The Journal of Chemical Physics* 53 (1970), pp. 1126–1130. DOI: 10.1063/1.1674108.

[74] R. Ischebeck et al. “Transverse profile imager for ultrabright electron beams”. *Physical Review Special Topics - Accelerators and Beams* 18 (2015), p. 082802. DOI: 10.1103/PhysRevSTAB.18.082802.

[75] U. Iriso, G. Benedetti, and F. Pérez. “Experience with YAG and OTR screens at ALBA”. *DIPAC 2009 - 9th European Workshop on Beam Diagnostics and Instrumentation for Particle Accelerators*. JACoW Publishing, Geneva, Switzerland, 2009, pp. 200–202.

[76] Ö. Mete. “Study and Experimental Characterization of a Novel Photo Injector for the CLIC Drive Beam”. en. PhD thesis. Lausanne: EPFL, 2011. DOI: 10.5075/epfl-thesis-5020. URL: https://infoscience.epfl.ch/handle/20.500.14299/64463.

[77] E. Granados et al. “Optical and laser systems for the AWAKE run 2C experiment”. English. *Proc. IPAC’25*. IPAC’25 - 16th International Particle Accelerator Conference. JACoW Publishing, Geneva, Switzerland, 2025, pp. 1604–1607. DOI: 10.18429/JACoW-IPAC2025-TUPS111. URL: https://indico.jacow.org/event/81/contributions/7765.

[78] E. Panofski et al. "Virtual cathode diagnostics with a large dynamic range for a continuous Wave SRF photoinjector". *IPAC 2014: Proceedings of the 5th International Particle Accelerator Conference*. 2014. DOI: 10.18429/JACoW-IPAC2014-WEPME001.

[79] A. Latina. *RF-Track Reference Manual Version 2.1.6*. Tech. rep. 2016. DOI: 10.5281/zenodo.3887084. URL: https://zenodo.org/records/3887085.

[80] P. Chen et al. "CAIN: Conglomérat d'ABEL et d'Interactions Non-linéaires". *Nuclear Inst. and Methods in Physics Research, A* 355 (1995). DOI: 10.1016/0168-9002(94)01186-9.

[81] W. J. Brown et al. "Experimental characterization of an ultrafast Thomson scattering x-ray source with three-dimensional time and frequency-domain analysis". *Physical Review Special Topics - Accelerators and Beams* 7 (2004), p. 060702. DOI: 10.1103/PhysRevSTAB.7.060702.

[82] W. J. Brown and F. V. Hartemann. "Three-dimensional time and frequency-domain theory of femtosecond x-ray pulse generation through Thomson scattering". *Physical Review Special Topics - Accelerators and Beams* 7 (2004), p. 060703. DOI: 10.1103/PhysRevSTAB.7.060703.

[83] Landau L.D. and Lifshitz E.M. *Mechanics and Electrodynamics*. Elsevier, 1972. DOI: 10.1016/C2009-0-06775-0.

[84] "TESLA Technical Design Report". *Physical Review E - Statistical, Nonlinear, and Soft Matter Physics* 71 (2005). DOI: 10.1103/PhysRevE.71.061919.

[85] M. G. Ronga et al. "Very High-Energy Electrons (VHEEs) and Their Potential Application in Radiation Therapy". *Cancers* 13 (2021), p. 4942. DOI: 10.3390/cancers13194942.

[86] A. Latina and V. Mușat. "An Inverse-Compton Scattering Simulation Module for RF-Track". *JACoW* FLS2023 (2024), TU4P33. DOI: 10.18429/JACoW-FLS2023-TU4P33.

[87] W. S. Graves et al. "Compact x-ray source based on burst-mode inverse Compton scattering at 100 kHz". *Physical Review Special Topics - Accelerators and Beams* 17 (2014), p. 120701. DOI: 10.1103/PhysRevSTAB.17.120701.

[88] C. Sun and Y. K. Wu. "Theoretical and simulation studies of characteristics of a Compton light source". *Physical Review Special Topics - Accelerators and Beams* 14 (2011), p. 044701. DOI: 10.1103/PhysRevSTAB.14.044701.

[89] B. Terzić et al. "Improving performance of inverse Compton sources through laser chirping". *EPL (Europhysics Letters)* 126 (2019), p. 12003. DOI: 10.1209/0295-5075/126/12003.

[90] A. Variola et al. *ThomX Technical Design Report*. Tech. rep. LAL, Laboratoire de l'accélérateur linéaire, 2014, 164 p. URL: https://in2p3.hal.science/in2p3-00971281.

[91] I. Drebot et al. "Brixs ultra high flux inverse compton source based on modified push-pull energy recovery linacs". *Instruments* 3 (2019). DOI: 10.3390/instruments3030049.

[92] N. Sei, H. Ogawa, and S. Okuda. "Demonstration of narrowband X-ray beam by inverse Compton scattering with stored spontaneous emission". *Journal of Applied Physics* 121 (2017). DOI: 10.1063/1.4973794.

[93] I. Chaikovska et al. "High flux circularly polarized gamma beam factory: coupling a Fabry-Perot optical cavity with an electron storage ring". *Scientific Reports* 6 (2016), p. 36569. DOI: 10.1038/srep36569.

[94] Y. Sakai et al. "Hard X-ray inverse Compton scattering at photon energy of 87.5 keV". *Scientific Reports* 14 (2024), p. 18467. DOI: 10.1038/s41598-024-68170-8.

[95] G. B. Dantzig. "Origins of the simplex method". *A history of scientific computing*. Association for Computing Machinery (ACM), New York, USA, 1990. DOI: 10.1145/87252.88081.

[96] J. Gallego et al. "High-finesse fiber Fabry–Perot cavities: stabilization and mode matching analysis". *Applied Physics B: Lasers and Optics* 122 (2016). DOI: 10.1007/s00340-015-6281-z.

[97] V. Mușat et al. "An efficient optimisation of a burst mode-operated Fabry-Perot cavity for Compton light sources". *Proceedings of FLS2023* (2023), pp. 46–49. DOI: 10.18429/JACoW-FLS2023-TU1C1.

[98] E. M. F. Curado and C. Tsallis. "Generalized statistical mechanics: Connection with thermodynamics". *Journal of Physics A: Mathematical and General* 24 (1992), p. L69. DOI: 10.1088/0305-4470/25/4/038.

[99] S. Umarov, C. Tsallis, and S. Steinberg. "On a q-central limit theorem consistent with nonextensive statistical mechanics". *Milan Journal of Mathematics* 76 (2008), p. 307. DOI: 10.1007/s00032-008-0087-y.

[100] D. H. Dowell and J. F. Schmerge. "Quantum efficiency and thermal emittance of metal photocathodes". *Physical Review Special Topics - Accelerators and Beams* 12 (2009), p. 074201. DOI: 10.1103/PhysRevSTAB.12.074201.

[101] Vikas and R. K. Sahu. "A review on application of laser tracker in precision positioning metrology of particle accelerators". *Precision Engineering* 71 (2021), pp. 232–249. DOI: 10.1016/j.precisioneng.2021.03.015.

[102] M. Krasilnikov et al. "Beam-based procedures for RF guns". *Proceedings of the IEEE Particle Accelerator Conference*. Vol. 2005. 2005. DOI: 10.1109/PAC.2005.1590627.

[103] J. Wang, D. Wang, and M. Reiser. "Beam emittance measurement by the pepper-pot method". *Nuclear Instruments and Methods in Physics Research Section A: Accelerators, Spectrometers, Detectors and Associated Equipment* 307 (1991), pp. 190–194. DOI: 10.1016/0168-9002(91)90182-P.

[104] A. W. Chao et al. "Space charge dynamics of bright electron beams". *Physical Review Special Topics - Accelerators and Beams* 6 (2003), p. 024201. DOI: 10.1103/PhysRevSTAB.6.024201.

[105] A. V. Fedotov. "Beam halo formation in high-intensity beams". *Nuclear Instruments and Methods in Physics Research Section A: Accelerators, Spectrometers, Detectors and Associated Equipment* 557 (2006), pp. 216–219. DOI: 10.1016/j.nima.2005.10.073.

[106] S. G. Kwak and J. H. Kim. "Central limit theorem: the cornerstone of modern statistics". *Korean Journal of Anesthesiology* 70 (2017), p. 144. DOI: 10.4097/kjae.2017.70.2.144.

[107] J. A. Holmes et al. "Space charge dynamics in high intensity rings". *Physical Review Special Topics - Accelerators and Beams* 2 (1999), p. 114202. DOI: 10.1103/PhysRevSTAB.2.114202.

[108] O. Tanaka et al. "New halo formation mechanism at the KEK compact energy recovery linac". *Physical Review Accelerators and Beams* 21 (2018), p. 024202. DOI: 10.1103/PhysRevAccelBeams.21.024202.

[109] R. Yang et al. "Numerical investigation of beam halo from beam gas scattering in KEK-ATF". *IPAC 2017 - Proceedings of the 8th International Particle Accelerator Conference*. 2017.

[110] L. Serafini and J. B. Rosenzweig. "Envelope analysis of intense relativistic quasilaminar beams in rf photoinjectors:mA theory of emittance compensation". *Physical Review E* 55 (1997), pp. 7565–7590. DOI: 10.1103/PhysRevE.55.7565.

[111] J. Qiang et al. "Three-dimensional quasistatic model for high brightness beam dynamics simulation". *Physical Review Special Topics - Accelerators and Beams* 9 (2006), p. 044204. DOI: 10.1103/PhysRevSTAB.9.044204.

[112] E. I. Gacheva et al. “Laser driver for a photoinjector of an electron linear accelerator (February 2014)”. *IEEE Journal of Quantum Electronics* 50 (2014). DOI: 10.1109/JQE.2014.2323472.

[113] B. Zhang et al. “High repetition-rate photoinjector laser system for S3FEL”. *Frontiers in Physics* 11 (2023). DOI: 10.3389/fphy.2023.1181862.

[114] G. De Stasio et al. “Feasibility tests of transmission x-ray photoelectron emission microscopy of wet samples”. *Review of Scientific Instruments* 71 (2000), pp. 11–14. DOI: 10.1063/1.1150151.

[115] S. Kapishnikov et al. “Oriented nucleation of hemozoin at the digestive vacuole membrane in Plasmodium falciparum”. *Proceedings of the National Academy of Sciences* 109 (2012), pp. 11188–11193. DOI: 10.1073/pnas.1118120109.

[116] A. Cruz-Adalia et al. “T Cells Kill Bacteria Captured by Transinfection from Dendritic Cells and Confer Protection in Mice”. *Cell Host & Microbe* 15 (2014), pp. 611–622. DOI: 10.1016/j.chom.2014.04.006.

[117] M. A. Le Gros et al. “Soft X-Ray Tomography Reveals Gradual Chromatin Compaction and Reorganization during Neurogenesis In Vivo”. *Cell Reports* 17 (2016), pp. 2125–2136. DOI: 10.1016/j.celrep.2016.10.060.

[118] M. Harkiolaki et al. “Cryo-soft X-ray tomography: using soft X-rays to explore the ultrastructure of whole cells”. *Emerging Topics in Life Sciences* 2 (2018), pp. 81–92. DOI: 10.1042/ETLS20170086.

[119] M. Benk et al. “Compact soft x-ray microscope using a gas-discharge light source”. *Optics Letters* 33 (2008), p. 2359. DOI: 10.1364/OL.33.002359.

[120] D. B. Carlson et al. “Laboratory-Based Cryogenic Soft X-Ray Tomography with Correlative Cryo-Light and Electron Microscopy”. *Microscopy and Microanalysis* 19 (2013), pp. 22–29. DOI: 10.1017/S1431927612013827.

[121] M. Berglund et al. “Cryogenic liquid-jet target for debris-free laser-plasma soft x-ray generation”. *Review of Scientific Instruments* 69 (1998), pp. 2361–2364. DOI: 10.1063/1.1148944.

[122] M. Wieland et al. “EUV and fast ion emission from cryogenic liquid jet target laser-generated plasma”. *Applied Physics B* 72 (2001), pp. 591–597. DOI: 10.1007/s003400100542.

[123] P. Skoglund et al. “High-brightness water-window electron-impact liquid-jet microfocus source”. *Applied Physics Letters* 96 (2010). DOI: 10.1063/1.3310281.

[124] V. Cardin et al. "Self-channelled high harmonic generation of water window soft x-rays". *Journal of Physics B: Atomic, Molecular and Optical Physics* 51 (2018), p. 174004. DOI: 10.1088/1361-6455/aad49c. URL: https://doi.org/10.1088/1361-6455/aad49c.

[125] G. K. Tadesse et al. "High speed and high resolution table-top nanoscale imaging". *Optics Letters* 41 (2016), p. 5170. DOI: 10.1364/OL.41.005170.

[126] A. Rockwood et al. "Compact gain-saturated x-ray lasers down to 685 nm and amplification down to 585 nm". *Optica* 5 (2018), p. 257. DOI: 10.1364/OPTICA.5.000257.

[127] M. Zürch et al. "Transverse Coherence Limited Coherent Diffraction Imaging using a Molybdenum Soft X-ray Laser Pumped at Moderate Pump Energies". *Scientific Reports* 7 (2017), p. 5314. DOI: 10.1038/s41598-017-05789-w.

[128] F. Albert and A. G. R. Thomas. "Applications of laser wakefield accelerator-based light sources". *Plasma Physics and Controlled Fusion* 58 (2016), p. 103001. DOI: 10.1088/0741-3335/58/10/103001. URL: https://doi.org/10.1088/0741-3335/58/10/103001.

[129] K. Sakaue et al. "Recent progress of a soft X-ray generation system based on inverse Compton scattering at Waseda University". *Radiation Physics and Chemistry* 77 (2008), pp. 1136–1141. DOI: 10.1016/j.radphyschem.2008.05.039.

[130] T. Gys. "Micro-channel plates and vacuum detectors". *Nuclear Instruments and Methods in Physics Research Section A: Accelerators, Spectrometers, Detectors and Associated Equipment* 787 (2015), pp. 254–260. DOI: 10.1016/j.nima.2014.12.044.

[131] S. Matsuura et al. "Characteristics of the Newly Developed MCP and Its Assembly". *IEEE Transactions on Nuclear Science* 32 (1985), pp. 350–354. DOI: 10.1109/TNS.1985.4336854.

[132] F. G. Kondev et al. "The NUBASE2020 evaluation of nuclear physics properties". *Chinese Physics C* 45 (2021), p. 30001. DOI: 10.1088/1674-1137/abddae. URL: https://doi.org/10.1088/1674-1137/abddae.

[133] W. Parkes, R. Gott, and K. A. Pounds. "Soft X-Ray Studies of Channel Multipliers and Multiplier Arrays". *IEEE Transactions on Nuclear Science* 17 (1970), pp. 360–366. DOI: 10.1109/TNS.1970.4325713.

[134] *MCP Assembly*. Tech. rep. Hamamatsu. URL: https://www.hamamatsu.com/content/dam/hamamatsu-photonics/sites/documents/99_SALES_LIBRARY/etd/MCP_TMCP1046E.pdf.

[135] C. Sun et al. “Energy and energy spread measurements of an electron beam by Compton scattering method”. *Physical Review Special Topics - Accelerators and Beams* 12 (2009), p. 062801. DOI: 10.1103/PhysRevSTAB.12.062801.

[136] T. Lefèvre. *Laser Wire Scanner*. Tech. rep. Geneva: CERN, 2002. URL: https://cds.cern.ch/record/535808.

[137] T. Shen et al. “Flexible Isosurface Extraction for Gradient-Based Mesh Optimization”. *ACM Transactions on Graphics* 42 (2023), pp. 1–16. DOI: 10.1145/3592430.

[138] T. Katayama et al. “X-ray optics for advanced ultrafast pump–probe X-ray experiments at SACLA”. *Journal of Synchrotron Radiation* 26 (2019), pp. 333–338. DOI: 10.1107/S1600577518018362.

[139] E. Esarey, S. K. Ride, and P. Sprangle. “Nonlinear Thomson scattering of intense laser pulses from beams and plasmas”. *Physical Review E* 48 (1993), pp. 3003–3021. DOI: 10.1103/PhysRevE.48.3003.

[140] Y. Y. Lau et al. “Nonlinear Thomson scattering: A tutorial”. *Physics of Plasmas* 10 (2003), pp. 2155–2162. DOI: 10.1063/1.1565115.

[141] M. Mirzaie et al. “All-optical nonlinear Compton scattering performed with a multi-petawatt laser”. *Nature Photonics* 18 (2024), pp. 1212–1217. DOI: 10.1038/s41566-024-01550-8.